

Diss.-No. ETH 23515

**PHOTOCATALYTICALLY ACTIVE LANTHANUM TITANIUM
OXYNITRIDES: AN INVESTIGATION OF STRUCTURAL,
ELECTRONIC AND PHOTOELECTROCHEMICAL PROPERTIES**

MARKUS PICHLER

DISS.-NO. ETH 23515

**PHOTOCATALYTICALLY ACTIVE LANTHANUM
TITANIUM OXYNITRIDES: AN INVESTIGATION OF
STRUCTURAL, ELECTRONIC AND
PHOTOELECTROCHEMICAL PROPERTIES**

A thesis submitted to attain the degree of
DOCTOR OF SCIENCES of ETH ZURICH

(Dr. sc. ETH Zurich)

presented by

MARKUS PICHLER

MSc Technical Physics, Vienna University of Technology

born on *27.09.1983*

citizen of Italy

accepted on the recommendation of

Prof. Dr. Alexander Wokaun (examiner)
Prof. Dr. Dr. *h.c.* Thomas Lippert (co-examiner)
Prof. Dr. Christophe Copéret (co-examiner)
Prof. Dr. Maria Dinescu (co-examiner)

2016

Contents

Table of Contents	v
Summary	ix
Zusammenfassung	xiii
1. Introduction	1
1.1. Motivation	1
1.2. Solar water splitting	5
1.2.1. Basics of the photoelectrochemical water splitting process .	5
1.2.2. Water Splitting Systems	8
1.2.3. Material requirements	11
1.2.3.1. Light absorbtion	11
1.2.3.2. Charge transport and separation	12
1.2.3.3. Stability	14
1.2.3.4. Efficiency	14
1.2.3.5. Low costs	17
1.2.4. Progress review of solar water splitting applications	17
1.2.4.1. Oxide materials for solar water splitting	17
1.2.4.2. Oxynitrides - shifting the response to visible light by anodic doping	19
1.2.5. Photocatalysts as thin films	31
1.2.6. Investigation of the electronic structure of oxynitrides . . .	33
1.3. Research questions and thesis outline	36
2. Methods	39
2.1. Thin Film Deposition	39
2.1.1. Pulsed Laser Deposition	39
2.1.1.1. Deposition of the current collector	41
2.1.1.2. Deposition of the Swiss Light Source samples . .	41
2.1.2. Pulsed Reactive Crossed-beam Laser Ablation	42

2.2. Thin Film Characterization	45
2.2.1. Chemical composition	45
2.2.2. Surface chemical analysis	46
2.2.3. Crystalline properties of thin films	48
2.2.4. Optical properties	48
2.2.5. Thickness measurements	50
2.2.6. Surface morphology and topography	51
2.2.7. Electronic structure (Measurements at the Swiss Light Source)	52
2.3. Photoelectrochemical Characterization	54
2.3.1. Photoelectrochemical test setup at EMPA	54
2.3.2. Photoelectrochemical test setup at PSI	55
3. X-ray spectroscopy experiments at the Swiss Light Source	57
3.1. Determination of conduction and valence band electronic structure of $\text{La}_2\text{Ti}_2\text{O}_7$ thin film	58
3.1.1. Results and discussion	58
3.1.2. Conclusion	61
3.2. Determination of conduction and valence band electronic structure of LaTiO_xN_y thin film	63
3.2.1. Results and discussion	63
3.2.2. Conclusion	72
4. Photoelectrochemical investigation of oxynitride thin films	73
4.1. Titanium nitride buffered substrates for photoelectrochemical measurements of oxynitride thin films	74
4.1.1. The current collector	74
4.1.2. The growth of the oxynitride photocatalyst on the selected current collector	78
4.1.3. Tuning the nitrogen content	81
4.1.4. Tuning the crystallographic properties	84
4.1.5. Proof of concept of the model system using photoelectro- chemical characterization	86
4.1.6. Conclusion	87

4.2. The role of the crystallographic surface orientation and chemical evolution of lanthanum titanium oxynitride in photoelectrochemistry	88
4.2.1. Thin film characterization	88
4.2.2. Photoelectrochemical characterization	94
4.2.3. Effect of the different crystallographic surface orientations on the visible light induced photocurrent	104
4.2.4. Conclusion	109
5. Final remarks	111
5.1. Conclusion	111
5.2. Outlook	114
Appendix	I
A. Photocatalytic Characterization	I
A.1. Introduction	I
A.2. Experimental	III
A.3. Short history of the preparation	V
A.4. Test measurements	VI
A.5. Measurement	XI
List of Figures	XIII
List of Tables	XVII
References	XIX
Acknowledgement	XXXIX

Summary

Our consumption of energy has drastically increased since the industrial revolution. Fossil fuels are a limited resource and will eventually be depleted. Furthermore, the combustion of fossil fuels has increased the atmospheric concentration of long-lived greenhouse gases (e.g. CO_2) and short-lived compounds (e.g. particulate matter, NO_x and SO_2). It is well noted that many of the combustion products are harmful towards health and the environment. Moreover, these emissions have led to the observation of global warming. To this end, sustainable energy resources must be developed and promoted in order to become independent of fossil fuels and preserve a sound environment.

Solar energy is one of the most promising sources of renewable and emission-free energy. While photovoltaic systems are already well established on the global energy market, they require adequate energy storage systems due to the intermittent nature of the sun. Thus, chemical fuels such as hydrogen offer an attractive alternative due to their transportability and accessibility. Hydrogen can be generated through so-called “artificial photosynthesis” whereby semiconducting materials act as photocatalysts that directly trigger the necessary water splitting reactions: namely hydrogen and oxygen evolution.

Since the 1970s, research into photocatalytic materials has been predominantly focused on oxide materials. The disadvantage of conventional oxide materials is the typically wide band gap, which requires photons with energies at least in the ultraviolet (UV) range to trigger water splitting reactions. The UV portion of the solar spectrum accounts for a small fraction of the solar spectrum (roughly 5 %). Thus, only a small amount of the total available energy is actually utilized.

Oxynitride materials offer high band gap tunability towards the visible light range, whereby oxygen may be partly substituted with nitrogen in the pristine oxide. In this thesis the lanthanum titanium oxynitride (LaTiO_2N) is investigated as a representative oxynitride material, where the nitrogen incorporation into the oxide ($\text{La}_2\text{Ti}_2\text{O}_7$) shifts the band gap energy from 3.8 eV to 2.1 eV. It is hypothesized that this is due to a hybridization of the oxygen and nitrogen or-

bitals forming energetically higher lying nitrogen states, thus shifting the valence band edge upwards in energy. It is widely accepted and confirmed with theoretical calculations that the nitrogen incorporation only affects the valence band, while the conduction band remains unchanged. However, experimental evidence to support this theoretical model remains elusive.

The first part of this thesis concentrates on determining how the incorporation of nitrogen into the oxide influences its electronic and optical properties. Samples with tunable nitrogen content were fabricated using a modified pulsed laser deposition technique, namely pulsed reactive crossed-beam laser ablation. To study the differences in electronic structure of the oxide and oxynitride, samples with the same crystalline structure were fabricated for X-ray absorption and emission spectroscopy measurements. In agreement with theoretical calculations, it was confirmed that additional states are formed at higher energy, which can be assigned to a hybridization of O 2p and N 2p orbitals resulting in an energetically upward shift of the valence band edge. However, an additional shift of the conduction band edge to lower energies was also observed, which was not predicted by theoretical calculations. This emphasizes the need to complement theoretical predictions with experimental observations.

An additional advantage of growing an oxynitride as a thin film is that both its nitrogen content and its crystalline properties may be controlled. Hitherto, investigating the relation between crystallographic surface orientation and photoelectrochemical activity has not been investigated in detail since this cannot be addressed by using conventional powder oxynitride samples.

However for photoelectrochemical investigations of oxynitride thin films to be possible a new sample design with stringent material properties has to be engineered. Lanthanum titanium oxynitrides, as with all oxynitride materials, are n-type semiconductors. Thus, they act as the photoanode and oxidize water by consuming photo-generated holes at the semiconductor surface. Therefore, this new model system requires a current collector that efficiently collects photo-generated electrons and transfers them to the counter electrode for the water reduction reactions. Besides being a good conductor, the current collector needs to be stable in a strongly reducing environment and at high temperatures ($> 800\text{ }^{\circ}\text{C}$) required for the oxynitride deposition. Furthermore, in order to grow

thin films with high crystalline quality and to control the crystallographic surface orientation, the current collector needs to exhibit proper lattice matching with the oxynitride material. TiN-coated substrates fulfill all these requirements imposed for a suitable current collector.

Initial photoelectrochemical experiments revealed a decrease of the measured photocurrent with the number of measurements. To elucidate the origin of this initial degradation we studied the material and found that the bulk remains unchanged, indicating a good stability of this material in the operando chemical environment. However, we observed that the surface changed during operation which resulted in a stronger oxidation of the top surface layers as determined by XPS. It should be noted that this surface evolution influences the photoresponse with time of operation and therefore a stabilization of the photocurrent of each sample is required for a further investigation. Thus, through our photocurrent stabilized measurements a strong influence of both the crystalline quality and crystallographic surface orientation on the photoresponse could indeed be found. Samples with higher crystalline quality generate a higher photocurrent and the choice of out-of-plane orientation of the oxynitride thin film samples could alter the performance of the system.

The application of X-ray spectroscopy to elucidate electronic structure and the development of a new model system to enable photoelectrochemical investigations has advanced our current understanding of oxynitrides. These newly developed competencies and investigatory frameworks can be used to further examine other photocatalytic-active oxynitride compounds, which may lead to the development of better photocatalysts.

Zusammenfassung

Seit der industriellen Revolution hat der globale Energiekonsum drastisch zugenommen. Der grösste Teil der Energie wird immer noch aus fossilen Brennstoffen gewonnen, die jedoch nur begrenzt auf der Erde vorhanden sind und stark klimaschädlich sind. Ihre Verbrennung führt zu einem weiteren Anstieg von langlebigen Treibhausgasen (zB. CO_2) und kurzlebigen Verbindungen (z. B. Feinstaub, NO_x , SO_2), welche schädlich für Gesundheit und Umwelt sind. Zusätzlich tragen sie massgeblich zu der heute beobachteten globalen Erderwärmung bei. Um eine gesunde Umwelt zu erhalten und unabhängig von fossilen Brennstoffen zu werden ist es deshalb wichtig, erneuerbare Energien zu entwickeln und zu fördern.

Solarenergie ist eine der vielversprechendsten alternativen Energiequellen, die sowohl erneuerbar als auch emissionsfrei ist. Während Photovoltaikanlagen sich bereits gut auf dem globalen Energiemarkt etabliert haben, bedarf es zusätzlich noch angemessene Energiespeichersysteme, die die unregelmässige Verfügbarkeit der Sonne kompensieren. Chemische Brennstoffe wie Wasserstoff sind leicht transportierbar und allgemein zugänglich. Aufgrund dieser Vorteile, stellen sie eine attraktive Alternative zu fossilen Brennstoffen dar. Wasserstoff kann mittels der sogenannten “künstlichen Photosynthese” aus Wasser hergestellt werden. Ein Halbleitermaterial fungiert dabei als Fotokatalysator der die beiden benötigten Reaktionen zur Wasserspaltung - die Freisetzung von Wasserstoff und Sauerstoff - steuert.

Seit den 1970er Jahren befasst sich die Forschung mit Strategien zur Entwicklung von geeigneten fotokatalytischen Materialien, wobei der Fokus überwiegend auf Oxiden liegt. Der Nachteil von herkömmlichen Oxiden ist die üblicherweise grosse Bandlücke, die es nur Lichtenergien im ultravioletten (UV) Bereich erlaubt, die Wasserspaltung auszulösen. Der Anteil an UV Strahlung ist allerdings nur ein Bruchteil des gesamten zur Verfügung stehenden Sonnenspektrums (circa 5%). Daher kann nur ein kleiner Teil der verfügbaren Sonnenenergie von Oxiden genutzt werden.

Die Gruppe der Oxynitride verfügt über eine besondere Eigenschaft: Ihre Bandlücke ist variabel und kann in Richtung sichtbaren Lichtbereich verscho-

ben werden. Dies kann durch die Substitution von Stickstoff durch Sauerstoff erreicht werden. Diese Eigenschaft wird in der hier vorgelegten Dissertation an einem repräsentativen Oxynitrid, dem Lanthan Titan Oxynitrid mit der chemischen Formel LaTiO_2N , untersucht, dessen Bandlücke durch Einbau von Stickstoff von 3.8 eV zu 2.1 eV verringert wird. Es wird angenommen, dass durch die Hybridisierung der Sauerstoff- und neu eingebauten energetisch höher liegenden Stickstofforbitale zusätzliche elektronische Zustände gebildet werden, welche eine Verschiebung der Valenzbandgrenze hin zu höheren Energien bewirken. Es ist allgemein anerkannt, dass der Einbau von Stickstoff nur das Valenzband beeinflusst, während das Leitungsband unverändert bleibt. Diese Annahme wurden zudem durch theoretische Berechnungen untermauert. Allerdings steht eine experimentelle Bestätigung dieses theoretischen Modells noch aus.

Im ersten Teil dieser Dissertation wird der Einfluss der Sauerstoffs substitution durch Stickstoff auf die elektronischen und optischen Eigenschaften von Oxynitriden untersucht. Mittels eines modifizierten Verfahrens des Laserstrahlverdampfens (englische Bezeichnung: Pulsed Reactive Crossed-beam Laser Ablation) können Oxynitrid Dünnschichtfilme produziert werden, deren Stickstoffanteil genau eingestellt werden kann. Um die Unterschiede in der elektronischen Struktur der Oxide und Oxynitride zu untersuchen, wurden Proben mit derselben kristallinen Struktur für die Röntgenabsorptions- und Röntgenemissionsspektroskopie hergestellt. Es konnte gezeigt werden dass durch die Hybridisierung von O 2p und N 2p Orbitalen tatsächlich zusätzliche elektronische Energiezustände oberhalb des Valenzbandes gebildet werden, die zu einer Verschiebung der Valenzbandkante hin zu höheren Energien führen. Durch diese Erkenntnis wurden die theoretischen Vorhersagen erfolgreich bestätigt. Jedoch wurde eine zusätzliche Verschiebung des Leitungsbandes zu niedrigeren Energien beobachtet, welche bisher noch nicht theoretisch vorausberechnet wurde. Dies unterstreicht die Notwendigkeit, theoretische Prognosen mit experimentellen Beobachtungen zu ergänzen.

Ein weiterer Vorteil dieser Oxynitrid dünnschichtfilme besteht darin, dass sowohl der Stickstoffanteil als auch die kristallinen Eigenschaften einfach kontrolliert werden können. Bisher konnte die Beziehung zwischen Orientierung der Kristalloberfläche und der fotoelektrochemischen Aktivität nicht im Detail untersucht werden, da dies mit konventionellen Oxynitridpulverproben nicht möglich ist. Um diese Untersuchungen zu ermöglichen, musste ein neues Design für die

Oxynitridproben mit strikten Materialeigenschaften entwickelt werden. LaTiO_2N , wie alle Oxynitride, sind n-Typ-Halbleiter und können daher als Fotoanode fungieren, die das Wasser durch den Verbrauch von Löchern an der Halbleiteroberfläche oxidieren. Das neue Modellsystem benötigt daher einen Stromabnehmer, der die durch Lichtenergie erzeugten Elektronen effizient einsammelt und zur Gegenelektrode transferiert, damit diese dort die Reaktionen für die Reduktion von Wasser durchführen können. Neben der guten Leitfähigkeit, muss der Stromabnehmer in der stark reduzierenden Umgebung und bei den hohen Temperaturen ($> 800^\circ\text{C}$), die während der Abscheidung des Oxynitriddünnfilms herrschen, stabil sein. Ausserdem, um Dünnfilme mit hoher kristalliner Qualität und bestimmter Orientierung der Kristalloberfläche herzustellen, müssen die Kristallgitter des Oxynitrid und des Stromabnehmer angepasst sein. TiN -beschichtete Substrate erfüllen alle vorher genannten Erfordernisse und eignen sich daher hervorragend als Stromabnehmer.

Erste fotoelektrochemische Experimente zeigten eine Abnahme des gemessenen Fotostroms mit zunehmender Anzahl von Messungen. Um den Ursprung dieser Verringerung zu erklären, wurden die Oxynitriddünnfilme genauer untersucht. Es wurde festgestellt, dass die Zusammensetzungen der Gesamtprobe an sich unverändert blieb und damit das Material höchstwahrscheinlich stabil in der chemischen Umgebung ist. Mittels XPS wurde allerdings gezeigt, dass die oberen Materialsichten durch die fotoelektrochemischen Experimente oxidiert wurden, was wiederum den Fotostrom stark beeinflusst. Da sich dieser Einfluss aber mit Dauer der Messung minimalisiert, muss vor jeder Messung der Fotostrom stabilisiert werden. Durch die Messungen unter Verwendung des stabilisierten Fotostroms konnte sowohl ein starker Einfluss der kristallinen Qualität als auch der Oberflächenorientierung auf den Fotostrom festgestellt werden. Es wurde gezeigt, dass Proben mit hoher kristalliner Qualität einen höheren Fotostrom produzieren können. Ebenso konnte mit der Wahl der Oberflächenorientierung des Oxynitriddünnfilms die Aktivität des Materials positiv beeinflusst werden.

Unser gegenwärtiges Verständnis von Oxynitriden konnte durch die Kombination von Röntgenspektroskopie zur Aufklärung elektronischer Strukturen und der Entwicklung eines neuen Modellsystems zur Messung fotoelektrochemischer Eigenschaften stark vorangebracht werden. Diese neu entwickelten Kompetenzen und Fähigkeiten ermöglichen weitergehende Untersuchungen von anderen Mate-

rialen aus der Familie der Oxynitriden, welche fotokatalytisch aktiv sind, was wiederum zur Entwicklung und Entdeckung von besseren Fotokatalysatoren führen kann.

1

Introduction

1.1. Motivation

Since the beginning of the industrial revolution (about 1850), the global energy demand has increased exponentially (Fig. 1.1). This increase is on one hand due to the increase in population and on the other due to the improved living standards enabled by accessibility of fossil fuels. Currently about 80% of the world's energy economy rely on fossil fuels, which will be depleted eventually^[1]. The increased combustion of these energy resources has caused the increase of greenhouse gases in the atmosphere (see CO₂ concentrations in Fig. 1.1) leading to the observed increase in global mean temperature, also known as global warming^[2]. Besides the long-lived greenhouse gases influencing the Earth's climate (such as CO₂), short-lived gases and particles are also emitted by the same sources such as soot, NO_x, SO₂ and particulate matter which influence not only the climate, but also cause adverse health effects for the environment and mankind^[2]. The possible and dramatic consequences of this anthropogenic influence is summarized in the fifth assessment report of the United Nations Intergovernmental Panel on Climate Change (IPCC)^[2]. Nevertheless, the demand of energy will further increase in the future and therefore Earth's atmosphere will be continuously influenced if we do not become independent from fossil fuels. Thus, alternative energy sources to replace the extensively used fossil fuels are needed in order to supply the energy demand *and* to maintain a sound environment.

Several sustainable energy sources offer an alternative to hydrocarbon fuels. Wind turbines, solar panels or hydroelectric systems which convert the kinetic energy from wind, solar energy or the energy of flowing or falling water into electrical power, respectively, are renewable resources already available on the energy

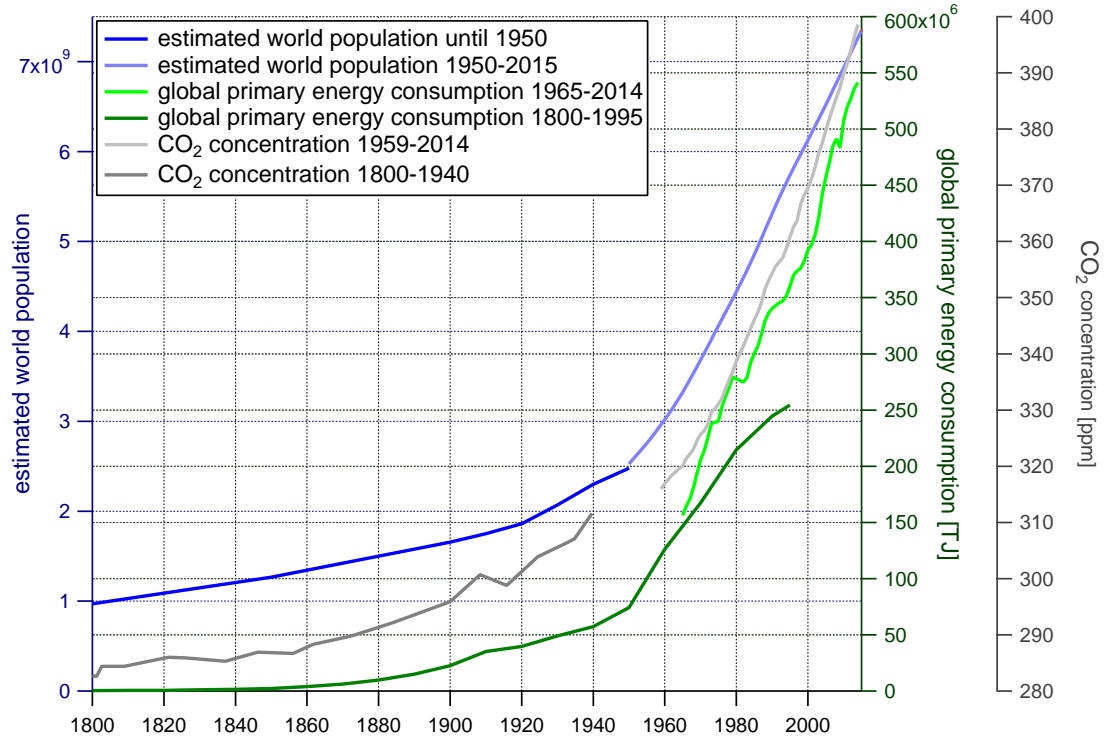


Figure 1.1.: Estimated world population (left axis): historical estimation until 1950 (dark blue)^[3], actual recorded population from 1950 to 2015 (blue), global primary energy consumption (right axis): estimation from 1965 to 2014 (green)^[4], estimation from 1800 to 1995 (dark green)^[5], CO₂ concentration (second right axis): CO₂ concentration from West Antarctic Ice Sheet Divide ice cores (dark gray)^[6] CO₂ annual mean data from Mauna Loa (gray)^[7]

market. Even though renewable and sustainable energy sources will not cover the energy demand in the near future, it is highly desirable to strongly increase their contribution to the total energy generation in the long term. This is only possible if society and politics are willing to undergo the necessary changes. Science is in charge of pushing forward the development of renewable and sustainable energies. Efficient and economical techniques are required not only to improve the output and increase the usability, but also for the acceptance in the world's society.

Among the available renewable energy sources, only solar energy has the potential to provide energy to supply the global energy needs without the emission of additional greenhouse gases after production^[8]. The technology with the currently highest impact that uses solar energy is photovoltaic for the generation of electricity. Even though photovoltaic technologies have the potential to supply

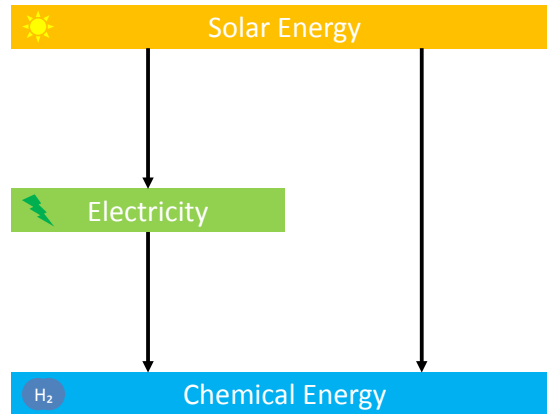


Figure 1.2.: Two ways of hydrogen production by using solar energy: Combination of photovoltaic and electrolysis or directly with photocatalytic water splitting

the global energy demand, they are not able to do so yet. Assuming a future energy demand of 20 TW, and a solar cell with 10 % conversion efficiency solar cells, an area of about 816 000 km² is required, which is approximately the area of France and Germany combined^[8]. A 24/7 production during 365 days per year of 650 m² of solar cell panels per second for the next 40 years would be necessary to realize such an undertaking^[8]. Additionally it is necessary to store the produced energy due to the intermittent nature of solar radiation.

How to store solar energy will be a key question in future renewable energy economy. Several storage methods are available such as batteries, pumped water reservoirs and chemical fuels (hydrogen, methane, methanol and other liquid hydrocarbon fuels). The advantage of the latter is the transportability and accessibility. Especially hydrogen is of large interest. The energy stored in the hydrogen bonds is easily released via the reaction with oxygen and only produces water as reaction product^[8]. Hydrogen fuel production currently relies to a major extent on fossil fuels (> 95 %^[8]). Using non-renewable energy, hydrogen is either refined via steam reforming and subsequent solid fuel gasification or (to a minor extent) via water electrolysis^[9].

There are sustainable alternatives to produce hydrogen. In a first step electricity from fossil fuels can be replaced by electricity originating from renewable energy sources such as photovoltaic. Photovoltaic-electrolysis is the second step process, which then generates the chemical fuel via electrolysis (Fig. 1.2). Alternatively, solar light could be directly used to split water. The idea of photoelectro-

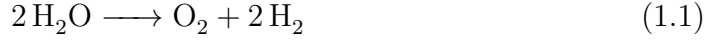
chemical (PEC) decomposition of water into hydrogen and oxygen was conceived in 1972 using TiO_2 as photocatalyst^[10] which induced numerous studies on this topic proving and discussing the possibility of heterogeneous photocatalytic water splitting^[11–13]. However, solar water splitting still remains a challenging task as the photocatalytic material needs to fulfill various requirements such as low costs, low or no toxicity, efficient light absorption and high photoconversion efficiency.

Besides conventional semiconductors^[14–17], wide band gap semiconductor oxides are the most studied solar water splitting systems, however their band gap only absorbs solar light in the UV range, which only comprises a few percentage of the total solar spectrum^[10–13,18]. By replacing oxygen ions in the crystal lattice of metal oxides partially (or fully) with nitrogen ions, oxynitrides (or nitrides) can be produced which can absorb solar light in the visible light range^[19,20]. This is because the N 2p orbitals have a higher energy than the O 2p orbitals, thus shifting the valence band upwards in energy and reducing the band gap. First successful tests with oxynitrides were only reported in 2002^[21,22].

1.2. Solar water splitting

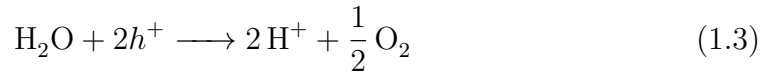
1.2.1. Basics of the photoelectrochemical water splitting process

Water splitting is the decomposition of water to molecular hydrogen and oxygen, which is an endothermic reaction, i.e. it requires additional energy to take place, as can be seen from the positive change in Gibbs free energy ΔG° [8,23,24].



$$\Delta G^\circ = +237.2 \text{ kJ mol}^{-1} \quad (1.2)$$

Water splitting can be achieved via electrolysis (see Fig. 1.3a). During this process two electrodes are brought in contact with water while an electric potential is applied between anode and cathode resulting in an electric current. The theoretical minimum potential difference to split water is 1.23 V. However, an excess energy is always needed (so-called overpotential) to overcome certain energy barriers and thus to enable the electrochemical water splitting reactions. Therefore, cell voltages of usually more than 1.6 V are required [25] to oxidize H_2O to O_2 at the anode and reduce H_2O to H_2 at the cathode. To drive these chemical reactions, the energy of the Fermi level of the anode has to be lower than the highest occupied molecular orbital (HOMO) of the species to be oxidized. By consuming a hole h^+ in the anode (transferring an electron e^- from the adsorbed species to the anode) the oxidation is performed [8,23].



In the same way, the energy of the Fermi Level of the cathode has to be higher than the lowest unoccupied molecular orbital (LUMO) of the species to be reduced. Here, the electron is transferred from the cathode to the adsorbed species to perform the reduction process [8,23].

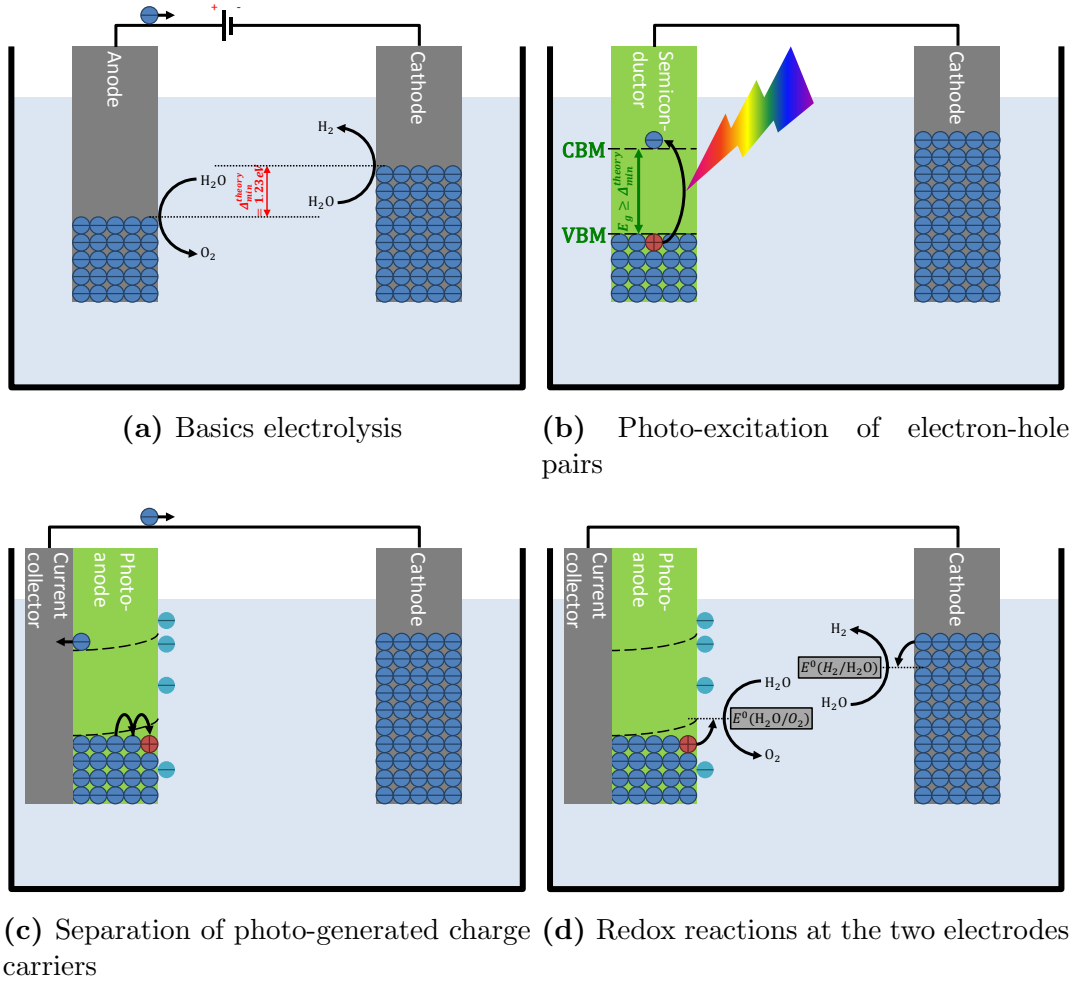


Figure 1.3.: (a) Schematic of the principle of electrolysis. A minimum applied voltage of 1.23 V (usually > 1.6 V due to overpotentials^[25]) between the two electrodes is needed to split H_2O into its constituents, thus H_2 and O_2 . (b) In PEC water splitting, at least one of the electrode is replaced by a semiconducting material, which is illuminated to generate electron-hole pairs. (c) Adsorption of ions (here anions) from the solution on the photoelectrode forms a space-charge layer at the surface of the semiconductor needed for charge separation. For a proper transfer of the the charge carriers (here electrons) to the counter electrode, a current collector is needed. (d) Oxidation of H_2O to O_2 with the holes at the photoanode and reduction of H_2O to H_2 with the electrons at the cathode.



The photoelectrochemical water splitting process is basically electrolysis

driven by light. To perform water splitting with light, at least one electrode is replaced by a semiconducting material, where the incident light has enough energy to excite electrons from the valence band (VB) to the conduction band (CB) forming electron-hole pairs (Figure 1.3b):



with h the Planck's constant and ν the frequency of the photon. To avoid unwanted recombination of the photo-generated charge carriers, electrons and holes have to be separated. The charge carrier separation is driven by the built-in electric field formed in the semiconductor close to the semiconductor/liquid interface.

Figure 1.3c shows an example of using a n-type semiconductor with mainly adsorbed anions from the solution. This forms a depletion of the majority charge carriers (electrons) at the surface of the semiconductor resulting in an excess of positive charges, the space-charge layer. The effect of this space-charge layer is the upward bending of the CB and VB close to the interface semiconductor/liquid and the consequent separation of the photo-generated charge carriers. While the holes are driven to the surface of the semiconductor, the electrons are transferred via the external circuit to the counter electrode (CE). This defines the semiconductor as the photoanode and the CE as the cathode. Analogous considerations can be done for a p-type semiconductor.

In theory, using a semiconductor with a band gap (E_g) larger or equal to 1.23 eV as indicated in Figure 1.3b ($E_g^{calc,min} = 1.23$ eV), the excited electron would have enough energy to perform the water reduction process (neglecting overpotentials). However, in the same way as for electrolysis, the highest energy state in the VB (VB maximum - VBM) has to be lower than the oxidation potential of water ($E^0(\text{H}_2\text{O}/\text{O}_2)$), which allows the transfer of the holes into the solution. Further, the lowest energy state in the CB (CB minimum - CBM) has to be higher than the reduction potential of water ($E^0(\text{H}_2/\text{H}_2\text{O})$), which allows the transfer of the electrons into the solution (Figure 1.3d). In other words, the band gap has to straddle the reduction and oxidation potentials of water as visualized in fig. 1.4.

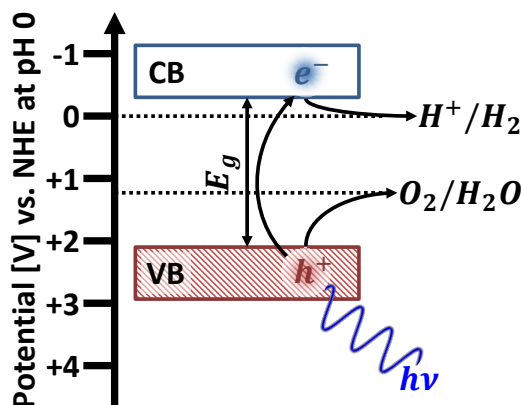


Figure 1.4.: Valence and conduction band position for straddling the reduction and oxidation potentials of water.

With the fact that a perfect matching of the energy state of the semiconductor's VBM and CBM with the oxidation and reduction potential, respectively, is not possible and that overpotentials are inevitable, the required band gap for the photoelectrochemical water splitting process increases ($E_g > 1.70 \text{ eV}$ [8,26,27]).

1.2.2. Water Splitting Systems

Above we considered the photoelectrochemical water splitting system used in this thesis where hydrogen and oxygen evolution take place on spatially separate electrodes. In this section I will shortly introduce alternative water splitting systems (Fig. 1.5).

Fig. 1.5a schematically shows a photoelectrochemical water splitting system using a photoanode as introduced above. An alternative version is depicted in Fig. 1.5b, where the photoanode is replaced by a photocathode. For this, a p-type semiconductor such as Cu_2O , $\text{Cu}(\text{InGa})\text{S}_2$ or GaInP_2 [27] is required for the hydrogen evolution, while oxygen evolution occurs at the counter electrode.

Fig. 1.5c shows a system in the so-called tandem configuration, which consists of a photoanode for the oxygen and a photocathode for the hydrogen evolution. In contrast to the systems depicted in Fig. 1.5a and Fig. 1.5b, which show a single step excitation system, the tandem configuration system is a two step excitation system. I.e., for the same number of photoelectrochemical reactions, twice as many photons are required in the tandem configuration system compared

to the single photoelectrode systems. In the case of the single photoelectrode system the band gap of the semiconductor has to straddle the redox potentials of hydrogen and oxygen evolution; by contrast, for the tandem configuration setup this is not required for each photocatalyst. One photocatalyst aims for hydrogen evolution and the other of oxygen evolution. For the photoanode the VBM has to be energetically lower compared to the oxygen evolution potential. For the photocathode the CBM has to be energetically higher compared to the hydrogen evolution potential. Many semiconductors do not straddle the redox potentials of hydrogen and oxygen evolution and cannot be used for the single photoelectrode system. These semiconductors can instead be used in a tandem configuration setup. Furthermore these semiconductors used in a tandem configuration setup can have a smaller band gap, since an ideal matching of the VBM and CBM is not required and the overpotentials of hydrogen and oxygen evolution are distributed to the corresponding photoelectrode.

In photocatalytic (PC) systems using one-step excitation (Fig. 1.5d), the semiconducting material has to fulfill the same requirements as for PEC systems, thus efficient charge carrier separation and the band gap has to straddle the oxidation and reduction potential of water (see section 1.2.1). In contrast to PEC systems, in PC systems the semiconductor photocatalyst is suspended in form of powder in the electrolyte and each particulate act as a microelectrode. That means, hydrogen and oxygen evolution take place on the surface of the same particle, while for PEC systems the hydrogen and oxygen evolution evolves at different and separated electrodes. This makes the charge separation easier in a PEC system, but in a PC system the charge carriers reach the surface faster since there is no external circuit.

Accordingly, the water splitting reaction products can be separated in a PEC system due to a spatially separated production, but not in a single excitation PC system. This separation in a PEC system can be achieved with a membrane (e.g. a porous glass filter) located between the two photoelectrodes.

A separation is possible with a two excitation step PC system, the so-called Z-scheme (see Fig. 1.5), where two photocatalysts are suspended in an electrolyte^[29]. One photocatalyst is again used for hydrogen evolution and the other for oxygen evolution. These two semiconducting materials are connected via an elec-

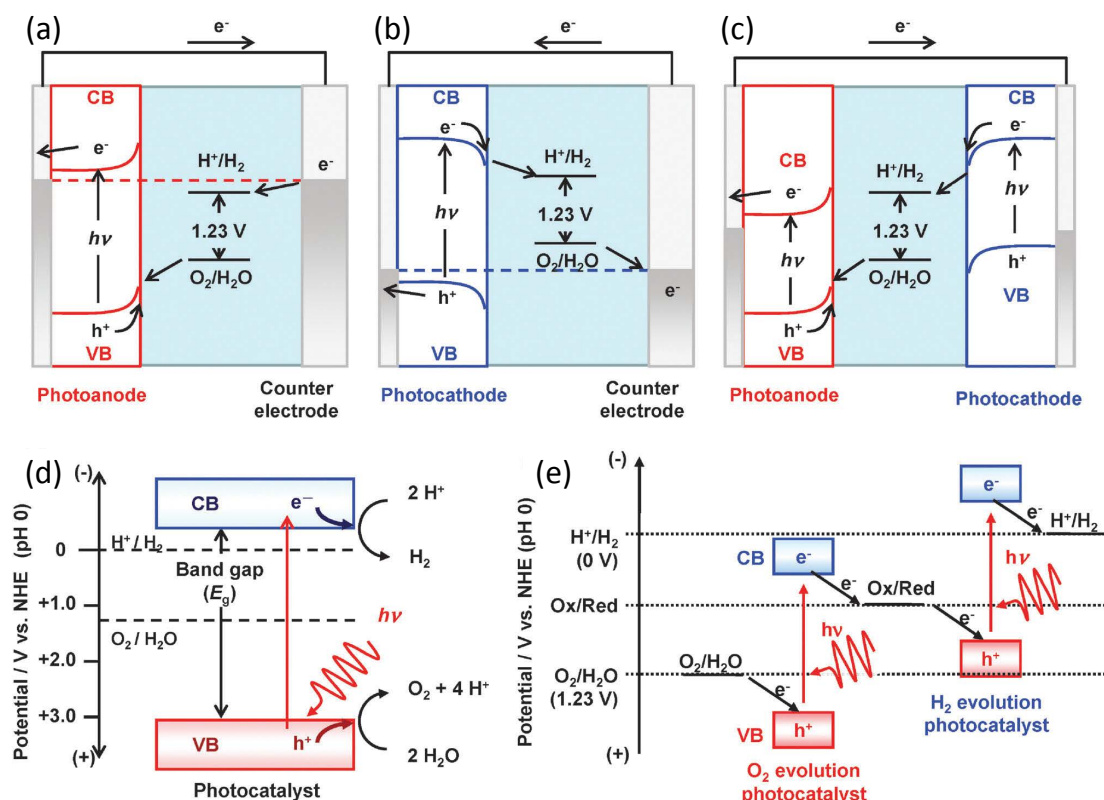


Figure 1.5.: To summarize alternative water splitting systems. (a) photoelectrochemical water splitting system using a photoanode (b) photoelectrochemical water splitting system using a photocathode (c) photoelectrochemical water splitting system using a photoanode and photocathode in tandem configuration. (d) photocatalytic water splitting system based on one-step excitation (e) photocatalytic water splitting system based on two-step excitation (Z-scheme). The tandem cell configuration (c) and the Z-scheme (e) allow the usage of semiconductors with smaller band gaps. (Figure modified from [28]).

tron transfer mediator. The electron transfer mediator is a redox couple, which is reduced at the oxygen evolution photocatalyst and oxidized at the hydrogen evolution photocatalyst.

Similar to the tandem configuration PEC system, the Z-scheme requires twice as many photons compared to single excitation PC systems.

For all these systems typically co-catalysts were used [30]. The favored co-catalysts are typically based on noble metals such as Ir [31], Ru [32], Rh [33], Pd [34], Pt [35], Au [36], and Ag [34]. While Pt is mainly loaded as metal, noble metal oxides such as RuO_2 [37], Rh_2O_3 [37] and IrO_2 [21] are used as well as co-catalysts. How-

ever, noble metals are not abundant and too expensive for a large-scale hydrogen generation. Promising earth-abundant and inexpensive co-catalysts for O_2 evolution are NiO_x [37], Co_3O_4 [38], CoO_x [39], cobalt phosphate (Co-Pi) [40], MnO_x [41], FeO_x [41] and Cu [42].

1.2.3. Material requirements

The requirements on photoelectrode materials are high. In the following we shall discuss the most important factors in more detail:

1.2.3.1. Light absorbtion

The maximum of the solar light spectrum lies in the visible and infrared light range (see Fig. 1.6). Conventional photocatalysts are mainly oxides of transition metals. These materials have a rather large band gap due to their high ionic character [27]. This leads to a large distance between the valence band composed of O 2p orbitals and the conduction band composed of empty d bands (d^0 cations), making these materials inefficient for the use of visible light. Thus, only a small fraction of the total solar energy can be harvested. To increase the usability additional states have to be inserted above the valence band edge for an energetic upwards shift of the valance band, thus reducing the band gap and increasing the harvestable portion of the solar spectrum. This is done via doping of the native oxides, which will be discussed in more detail in section 1.2.4.

Additionally, light absorption does strongly depend on the wavelength λ which can be described by the Lambert-Beer law [43]

$$I(\lambda) = I_0 e^{-\alpha(\lambda) \cdot d} \quad (1.6)$$

with I_0 the incident light intensity, d the penetration depth of the photons in the material and α the wavelength and material dependent absorption coefficient. The latter defines where the photons are absorbed and produce electron-hole pairs. The amount of charge carriers participating in the electrochemical reactions, will depend on the location of the excitation, and the charge transport and separation, as will be discussed in the following section.

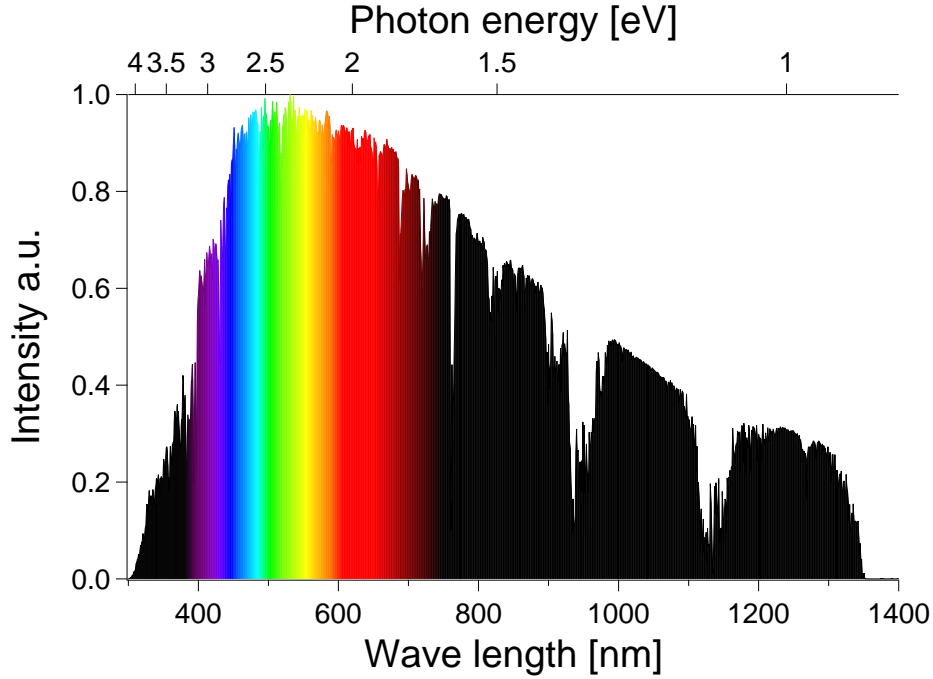


Figure 1.6.: Reference Solar Spectral Irradiance: Air Mass 1.5 from Ref. ^[44] showing the direct and circumsolar radiation.

1.2.3.2. Charge transport and separation

Before the produced electron-hole pairs can participate in the electrochemical reactions, they need to be separated and transported to the reaction site before they recombine. As described in section 1.2.1, the charge carriers can be separated via the built-in electric field to reach to surface.

In the case of an n-type semiconductor, the majority charger carriers are electrons and the minority charge carriers are holes. In such a photoanode the holes drive the oxygen evolution reactions. For this they have to diffuse to the surface. The minority carrier diffusion length L_p is expressed as ^[45]

$$L_p = \sqrt{D\tau} = \sqrt{\frac{kT\mu\tau}{q}} = \sqrt{\frac{kT\tau^2}{m^*}} \quad (1.7)$$

with D the diffusivity of the free carrier, τ the carrier lifetime, k the Boltzmann constant, T the temperature, μ the carrier mobility, q the elementary charge and m^* the effective mass of the minority charge carrier. The diffusion

length also depends on impurities and crystal defects. These introduce favorable energy levels for recombination^[46]. Thus, the reported diffusion length in metal oxides are shorter compared to high purity semiconductors such as silicon^[47].

The charge-carrier separation depends on the band bending (the built-in electric field described in section 1.2.1). The band bending occurs in the so-called space-charge width L_{SC} , which can be estimated as follows^[45]:

$$L_{SC} = L_D \left[\frac{2q(V - V_{fb})}{kt} \right]^{1/2} \quad (1.8)$$

with L_D the Debye length, V the applied potential, V_{fb} the flat band potential. L_D is defined as:

$$L_D = \sqrt{\frac{\epsilon_0 \epsilon kT}{q^2 (n_0 + p_0)}} \quad (1.9)$$

with ϵ_0 and ϵ the vacuum and the relative dielectric constant, respectively, and n_0 and p_0 are the electron and hole concentration in the semiconductor, respectively. In an n-type semiconductor $n_0 \gg p_0$, whereby $n_0 \approx n_D$, with n_D the donor concentration^[8].

As a consequence L_{SC} depends on the donor concentration as well as on the applied potential, whereby high charge carrier concentrations lead to a small L_{SC} . L_{SC} typically ranges from several nanometres to micrometres^[48,49].

Depending on where the electron-hole pairs are produced they will recombine or be able to participate in the water splitting process. If the photon penetrates deep within the material and produces charge carriers there, it is very unlikely that the minority carrier will reach the surface before recombination. If the electron-hole pairs are produced within the space-charge layer, the charge carriers will be efficiently separated and the minority charge carrier transported to the surface enabling the corresponding electrochemical reactions. Here the diffusion length L_p plays a role. Even if electron-hole pairs are produced away from the space-charge layer but within the diffusion length L_p , a fraction of those will reach the space-charge layer via diffusion. Summarizing, high crystalline quality and purity allows for a high diffusion length, which enables the charge carriers to

diffuse to the space-charge layer, where space separation and transport to the surface is possible, allowing for the relevant reactions at the surface. Still, the photoelectrode should be thick enough to absorb all photons.

1.2.3.3. Stability

During photoelectrochemical water splitting, the photocatalyst has to be chemically and structurally stable in the aqueous solution. Photocorrosion can take place if the produced charge carriers are not used for the water splitting reactions, but to oxidize or reduce the photocatalyst itself. This happens if the chemical reaction of the (anodic or cathodic) decomposition is energetically favorable compared to the chemical decomposition of water. However, large band gap photocatalysts (band gap > 3 eV) have been found to be very stable in terms of photocorrosion^[50,51]. Further, the decomposition of the photocatalyst can be minimized if the kinetics of the decomposition reactions are slower than the hydrogen and oxygen evolution reactions. As examples, TiO_2 and Fe_2O_3 are stable materials for water oxidation, even though their anodic decomposition potentials are energetically higher^[8,52]. For other materials prone to photocorrosion, co-catalysts or protection layers can be used to overcome the stability issue^[53,54].

1.2.3.4. Efficiency

The efficiency of the photoelectrochemical activity is closely related to the conversion of the photon energy to chemical energy. The band gap determines which fraction of the incident photons can be absorbed. This inevitably defines the upper limit of efficiency. Photons with energies below the band gap ($h\nu < E_g$) are not absorbed, photons with energies above the band gap energy ($h\nu > E_g$) create electron-hole pairs, which may contribute to the electrochemical reactions. As mentioned in section 1.2.1, the theoretical minimum energy that is required for solar water splitting is $E_g^{\text{calc},\text{min}} = 1.23$ eV. This energy corresponds to a photon with the wavelength of approximately 1000 nm according to Fig. 1.6. Photons with a higher wavelength do not allow for solar water splitting due to the too low energy. This applies to about 24.5% of the solar spectrum, which cannot produce enough energy to enable the required chemical reactions. Accounting

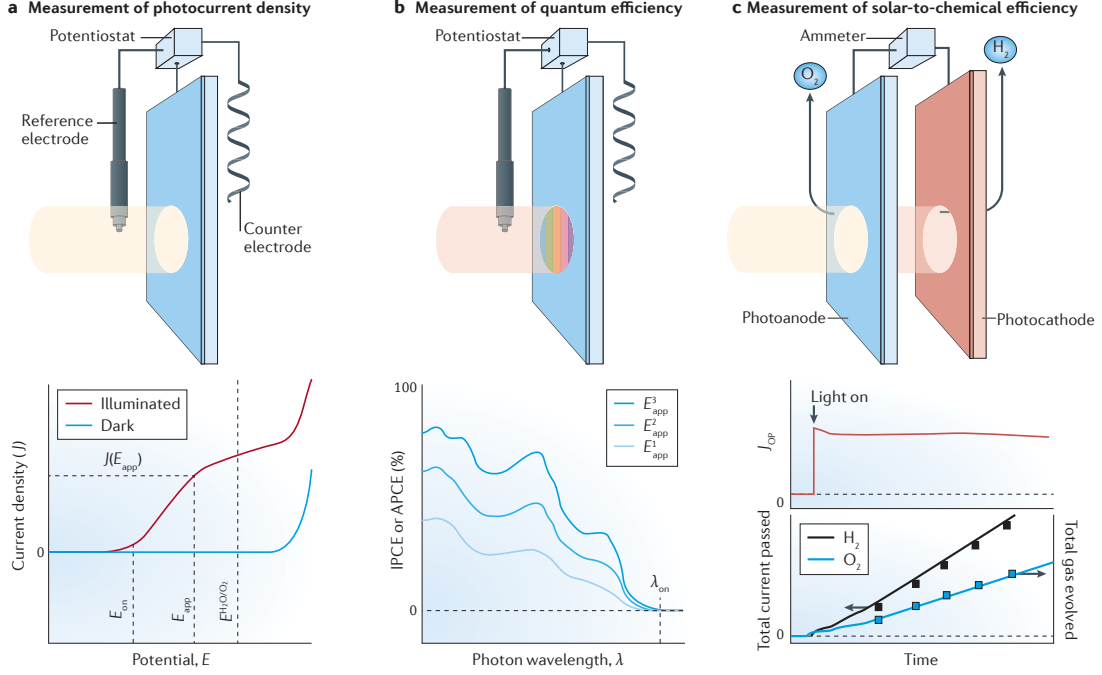


Figure 1.7.: Measurements used for efficiency calculations (Figure modified from Ref. [27]).

for the overpotentials for hydrogen and oxygen evolution reactions (about 0.3 eV to 0.4 eV [55]), the required energy increases to about 1.70 eV. Thus, the solar energy that cannot be used further increases to about 49.0%. Considering a minimum band gap value of 2.03 eV according to Ref. [56] increases the solar energy loss up to 64.7%. Having a band gap in the UV range, e.g. 3.20 eV of TiO_2 , only 3.7% of the solar spectrum can be used. These considerations highlights the need of reducing the band gap of the photocatalyst to target higher efficiencies. Due to thermodynamic and kinetic limitations, the band gap of the photocatalyst for one-step excitation is significantly higher compared to the theoretical minimum. Therefore, the previously described Z-scheme and tandem cells configurations are very attractive alternatives to achieve high efficiencies for solar water splitting [8, 36, 57].

In PEC, different definitions of efficiency are used (see Fig. 1.7) [8, 23, 27].

The overall efficiency of a PEC system is described by the solar-to-hydrogen efficiency (STH) measured in a two-electrode configuration. This term relates the converted chemical energy to the input solar energy (Fig. 1.7c):

$$STH = \frac{J_{sc} \times 1.23 \text{ V} \times \eta_F}{P_{in}} \quad (1.10)$$

with J_{sc} the short-circuit photocurrent density, η_F the faradaic efficiency, P_{in} the total light intensity and the value 1.23 V from the Gibbs free energy ΔG° of the reaction.

When applying an external potential E_{app} , the STH value does not reflect the true solar-to-hydrogen efficiency anymore, as the photocurrent typically increases with the applied potential. Instead the applied-bias photon-to-current efficiency (ABPCE) can be used as follows:

$$ABPCE = \frac{J_{ph} \times (E^{H_2O/O_2} - E_{app})}{P_{in}} \quad (1.11)$$

where J_{ph} is the measured photocurrent density at the applied potential E_{app} in a three-electrode configuration (Fig. 1.7a), E^{H_2O/O_2} is the water oxidation potential (1.23 V vs. reversible hydrogen electrode (RHE)) and P_{in} is the power density of the used illumination. This efficiency is mainly used as diagnostic measurements during material development. However, increasing the potential to values higher than the thermodynamic water splitting potential (1.23 V vs. RHE), one needs to be careful if the PEC system is still more advantageous compared to a standard electrolysis system without light.

For PEC, the incident-photon-to-current (IPCE) efficiency is a useful measure. It relates the produced current to the number of incident photons in dependence of the wavelength λ :

$$IPCE(\lambda) = \frac{J_{ph}(\lambda) \times \frac{hc}{e}}{P_{in}(\lambda) \times \lambda} \quad (1.12)$$

with $J_{ph}(\lambda)$ the photocurrent density at wavelength λ and $P_{in}(\lambda)$ the monochromatic intensity, h the Planck constant, c the speed of light and e the elementary charge ($\frac{hc}{e} = 1240 \text{ V nm}$). At constant applied potential, the photocurrent is measured by varying the wavelength of the monochromatic incident light (Fig. 1.7b). The minimum wavelength, where a photocurrent can still be measured is closely related to the band gap of the semiconductor.

The absorbed-photon-to-current (APCE) efficiency can be easily determined by dividing the IPCE value with the absorbance \mathcal{A} :

$$APCE(\lambda) = \frac{IPCE}{\mathcal{A}} = \frac{J_{ph}(\lambda) \times \frac{hc}{e}}{P_{in}(\lambda) \times \lambda \times \mathcal{A}} \quad (1.13)$$

1.2.3.5. Low costs

To allow for a feasible and sustainable production of the photocatalyst the necessary elements have to be readily available, non-toxic, but also relatively cheap and abundant. Similar to photovoltaics where the most used technologies are not based on materials with the highest performance (too expensive), also for solar water splitting a good balance between high efficiency and low costs should be desirable^[27].

1.2.4. Progress review of solar water splitting applications

1.2.4.1. Oxide materials for solar water splitting

Since the discovery of splitting water into molecular oxygen and hydrogen using TiO_2 as a photoelectrode^[10,58], the field of photoelectrochemistry assumed the challenge of finding materials for efficient and sustainable hydrogen production using solar radiation. A plethora of oxide materials were found to be active for solar water splitting and were subject of further investigations, both experimentally (e.g. FeO_3 ^[59–61], BiVO_4 ^[62,63], WO_3 ^[64] and other^[27,65–67]) and theoretically^[68–74]. These metal oxides are very stable materials due to the high electronegativity of oxygen^[20,27]. However, also non-oxide compounds e.g. typically used for photovoltaic application were tested towards their activity for solar water splitting^[14–17,27] (see Fig. 1.8).

For the oxide compounds, the valence band position depends on the filling of the metal d band. For d^0 materials with an empty d band (Ti^{4+} , Zr^{4+} , V^{5+} , Nb^{5+} , Ta^{5+} , W^{6+})^[26,27,66] and for d^{10} materials with a filled d band (Ga^{3+} , In^{3+} , Ge^{4+} , Sn^{4+} , Sb^{5+})^[26,66], the valence band is composed of O 2p states. The high ionic character of such compounds leads to a large separation of the

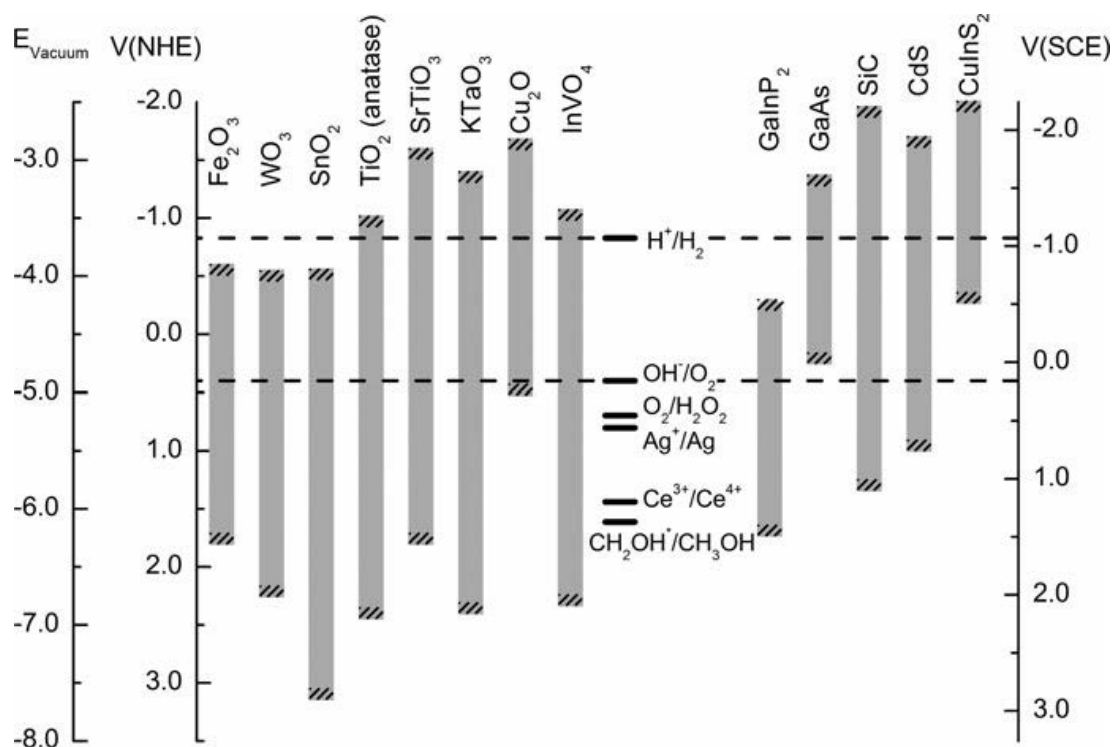


Figure 1.8.: Valence and conduction band positions (including uncertainties) of some semiconductors used in photoelectrochemistry. Figure also shows some important redox potentials at pH 14. (Figure modified from Ref. [8]).

conduction band and the valence band^[27], resulting in a large band gap (> 3 eV) with their photo-responses in the UV range. Overall water splitting (ratio of 2:1 for the evolution of hydrogen and oxygen, respectively) could be achieved for large band gap semiconductors, such as Ga_2O_3 ^[75] and the perovskite oxides SrTiO_3 ^[76], KTaO_3 ^[77], and lanthanum-doped NaTaO_3 ^[78].

Like TiO_2 , WO_3 is another example of such binary compounds of transition metal oxides, where the valence band is composed of O 2p states. WO_3 has a band gap in the visible light range (2.8 eV^[27,70]), which would increase the amount of solar light that can be used, but it has a conduction band that is energetically too low for hydrogen evolution. However, in a Z-scheme or tandem cell configuration, WO_3 can be used as photoanode^[79]. Further, WO_3 doped with hafnium shifts both, the valence and conduction band, upwards in energy with no effect on the band gap value^[70]. This makes hydrogen and oxygen evolution again possible.

Another metal oxide photocatalyst that straddles only the oxidation potential is Fe_2O_3 , a very stable compound and composed of abundant elements. Fe_2O_3

is not one of the d^0 or d^{10} transition metal oxides. For Fe_2O_3 the d band is neither full nor empty (d^n electronic configuration) and excitation of electrons from the valence band to the conduction band are influenced by d-d transitions^[27]. For this kind of material, the charge separation and transport is problematic^[27,80]. Further, Fe_2O_3 reveals a relatively positive flat-band potential and a high onset potential for the photocurrent. Heavily doped Fe_2O_3 forming ternary compounds (such as ZnFe_2O_4) have been investigated to improve the photoelectrochemical properties but with little success^[81].

Ternary compounds, such as the mentioned ZnFe_2O_4 and $\text{Hf}_x\text{W}_{1-x}\text{O}_3$, and quaternary compounds have recently attracted attention due to the limitations of the binary oxides^[27]. A promising strategy to find compounds with a proper engineered band gap is the mixing of s^2 ($\text{Sn}^{2+}, \text{Bi}^{3+}$) cations with d^0 cations^[26,27]. The coupling of the s states and the O p states forms additional energy levels by shifting the valence band upwards in energy^[82].

One of the most successful ternary compound is BiVO_4 with a band gap of 2.4 eV^[83,84], where the valence band is composed of Bi 6s and O 2p states. By nanostructuring, this compound used as photoanode reaches photocurrents up to 6.72 mA cm^{-2} (1.23 V vs. RHE and AM1.5 simulated solar light) and, by a combination of photovoltaic cells, BiVO_4 based devices can reach STH efficiencies up to 8.1 %^[85] (for definition see section 1.2.3.4).

1.2.4.2. Oxynitrides - shifting the response to visible light by anodic doping

General considerations: As mentioned in the previous section, oxides have, with some exceptions, a large band gap of more than 3 eV, therefore only absorbing UV radiation (about 5 % of the solar spectrum)^[86]. A greater portion of the solar spectrum can be captured by narrowing the band gap, thus expanding the absorption window. Cation-doping (e.g. WO_3 doped with hafnium^[70] or TiO_2 doped with iron^[87]) and the formation of more complex compounds (ternary and quaternary compounds such as BiVO_4 , ZnFe_2O_4 and the perovskite oxides) as described in the previous section, are typically used for oxides to modify the electronic structure and the optical properties of the oxide compound. A band gap reduction is mainly achieved by shifting the valence band edge upwards in energy, as realized for example for BiVO_4 with a coupling of occupied Bi 6s states with

the O 2p states. The reason for this strategy of valence band modification is the energetically low O 2p orbital compared to the oxidation potential of water.

Besides these strategies, other successful strategies are the formation of solid solutions (e.g. $(1-x)\text{GaN}:x\text{ZnO}$ as described at the end of this section), anion-doping (e.g. nitrogen-doped TiO_2) and anion-incorporation (described in the following), where for example oxygen is partly or fully substituted with nitrogen forming oxynitrides or nitrides, respectively^[20,26,88–92]. The smaller band gap is the result of the hybridization of the O 2p and N 2p orbitals which is most likely to create additional available energy levels above the valence band of the original oxide, while leaving the conduction band unaffected. Density functional theory calculations for BaTaO_2N support this hypothesis^[93]. TiO_2 , as the most studied photocatalyst, was investigated towards band gap reduction by nitrogen doping and improvements towards solar water splitting were reported^[94–99].

An example of how nitrogen incorporation into the native oxide influences the electronic structure is shown in Fig. 1.9 for Ta_2O_5 , TaON and Ta_3N_5 . The band gap value decreases continuously by increasing the nitrogen content from 3.9 eV for Ta_2O_5 to 2.4 eV for TaON and to 2.1 eV for Ta_3N_5 by shifting the valence band edge upwards in energy, while the conduction band remains almost the same. More details about the change of the electronic structure will be given later in section 1.2.6.

d⁰ materials: TaON was one of the first oxynitride investigated towards solar water splitting^[22]. TaON and Ta_3N_5 are promising materials for photooxidation of water with band gap values of 2.4 eV and 2.1 eV, respectively. Photoactivity in the visible light has been demonstrated^[22,93,100–105]. TaON showed a remarkable O_2 evolution rate of $660 \mu\text{mol h}^{-1}$ in the first 30 min^[22]. Using an aqueous AgNO_3 solution as sacrificial reagent, the rate decreases with increasing operation time due to covering of Ag particles on the surface of the photocatalyst and due to a degradation of the photocatalyst. This degradation yields an oxidation of the photocatalyst as N_2 evolution was observed during operation. However, N_2 evolution was mainly observed at the beginning of the measurements, indicating a proper stability of this material after the initial nitrogen loss.

Further nitridation of TaON leads to Ta_3N_5 (Fig. 1.9). Ta_3N_5 decorated with

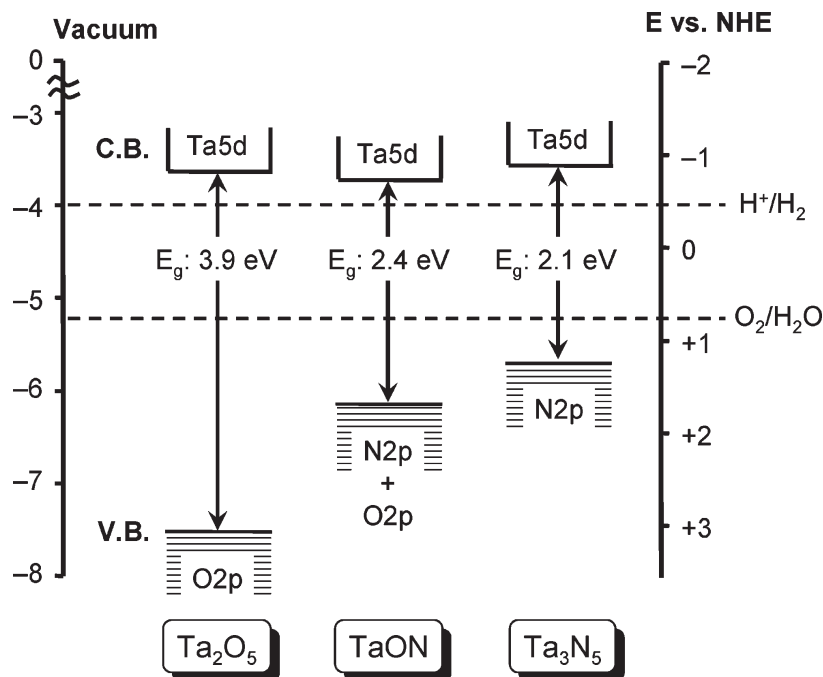


Figure 1.9.: Valence and conduction band positions of Ta_2O_5 , TaON and Ta_3N_5 to visualize the effect of the nitrogen incorporation. (Figure modified from Ref. [93]).

2 wt % CoO_x revealed an initial oxygen evolution rate of about $142 \mu\text{mol h}^{-1}$ [100] using $\text{Na}_2\text{S}_2\text{O}_8$ as sacrificial reagent. With increasing time the activity decreased but could be stabilized at a value of $100 \mu\text{mol h}^{-1}$ for 10 h.

As described above, both materials, TaON and Ta_3N_5 , can be used for water oxidation reactions. Theoretically, these two materials would also have a suitable conduction band for hydrogen evolution, but photoreduction of water using these compounds was suppressed, showing only small hydrogen evolution rates using methanol as sacrificial reagent ($\approx 10 \mu\text{mol h}^{-1}$) [22,105]. It is commonly assumed that surface imperfection causes this low activity for hydrogen evolution [102]. A modification by introducing ZrO_2 into the TaON compound ($\text{ZrO}_2\text{-TaON}$) improved the H_2 evolution significantly with H_2 generation rates up to $445 \mu\text{mol h}^{-1} \text{g}^{-1}$ [102].

Both materials, TaON and Ta_3N_5 , qualify for the use in Z-scheme applications. Already in 2005, TaON could be used for stoichiometric water splitting for the first time [57]. This was achieved with a photocatalytic Z-scheme water splitting system, by using Pt loaded TaON for hydrogen evolution and Pt loaded

WO₃ for oxygen evolution. The photocatalytic reactions were performed under irradiation with visible light (cut-off filter at $\lambda = 420\text{ nm}$ and IO₃[−]/I[−] as redox mediator. Initial hydrogen and oxygen evolution rates of 24 $\mu\text{mol h}^{-1}$ and 12 $\mu\text{mol h}^{-1}$, respectively, were achieved.

TaON as hydrogen evolution catalyst was also combined with Ta₃N₅ in a Z-scheme system using IO₃[−]/I[−] as redox mediator and visible light irradiation ($\lambda > 420\text{ nm}$)^[31]. The former was modified as described above using ZrO₂ and additional Pt, the latter with nanoparticulate Ir and rutile TiO₂. Such a modification using rutile TiO₂ suppresses the adsorption of I[−] on the surface of the photocatalyst allowing for improved oxygen evolution reactions. This highlights the possibility of using different photocatalyst for Z-scheme applications by controlling the adsorption of redox mediators at the surface.

For application in a PEC system, Ref. [106] showed that a Ta₃N₅ photoelectrode can be fabricated by nitridation of Ta foils. Additional loading with Co(OH)_x yields photocurrents of up to 5.5 mA cm^{−2} at 1.23 V vs. RHE using 1-sun AM 1.5G illumination^[106]. This photocurrent can be further increased by doping Ta₃N₅ with Ba and modified with Cobalt phosphate (Co-Pi)^[107] yielding a photocurrent of up to 6.7 mA cm^{−2} at 1.23 V vs. RHE using again 1-sun AM 1.5G illumination was measured. Overall water splitting was achieved with a 1.5 % conversion efficiency from solar to chemical energy.

Except for TaON and Ta₃N₅, most of the promising oxynitride photocatalysts have a perovskite structure. The general composition of the perovskite-like oxynitrides can be written as ABX₃. For the A-side, cations like Ca²⁺, Sr²⁺, Ba²⁺ and La³⁺, and for the B-side, cations like Ti⁴⁺, Nb⁵⁺ and Ta⁵⁺ are used. Depending on the valence states of the A-side and B-side cation, the nitrogen-to-oxygen ratio is changed, e.g. LaTaON₂ and LaTiO₂N. For the ABO₂N-type perovskite oxynitride, candidates for solar water splitting are ANbO₂N (with A=Ca^[108], Sr^[109]), ATaO₂N (with A=Ca^[110–112], Sr^[110,112], Ba^[110,112–114]) and LaTiO₂N^[90,115–117]. For the ABON₂-type perovskite oxynitride, LaTaON₂^[112,118,119] and LaNbON₂^[120] are promising candidates.

Together with TaON, LaTiO₂N, the investigated oxynitride compound in this thesis, was one of the first studied oxynitrides for solar water splitting^[21].

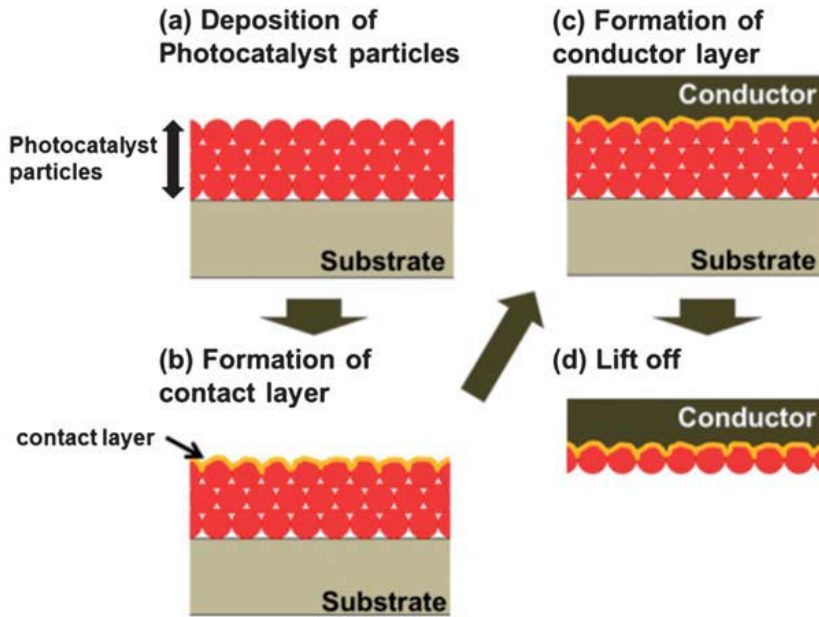


Figure 1.10.: Schematically shown particle transfer method. (Figure modified from Ref. [116]).

This oxynitride has a band gap of about 2.1 eV and is composed of relatively abundant elements. The band gap of LaTiO_2N also straddles the oxygen and hydrogen evolution potential [27,68] and therefore this oxynitride compound is theoretically capable of generating both, hydrogen and oxygen, individually from water.

A standard deposition technique of LaTiO_2N (and also other oxynitrides) for photoelectrochemical measurements is electrophoretic deposition [121], since the investigation of oxynitride materials is mainly done using powder samples. For electrophoretic deposition a solution with the oxynitride powder, iodine and acetone is prepared. Two electrodes coated with a current collector (typically a transparent conducting oxide, i.e. FTO) are immersed into this solution and by applying an electric field the positively charged LaTiO_2N particles are deposited on the cathode. By varying deposition time and voltage, the sample thickness can be optimized. In Ref. [116] a particle transfer method is introduced for the preparation of LaTiO_2N photoanodes with better electrical contact to the conducting substrate for PEC characterization (see Fig. 1.10). For this technique, a glass substrate is coated with LaTiO_2N powder followed by a deposition of a “contact layer” by sputtering. Again by sputtering, the “conductor layer” (here

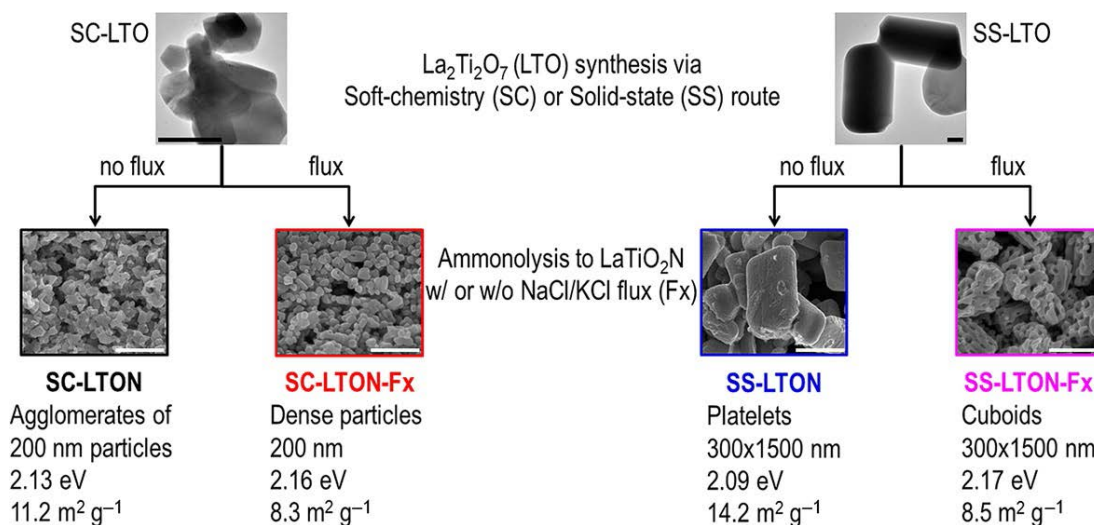


Figure 1.11.: Different powder synthesis routes for LaTiO_2N : the soft-chemistry (SC) route and the solid-state (SS) route with and without NaCl/KCl flux (Fx). Typical characteristics (shape, particle size, band gap, BET surface area) are reported in the figure. (Figure modified from Ref. [121]).

a metal) is deposited on top of the contact layer where a second glass plate was connected using epoxy resin. The primary glass plate was then peeled off carefully and, by ultrasonication in water, excess LaTiO_2N particles, that are piled up, were removed.

LaTiO_2N powder is obtained by ammonolysis of the $\text{La}_2\text{Ti}_2\text{O}_7$ precursor, which is mainly prepared as powder using two techniques (see Fig. 1.11):

- soft-chemistry or polymerized complex routes
- solid-state or ceramic routes

The influence of the synthetic route of the oxides and the flux, used during the ammonolysis, on the PEC performance for LaTiO_2N powder samples, with a-TiO_2 as necking material and CoO_x as co-catalyst, can be seen in Fig. 1.12. Using the solid-state or ceramic route, the particle size becomes typically larger. Larger particle sizes are preferred due to the smaller number of grain boundaries for a certain thickness. Since grain boundaries are possible recombination centers of the photo-generated charge carriers the previously described particle transfer method is advantageous. Nitridation is performed under an ammonia flow and usually at relatively high temperature (typically above 850°C) to obtain oxynitride powders [116,122]. This ammonolysis can be done with and without NaCl/KCl

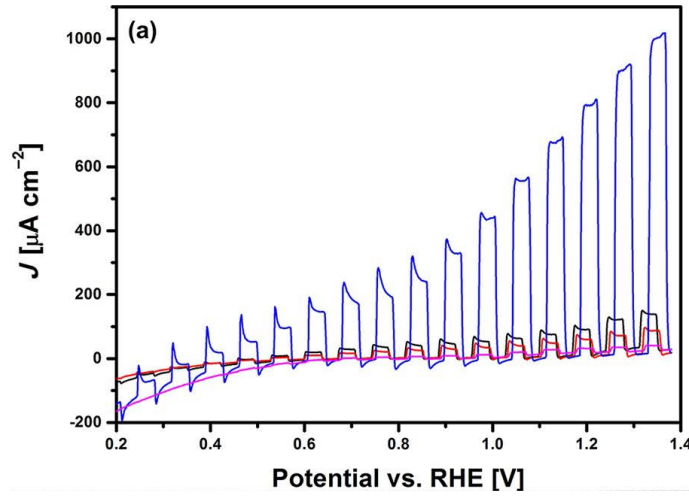


Figure 1.12.: Photocurrents LaTiO₂N photoanodes with CoO_x loading: soft-chemistry synthesis without flux (black), soft-chemistry synthesis with flux (red), solid-state synthesis without flux (blue), solid-state synthesis with flux (magenta). The measurements are performed in 0.1 mol dm⁻³ aqueous solution of Na₂SO₄ (NaOH adjusted pH to 13.40), with a scan rate of 10 mV s⁻¹ and with chopped illumination (100 mW cm⁻², cut-off filter at $\lambda = 420$ nm). (Figure modified from Ref. [121]).

flux.

Ref. [121] introduces five rules that are required to obtain high-efficient powder photoanodes:

1. The necking procedure is important for a better inter-particle charge carrier transfer. But the so-called necking is only required at the inter-particle boundaries. The hole injection into the electrolyte could be blocked by a total coating of the particle surface with the necking material.
2. As already discussed above the use of large particles in the micrometer range allows the fabrication of powder samples with less inter-particle boundaries at constant thickness. This also means that by increasing the sample thickness a higher light absorption with a simultaneous low number of recombination centers can be achieved.
3. To increase the photocatalytic output, a large surface area is required. This can be achieved by powder samples with a high porosity. This increases the active surface area, which provides an increased number of active sites for hole injection into the electrolyte. However, high porosity is desirable if the hole injection into the electrolyte is the limiting factor and not the

electron transport in the oxynitride material.

4. Increasing the size of the CoO_x nanoparticles loaded on the oxynitride semiconductor particles improves the photocurrent. Further a cathodic shift of the onset potential is observed with the use of larger CoO_x nanoparticles.
5. To enable good conductivity of the photo-generated electrons and holes, the particles used for the powder sample needs to be a dense film. Powder samples in form of close-packed spheres or layered plate-like structures are mentioned as examples.

In Ref. [121], CoO_x was used as co-catalyst for the photoelectrochemical investigation of LaTiO_2N . Another co-catalyst often used is IrO_2 ^[117], but the disadvantage of IrO_2 is the price. While the price for Iridium is about \$16 700 /kg^[123,124], Cobalt only costs about \$23 /kg^[125,126]. Co-catalysts are essential for high-performance and therefore cheap materials should be readily available and of low cost to be competitive compared to state-of-the-art technologies.

Generally, LaTiO_2N is a very promising compound for solar water splitting. However, LaTiO_2N suffers from relatively large number of defect states^[127]. These defects originates from reduced titanium (Ti^{3+}), excess of oxygen (O^{2-}) and deficiency of nitrogen (N^{3-}). Nitrogen deficiency can be corrected by prolonging the ammonolysis, but it does not increase the efficiency of LaTiO_2N . To reduce the amount of Ti^{3+} deficiencies, the A-site cation (La^{3+}) can be partly substituted with an ion with a lower valence state (Ca^{2+} or Sr^{2+}) to oxidize Ti^{3+} to Ti^{4+} without changing the anion composition^[127,128].

Ref. [127] reported two different methods for the synthesis of Ca^{2+} -modified LaTiO_2N :

- A soft-chemistry route to add Ca^{2+} to the precursor (Ca^{2+} -substitution)
- Preparing a lanthanum deficient precursor ($\text{La}_{1-x}\text{TiO}_{3.5-3x/2}$) for a post-treatment in $\text{Ca}(\text{NO}_3)_2 \cdot 4\text{H}_2\text{O}$ -containing aqueous solution (Ca^{2+} -backfilled).

The synthesis method was essential for the photoactivity of Ca^{2+} -modified LaTiO_2N (see Fig. 1.13). The Ca^{2+} -substituted LaTiO_2N sample yielded a reduced photocurrent, while the Ca^{2+} -backfilled LaTiO_2N sample yielded a significantly improved photoactivity compared to the untreated sample. In contrast

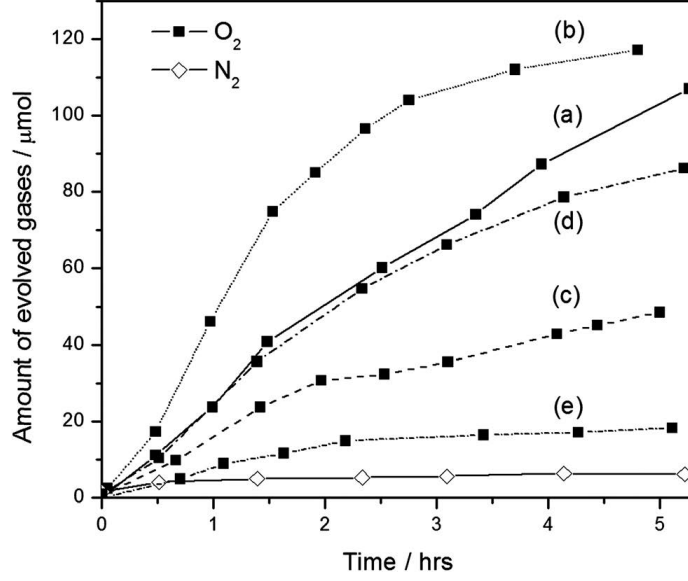


Figure 1.13.: O₂ gas evolution measured over time for (a) untreated LaTiO₂N, (b) LaTiO₂N with 5 % Ca²⁺-backfilled, (c) LaTiO₂N with 5 % Ca²⁺-substituted, (d) LaTiO₂N with 5 % Ca²⁺-excess as reference sample prepared using stoichiometric La₂Ti₂O₇ (backfilling synthesis method) and (e) TiO₂ reference (Degussa P25). N₂ evolution was approximately the same for all samples (including TiO₂). (Figure modified from Ref. [127]).

to the Ca²⁺-substituted LaTiO₂N sample, the Ca²⁺-backfilled LaTiO₂N sample preserved the crystalline structure of the native oxide, but also revealed a better crystalline quality and larger particles size. For all the investigated samples in Ref. [127] (including TiO₂), N₂ evolution was observed together with O₂ evolution. Therefore it was concluded that the nitrogen loss could originate from air dissolved in the electrolyte (solution containing N₂ originating from air and not from the oxynitride sample) or from a leakage in the photocatalytic system (N₂ diffused from outside into the system).

Even though the detected nitrogen loss in Ref. [127] probably did not originate from a decomposition of the LaTiO₂N samples, nitrogen loss is an often observed and unwanted side-effect and is explained by an oxidation of the (oxy)nitride^[39,90,109,116,129,130]. For (oxy)nitrides, an oxidation of the material is usually more favorable than performing the water oxidation reactions^[27]. The incorporated nitrogen of the (oxy)nitrides is oxidized by holes, which are not used up for water oxidation or not lost due to recombination. The reaction occurs

according to



and is followed by an evolution of molecular nitrogen (N_2)^[130].

Another example of cation co-substitution is the complex perovskite oxynitride $\text{LaMg}_x\text{Ta}_{1-x}\text{O}_{1+3x}\text{N}_{2-3x}$ ($x \geq \frac{1}{3}$), where Ta is partly substituted with Mg starting from the oxynitride perovskite LaTaON_2 . LaTaON_2 is not able to perform oxygen evolution under sacrificial conditions^[26]. After incorporation of Mg into LaTaON_2 to form $\text{LaMg}_x\text{Ta}_{1-x}\text{O}_{1+3x}\text{N}_{2-3x}$, overall water splitting using visible light up to 600 nm was achieved^[131]. Both examples of cation co-substitution in the A-side^[127] and B-side^[131] show that with proper material engineering the material properties can be improved.

Another very promising tantalum-based perovskite oxynitride photocatalyst is BaTaO_2N with a visible light absorption up to 660 nm (1.8 eV)^[112,132]. Assuming an IPCE value of 100 % for wavelengths smaller than 660 nm, BaTaO_2N would be able to generate photocurrents of about 18 mA cm^{-2} ^[114]. This theoretical limit of 18 mA cm^{-2} cannot be achieved yet, still BaTaO_2N with its low band gap of 1.8 eV^[112,132] is one of the most promising compounds among the studied oxynitrides for solar water splitting.

Thus, several studies aimed to improve the performance of the BaTaO_2N photocatalyst. Ref. [132] reported an IPCE value of 10 % at $\lambda = 600\text{ nm}$ by co-loading of CoO_x and RhO_x to facilitate the hole transfer and pretreating the BaTaO_2N powder samples with H_2 to decrease electrical resistance. $\text{BaTaO}_2\text{N}/\text{Ta}/\text{Ti}$ samples prepared by particle transfer method also showed an IPCE value of 10 % at $\lambda = 600\text{ nm}$. Photocurrents of about 4.2 mA cm^{-2} at 1.2 V vs. RHE and H_2 and O_2 evolution with unity faradaic efficiency was reported^[114].

An additional approach includes BaTaO_2N in Z-scheme water splitting applications^[133]. By modifying BaTaO_2N with BaZrO_3 for H_2 evolution and by using PtO_x -loaded WO_3 as photocatalyst for O_2 evolution (IO_3^-/I^- redox couple as mediator), $67.4\text{ }\mu\text{mol}$ of H_2 and $27.9\text{ }\mu\text{mol}$ of O_2 was generated in 3 h. The observed hydrogen and oxygen evolution was only possible using Pt as co-catalyst. However, a 2:1 ratio for H_2 and O_2 was not achieved (no overall water splitting), due to undesirable backward reactions and poor quality of the material.

	1	2	3	4	5	6	7	8	9	10	11	12	13	14	15	16	17	18
1	H																	He
2	Li	Be											B	C	N	O	F	Ne
3	Na	Mg											Al	Si	P	S	Cl	Ar
4	K	Ca	Sc	Ti	V	Cr	Mn	Fe	Co	Ni	Cu	Zn	Ga	Ge	As	Se	Br	Kr
5	Rb	Sr	Y	Zr	Nb	Mo	Tc	Ru	Rh	Pd	Ag	Cd	In	Sn	Sb	Te	I	Xe
6	Cs	Ba	Ln	Hf	Ta	W	Re	Os	Ir	Pt	Au	Hg	Tl	Pb	Bi	Po	At	Rn
7	Fr	Ra	An															

d⁰-group *d¹⁰-group*

Ln:	La	Ce	Pr	Nd	Pm	Sm	Eu	Gd	Tb	Dy	Ho	Er	Tm	Yb	Lu
An:	Ac	Th	Pa	U	Np	Pu	Am	Cm	Bk	Cf	Es	Fm	Md	No	Lr

Figure 1.14.: Cations used for solar water splitting: in red materials of the d^0 -group and in green the materials of the d^{10} -group. (Figure modified from Ref. [93]).

Overcoming these drawbacks by improving the material quality and refining the preparation of the catalyst could further enable nonsacrificial water splitting.

d^{10} materials: Up until this point, the reported oxynitride photocatalysts are composed of d^0 materials. As mentioned in the previous section, promising photocatalysts can be found also among the d^{10} -type materials. d^{10} -type oxynitride compounds such as $(1-x)\text{GaN}:x\text{ZnO}$ and $(1-x)\text{ZnGeN}_2:2x\text{ZnO}$ have been investigated^[134]. Metals used for d^0 and d^{10} -type photocatalysts are shown in Fig. 1.14.

Solid solutions of $(1-x)\text{GaN}:x\text{ZnO}$ usually have an absorption edge around 2.50 eV to 2.75 eV and are thus not able to make use of a large portion of the solar spectrum^[26]. However, it is not clear, why a solid solution fabricated by mixing two compounds with band gaps in the UV (3.4 eV for GaN and 3.2 eV for ZnO) results in a compound with visible light response^[134]. Theoretical calculations were performed using density functional theory^[135–138], but the reason for the band gap reduction is not yet fully understood. Experimental investigations were carried out to systematically investigate the effect of the x -value in $(1-x)\text{GaN}:x\text{ZnO}$ on the optical properties, whereby an increase of the x -value shifts the absorption edge towards larger wavelength, thus reducing the band gap.

Ref. [139] observed a decreasing x -content with increased temperature (650 °C to 850 °C) during ammonolysis of a gallium zinc oxide precursor (sol-

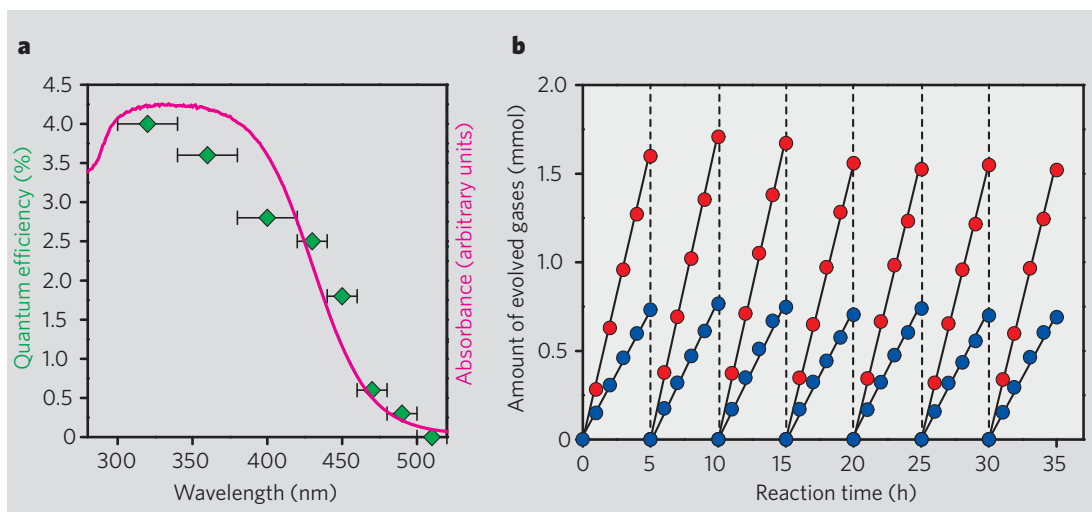


Figure 1.15.: Optical and photocatalytic investigation of $(1-x)\text{GaN}:x\text{ZnO}$: (a) Quantum efficiency and absorbance vs. wavelength, and (b) 35 h time course of the H_2 and O_2 gas evolution with evacuation of the system every 5 h showing a ratio of almost 2:1, respectively, indicating overall water splitting. (Figure modified from Ref. [92]).

gel method). The minimum band gap of about 2.21 eV (≈ 560 nm) was observed for $x = 0.482$ and the largest band gap of about 2.65 eV (≈ 470 nm) was observed for the $x = 0.088$.

Ref. [140] used a mixture of ZnO and ZnGa_2O_4 as precursor with a following nitridation at 650°C under NH_3 gas flow for 10 h. By varying the ratio between ZnO and ZnGa_2O_4 , $(1-x)\text{GaN}:x\text{ZnO}$ compounds with $0.30 < x < 0.87$ were achieved. The band gap value shifted almost linearly with the x -value from $x = 0.30$ (2.70 eV $\hat{=}$ 460 nm) to $x = 0.87$ (2.20 eV $\hat{=}$ 565 nm). Since the band gap of pure ZnO ($x = 1$) is about 3.2 eV, a sharp increase is expected between an x -value of 0.87 and 1.

These low band gap $(1-x)\text{GaN}:x\text{ZnO}$ compounds described above were not yet investigated towards their photocatalytic activity. However, literature reports overall water splitting using $(1-x)\text{GaN}:x\text{ZnO}$ compounds with a typical absorption edge around 2.50 eV to 2.75 eV [26,92].

Fig. 1.15 shows the photocatalytic performance of this oxynitride by loading with a mixture of rhodium and chromium oxides. The measurement was performed under visible light illumination ($\lambda > 400$ nm) and showed a linear increase of the evolved gases over time. Further more, the ratio of hydrogen and

oxygen was about 2:1, indicating overall water splitting.

1.2.5. Photocatalysts as thin films

Photocatalysts are usually characterized using powder samples^[113,115,121,141]. However, with powders it is difficult to probe specific material properties, such as the crystalline quality and/or crystallographic surface orientation. Moreover, in the specific case of oxynitride powders, the amount of incorporated nitrogen is usually set by the fabrication procedure which hampers the possibility of probing the effect of different nitrogen contents on the performance of the photocatalysts. Highly textured or epitaxial thin films can be used as model system to address these challenges.

Different experimental approaches are used to probe the photocatalytic activity of materials. Using powders one can measure directly the amount of gas produced as a consequence of specific photo-induced chemical reactions^[90,142]. Alternatively, the powders can be dispersed in aqueous solution with an organic dye that decomposes changing its absorbance as a result of the chemical reactions occurring at the photocatalyst under illumination^[143–145]. These techniques generally belong to the family of so-called photocatalytic characterizations as introduced in section 1.2.2. However, for the same illuminated area of the photocatalyst, the active surface area is orders of magnitudes smaller using thin films compared to powders. As a consequence, the yield per unit area is much smaller for thin films than for powders hindering a direct photocatalytic characterization since the effect of the photo-induced reactions could be difficult to follow. On the other hand, a photoelectrochemical study (see section 1.2.1) is a suitable technique to investigate thin film photocatalysts towards solar water splitting. Since relatively small current densities can be measured with high accuracy, a photoelectrochemical characterization is very useful for thin films studies if an appropriate conducting substrate or buffer layer for the growth of the photocatalyst is available.

In the literature only a few studies using thin films for PEC measurements have been reported, for example $\text{Bi}_2\text{FeCrO}_6$ to investigate the effect of the ferroelectric polarization on the photoelectrochemical performance^[146] and BiFeO_3

to test towards photoelectrochemical activity^[147]. Further, TiO₂ was investigated towards the dependence of the crystallographic surface orientation on the photochemical reactions^[148–151].

Thin film samples of (100), (001), (101), (110) and (111) oriented rutile TiO₂ were fabricated with sputtering and tested towards their ability to reduce Ag⁺ to Ag^[148]. It was concluded that (001), (101) and (111) orientations revealed an order of magnitude higher photoactivity compared to (100) and (110) orientations. Ref. [149] further concluded that the most active surfaces of rutile TiO₂ are close to the (101) orientation. Similar investigation was performed using TiO₂ powder^[151]. In Ref. [151] PbO₂ was photocatalytically deposited on different surfaces of Pt-loaded TiO₂ by oxidizing Pb²⁺ in a Pb(NO₃)₂ solution. They concluded that the (101) orientation provides holes for the oxidation, while the (110) orientation provides electrons for the reduction.

Also photoetching with H₂SO₄ was performed on TiO₂ surfaces^[152]. Since photoetching is competitive to photooxidation of water, both occurs on the surfaces of TiO₂, but with different probabilities for different surface orientations. Surface orientations such as (001) and (110) were strongly affected by photoetching and gradually changed to other faces. Photoetching of (100) surfaces was much slower compared to photooxidation of water. It was concluded that (001) and (110) orientations are changed to (100) orientation with time of photoetching resulting in the formation of rectangular holes and grooves. Thermodynamically speaking, the (100) orientation is not the most stable surface and is exposed only by photoetching.

Concerning oxynitrides, thin films can be grown using different deposition methods, for example sputtering (TaO_xN_y^[153], TiO_xN_y^[154,155] and LaTiO_xN_y^[156]), pulsed laser deposition (LaTiO_xN_y^[157], TiO_xN_y^[99], BaTaO₂N^[158]) and chemical vapor deposition (TiO_xN_y^[159,160]).

However, the reported studies on their photocatalytic activity are quite rare. PEC measurements of polycrystalline titanium oxynitride films were performed using transparent conducting glasses as substrates^[155]. The influence of the crystalline quality on the photo-activity of LaTiO_xN_y was studied using Nb-doped SrTiO₃ as a substrate and IrO₂ as co-catalyst^[156]. In both cases, reactive magnetron sputtering was applied to grow the oxynitride films. It was concluded that the

crystalline quality is important^[156]. Polycrystalline samples showed lower photocurrents compared to highly oriented samples using a Xe lamp for illumination with a cut-off filter at 420 nm, even though the polycrystalline samples had a higher nitrogen content (determined with EDS), thus lower band gap and higher absorption (confirmed with UV-Vis spectroscopy).

This work further investigates the effect of the nitrogen content and different surface orientations on the PEC performance. Based on previous studies^[157,161], highly ordered oxynitride thin films with different nitrogen content can be grown using a modified pulsed laser deposition method called Pulsed Reactive Crossed-beam Laser Ablation (PRCLA) (see section 2.1). PRCLA enables growth from a target of the native oxide, thus making this method potentially applicable to any oxynitride material circumventing the need of an oxynitride target whose preparation is often difficult due to the high temperatures required for the sintering process and the potential for fragmentation. Additionally, this technique allows a systematic variation of the nitrogen content in the films, which was quantitatively investigated to minimize the presence of potential anionic vacancies. It is worth mentioning that the so-called native oxide used as target in Ref. [157] and in this work for the deposition of the orthorhombic perovskite LaTiO_xN_y is the monoclinic pyrochlore-type $\text{La}_2\text{Ti}_2\text{O}_7$ and not the orthorhombic perovskite-type LaTiO_3 due to the difficulty of fabricating a stoichiometric LaTiO_3 target.

However, using PRCLA, the strongly reducing environment and the high temperatures needed for a sufficient incorporation of nitrogen into the oxynitride thin films^[156,157], precludes the use of several materials as current collector. Therefore it is important to identify a stable and conducting material that allows the epitaxial growth of oxynitride photocatalyst thin films for PEC characterization.

1.2.6. Investigation of the electronic structure of oxynitrides

As mentioned in the previous sections, the relatively large band gaps of conventional oxide photocatalysts (typically $\geq 3\text{ eV}$) limit the efficiency for solar water splitting and encourages the use of oxynitride materials due to their photoresponse towards the visible light range of the solar spectrum. The main mechanism that explains the narrowing of the band gap as a consequence of the nitrogen

incorporation is the creation of additional electronic states just above the valence band due to the hybridization of N 2p orbitals at higher energy level with O 2p orbitals at lower energy level^[20,26]. Thus, the VBM is shifted upwards in energy, while the CBM is considered to be only slightly affected by the nitrogen incorporation. This results in a reduced overall band gap.

A representative example is given in Ref. [162] where the valence and conduction band positions of Ta₂O₅, TaON, and Ta₃N₅ were determined (see Fig. 1.9). Large upward energy shifts of the VB maxima were measured from the oxide to the nitride, while the CB minima of the three materials, mainly composed by empty Ta 5d orbitals, remained at similar potentials, between -0.3 V and -0.5 V vs. NHE. However, it must be highlighted here that the nitrogen substitution in metal oxides like Ta₂O₅ and TiO₂ affects not only the electronic (and optical) properties, but also the crystalline structure. It is thus difficult to distinguish only the effect of the nitrogen substitution on the electronic band structure.

Also in perovskite oxynitrides with the typical composition ABO₂N the partial nitrogen substitution in the oxygen site of the pristine oxide typically leads to a change of the crystalline structure. The VBM significantly shifts upward in energy reducing the band gap, while the width and the energetic position of the CB can be tuned by changing the A and the B cation respectively^[163]. Concerning the A cation, it has been shown that in BaTaO₂N, SrTaO₂N, and CaTaO₂N the width of the CB progressively decreases with decreasing the ionic radius of the A cation from Ba to Ca, leaving the energetic center of the CB unchanged. This results in an overall increase of the band gap induced by the size mismatch of the A cation, which is explained by considering the distortion of the unit cell (cubic for A=Ba, tetragonal for A=Sr, and orthorhombic for A-Ca) affecting the Ta-(O,N)-Ta bond angle^[163,164]. On the other hand, different electronegativity of the B cation can alter the band structure in oxynitride perovskites. By comparing the band structure of Ba and Sr tantalates with the respective niobates, the energetic position of the CB increases with decreasing the electronegativity of the B cation from Nb to Ta. Since the B cation has a minor effect on the width of the CB, the overall result is a significant decrease of the band gap with increasing the electronegativity of the B cation^[163].

To the best of our knowledge no experimental investigation has reported

on the modification of the electronic properties solely induced by the oxygen to nitrogen substitution comparing the shifts of the VB and CB of oxide and oxynitride with the same crystalline structure and cationic composition.

Using thin films fabricated by PRCLA and adjusting the deposition parameters not only the crystallographic properties, but also the nitrogen content of the film can be carefully controlled^[157,161,165]. In particular, the nitrogen content can be almost continuously tuned up to a nitrogen-to-oxygen ratio of about 0.4. As mentioned in the previous section, it is difficult to achieve this with powder samples. Using thin films allows the investigation of the changes of the electronic structure and, as a consequence, of the optical properties, as a function of a different nitrogen content of the sample. Therefore the use of thin films is particularly suited for this investigation.

Therefore, the electronic structure of oxides and oxynitrides with the same crystalline structure and cationic composition around the Ti-centers can be probed using thin films by non-resonant X-ray emission spectroscopy (XES) and X-ray absorption spectroscopy (XAS)^[166–170]. Both techniques are commonly used for sample characterization in many scientific areas providing detailed electronic and structural information with element selectivity^[171–175]. By using hard X-rays, the materials can be studied at ambient environment conditions to obtain the electronic properties of the bulk material. XAS provides information about the unoccupied density of states of an atom, whereas XES reflects the occupied density of states, and when applied together, detailed information of the electronic orbitals can be achieved, giving insight into the oxidation state, spin state, and chemical environment around a specific absorbing atom (see Chapter 2.2.7).

The investigation of the samples can be performed according to the Szlachetko & Sá methodology for resonant XES data interpretation aiming at a rational design of photo-catalytic materials^[175–179]. The experimental XES and XAS data can then be compared with theoretical calculations of electronic density of states^[180,181] for a detailed interpretation of spectral features as well as to determine the effects of nitrogen-doping in the oxide thin film samples.

1.3. Research questions and thesis outline

Despite recent efforts, no material was found to fulfill all the requirements for photocatalytic water splitting. An improvement of our understanding of the material properties is still needed to make photoelectrochemical and/or photocatalytic water splitting more competitive compared to state-of-the-art technologies. Since oxynitrides are one of the most promising class of materials, LaTiO_2N is used as representative compound for this thesis to introduce a new model system that can be used for photoelectrochemical investigation of oxynitride materials. To gain further insights into the solar water splitting process, the following questions are targeted:

- What is the effect of the nitrogen incorporation on the electronic structure of the oxynitride photocatalyst, and thus its optical properties?
- Which materials can be used as a suitable current collector using thin films as model system for photoelectrochemical investigations to gain further insight into the solar water splitting process?
- Using the model system, what is the effect of the crystalline quality and crystallographic surface orientation on the performance of the oxynitride photocatalyst?

To address these research questions, Chapter 3.1 focuses on the investigation of the electronic structure of the monoclinic pyrochlore-type $\text{La}_2\text{Ti}_2\text{O}_7$ thin films as proof of concept for the use of lanthanum titanate compounds for the Szlachetko & Sá methodology and to test the suitability of using thin film samples for X-ray spectroscopy. To further investigate the effect of nitrogen incorporation into the oxide material, the electronic structure of LaTiO_3 thin films is compared with the electronic structure of LaTiO_xN_y thin films (both orthorhombic perovskites) in Chapter 3.2. Using X-ray Absorption and non-resonant X-ray Emission Spectroscopy measurements at the Swiss Light Source (SLS), it is possible to quantify the influence of the material changes caused by the nitrogen incorporation on the optical properties such as the position of the valence and conduction band edge.

Chapter 4.1 investigates different materials as possible current collectors, whereby TiN was the only feasible candidate. In the following a new model sys-

tem was introduced. This model system consists of a LaTiO_xN_y thin film with a TiN-buffered substrate which were produced using Pulsed Reactive Crossed-beam Laser Ablation (see Chapter 2). The new model system using this deposition technique opens the possibility to investigate the photoelectrochemical performance of oxynitride photocatalysts with different crystallographic surface orientation and nitrogen content.

Using this model system, Chapter 4.2 further quantifies the effects of crystalline quality and crystallographic orientation of the active surface of LaTiO_xN_y photocatalysts on the photoelectrochemical performance. Further, the surface changes caused by the photoelectrochemical measurements is investigated.

The fundamentals of the used sample preparation and measurement technique are described in Chapter 2.

2

Methods

2.1. Thin Film Deposition

For this project two deposition techniques were used, the conventional Pulsed Laser Deposition described in section 2.1.1 and a modified Pulsed Laser Deposition technique called Pulsed Reactive Crossed-beam Laser Ablation as described in section 2.1.2.

2.1.1. Pulsed Laser Deposition

Pulsed Laser Deposition (PLD) is a well-established technique used for the growth of thin films^[182]. The working principle of PLD is schematically shown in Fig. 2.1 and, in terms of equipment, PLD is a fairly simple deposition technique. This method requires a laser to ablate the target material, which is pressed as a rod or as a pellet and mounted in a vacuum chamber. The laser is operated in pulsed mode and focused on the target surface. The power of the laser pulse should be sufficiently high to vaporize the target material forming a plasma plume, which is dependent on the target material and morphology, and the laser pulse wavelength and duration.

The high-energetic plasma species are transferred to a typically heated substrate placed in the center of the plasma propagation. The transferred plasma species condense on the substrate forming the thin film. By varying deposition parameters, such as substrate temperature, target-to-substrate distance, laser fluence and background pressure, thin film properties such as crystallographic orientation, crystalline quality, composition can be modified. In contrast to the

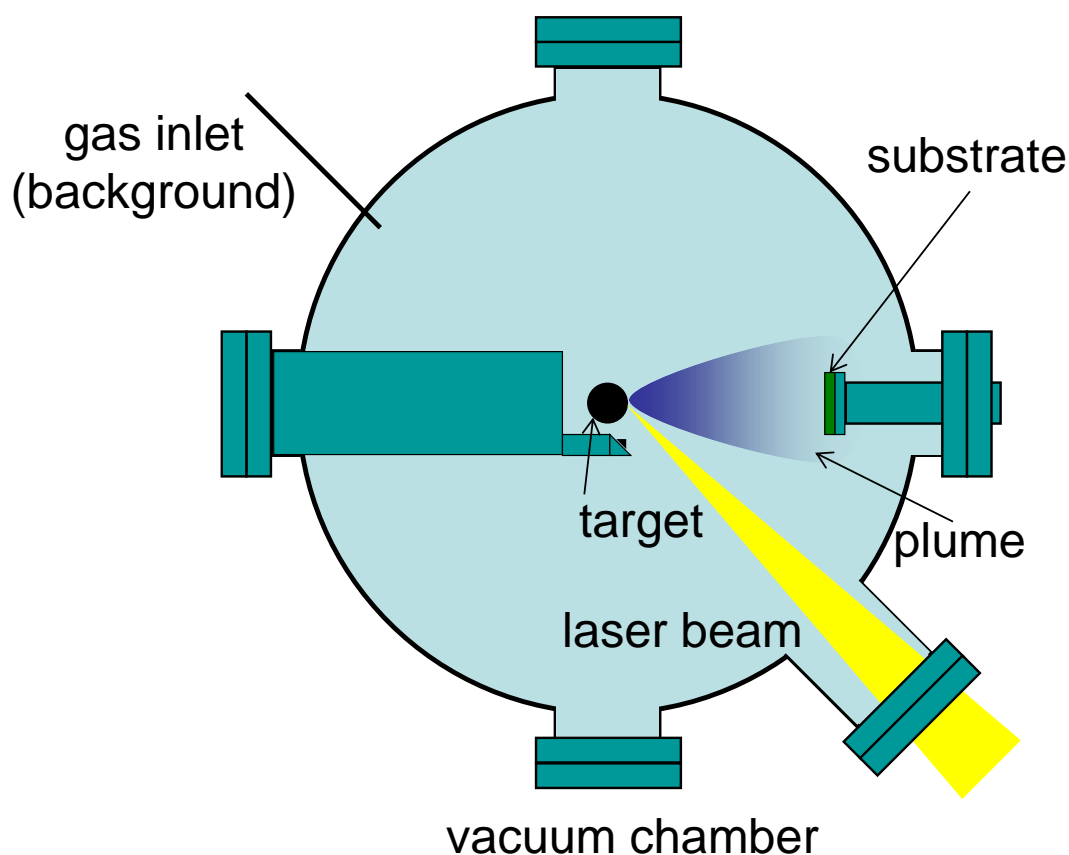


Figure 2.1.: Schematically shown working principle of a pulsed laser deposition (PLD) setup.

simplicity in hardware, the physicochemical processes occurring in PLD are complex and are strongly dependent on the chosen laser parameters and the target material.

PLD was used for the growth of buffer layers which were used as current collectors. These buffer layers were essential for the photoelectrochemical (PEC) measurements in chapter 4.1 and chapter 4.2 (section 2.1.1.1). Further, PLD was performed for the growth of the samples used for the measurements at the Swiss Light Source (SLS) and are reported in chapter 3 (section 2.1.1.2).

For all the following described depositions, a KrF excimer laser ($\lambda = 248$ nm, pulse width of 30 ns) was used, the substrates were ultrasonically cleaned with acetone and ethanol, the vacuum chamber was evacuated down to 5×10^{-6} mbar and the substrate temperature was monitored by a pyrometer.

2.1.1.1. Deposition of the current collector

For PEC characterization an electronic conducting substrate or buffer layer is required for the growth of LaTiO_xN_y . Beside the conducting substrate Nb-doped SrTiO_3 used in Ref. [156] for the growth of oxynitride films by sputtering, the use of thin SrRuO_3 and TiN buffer layers was investigated (chapter 4.1).

SrRuO_3 thin films were grown by PLD on (100)-oriented SrTiO_3 . For the deposition, an O_2 partial pressure of 0.1 mbar was set. A SrRuO_3 disc target was ablated using the KrF excimer laser at a repetition rate of 4 Hz and a laser fluence of about 1.8 J cm^{-2} . The target-to-substrate distance was 50 mm and the substrate was heated up to 800°C .

Initially to test feasibility, TiN thin films were grown by DC reactive sputtering (Mantis Deposition Ltd, UK, Model: QPrep) at the EMPA Laboratory for Mechanics of Materials and Nanostructures (Swiss Federal Laboratories for Materials Science and Technology, Feuerwerkerstrasse 39, 3602 Thun, Switzerland). For the deposition, a Ti target in an Ar/ N_2 gas mixture was used. (100)-oriented MgO substrates were used setting a temperature of 700°C of the heating stage. From a base pressure of 2.0×10^{-7} mbar, gas flows of 35 and 15 sccm of Ar and N_2 respectively were introduced into the vacuum chamber reaching a pressure of 2.9×10^{-3} mbar. The sputtering process was performed by applying an accelerating voltage of 446 V which set a current of about 300 mA.

For subsequent investigations, TiN thin films were grown in-situ on (001)-oriented MgO and on (0001)-oriented Al_2O_3 substrates using PLD. The deposition temperature was set to 800°C . Pt paste was used to provide good thermal contact between the substrate and the heater. No background gas was applied during the deposition. A commercially available TiN rod target (Stanford Advanced Materials) was used as an ablation target. A laser fluence of about 3.5 J cm^{-2} and a laser repetition rate of 10 Hz were applied.

2.1.1.2. Deposition of the Swiss Light Source samples

For the Resonant Inelastic X-ray Scattering measurements described in section 2.2.7 and used for section 3.1, $\text{La}_2\text{Ti}_2\text{O}_7$ thin film samples were prepared.

The $\text{La}_2\text{Ti}_2\text{O}_7$ thin films were prepared using the KrF excimer laser. The energy density of the laser was about 2 J cm^{-1} at a repetition rate of 10 Hz. The deposition was performed in a background pressure of 0.05 mbar. The sintered pellet of $\text{La}_2\text{Ti}_2\text{O}_7$ was used as target for the PLD process. The target to substrate distance was set at 50 mm. The substrates were clamped on a Si plate with the same size, which was then heated resistively up to 600°C . Commercially available (110)-oriented single crystalline wafers (Crystec GmbH) of YAlO_3 were used as deposition substrates.

PLD was also used to produce the LaTiO_3 sample needed for the non-resonant X-ray Emission Spectroscopy and for X-ray Absorption Spectroscopy measurements described in section 2.2.7 and used for section 3.2. Pt paste was used to provide good thermal contact between the (0001)-oriented Al_2O_3 substrate and the heater. The substrate temperature was set to 800°C . N_2 was introduced as background gas with a partial pressure of 0.1 mbar. The KrF excimer laser with a repetition rate of 10 Hz and with a laser fluence of 2.0 J cm^{-2} was used for the ablation of the $\text{La}_2\text{Ti}_2\text{O}_7$ rod target. The target-to-substrate distance was fixed to 45 mm.

2.1.2. Pulsed Reactive Crossed-beam Laser Ablation

Pulsed Reactive Crossed-beam Laser Ablation (PRCLA) is a modification of the conventional PLD technique as shown in Fig. 2.2. During PRCLA gas jets are injected into the vacuum chamber through a nozzle valve triggered by the laser pulses and crossing the ablation plume near the surface of the target allowing for a chemical modification of the ablated species. The specific features of this technique are described in detailed elsewhere^[183], as well as a comparative study of the unique characteristics that distinguish PRCLA from conventional PLD^[184].

Briefly, during PRCLA pulsed gas jets synchronized with the laser pulses are injected through a piezoelectric nozzle valve into the deposition chamber near the ablation spot at the target. Here the gas jets cross the ablation plume. By appropriately tuning the delay time (with respect to the laser pulse) and the opening time of the nozzle valve, it is possible to create a temporary strong pressure gradient along the direction of the expansion of the ablated material. The relatively

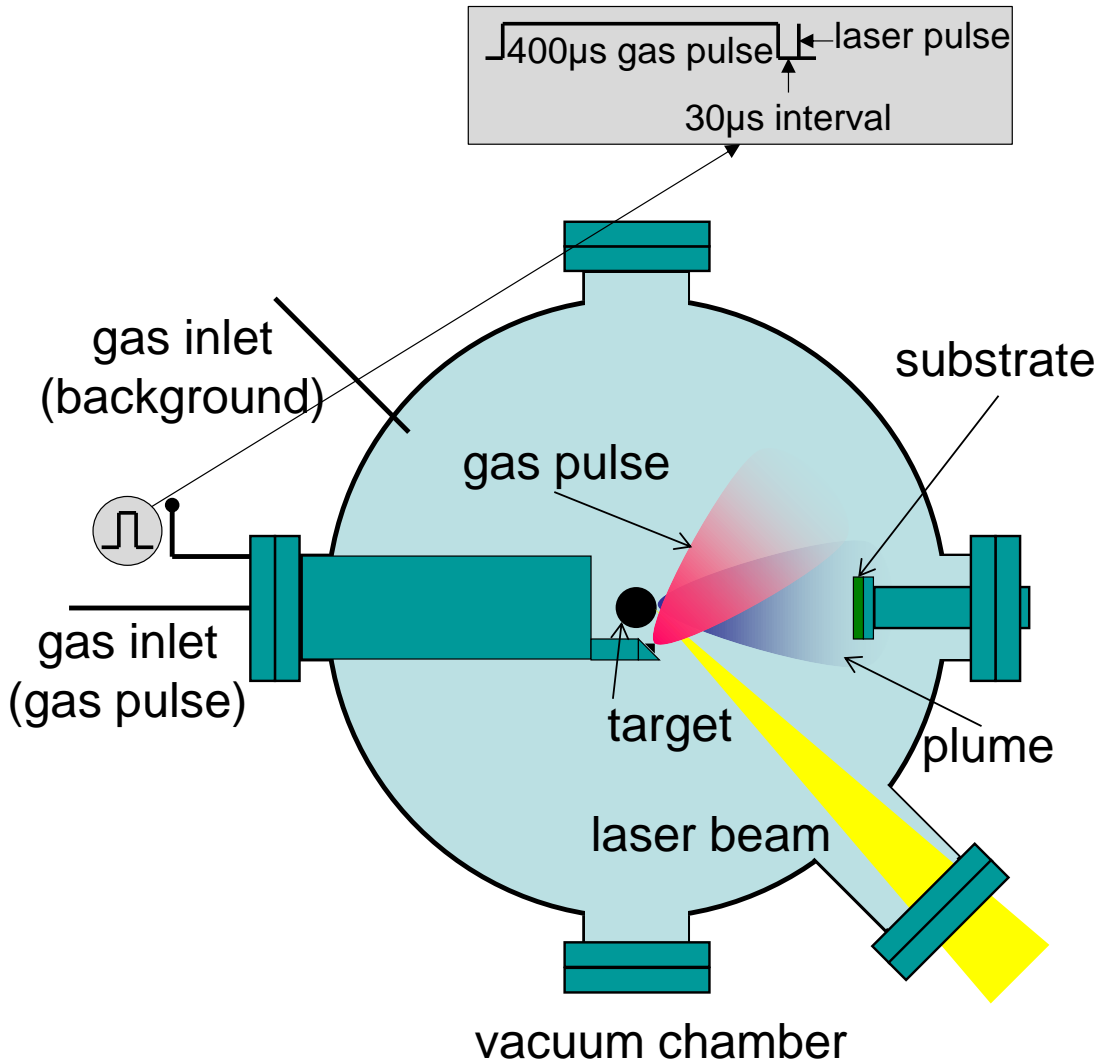


Figure 2.2.: Schematically shown working principle of a PRCLA setup.

high pressure at the very early stage of the propagation of the ablated species allows efficient physicochemical interaction with the gaseous environment. Moving away from the target toward the substrate the partial pressure rapidly decreases hindering further physicochemical evolution of the plasma species.

Using an oxide target of $\text{La}_2\text{Ti}_2\text{O}_7$ and NH_3 for the pulsed gas jets, nitrogen can effectively be substituted into the oxygen sites allowing the growth of LaTiO_xN_y thin films^[157]. For this work, a $\text{La}_2\text{Ti}_2\text{O}_7$ target for laser ablation was prepared in our laboratory as a sintered ceramic rod. For all the depositions using PRCLA, the substrates were ultrasonically cleaned with acetone and ethanol.

The vacuum chamber was evacuated to a base pressure of about 5×10^{-6} mbar. For LaTiO_xN_y deposition a N_2 background partial pressure of 8.0×10^{-4} mbar was set and NH_3 was used for the pulsed gas jets. A delay time of 30 μs was set between the opening of the nozzle valve and the laser pulse, while the opening time of the nozzle valve was 400 μs for each laser pulse. The laser (KrF excimer laser with $\lambda = 248$ nm and pulse width of 30 ns) was operated at a repetition rate of 10 Hz. In this condition, the average pressure in the vacuum chamber raises from the N_2 background pressure up to about 1.8×10^{-3} mbar.

LaTiO_xN_y thin films were fabricated using different laser fluences. Laser fluences from 2 J cm^{-2} to 4 J cm^{-2} were applied for the work in chapter 4.1. The applied laser fluences in chapter 4.2 were 2.2 J cm^{-2} , 3.1 J cm^{-2} and 3.8 J cm^{-2} . For chapter 3 only a laser fluence of 3.9 J cm^{-2} was used. The spot size of the laser at the target was about 1 mm^2 and the target-to-substrate distance was set to 50 mm.

Single crystals of (001)-oriented SrTiO_3 and LaAlO_3 , (110)-oriented YAlO_3 , and (0001)-oriented Al_2O_3 were used as transparent substrates, as well as TiN-coated (001)-oriented MgO and (0001)-oriented Al_2O_3 substrates for photoelectrochemical characterization. Initially, the substrates were clamped on a Si plate with the same size, which was then heated resistively up to 870°C (chapter 4.1).

During this project the heating system in the vacuum chamber was changed (chapter 4.2 and chapter 3). The new system uses an inconel plate heated by halogen bulb radiation. The change of the heating system had a minor impact on the oxynitride deposition. The crystalline quality improved visibly as can be seen in narrower reflexes of the X-Ray Diffraction spectra. Here, Pt paste was used to provide good thermal contact between the used substrates and the heater and a substrate temperature was set to 800°C . In both cases, the temperature was controlled with a pyrometer.

2.2. Thin Film Characterization

2.2.1. Chemical composition

The chemical composition of the thin films was determined by a combination of Rutherford Backscattering (RBS) and Heavy-Ion Elastic Recoil Detection Analysis (ERDA) measurements. Due to the higher sensitivity to heavy elements, the concentration ratio of the heavy cations and oxygen (for example La:Ti:O) was determined by RBS and the nitrogen-to-oxygen ratio was determined by ERDA due to the higher sensitivity to lighter elements.

For RBS measurements a 2 MeV ^4He beam and a silicon PIN diode detector under an angle of 168° towards the incident beam is used. The measurements were performed at the laboratory of Ion Beam Physics (ETH Zurich, 8093 Zurich, Switzerland) and the collected data were analyzed using the RUMP program^[185]. The uncertainty of RBS is dependent on the obtained data. If a peak consists of a single element (see Fig. 2.3), then the uncertainty is defined via the Poisson statistics ($\frac{1}{\sqrt{N}}$ with the number of counts N). Usually, the error of the composition of elements determined via a free-standing peak is in the range of 0.5 %. If the composition of an element has to be determined with a peak overlapping with another signal in the RBS spectrum (e.g. oxygen peak on the substrate signal), an error of about 3 % to 5 % is specified.

For ERDA measurements a 13 MeV ^{127}I beam and a combination of a time-of-flight spectrometer with a gas ionization detector is used^[186]. To further increase the sensitivity for hydrogen detection the beam is changed to 2 MeV ^4He . In the composition depth profile using ERDA a region between 20 nm and 100 nm was chosen for integration of the oxygen and nitrogen signal. The surface and the interface to the conducting substrate or buffer layer were carefully excluded. The depth resolution of ERDA at the surface of the thin film is in the range of 5 nm. With increasing depth the resolution decreases and at the depth of about 150 nm the depth resolution is about 20 nm to 30 nm. Also ERDA was performed at the laboratory of Ion Beam Physics.

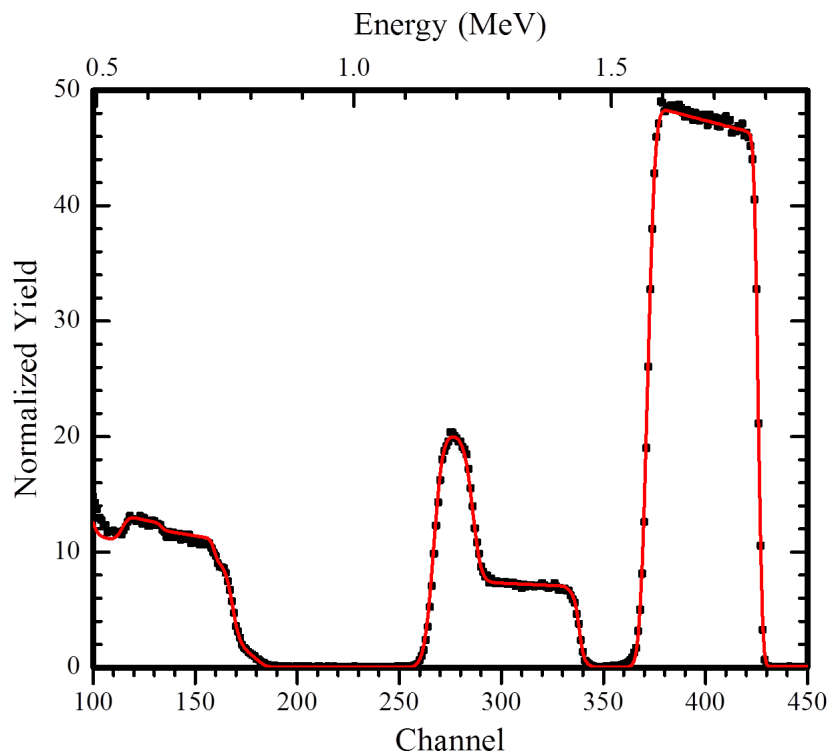


Figure 2.3.: Example of an RBS spectrum of a LaTiO_xN_y sample grown on TiN-coated MgO substrate.

2.2.2. Surface chemical analysis

X-ray Photoelectron Spectroscopy (XPS) was performed at the Electrochemistry Laboratory (LEC, PSI) to investigate the chemical environment and oxidation state of the corresponding elements at the surface of LaTiO_xN_y . XPS was further used to estimate the surface chemical composition of the LaTiO_xN_y thin films. XPS measurements were performed using a VG ESCALAB 220iXL spectrometer (Thermo Fischer Scientific) equipped with an Al K_α monochromatic source and a magnetic lens system. The binding energies of the acquired spectra were referenced to the C 1s line at 284.6 eV. Background subtraction has been performed according to Shirley^[187], and the atomic sensitivity factors (ASF) of Scofield were applied to estimate the atomic composition^[188].

Time-of-Flight Secondary Ion Mass Spectrometry (ToF-SIMS) analyzes were performed at the International Institute for Carbon-Neutral Energy Research (I2CNER, Electrochemical Energy Conversion Division, Kyushu University, Japan) on a ToF-SIMS V instrument (IonToF GmbH, Germany), using a bunched

30 keV Bi^+ analytical beam. Depth profiling was performed by using a second ion beam of 1 keV Cs^+ at 45° incidence. To compensate for charging of the samples under the high currents of the sputter beam, low energy electrons were supplied by a flood gun. The use of cesium to perform the sputtering affords the analysis of Cs_nM^+ clusters, which serves two purposes; firstly, it mitigates the difference in secondary ion yields as the profile proceeds through different matrices (LaTiO_xN_y / TiN / MgO), and secondly, Cs_2N^+ and Cs_2O^+ clusters can be monitored to follow the depth distributions of oxygen and nitrogen. The latter is beneficial in the present case, because of the complicated overlapping distribution of TiO^+ and TiN^+ fragment ions corresponding to the isotope distribution of titanium.

Surface and near-surface characterization of the polycrystalline LaTiO_xN_y thin film was performed at the International Institute for Carbon-Neutral Energy Research (I2CNER, Electrochemical Energy Conversion Division, Kyushu University, Japan) by Low-Energy Ion Scattering (LEIS) (Qtac100 spectrometer, Ion-ToF GmbH, Germany). LEIS provides information of the elemental chemical composition of the first atomic layer of the surface by analyzing the energy distribution of the backscattered noble gas ions^[189,190]. After introduction of samples into the LEIS instrument, they are exposed to a neutral flux of reactive atomic oxygen at room temperature that removes any adventitious contamination that would hinder the detection of the elements present at the outer surface. This cleaning method avoids any surface damage or atomic rearrangements that could be induced by other standard cleaning procedures, such as ion sputtering or annealing at high temperature^[191].

The primary ion beam is produced by a high brightness plasma source and directed towards the surface at normal incidence, while the backscattered ions are collected at a scattering angle of 145° from the entire azimuth by a double toroidal analyzer. Different primary ion species were used for the characterization in order to obtain information of light elements (e.g. light elements with a mass < 20 u are detected by 3 keV He^+ primary ions) and good sensitivity and resolution for the heavier cationic species (analysis by 6 keV Ne^+ primary ions). The analysis areas were chosen to be rather large (1 mm^2) in order to minimize the surface damage during the analysis by keeping a low ion dose, while assuring that random distribution of grain orientations in the polycrystalline LaTiO_xN_y surface was probed. Nevertheless, some light species present at the outer surface (e.g. light

species present at the surface or adsorbed molecules from the residual gas) might be sputtered during the analysis using 6 keV Ne^+ ions, leading to a background signal that makes the detection of light cations difficult. In order to improve the detection of Ti at the surface, the cation surface analysis was performed by time-of-flight (ToF) filtering of the species arriving to the detector, allowing to discriminate the secondary ion signal from the signal originated from Ne^+ primary ions scattered by Ti atoms at the surface^[192].

In addition to the surface characterization, the near-surface distribution of the cations was investigated by LEIS depth profiling. In this case, a dual beam analysis was performed by alternating the analysis with the 6 keV Ne^+ primary ions and a sputter cycle using a second sputtering beam. The sputtering was performed using a low-energy Ar^+ source (500 eV) at an incidence angle of 59° . To avoid edge effects during depth profiling, the sputter Ar^+ beam was rastered over a $1.3 \times 1.3 \text{ mm}^2$ area.

2.2.3. Crystalline properties of thin films

The crystalline properties of thin films were obtained using a Bruker-Siemens D500 X-Ray diffractometer (XRD) with a characteristic Cu K_α radiation. XRD measurements were performed using $\theta/2\theta$ -scans and 2θ -scans in grazing incidence mode ($\theta = 1^\circ$). XRD patterns obtained using the first method provides details of the out-of-plane orientation of the grown thin film. The latter method was used to get information about the crystalline quality. An epitaxial grown thin film measured in grazing incidence mode does not show any reflexes. On the other hand, a polycrystalline thin film is composed of randomly oriented crystallites and the XRD pattern in grazing incidence mode shows reflexes from all the containing crystallographic planes. Such an XRD pattern can be used to confirm the crystallographic phase of the thin film.

2.2.4. Optical properties

Transmittance data were collected with a Cary 500 Scan UV-Vis-NIR spectrophotometer in the wavelength range of 200 nm to 1000 nm (6.20 eV to 1.24 eV). The

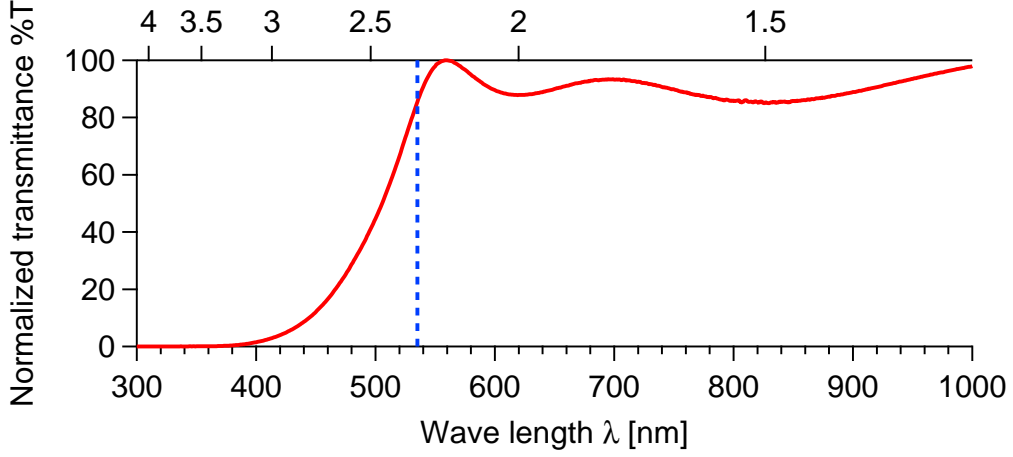


Figure 2.4.: Example of an UV-Vis spectrum of a LaTiO_xN_y sample grown on a double-side polished Al_2O_3 substrate.

measurements were performed using the dual-beam configuration with a blank substrate as reference. The thin film samples were grown on double-side polished substrates to reduce scattering at the backside of the sample and to increase the signal-to-noise ratio. Transmittance measurements were only performed using transparent substrates and not TiN-coated substrates. Thin films of TiN in the range of 10 nm to 20 nm can be used as transparent conducting nitride layers, but transmittance reduces strongly with increasing thickness^[193–195]. TiN layers fabricated for this project are above 50 nm and therefore not transparent enough for transmittance measurements.

Fig. 2.4 shows an example of an UV-Vis measurement using a LaTiO_xN_y thin film sample grown on a double-side polished Al_2O_3 substrate. This transmittance measurement also reveals the characteristic interference fringes typically visible for thin films with a smooth surface^[196]. These interference fringes are detrimental when determine the nature and the value of the band gap by the Tauc plot^[197]. For the tauc plot, the transmittance data T has to be transformed to absorbance A using the equation

$$A = -\ln T \quad (2.1)$$

The absorbance is then used in the tauc equation

$$(Ah\nu)^{\frac{1}{r}} = B(h\nu - E_g) \quad (2.2)$$

where $h\nu$ is the photon energy, B is a proportionality factor and E_g is the optical band gap. The exponent r can be either $\frac{1}{2}$ (direct allowed transitions), $\frac{3}{2}$ (direct forbidden transitions), 2 (indirect allowed transitions) and 3 (indirect forbidden transitions). Due to the interference fringes, it was not always possible to determine the band gap value with the Tauc plot. Further, it was also possible to clearly identify the nature of the transition as direct or indirect. The band gap value can also be estimated using the transmittance data as indicated by the blue dashed line in Fig. 2.4.

2.2.5. Thickness measurements

For the calibration of the deposition rates, the thicknesses of the samples were measured by surface profilometry (Dektak 8, Veeco Instruments) or by X-Ray Reflectometry (XRR) using the XRD instrument from section 2.2.3.

The profilometry measurements were performed in contact mode with a constant (about 8 mg) force between the moving tip (tip diameter of 5 μm) and surface. The film thickness was determined by measuring the step height from the bare substrate to the thin film covering the substrate with a constant scan speed of about 1 mm min⁻¹ (Fig. 2.5).

In XRR the constructive interference between X-rays reflected from the surface and X-rays reflected at the interface film/substrate is utilized. Due to the short wavelengths of X-rays, small angles have to be applied and $\theta/2\theta$ -scans are performed from about 0.5° to 3°. From the XRR pattern, the maxima with number m and the corresponding angle θ_m were collected. m^2 is then plotted over θ_m and fitted with a linear regression $m^2 = k\theta_m + d$. With $k = \left(\frac{\lambda}{2t}\right)^2$, the film thickness can then be determined by

$$t = \frac{\lambda}{2\sqrt{k}} \quad (2.3)$$

with the wavelength $\lambda = 0.15418$ nm of the Cu K $_{\alpha}$ radiation^[198].

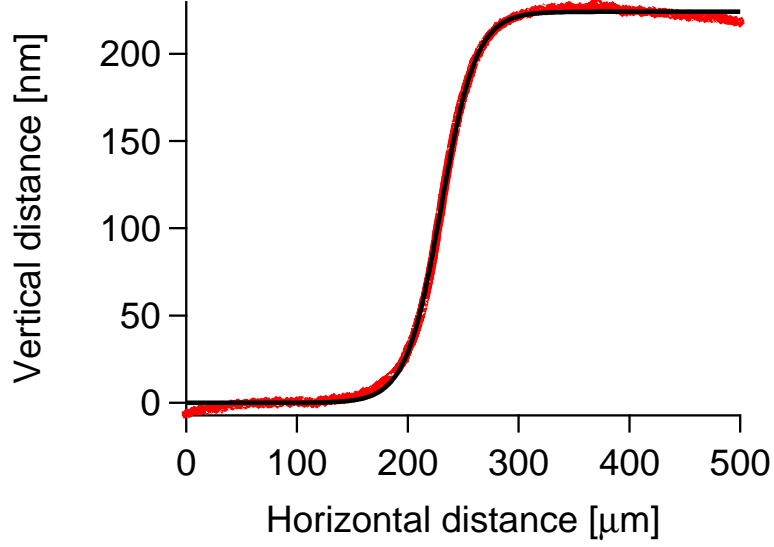


Figure 2.5.: Example of a profilometry measurement of a LaTiO_xN_y sample grown on a Al_2O_3 substrate. The data (red) was fitted with the function $f(x) = y_0 + \frac{A}{\exp \frac{x_0 - x}{c} + 1}$ (black) to better estimate the thickness of the measured sample. A corresponds to the thickness, x_0 is the x-value of the inflection point, c defines the slope of the function and y_0 is the offset.

2.2.6. Surface morphology and topography

A Zeiss Supra VP55 Scanning Electron Microscope (SEM) was used to investigate surface and cross sectional morphology of thin films. An in-lense detector was used with a typical acceleration voltage of 5 kV and a working distance of about 5 mm.

An XE100 Atomic Force Microscope (AFM) from Park Systems was used to determine the surface topography of the samples. The RMS of the height distributions from the AFM images was taken as a measure of the roughness of the surfaces. The scans were made in non-contact mode, using NCHR silicon tips from Nanosensors (nominal force constant 42 N m^{-1} and resonance frequency 330 kHz). The AFM measurements were performed at the Photonic Processing of Advanced Materials group (National Institute for Laser, Plasma and Radiation Physics, Magurele, Bucharest, Romania).

2.2.7. Electronic structure (Measurements at the Swiss Light Source)

Traditional characterization methods, such as UV-Vis-NIR spectroscopy (see section 2.2.4), allow an indirect estimation of the absorption coefficient and band gap of photo-catalysts^[199,200]. However, this technique does not provide information on the valence and conduction band electronic structure, which is essential for the rationalization of the photo-catalytic activity. Szlachetko and Sá^[176] used a combination of Resonant Inelastic X-ray Scattering (RIXS) and theoretical calculations to determine the electronic structure of undoped anatase TiO₂ and N-doped TiO₂. This strategy allowed mapping the complete electronic structure of occupied and unoccupied states, which, in semiconductor terminology, correspond to valence and conduction band, respectively. In this work, the mapped electronic structure of the investigated thin film samples will be reported, determined by using the same strategy adopted by Szlachetko and Sá^[176].

RIXS includes X-ray absorption and emission spectroscopy, where a core electron (here Ti 1s) is excited to an unoccupied electronic state close to the absorption threshold (CB) and an electron from a valence state decays to the empty core state by emitting an X-ray photon (see Fig. 2.6a)^[201]. This occurs in resonance since the X-ray energy is tuned for the excitation of a core electron to an unoccupied electronic state. RIXS maps were collected at the SuperXAS beamline of the Swiss Light Source (SLS) by scanning with 0.5 eV steps around the absorption edge, and recording at each incident energy the emission spectrum with eV resolution using a wavelength dispersive spectrometer operated in the von Hamos geometry^[202] (see section 3.1). The complete electronic structure of the film was determined by measuring simultaneously the K _{β} and valence-to-core transitions around the Ti K-edge. We used a Ge(400) crystal in the von Hamos spectrometer, which provides a relative experimental resolution of 2×10^{-4} . RIXS maps were compared to the theoretical results calculated using the FEFF9.0 code^[203–206]. The code enables the retrieval of the orbital constitution of the La₂Ti₂O₇ valence and conduction bands.

Additional X-ray Absorption Spectroscopy (XAS) and non-resonant X-ray Emission Spectroscopy (XES) experiments were also performed at the SuperXAS beamline of the SLS (see section 3.2). For XAS and XES experiments, the core

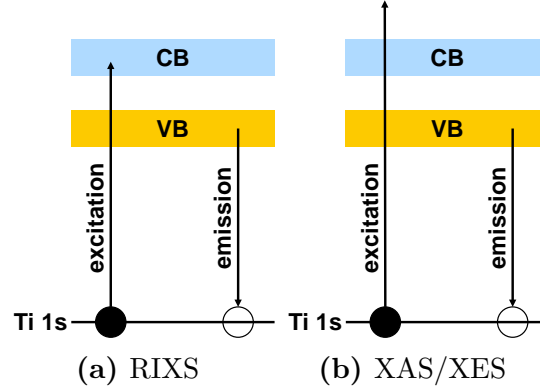


Figure 2.6.: Schematically shown working principle of the X-ray spectroscopy measurements performed at the SuperXAS beamline of the Swiss Light Source at PSI^[201]: (a) Resonant Inelastic X-ray Scattering (RIXS) and (b) X-ray Absorption Spectroscopy (XAS) and non-resonant X-ray Emission Spectroscopy (XES).

electron (Ti 1s) is excited to a high energy continuum (well above the threshold for electronic excitation) and an electron from a valence state decays to the empty core state by emitting an X-ray photon (see Fig. 2.6b)^[201]. This does not occur in resonance since the X-ray energy is high enough for the excitation of a core electron to the continuum. The X-rays, delivered by bending magnets, were monochromatized with double Si(111) crystals, and focused down to a size of $100 \times 100 \mu\text{m}^2$ by a Pt mirror. The X-ray absorption spectra were measured around the Ti K absorption edge at 4966 eV by a Silicon Drift Detector. A fixed incidence X-ray energy at 5000 eV was used for measurements of the X-ray emission spectra for Ti valence-to-core transitions and by a dispersive-type von Hamos spectrometer^[202] with curvature radius of 25 cm. The spectrometer was aligned in vertical scattering geometry with the Ge(400) reflection and the Bragg angle around 62° . To preserve high energy resolution for X-ray detection, we employed a segmented-type crystal consisting of 50×1 mm segments, with a total crystal dimension of 50×100 mm (dispersion \times focusing). The X-rays diffracted by the crystal, were registered with a 2D Pilatus detector having a pixel size of $175 \mu\text{m}$. The sample was aligned in the grazing incidence geometry, in order to enhance the XES signal recorded by the von Hamos spectrometer. We would like to note that the so-obtained line-source does not influence the overall energy resolution of the setup, but greatly increases the number of events registered by the spectrometer^[207].

2.3. Photoelectrochemical Characterization

Within this project, two photoelectrochemical (PEC) setups were used:

- The PEC setup at the EMPA Laboratory Materials for Energy Conversion (Swiss Federal Laboratories for Materials Science and Technology , Überlandstrasse 129, 8600 Dübendorf, Switzerland) - introduced in chapter 2.3.1.
- The new PEC setup established in the Materials Group at PSI especially for this project - introduced in chapter 2.3.2.

2.3.1. Photoelectrochemical test setup at EMPA

The PEC measurements at EMPA (Fig 2.7) were performed using LaTiO_xN_y thin film grown on TiN-buffered MgO substrates in a three-electrode configuration. The oxynitride film on TiN-buffered MgO was used as the working electrode, while a Pt wire was the counter electrode. The third electrode was a Ag/AgCl reference electrode in 3 M KCl aqueous solution. The TiN current collector was electrically connected to the electronics using Cu wires and Ag paste.

The samples were placed in the PEC cell^[208] for front-side illumination, since TiN is not transparent. The cell was filled with an aqueous solution of 0.2 M sodium borate (H_3BO_3 and $\text{Na}_2\text{B}_4\text{O}_7 \cdot 10\text{H}_2\text{O}$) buffered at a pH of 9 as electrolyte. An insulating varnish was used to get the electrolyte in contact with the sample under investigation only on a selected area of the LaTiO_xN_y film surface.

The samples were illuminated with a 300 W Xe lamp (LOT-Oriel) equipped with an UV cutoff filter ($\lambda = 420\text{ nm}$). The light intensity was adjusted to 100 mW cm^{-2} . A rotating shutter was used to alternately measure the dark current (no light on the sample) and the photocurrent. A Versastat 4 potentiostat was used to measure the photocurrent and a scan rate of 10 mV s^{-1} was used for linear scan voltammetry measurements.

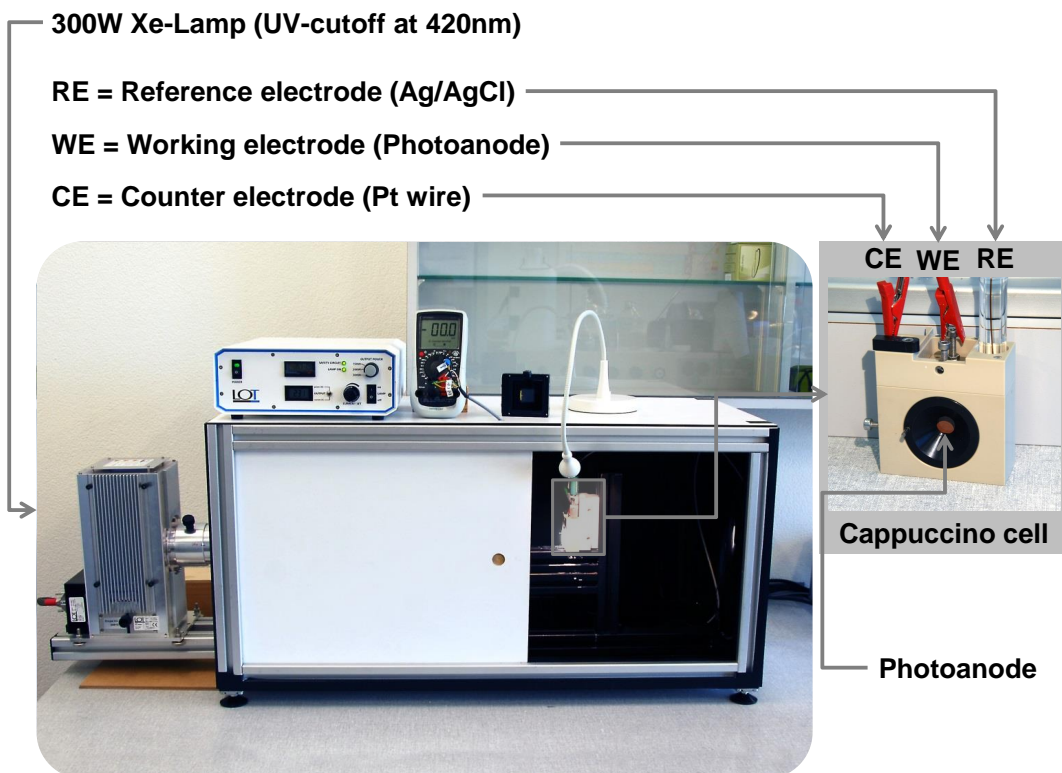


Figure 2.7.: Photoelectrochemical test setup at EMPA using the so-called “cappuccino cell” [208]. The light intensity is adjusted to 100 mW cm^{-2} with a reference Si photodiode.

2.3.2. Photoelectrochemical test setup at PSI

The PEC measurements at PSI (Fig 2.8) were performed using LaTiO_xN_y thin films grown on TiN-buffered MgO and Al_2O_3 substrates in a three-electrode configuration. LaTiO_xN_y thin films acted as the working electrode and a Pt wire was the counter electrode. The third electrode was a Ag/AgCl reference electrode immersed in saturated KCl electrolyte. TiN acted as the current collector.

TiN is not transparent, thus only front-side illumination was possible. The PEC quartz cell and the Ag/AgCl reference electrode are commercially available from Pine Research Instrumentation. An aqueous solution of 0.5 M NaOH (pH = 13) was used as electrolyte. At one edge of the sample, the LaTiO_xN_y layer was carefully removed to expose the TiN layer. Silver paste was coated on the exposed TiN to provide the electrical contact between the current collector and

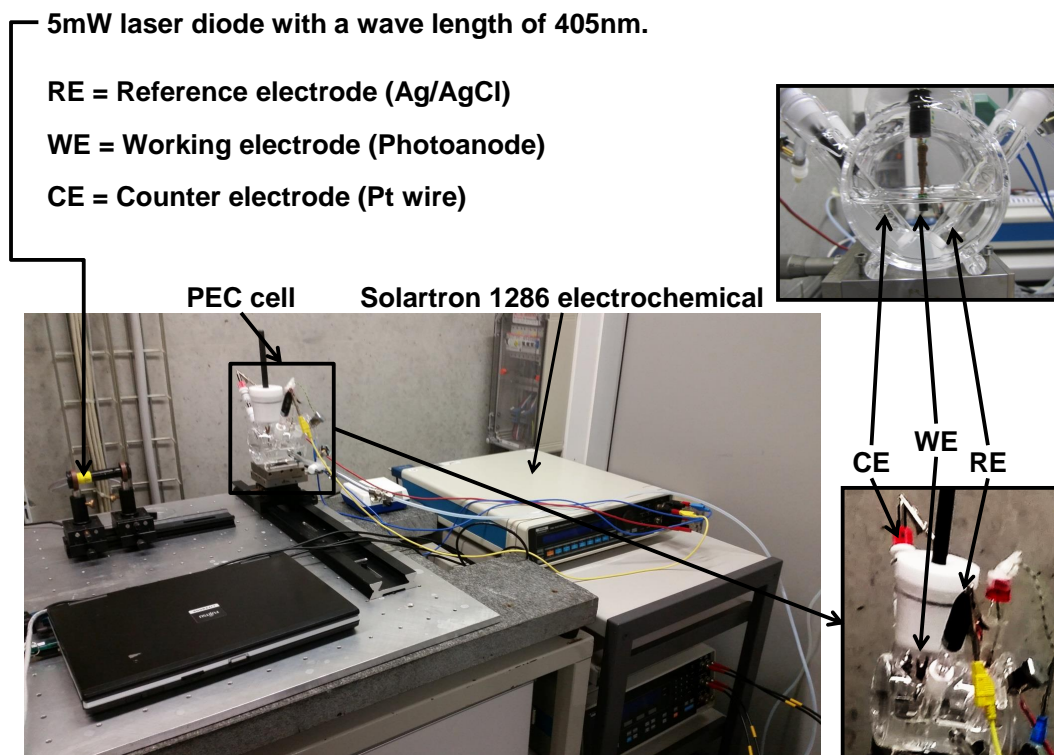


Figure 2.8.: The new photoelectrochemical test setup established for this project. The light intensity is about 130 mW cm^{-2} (reflection losses corrected).

the read out electronics. The samples were cleaned by rinsing with de-ionized water and only the LaTiO_xN_y -coated part of the sample was immersed into the electrolyte. In this way the conducting elements of the sample were electrically isolated from the electrolyte and no insulating varnish was required.

The samples were illuminated with a 405 nm laser diode (Laser2000) with 5 mW power output and a spot size of about 0.0308 cm^2 . The light intensity was estimated to be about 130 mW cm^{-2} considering reflection losses at the quartz cell and at the surface of the sample. To measure the dark current (no light on the sample) and the photocurrent consecutively, an asymmetrical time lag relay pulse generator was used to intermittently irradiate the sample.

A Solartron 1286 electrochemical interface was used to measure the current. For potentiodynamic measurements, we chose a scan rate of 10 mV s^{-1} and a potential range of 0.1 V to 1.5 V vs. RHE.

3

X-ray spectroscopy experiments at the Swiss Light Source

To address the open question of how the nitrogen content affects the electronic structure in oxynitrides, thin film samples are prepared using conventional pulsed laser deposition for the oxide (see Chapter [2.1.1](#)) and modified pulsed laser deposition technique for the oxynitride (see Chapter [2.1.2](#)). The thin film samples are investigated with X-ray spectroscopy as described in Chapter [2.2.7](#).

In Chapter [3.1](#), the Szlachetko & Sá methodology is applied to $\text{La}_2\text{Ti}_2\text{O}_7$ thin films to serve as the basis for future electronic structure studies and to verify the suitability of thin film samples for X-ray spectroscopy. The effect of nitrogen incorporation into the oxide material is investigated in Chapter [3.2](#), where the electronic structures of LaTiO_3 and LaTiO_xN_y thin films is compared.

3.1. Determination of conduction and valence band electronic structure of $\text{La}_2\text{Ti}_2\text{O}_7$ thin film

The results of this section have been adapted with permission of The Royal Society of Chemistry:

J. Szlachetko, M. Pichler, D. Pergolesi, J. Sá, and T. Lippert. [RSC Adv., 2014, 4, 11420-11422.](#)

The samples were fabricated and characterized by Markus Pichler. X-ray spectroscopy and data analysis was performed under the guidance of Jakub Szlachetko. The manuscript^[177] was written with contributions of all authors.

3.1.1. Results and discussion

The film diffraction pattern was found to be in agreement with the $\text{La}_2\text{Ti}_2\text{O}_7$ crystal structure. Chemical analysis revealed a slightly smaller concentration of Ti and O compared to stoichiometry (ca. less than 1 %). This can be explained by the thin film deposition process, where lighter elements are prone to get lost during deposition^[209,210].

The measured K_β and v2c (valence-to-core) RIXS (resonant inelastic X-ray scattering) planes for $\text{La}_2\text{Ti}_2\text{O}_7$ are plotted in Fig. 3.1. For excitation energies above 4980 eV, the RIXS plane consists of the K_β main emission line resulting from the $3p \rightarrow 1s$ transition at an emission energy around 4931 eV. The diagonal spectral feature, crossing the RIXS plane at equal incoming and emitted X-ray energies, relates to the elastically scattered X-rays in the sample. Since the experiments were performed using a dispersive von Hamos spectrometer, which has no moving optical components, the XES (X-ray emission spectroscopy) spectra are measured at once on a shot-to-shot basis, and the elastically scattered X-rays allow calibration of the RIXS plane with a precision of about 100 meV. Before starting the discussion of the RIXS map, we would like to emphasize that the experiments were carried out in grazing incidence geometry, which circumvents the problem of sample volume caused by thin films, i.e., grazing incident geometry equals “infinitively” thick sample.

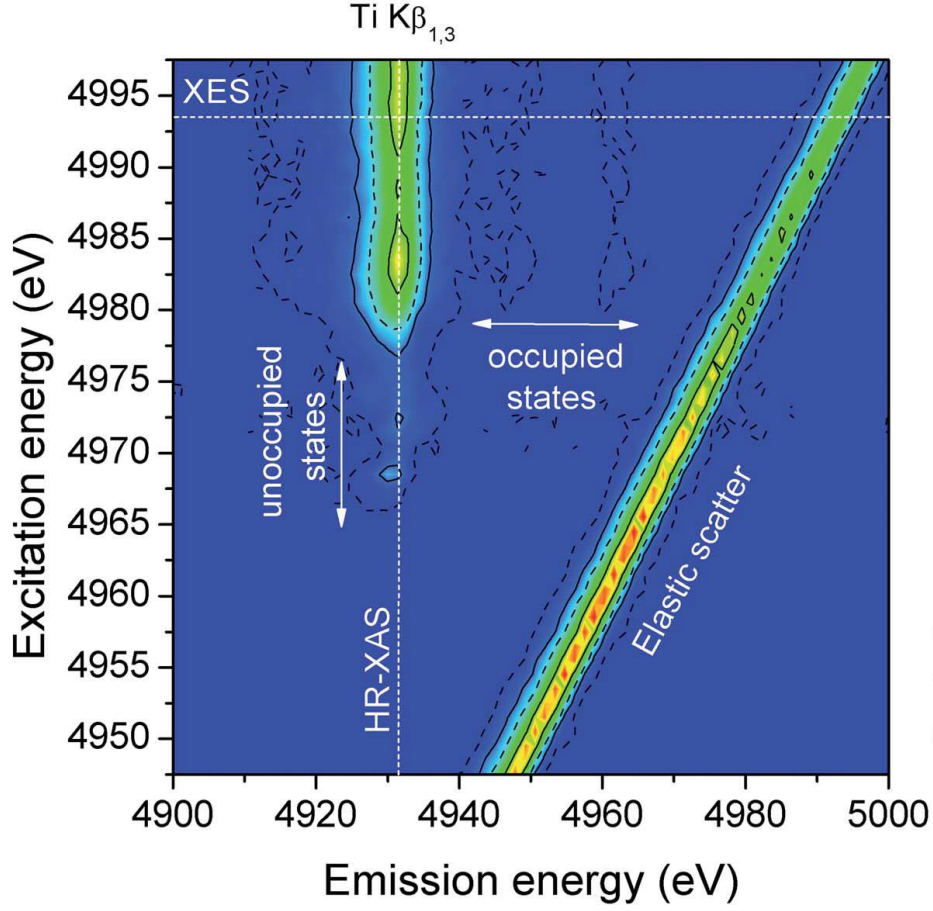


Figure 3.1.: RIXS map of $\text{La}_2\text{Ti}_2\text{O}_7$.

There are several parameters that can be extracted from the RIXS plane. It should be mentioned that the presented RIXS experiments relate to the p-projected density of states (DOS) of the Ti-sites around the Fermi level. Firstly, one can determine the occupied electronic states (valence band) from the non-resonant XES spectrum (valence-to-core XES (v2c-XES)), shown in Fig. 3.2a. Two peaks located at 4945 eV and 4960 eV dominate the v2c-XES spectrum. The spectral features can be interpreted based on DOS calculations with the FEFF9.0 code^[203–206] (Fig. 3.2b). In order to compare the measured v2c structures with calculations, the XES and HR-XAS spectra were scaled down in energy by a value of 4963 eV. The latter was determined from the position of the high-energy side of the v2c structure (half width) and is assigned as the Fermi energy (highest occupied electronic orbitals). The v2c-XES peak lying just below the Fermi

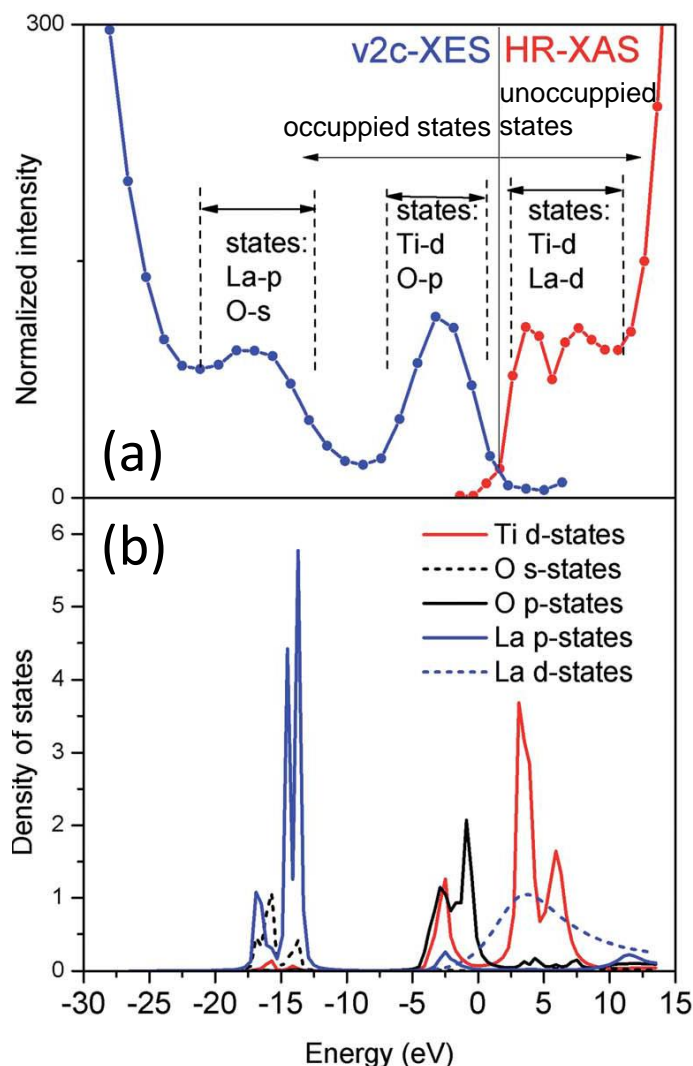


Figure 3.2.: (a) extracted spectra of HR-XAS (red) and valence-to-core XES (blue); (b) FEFF calculated orbital contribution.

energy (-3 eV) consists mostly of Ti-d and O-p orbitals, with a small contribution from La-p orbitals. The upper level of the valence band is primarily composed of O-p orbitals, similar to TiO_2 [176]. The v2c-XES peak at -16 eV is composed of O-s and La-p orbitals. There is a very good overlap between the O-s and La-p orbitals, which explains the pronounced peak detected experimentally, contrary to what was observed with TiO_2 (Ref. [176]) where only a weak feature related to the O-s states could be detected.

The second parameter that can be extracted is the material's unoccupied

electronic states (conduction band) from the HR-XAS (high-resolution X-ray absorption spectroscopy) spectrum. HR-XAS relates to the cut across the maximum of the K_β X-ray emission where the spectral features were assigned based on DOS calculations with the FEFF9.0 code^[203–206]. The two peaks detected on HR-XAS are associated to the Ti d-orbitals (at energies of around +4 eV and +8 eV), which are split by ca. +4 eV according to the crystal field into t_{2g} (lower energy) and e_g (higher energy) levels^[211], similar to TiO_2 ^[212], and by a broad contribution from the La-d orbitals. FEFF calculations were performed using the crystal structure of $\text{La}_2\text{Ti}_2\text{O}_7$, and a total of 100 atoms.

The measured occupied (red) and unoccupied (blue) p-projected DOS profiles are separated by ca. 2.8 eV to 4.0 eV, which encompasses the $\text{La}_2\text{Ti}_2\text{O}_7$ band-gap energy^[213]. The result implies that the RIXS experiment provides band gap-like information, which can be used to evaluate changes to the band gap induced for example by doping. However, it should be mentioned that the band gap values estimated with this method are slightly different from the ones obtained by optical spectroscopy due to the electron-electron interaction between the 1s-excited and valence decaying electrons as well as due to core-hole screening effects. Nevertheless, the dependence on band gap narrowing or broadening by means of v2c-RIXS should be easy and straightforward to detect.

3.1.2. Conclusion

In conclusion, the presented method enabled the determination of $\text{La}_2\text{Ti}_2\text{O}_7$ conduction and valence band orbital composition for thin films with a thickness of 180 nm. The information can be used to rationally design doped materials with enhanced visible light absorption since it is possible to determine what the orbitals contribution and the shift on the band structure edges are. The possibility to carry out the experiments in grazing incidence geometry circumvents the problem of sample volume, often a challenge performing high-resolution X-ray experiments with thin films. Finally, since the measurements were performed with hard X-rays, the experiments were carried out under atmospheric conditions, enabling in the future measurements to follow changes in the orbitals during water splitting under realistic in-situ conditions.

Although RIXS was used for this investigation, inelastic scattering was not considered in the discussion. However, this can be examined in future studies (see chapter [5.2](#)).

3.2. Determination of conduction and valence band electronic structure of LaTiO_xN_y thin film

The results of this section are currently in preparation for submission. Authors are:

M. Pichler, J. Szlachetko, I. E. Castelli, M. Döbeli, A. Wokaun, D. Pergolesi, and T. Lippert.

The samples were fabricated and characterized by Markus Pichler. Max Döbeli supervised RBS and ERDA measurements. X-ray spectroscopy and data analysis was performed under the guidance of Jakub Szlachetko. DFT simulations were performed by Ivano E. Castelli. The manuscript under preparation was written with contributions of all authors.

3.2.1. Results and discussion

For this study, the electronic structure of thin films of the perovskite oxynitride LaTiO_xN_y (LTON) was determined by combining X-ray absorption and non-resonant emission spectroscopy (XAS and XES) and compared to lanthanum titanate (LTO) thin films with the same crystal structure. The use of thin films is particularly suited for this investigation, by selecting different deposition parameters not only the crystallographic properties, but also the nitrogen content of the film could be carefully controlled^[165] allowing the investigation of the changes of the electronic structure (and optical properties) as a function of a different nitrogen content of the sample.

LTON thin films, about 350 nm thick, were deposited on (0001)-oriented Al_2O_3 substrates by Pulsed Reactive Crossed-beam Laser Ablation (PRCLA) using ammonia for the reactive gas pulses and a target of $\text{La}_2\text{Ti}_2\text{O}_7$. Due to the different crystalline structure, the use of sapphire substrates is expected to lead to polycrystalline thin films. X-Ray Diffractometry (XRD) was performed at grazing incidence and the measured reflexes (Fig. 3.3a) confirm the orthorhombic perovskite structure.

Using Rutherford Backscattering (RBS) and Heavy-Ion Elastic Recoil Detection Analysis (ERDA), the composition was determined to be

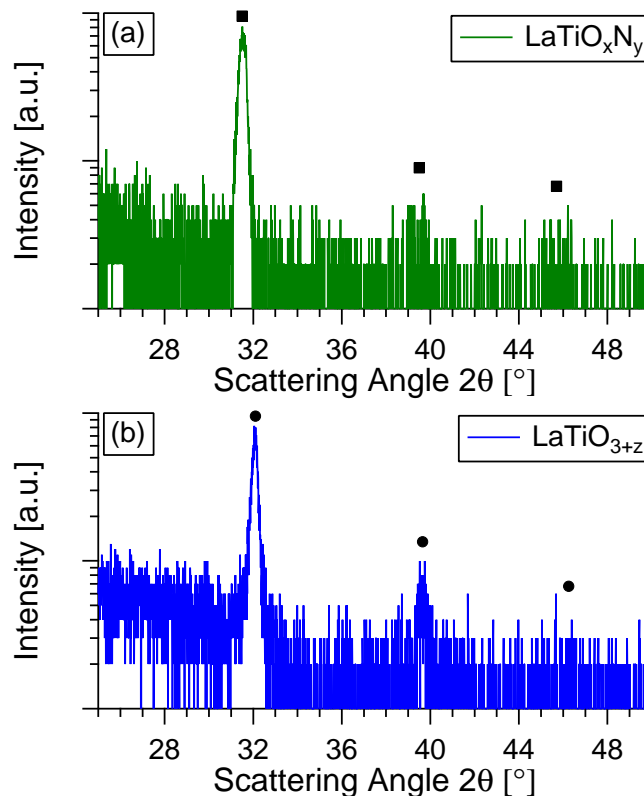


Figure 3.3.: X-Ray Diffraction pattern of (a) polycrystalline LaTiO_xN_y and (b) polycrystalline LaTiO_{3+z} thin film samples performed in grazing incidence mode.

$\text{La}_{1.03}\text{Ti}_{0.97}\text{O}_{2.28}\text{N}_{0.66}$. In agreement with previous studies^[165,209,210] the ablation process led to a slightly overstoichiometric content of the heavier cation (La) at the expense of the lighter element (Ti). Slight shifts to smaller 2θ angles of the reflexes were measured compared to the stoichiometric composition of LaTiO_2N (ICSD Coll.Code: 168551). This was already observed for LTON samples prepared by sputtering^[156] and PRCLA^[165] and can be explained by the smaller nitrogen content compared to the fully nitrated composition. A lower stoichiometric nitrogen content is often observed also for powder samples due to the competing mechanisms of nitrogen incorporation into the LTON structure and the formation of secondary phases of $\text{TiO}_{1-x}\text{N}_x$ and TiN during prolonged high temperature ammonolysis processes. As a result of a nitrogen to oxygen ratio < 0.5 , in oxynitride titanates Ti can often be found in both the Ti^{3+} and Ti^{4+} oxidation states.

The same experimental set up was also used for conventional PLD to grow

on the same kind of substrates the LTO thin films. The phase diagram of the LaTiO_x system has been investigated^[214] in the range from LaTiO_3 to $\text{La}_2\text{Ti}_2\text{O}_7$ ($x = 3.5$). The two extremes of the LTO phase diagram are not suitable to be compared with LTON. In fact, on one side LTO with low oxygen content (x close to 3) has the same crystal structure as LTON (orthorhombic perovskite), however Ti is mainly in the Ti^{3+} oxidation state ($3d^1$) and the material shows metallic-like electronic properties (no band gap). On the contrary, at high oxygen content we have $\text{La}_2\text{Ti}_2\text{O}_7$ where Ti is only in the Ti^{4+} oxidation state ($3d^0$) and the crystal structure (layered monoclinic perovskite) is different compared to LTON.

For the growth of suitable LTO thin films the KrF excimer laser ($\lambda = 248 \text{ nm}$) with a repetition rate of 10 Hz and a laser fluence of 2.0 J cm^{-2} was used to ablate the $\text{La}_2\text{Ti}_2\text{O}_7$ target placed at 45 mm distance from the substrate. The deposition temperature was set to 800°C . N_2 was introduced as background gas at a partial pressure of 0.1 mbar with the intent to grow thin films with reduced oxygen content compared to $\text{La}_2\text{Ti}_2\text{O}_7$ ^[215], i.e. with Ti in mixed Ti^{3+} and Ti^{4+} oxidation state, still preserving the semiconducting nature of the material but with a crystal structure similar to LTON.

Fig. 3.3b shows the XRD pattern of the lanthanum titanium oxide film with reflexes at very similar 2θ values as observed for our LTON films indicating the orthorhombic perovskite structure. However, the angular positions of the XRD reflexes are shifted toward larger 2θ values compared to the stoichiometric composition of LaTiO_3 (ICSD Coll.Code: 63575), indicating an enlargement of the unit cell volume. RBS and ERDA showed the film chemical composition to be $\text{La}_{1.09}\text{Ti}_{0.91}\text{O}_{3.44}$. According to the LaTiO_x phase diagram proposed in^[214] an oxygen content of 3.44 should lead to a monoclinic layered perovskite of the family $\text{A}_n\text{B}_n\text{O}_{3n+2}$ with $n = 4.5$ representing the well-ordered layered stacking sequence $n = 5, 4, 5, 4$, etc^[216]. The growth of this material as thin film and/or the off-stoichiometric La/Ti ratio observed also for this film^[209,210] may have helped the crystallization of the orthorhombic perovskite phase.

Moreover, the LTON and LTO films not only show very similar crystal structure but comparing their compositions, $\text{La}_{1.03}\text{Ti}_{0.97}\text{O}_{2.28}\text{N}_{0.66}$ for LTON and $\text{La}_{1.09}\text{Ti}_{0.91}\text{O}_{3.44}$ for LTO, it can be seen that also the Ti^{4+} and Ti^{3+} contents are very similar in both samples.

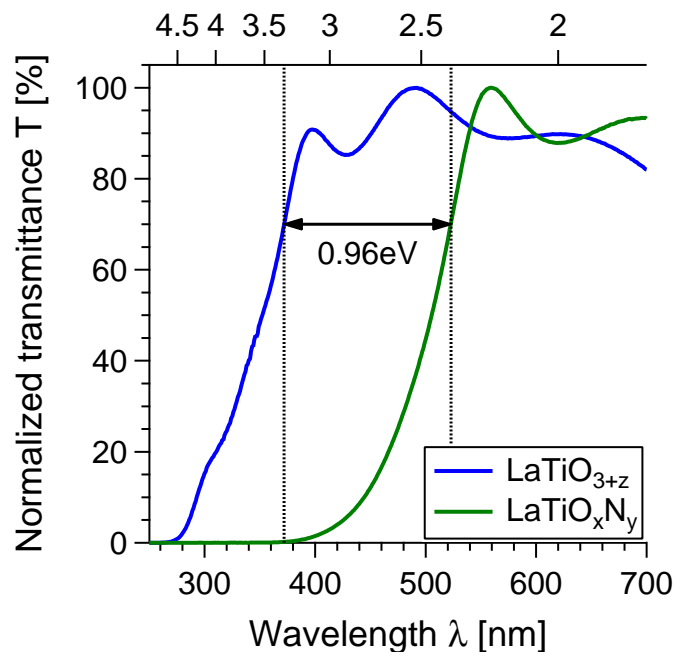


Figure 3.4.: Normalized UV-Vis transmittance spectra of LaTiO_{3+z} and LaTiO_xN_y thin film samples grown on double-side polished Al_2O_3 substrates. Due to the thicknesses of the samples, interference fringes are observed during the UV-Vis measurement^[196]. The dashed lines mark approximately the band gap values of the samples. For the ease of comparison, the transmittance data is normalized to 100 %.

We will refer to these two samples as LTON and LTO.

Fig. 3.4 shows the normalized transmittance of the two samples measured by UV-Vis spectrometry.

LTO has a band gap of about 3.26 eV, i.e. transparent for the visible light range (between 390 nm to 700 nm), whereas a shift in the absorption edge for the oxynitride sample towards smaller photon energies of about 0.96 eV is observed. This confirms the successful incorporation of nitrogen as observed by RBS and ERDA, and its effect on the reduction of the band gap. The estimated band gap value of LTON is about 2.30 eV. This value is about 0.2 eV to 0.3 eV larger than the literature values measured for LaTiO_2N powder samples^[21,88,90,217], which is related to the smaller nitrogen content of our films compared to the fully nitrated compound.

The electronic structure of the two films was probed by X-ray Absorption Spectroscopy (XAS) and non-resonant X-ray Emission Spectroscopy

(XES^[166–175]). The experimental XES and XAS data are compared with theoretical calculations of Density of States (DoS)^[180,181] to assign the different features visible in the acquired spectra. The results of both, experiments and theoretical calculations are shown in Fig. 3.5.

Fig. 3.5a shows the XES spectra (occupied states) representing the VB and the XAS spectra (unoccupied states) representing the CB for LTO (blue) and LTON (green). For both materials, the total XES and XAS spectrum is shifted in energy by 4967.5 eV, which is the energy value at the inflection point of the CB edge of the LTO film. This allows a better comparison of the measured data with the calculated orbital contributions. It is noteworthy that the measured XES and XAS spectra represent the p-projected DoS because the measurements are performed at Ti K-edge (i.e. s-type core-electron). The electronic transitions involved in the experiment are dominated by selection rules with highest probabilities for dipole transitions. Fig. 3.5b shows the calculated orbital contributions (DoS).

Fig. 3.5 is further subdivided into 3 sections highlighted with light blue boxes:

- Section I (−22.5 eV to −13.5 eV) includes strongly bonded occupied states.
- Section II (−10.5 eV to −3.5 eV) includes the occupied states close to the VB edge.
- Section III (−1 eV to 7.5 eV) includes the unoccupied states.

In section I of the LTO XES spectrum, two small features at about −17.5 eV and −21 eV can be observed. Both features are identified with support of DoS calculations as La-p and O-s states, respectively. In the LTON spectrum of section I an additional feature at about −15 eV is detected and assigned to N-s states, while the feature at −17.5 eV became stronger and is composed of La-p and N-s states. On the other hand, the peak at −21 eV became smaller reflecting the reduction of the LTON oxygen content compared to LTO.

section II of the LTO XES spectrum shows the superposition of O-p and Ti-d states forming the distinctive peak at −6.5 eV in Fig. 3.5a. Comparing to the LTON XES spectrum, this peak shifts toward slightly lower energies while a relatively large shift toward higher energies of the VBM can be observed (Fig. 3.5a, section II). The extent of this energy shift is $\Delta_{VB} \approx 0.66$ eV, determined at the

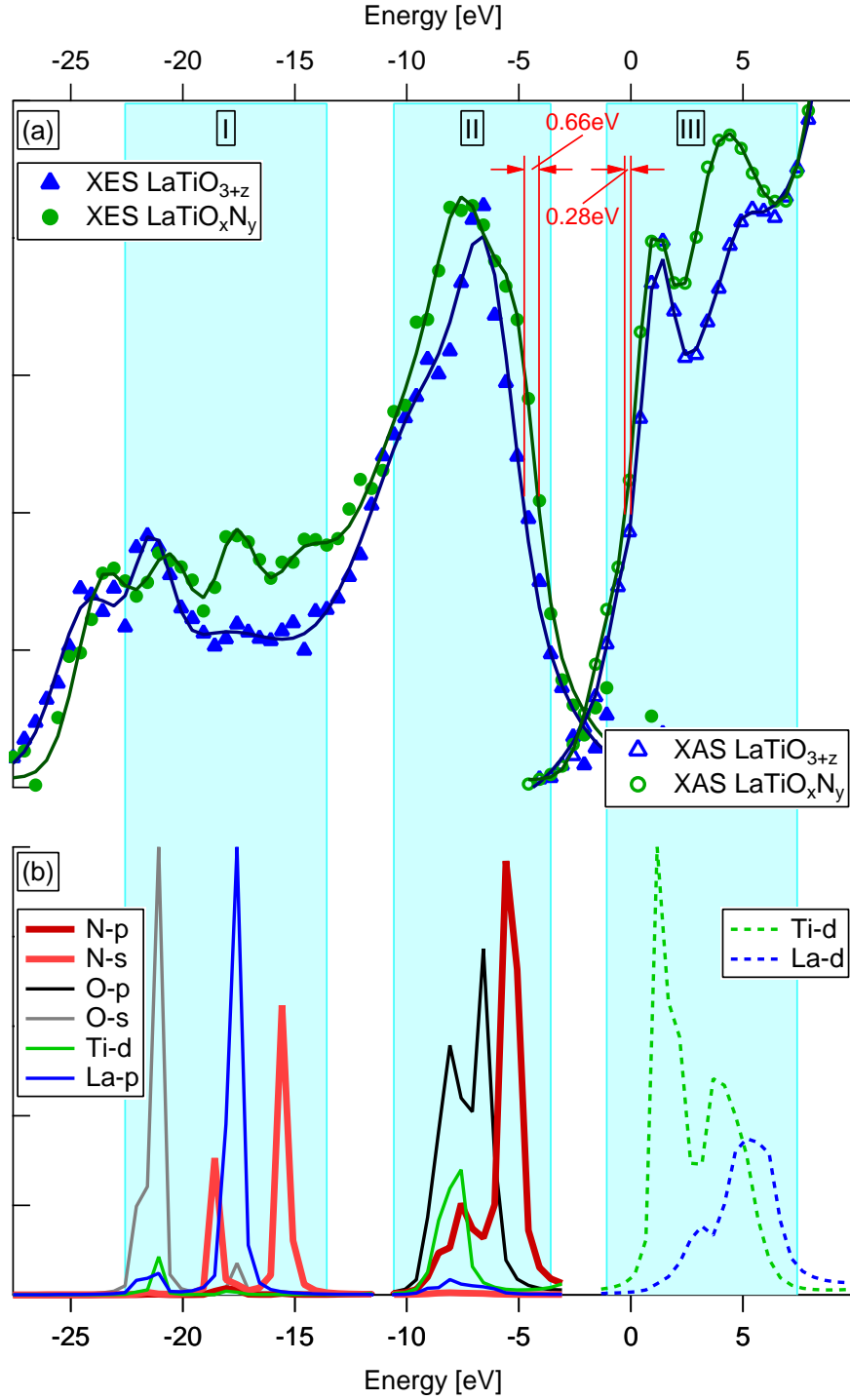


Figure 3.5.: (a) Conduction and valence band electronic structure determined from X-ray emission and absorption spectroscopy measurements of LaTiO_{3+z} and LaTiO_{xN_y} thin films. (b) Calculated orbital contributions. (The markers in (a) correspond to the measured data and the lines act as a guide.)

inflection point of the VBM of both samples. As mentioned above, according to literature the observed shift of the VBM to higher energies, resulting in a reduced band gap for the oxynitride material, is explained with the lower electronegativity of the N 2p orbitals compared to O 2p orbitals^[20,176,218,219]. A hybridization of the energetically higher N 2p and lower O 2p orbitals takes place, forming new electronic states just above the VB states of the native oxides thus shifting the VBM upwards in energy. This explanation is confirmed by our results, where additional electronic states, assigned to N 2p states by theoretical calculations, can be measured experimentally with XES. Fig. 3.5b shows the calculated orbital contributions: the N-p orbitals form additional states at about -5.5 eV (about 1 eV higher in energy than the O 2p contribution).

However, the positive shift of 0.66 eV observed for the VB is not enough to explain the total reduction of the band gap from 3.26 eV to 2.30 eV ($\Delta_{UV-Vis} \approx 0.96\text{ eV}$) observed in the UV-Vis transmittance spectra (Fig. 3.4) as a consequence of the nitrogen incorporation. In other words, the additional energy levels created just above the VBM of the native oxide by the nitrogen substitution (preserving the same crystal structure) only account for less than 70 % of the total band gap reduction.

The analysis of the XAS spectra plotted in section III of Fig. 3.5a accounts for this inconsistency.

The XAS spectrum of LTO in section III consists of two features located at about 1 eV and 4 eV. The first is composed of Ti-d states, while the second arises from the hybridization of the Ti-d and La-d states (Fig. 3.5b). The LTON XAS spectrum shows that the oxygen to nitrogen substitution leads to no additional features in the unoccupied electronic states. This is confirmed with theoretical simulations that also do not show any significant orbital contribution of nitrogen (Fig. 3.5b). However, a significant shift of the CBM of LTON to lower energies compared to LTO is visible in Fig. 3.5a. The extent of such a shift can be quantified in $\Delta_{CB} \approx 0.28\text{ eV}$ at the inflection point of the CBM of both samples. Together with the positive shift of 0.66 eV observed for the VBM, the total band gap reduction measured by XES and XAS is with $\Delta_{VB} - \Delta_{CB} = 0.94\text{ eV}$ in very good agreement with the UV-Vis result.

Since no additional orbital contributions arising from the nitrogen incorpora-

tion were detected in the unoccupied electronic states, the origin of this downward shift of the CBM is difficult to assign.

The shift of the CBM to lower energy may result from a stronger localization of the lowest unoccupied d states of Ti due to the nitrogen incorporation. The effects of localized and delocalized orbitals on the energy position of the CBM were detected in the case of TiO_2 as additional pre-edge features visible in the XAS spectrum acquired in total fluorescence yield^[176,220].

The lattice distortions may also justify the lower energy position of the CBM. It has been reported that in BaTaO_2N , SrTaO_2N , and CaTaO_2N the width of the CB progressively decreases with decreasing the ionic radius of the A cation from Ba to Ca, leaving the energetic center of the CB unchanged. The result is an overall increase of the band gap induced by the size mismatch of the A cation. This is explained by considering the distortion of the unit cell (cubic for A=Ba, tetragonal for A=Sr, and orthorhombic for A=Ca) affecting the Ta-(O,N)-Ta bond angle which is 180° for the cubic structure and progressively smaller in the tetragonal and orthorhombic cells^[163,164].

We speculate that a similar mechanism could explain our experimental results. To support this hypothesis, we performed density functional theory simulations of the $\text{LaTiO}_{2.25}\text{N}_{0.75}$ and $\text{LaTiO}_{3.4}$ crystal structures in their orthorhombic symmetry shown in Fig. 3.6. The relation between the distortions in the octahedra of the two materials was investigated using the GPAW code^[221,222] and PBEsol as exchange-correlation functional^[223]. The calculations show that the octahedral distortions lead to a Ti-(O,N)-Ti bond angle of 161.5° in LTON, while 158° is the calculated value for the Ti-O-Ti bond angle in LTO. Thus, in comparison to the ideal cubic perovskite structure, the orthorhombic distortion of $\text{La}_{1.03}\text{Ti}_{0.97}\text{O}_{2.28}\text{N}_{0.66}$ is expected to be smaller than that of $\text{La}_{1.09}\text{Ti}_{0.91}\text{O}_{3.44}$, corroborating our hypothesis. Furthermore, LTON shows a continuous displacement of the $\text{Ti}(\text{O,N})_6$ octahedra in the c direction (Fig. 3.6a), while for the layered LTO, we have alternating layers of 4 and 5 unit cells along the c axis with a shift of $(\frac{1}{2} a, \frac{1}{2} b)$ between the layers. These periodic displacements create a discontinuity in the TiO_6 octahedra arrangement, as shown in Fig. 3.6b. It has been shown^[224] that this shift in the octahedra has the effect of making the optical transition at the band gap weak or forbidden.

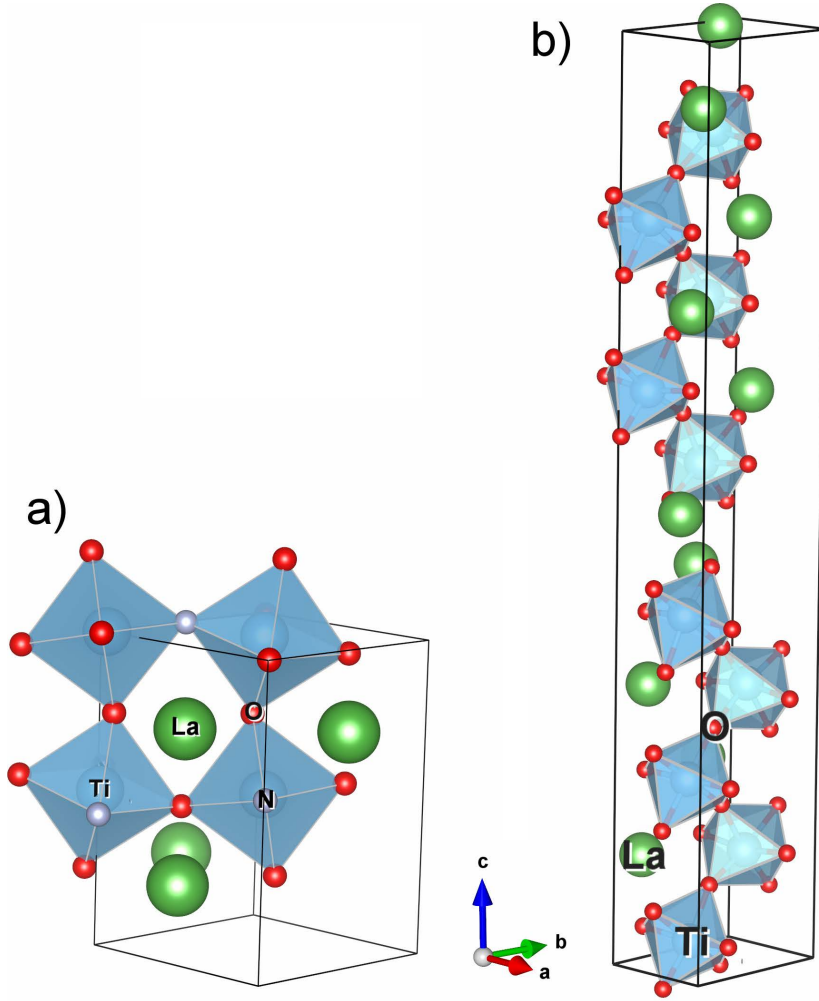


Figure 3.6.: Representation of the crystal structures of (a) $\text{LaTiO}_{2.25}\text{N}_{0.75}$ and (b) $\text{La}_5\text{Ti}_5\text{O}_{17}$ (i.e., $\text{LaTiO}_{3.4}$).

Beside the lattice distortion, also the electronegativity of the B cation influences the position of the CBM. Decreasing the electronegativity of the B cation causes in fact an upward shift in energy of the center of the CB without affecting the width, thus resulting in an overall wider band gap^[163]. We consider the fact that the smaller gap of LTON with respect to LTO could be caused by a change in the electronegativity in the anions with the consequent change in the charge transfer from the A and B cations as well as in their valence.

We calculate the charge transfer for LTO and LTON by means of the so-called Bader analysis^[225,226]. For LTO, in average La releases 2.2 electrons and Ti 2.0 electrons while O receives around 1.2 electrons. For LTON, in average

La and Ti release 2.1 electrons, which gives again a total of 4.2 electrons that are released from the cations. On the anion side, O and N receive 1.3 and 1.5 electrons, respectively, which makes them more negatively charged than in the LTO case. However, further calculations are required to clarify why a negative charge (0.1 electrons) is transferred from Ti to La for LTON and how the different charge separation influences the electronic structure.

We thus conclude that the downward-shift of the CBM from LTO to LTON could have two different origins, i.e. a weaker structural distortion of the nitrogen substituted material or an influence of the possible change in the valence of the cations and anions.

3.2.2. Conclusion

In summary, lanthanum titanium oxynitride and lanthanum titanium oxide thin films with the same orthorhombic perovskite crystalline structure were fabricated to investigate the effect of nitrogen incorporation on the electronic and optical properties. Non-resonant X-ray emission and absorption spectroscopy were performed to map the occupied and unoccupied electronic states. Density of state calculations were used to assign the detected features in the X-ray spectra to atomic orbitals. As expected, the X-ray emission spectrum of the oxynitride clearly shows a shift of the valence band maximum to higher energies compare to the oxide due to the hybridization of O 2p orbital with the energetically higher N 2p orbital. However, the resulting band gap reduction does not match the value measured by UV-Vis spectroscopy. Only by taking into account the X-ray absorption spectroscopy measurement of a significant downward shift in energy of the conduction band minimum, normally considered to be unaffected by the nitrogen incorporation, the overall band gap reduction can be explained.

With the support of density functional theory simulations, we conclude that in perovskite oxynitrides the nitrogen incorporation can also significantly shift the energy position of the conduction band minimum compare to the oxide material with the same crystal structure by affecting the distortions of the unit cell and/or ordering of the lattice.

4

Photoelectrochemical investigation of oxynitride thin films

Photoelectrochemical investigation of different materials as possible current collectors are discussed in Chapter 4.1 where a new model system is introduced. The new model system using the modified pulsed laser deposition technique (see Chapter 2.1.2) enables the photoelectrochemical activity of oxynitrides used as photocatalysts with different nitrogen content to be investigated.

This model system is used in Chapter 4.2 to further quantify the effects of crystalline quality and crystallographic surface orientation of the LaTiO_xN_y photocatalysts on the photoelectrochemical performance. Additionally, surface changes with the photoelectrochemical measurements are investigated.

4.1. Titanium nitride buffered substrates for photoelectrochemical measurements of oxynitride thin films

The results of this section have been adapted with permission of Elsevier:

M. Pichler, D. Pergolesi, S. Landsmann, V. Chawla, J. Michler, M. Döbeli, A. Wokaun, and T. Lippert. [Applied Surface Science 369 \(2016\) 6775](#).

The oxynitride samples were fabricated and characterized by Markus Pichler. The TiN-coated substrates were fabricated by Vipin Chawla. Max Döbeli supervised RBS and ERDA measurements. Photoelectrochemical measurements were performed under the guidance of Steve Landsmann. The manuscript^[165] was written with contributions of all authors.

4.1.1. The current collector

To collect the photo-generated charge carriers, the photocatalyst has to be in contact with an electronic conducting electrode. The material used for such a current collector has to be chemically stable during the oxynitride film growth, i.e. at temperatures as high as about 800 °C and in NH₃ environment. To enable the investigation of the potential effects of the crystalline properties and surface orientation on the PEC performance, the conducting material has to be lattice matched for an epitaxial growth of the oxynitride thin film with good crystalline quality.

Two different experimental approaches can be followed, either the use of a conductive substrate or the use of a conducting thin film as seed layer for the growth of the oxynitride photocatalyst.

Among the suitable electronic conducting substrates, single crystal Nb-doped SrTiO₃ (STO) show very good lattice matching to LaTiO_xN_y (the STO lattice parameter is about 3.90 Å (ICSD Coll.Code: 94573), while for LaTiO₂N the lattice constant is in the range of 3.95 Å (ICSD Coll.Code: 168551), which can vary depending on the nitrogen content). These substrates were successfully used

in Ref. [156] for the growth and characterization of epitaxial LaTiO_xN_y films made by sputtering using a target of the cold pressed oxynitride powders. With our experimental conditions, it was not possible to obtain single phase LaTiO_xN_y thin films on Nb-doped or un-doped STO substrates by PRCLA. The thin films grown on STO were (001) epitaxially oriented with the substrates, but the LaTiO_xN_y diffraction reflexes appear as the result of the overlapping of multiple reflexes, as can be seen for example in the (400) diffraction reflex of LaTiO_xN_y in Fig. 4.1. This may be explained due to the presence of multiple phases of LaTiO_xN_y layers with different nitrogen content in the thin film. It has been shown that STO substrates can easily lose oxygen in reducing environment and exchange oxygen with the film growing on its surface [227]. The substrate itself can indeed provide a large part of the oxygen content of the growing film. When an oxynitride film grows on STO, this effect is particularly detrimental since oxygen atoms from the substrate can be incorporated into the film hindering the nitrogen substitution. In addition, the Nb-doped STO substrates showed strongly reduced conductivity after the oxynitride deposition, suggesting a decomposition of this material under the film growth conditions differently to what was observed for sputtering [156].

Concerning the use of conducting seed layers, for the conventional characterization of powder samples glass substrates coated with transparent conducting oxides are used to collect the photo-generated charge carriers. Typical coatings are made of aluminum-doped zinc oxide, fluorine-doped tin oxide or indium tin oxide. Polycrystalline TiON films were grown by sputtering at relatively low temperature ($> 250^\circ\text{C}$) on these kind of conducting glasses [155]. These commercially available substrates are amorphous, thus only polycrystalline films can be obtained. Moreover, at the high temperatures required for the growth of oxynitride films with high crystalline quality ($> 700^\circ\text{C}$), transparent conducting oxides undergo a thermal decomposition and their conductivity significantly decreases [8]. This makes these materials unsuitable for our purpose even if coatings with high crystalline quality were used.

Thin films of non-transparent electronic conductive oxides could also be used as current collectors. Unfortunately, most of the electronic conducting oxides show suitable electronic conductivity only at relatively high temperatures. But the main problem here is that we could not find any electronic conducting oxide able to provide the required physicochemical stability during the oxynitride

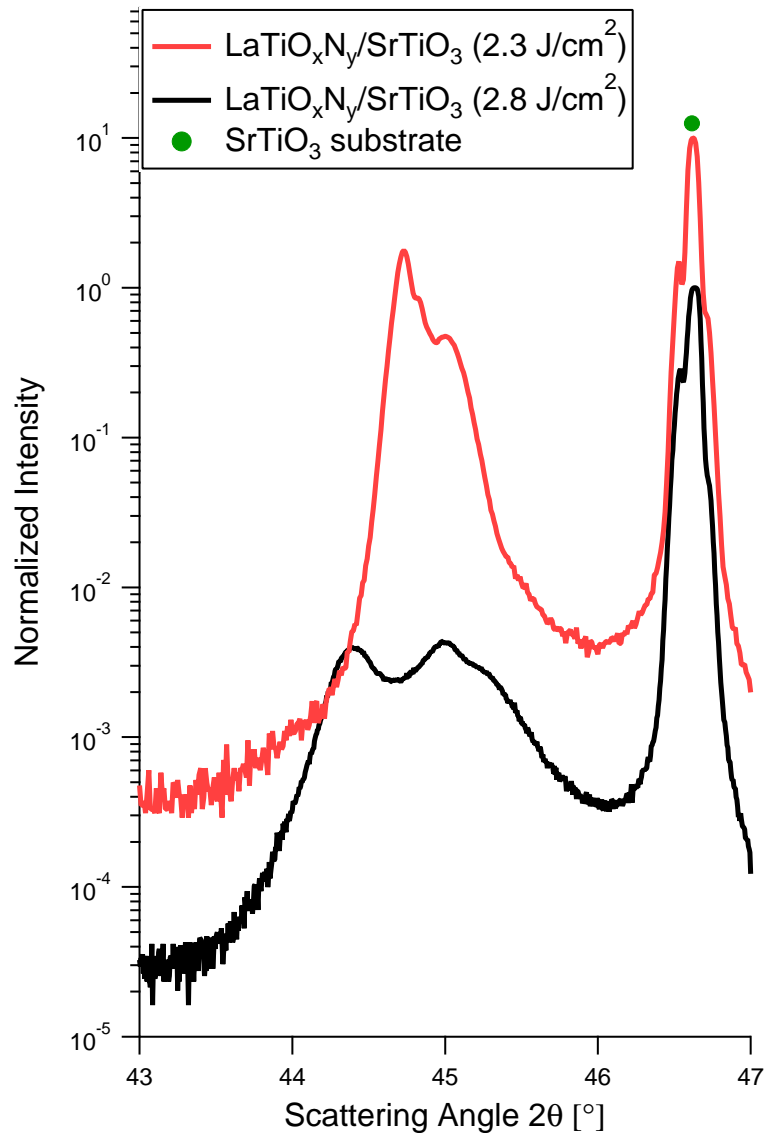


Figure 4.1.: XRD patterns of two representative LaTiO_xN_y samples grown on SrTiO_3 substrates by PRCLA with different laser fluences.

growth condition using PRCLA of the native oxide target, i.e. a strongly reducing environment at high temperatures. Literature reports that SrRuO_3 -buffered substrates were used for the growth of $\text{BaTaO}_{3-x}\text{N}_x$ [158]. This was achieved by conventional PLD using the oxynitride material as the target and an O_2/N_2 gas mixture, i.e. in oxygen-containing environment. For this work we also have attempted the use of SrRuO_3 . Thin films of this material were epitaxially grown on STO substrates at $> 800^\circ\text{C}$ in an oxygen partial pressure of 0.1 mbar. After

XRD analysis, the as-grown films were heated up in vacuum at a temperature of about 600 °C. Such a thermal treatment in vacuum was enough to decompose the SrRuO₃ film, as revealed by XRD analysis, confirming the poor stability of this material in low oxygen-containing environment at high temperature, as already reported in the literature^[228,229]. In the specific case of LaTiO_xN_y, a sufficient nitrogen substitution by PRCLA using the native oxide target requires a gaseous environment with very low oxygen partial pressure (using N₂ and NH₃). This precludes the use of SrRuO₃ as seed layer.

Other possible alternative current collectors are thin films of noble metals, such as Pt or Au, which also have the advantage of a cubic crystalline structure with lattice parameter similar to that of LaTiO_xN_y (3.92 Å for Pt (ICSD Coll.Code: 180880), 4.08 Å for Au (ICSD Coll.Code: 52700), and about 3.95 Å for LaTiO₂N (ICSD Coll.Code: 168551), as an example). However, at the high temperatures required for the oxynitride growth, noble metals show very poor adhesion on the polished surface of single crystal substrates^[230] and typically dewet the substrate surface. The use of additional adhesion layers (typically Ti or Cr are used) would be necessary. Beside the additional complication of the growth of a further layer, the typical metals used to aids Pt or Au adhesion show different crystalline structures compared to Pt and Au, thus precluding the growth of current collectors with high crystalline quality which is a fundamental prerequisite for the growth of high quality epitaxial oxynitride films.

In a different approach, the group of metal nitrides comprises electronically conducting compounds that are known to be chemically very stable over a wide range of chemical environments and temperatures. Within these materials TiN was chosen. Besides being a good electronic conductor, this material has a lattice parameter of about 4.24 Å (ICSD Coll.Code: 656836) which is very similar to that of single crystal MgO substrates (about 4.21 Å, ICSD Coll.Code: 52026). Thus in principle it is possible that TiN epitaxial layers could be grown on MgO with very high crystalline quality and may become a suitable seed layer for the growth of highly textured LaTiO_xN_y films.

The most important issue is the lattice mismatch between LaTiO_xN_y and TiN which is $(a_{\text{LaTiO}_2\text{N}} - a_{\text{TiN}}) / a_{\text{TiN}} \approx -6.8\%$. This is a very large value that cannot be elastically accommodated at the interface between the two materials.

However, the literature reports examples of high quality STO films (which have similar crystal structure and lattice parameter to LaTiO_2N) grown on MgO substrates showing cube-on-cube epitaxial relation and small degree of misalignment between adjacent crystallites^[231,232]. Even examples of multilayered epitaxial heterostructures of $\text{TiN} + \text{MgO} + \text{STO}$ grown on (100)-oriented Si wafers are reported^[233–235], showing that materials like MgO and TiN on one side and STO, thus potentially also LaTiO_xN_y , on the other side can indeed be coupled in highly ordered epitaxial heterostructures.

The large interfacial lattice mismatch can in fact be accommodated at the interfaces in some cases by introducing misfit dislocations that fully relax the excess stress still preserving the epitaxial relation. Examples of such a mechanism can be found in^[236,237] where highly textured epitaxial films of ceria-based materials were grown on MgO substrates via an almost continuous line of interfacial misfit dislocations capable of adjusting a lattice mismatch as large as 29 %.

4.1.2. The growth of the oxynitride photocatalyst on the selected current collector

On the basis of these considerations, we attempted the growth of LaTiO_xN_y on TiN-buffered MgO substrates. Fig. 4.2a shows the $2\theta/\theta$ scan of one samples. As expected the TiN layer grew epitaxially oriented with the substrate. On the contrary, under the selected growth parameters, the oxynitride film clearly shows multiple crystallographic orientations. Further, small shifts toward smaller 2θ angles of the LaTiO_xN_y peak positions can be measured in Fig. 4.2a compared to the literature values of the stoichiometric LaTiO_2N composition (ICSD Coll.Code: 168551). This difference indicates slightly larger out-of-plane lattice parameter which could be explained by a lower nitrogen content ($x < 1$).

The cross sectional Scanning Electron Microscopy (SEM) micrograph in Fig. 4.2b shows a well-defined interface between LaTiO_xN_y and TiN. At the applied magnification the morphology of the TiN layer looks uniform without evidence of clear grain separation, while the oxynitride film shows the typical features of polycrystalline morphology with columnar grains of about 50 nm in diameter elongated along the substrate surface normal. This columnar micro-morphology

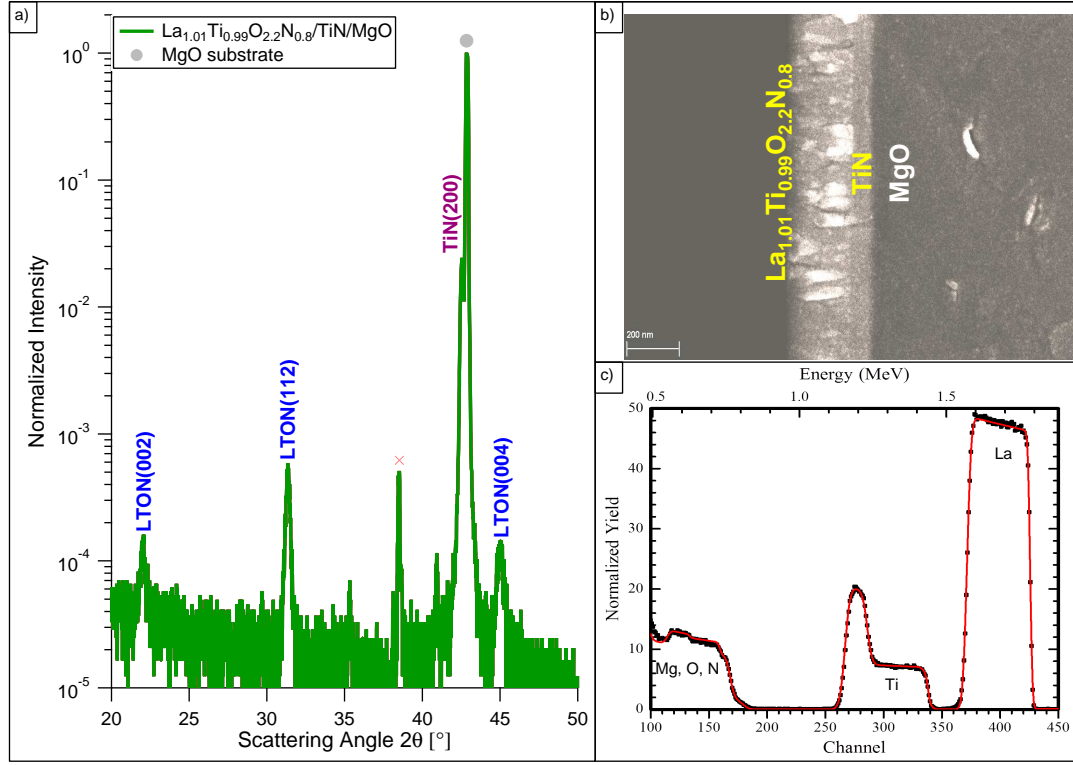


Figure 4.2.: a) XRD pattern of a polycrystalline $\text{La}_{1.01}\text{Ti}_{0.99}\text{O}_{2.2}\text{N}_{0.8}$ thin film deposited on TiN-buffered MgO substrate using PRCLA with a laser fluence of 3.7 J cm^{-2} . The peak marked with an X is the K_{β} diffraction reflex from the MgO substrate. b) Cross section micrograph (fractured surface). c) The corresponding RBS spectrum (black points) analyzed with the RUMP program (red line) and using the N/O ratio determined by ERDA.

is often observed for thin films grown by PLD. The thicknesses measured by SEM for the two layers (about 230 nm for LaTiO_xN_y and 65 nm for TiN) are in good agreement with the values expected from the calibration of the deposition rates.

Before addressing the issue of improving the crystallographic properties of the oxynitride film, we focused on the analysis of its chemical composition performed by Rutherford Backscattering Spectroscopy (RBS) and Elastic Recoil Detection Analysis (ERDA).

Fig. 4.2c shows an RBS spectrum of a LaTiO_xN_y film. At high energies, the first peak corresponds to La, the heavy element, present in the oxynitride film. At intermediate energies, signals from Ti were detected and since Ti is in both layers, a double peak is formed, where the right part at higher energies belongs

to the outer LaTiO_xN_y layer and the left part at lower energies belongs to the buried TiN current collector. The different yields reflect the different Ti content of the two materials.

The thicknesses of the two layers of LaTiO_xN_y and TiN as evaluated by the La and Ti peaks shown in Fig. 4.2c are in good agreement with the SEM cross section measurement of Fig. 4.2b. Finally, at low energies the lighter elements are detected; Mg and O from the substrate, but also O and N from the current collector and the oxynitride photocatalyst.

For a precise investigation of the composition of the oxynitride, ERDA measurements are required to determine the nitrogen-to-oxygen ratio (N/O) which turned out to be about 0.36. This value, compared to $N/O = 0.5$ of the fully nitrated compound ($x=1$), indicates an under-stoichiometric nitrogen content in this film, which is in agreement with the result of the XRD analysis of Fig. 4.2a.

For the specific sample described in Fig. 4.2, using the combination of both techniques, RBS and ERDA, a chemical composition of $\text{La}_{1.01}\text{Ti}_{0.99}\text{O}_{2.2}\text{N}_{0.8}$ could be very precisely determined with an error of $< 3\%$ to 5% . Other phases originating from the oxide LaTiO_{3+x} ($0 < x < 0.5$) were not detected by XRD (Fig. 4.2a). Moreover, RBS and ERDA measurements show a uniform compositional depth profile (Fig. 4.2c).

Further, literature reports hydrogen incorporation in form of NH_x species into oxynitride samples as a consequence of the ammonolysis^[94,95]. In Ref. [94] the hydrogen incorporation in single-crystal TiO_2 substrates by measuring the N 1s spectra with X-ray Photoelectron Spectroscopy (XPS) after nitridation with NH_3 was investigated. After removing a 60 Å thick surface layer by Ar^+ sputtering, the N 1s XPS spectra showed peaks at 396.7 eV and at 399.6 eV. The peak at 396.7 eV is generally assigned to the “nitride” peak^[238], thus correlated to nitrogen that replaced oxygen in the lattice of the native TiO_2 . The peak at 399.6 eV was assigned to interstitial NH_x , thus indicating that nitrogen is chemically bonded to hydrogen, but not incorporated into the lattice. Further it was concluded that only interstitial nitrogen (NH_x) reduces the photon energy threshold needed for generating electron-hole pairs, while substitutional nitrogen incorporated into the lattice does not affect the band gap. Ref. [95] reports the investigation of the mechanism of the visible-light responses in N-doped TiO_2 . The XPS N 1s spec-

trum showed a peak around 400 eV binding energy after nitridation, which was assigned to NH_x . It was concluded that the presence of NH_x species is responsible for the reduced oxidation power of the photo-generated holes in N-doped TiO_2 using visible light radiation compared to UV radiation. This is explained by a difference in the reactivity of the photo-generated holes originating from the UV excitation of electrons from the valence band (O 2p states) and from the visible light excitation of electrons from the mid-gap energy levels formed above the valence band by NH_x . ERDA was used here to investigate the potential hydrogen incorporation in the LaTiO_xN_y films which may alter the material properties. However, no hydrogen could be detected in our LaTiO_xN_y thin films by ERDA measurements. To increase the sensitivity for hydrogen during the ERDA measurement a ^4He beam instead of a ^{127}I beam was used. In this case the detection limit was $\approx 0.3\text{at}\%$.

4.1.3. Tuning the nitrogen content

The reason for the under-stoichiometric nitrogen content was investigated to understand up to which extent the nitrogen content could be tuned in our films. Previous studies on LaTiO_xN_y film growth by PRCLA showed that high laser fluence and high deposition temperatures are required to achieve high nitrogen substitution^[157]. For this work we systematically investigated the effect of the laser fluence and substrate material on the N/O ratio as determined by ERDA for several LaTiO_xN_y films. For this investigation the laser fluence was varied from 2 J cm^{-2} to 4 J cm^{-2} and (100)-oriented SrTiO_3 (STO) and LaAlO_3 (LAO), (110)-oriented YAlO_3 (YAO), as well as (100)-oriented TiN-coated MgO substrates were used. Following this approach, the typical composition of the oxynitride thin films determined by RBS and ERDA can be written as $\text{La}_{1+y}\text{Ti}_{1-y}\text{O}_{3-x}\text{N}_z$ where $0 < y < 0.03$ and $0.5 < x < 0.85$, depending on deposition parameters. Further, the sum of the oxygen and nitrogen content is close to 3 ($x \approx z$), thus forming the LaTiO_xN_y perovskite with a very small amount of anionic vacancies.

In particular, Fig. 4.3 shows the measured N/O ratio as a function of laser fluence for the different substrates. As a first observation, it appears clearly that a TiN-buffered substrate allows a more reliable control of the nitrogen content by only changing the laser fluence. The points corresponding to TiN-buffered MgO

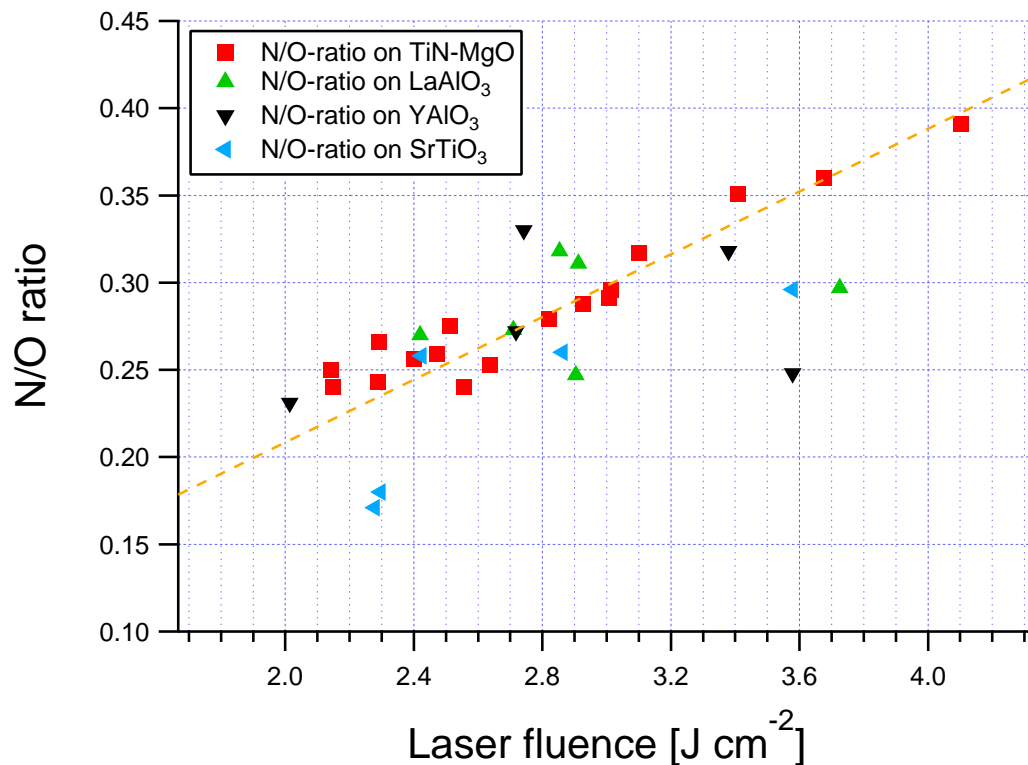


Figure 4.3.: N/O ratio of LaTiO_xN_y thin films grown on different substrates as a function of laser fluence. Used substrates are SrTiO_3 (blue \triangleleft), YAlO_3 (black \blacktriangledown), LaAlO_3 (light green \blacktriangle), TiN -coated MgO (red \blacksquare). All thin films are grown at 870°C and are $\sim 200\text{ nm}$ thick.

show an almost linear increase of the N/O ratio with increasing fluence (from 2.5 J cm^{-2} to 4.1 J cm^{-2}). The points corresponding to the oxide substrates are more scattered. As mentioned previously, STO substrates do not preserve their oxygen content at high temperatures and in reducing environment. Oxygen atoms from the substrate can even migrate into the growing film hindering the nitrogen substitution. In fact, a clear dependence of the N/O ratio on the laser fluence using STO substrates is not visible, neither at low nor at high fluence.

Using the other oxide substrates, YAO and LAO , we observed a trend similar to that observed for TiN -buffered MgO at lower fluences (2.0 J cm^{-2} to 3.0 J cm^{-2}), but with increasing fluence the values of N/O ratio measured for the LaTiO_xN_y films are much more scattered. More importantly, the maximum achievable nitrogen content is lower when the oxynitride films grow directly on the oxide surfaces than on the TiN -coated substrates. The effect of oxygen diffusion

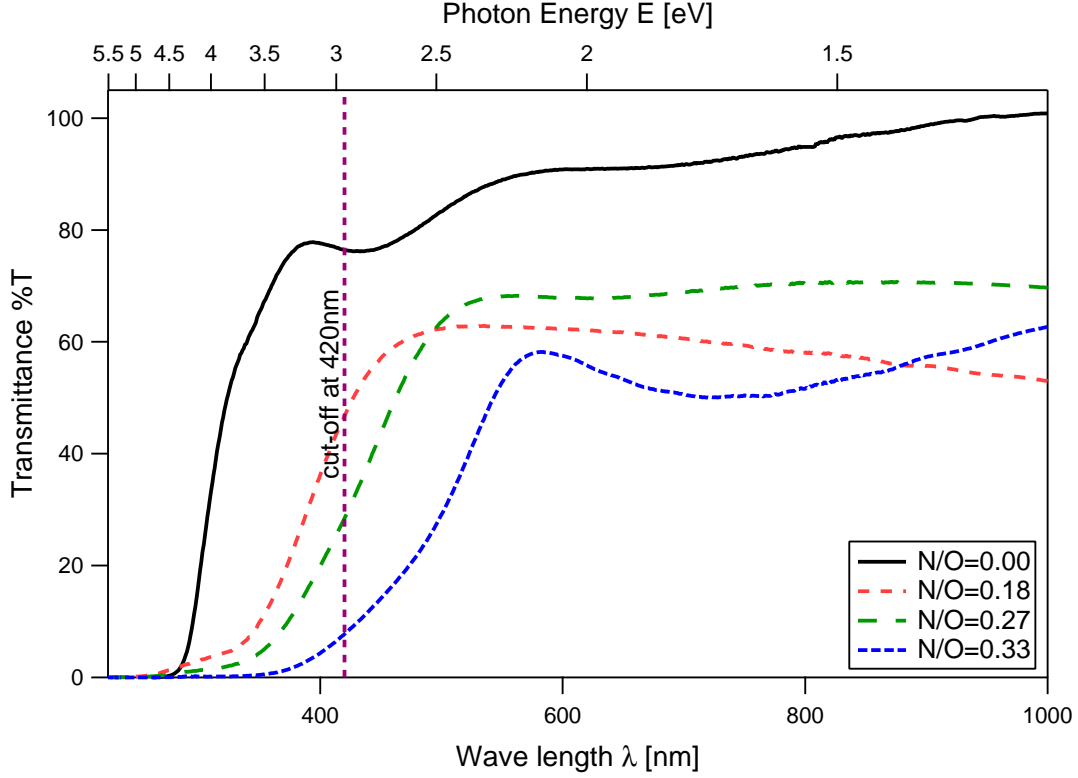


Figure 4.4.: UV-Vis spectra of three LaTiO_xN_y samples grown on LaAlO_3 substrates with different nitrogen content showing the effect on the optical properties of nitrogen substitution into the native oxide. All samples are about 200 nm thick and therefore interference fringes are observed during the UV-Vis measurement^[196]. For comparison, the transmittance spectrum of the $\text{La}_2\text{Ti}_2\text{O}_7$ thin film of the same thickness is also shown.

into the film as described before for STO, is also known for LAO substrates^[227]. This suggests that with YAO substrates such a mechanism may also be present, but it is less significant when using YAO or LAO instead of STO. However, the possible presence of a gradient in the nitrogen content of the film along the growth direction should be taken into account. Fig. 4.3 shows that to achieve a better control of the nitrogen content and a larger amount of nitrogen substitution in the oxynitride film a nitride-coated substrate like TiN-buffered MgO is preferable and underlines the advantage of the sample design proposed here for the PEC characterization of oxynitride photocatalysts.

Fig. 4.4 shows the effect of different nitrogen contents on the optical properties of the LaTiO_xN_y films. For this measurement double-side polished LAO substrates were used to acquire UV-Vis spectra in transmission mode. The trans-

mittance is plotted as a function of the incident wavelength showing a shift of the band gap towards longer wavelengths with increasing nitrogen content, as expected. Out of the UV-Vis spectra a band gap of about 2.35 eV to 2.85 eV can be estimated for the oxynitride thin films^[157]. For comparison, the UV-Vis spectrum of a thin film of $\text{La}_2\text{Ti}_2\text{O}_7$ grown on LAO by conventional PLD is also shown.

4.1.4. Tuning the crystallographic properties

Concerning the crystalline quality and crystallographic orientation of the oxynitride films grown on (100)-oriented TiN-buffered MgO we observed a remarkable effect of the laser fluence. The polycrystalline film discussed in Fig. 4.2 were grown using a laser fluence of about 3.7 J cm^{-2} . By keeping all other deposition parameters constant but lowering the fluence to 3.0 J cm^{-2} , the LaTiO_xN_y thin films grew epitaxially oriented with the substrate, as shown in Fig. 4.5. In this case, it comes at the cost of a lower nitrogen content. As shown in Fig. 4.3, for a laser fluence of about 3.0 J cm^{-2} the N/O ratio is about 0.30, while 0.36 was the value measured for a laser fluence of about 3.7 J cm^{-2} , though in the second case only polycrystalline samples could be grown.

This experimental observation could be explained in analogy with the equivalent effect often encountered during conventional PLD; by increasing the laser fluence both the kinetic energy of the ablated species and the deposition rate increase. Above a certain threshold this may hinder the ordered growth of the film. Literature on PRCLA is scarce and we cannot refer to any specific examples to support this speculation but it is likely that the same mechanism can occur also for PRCLA.

While higher laser fluences favors the growth of polycrystalline thin films with higher nitrogen content, reduced laser fluences lead to an epitaxial film growth with lower nitrogen content. A similar effect was observed for LaTiO_xN_y films grown by reactive radio-frequency sputtering^[156]. The N/O ratio was estimated by coupled energy-dispersive spectroscopy. Films with higher nitrogen content were polycrystalline while those with lower nitrogen content were epitaxially grown.

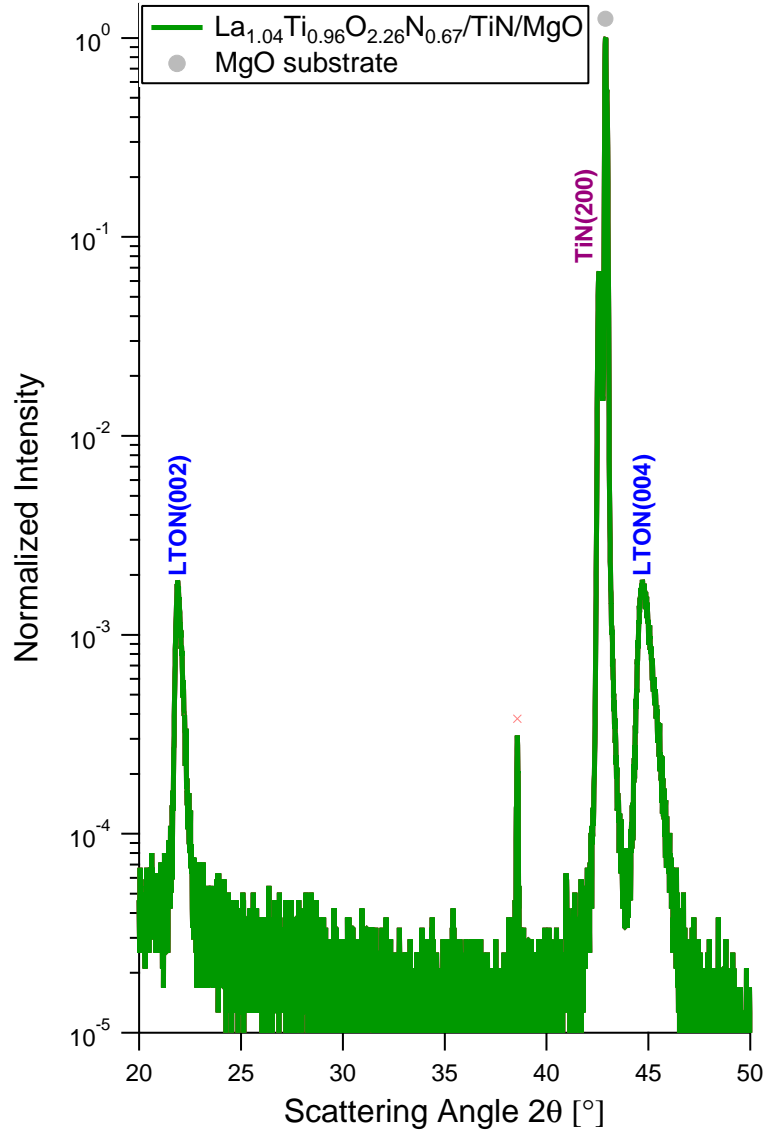


Figure 4.5.: XRD pattern of the epitaxial (001)-oriented $\text{La}_{1.04}\text{Ti}_{0.96}\text{O}_{2.26}\text{N}_{0.67}$ thin film grown by PRCLA with a laser fluence of 3.0 J cm^{-2} . The peak marked with an X is the K_β diffraction reflex from the MgO substrate.

A comparative investigation of the effect of the surface orientation and crystalline quality on PEC performance should be performed using films with similar nitrogen content. This could be achieved by keeping the laser fluence within a range that promotes the epitaxial highly ordered growth on TiN-buffered MgO but changing the substrate material and/or deposition parameters, such as substrate temperature, in order to grow TiN layers with different orientations or as

polycrystalline seed layers for the growth of the oxynitride films. The oxynitride films will thus show different crystallographic and morphological properties but their nitrogen content will be comparable with that of the highly ordered epitaxial film.

4.1.5. Proof of concept of the model system using photoelectrochemical characterization

As a preliminary test experiment to validate our sample design, the polycrystalline $\text{La}_{1.01}\text{Ti}_{0.99}\text{O}_{2.2}\text{N}_{0.8}$ sample grown on TiN-buffered MgO substrate was characterized in a PEC setup. The photocurrent generated under the effect of Xenon lamp front-illumination was measured while sweeping the applied voltage from 0.2 V to 1.4 V versus the reversible hydrogen electrode (RHE). A rotating shutter was used to chop the light allowing the simultaneous measurement of the so-called dark current (no illumination of the sample). ERDA analysis showed that a small but measurable amount of oxygen is present in the TiN current collector (N/O ratio > 6.5). In order to exclude any contribution to the photocurrent from the buried TiN layer, a PEC measurement was performed using a bare TiN-buffered MgO sample. As expected no photoresponse was detected.

For an unoptimized system the result of our preliminary PEC measurements for $\text{La}_{1.01}\text{Ti}_{0.99}\text{O}_{2.2}\text{N}_{0.8}$ is promising, as shown with the linear voltammetry measurements in Fig. 4.6. We note that the measured photocurrents are lower than what has been reported for powder based oxynitrides. This is expected due to the larger exposed area for powder samples compared to thin film samples. Furthermore, the specific morphology of this sample, which is characterized by extended grain boundary regions where untimely recombination of the photo-generated charge carriers is strongly favored, likely represents a possible loss channel. We anticipate that by employing sacrificial reagents acting as hole scavengers or co-catalysts instead of just the semiconductor in direct contact with the electrolyte, will improve the performance^[156]. Finally, the very broad absorption edge of this sample as shown in Fig. 4.4 may negatively influence the values of the photocurrent.

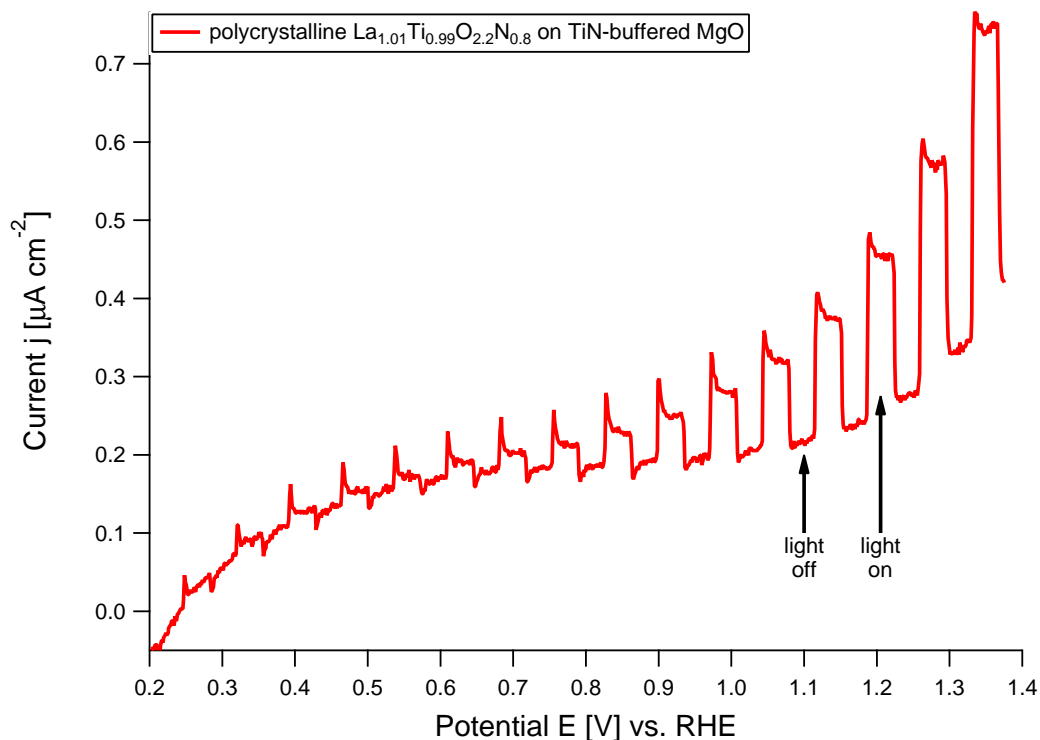


Figure 4.6.: PEC measurement of the polycrystalline $\text{La}_{1.01}\text{Ti}_{0.99}\text{O}_{2.2}\text{N}_{0.8}$ sample prepared on a TiN-buffered MgO substrate. The measurement was performed under chopped illumination (100 mW cm^{-2} with UV cutoff filter at $\lambda = 420 \text{ nm}$) to simultaneously measure the dark current and the photocurrent. The cell was filled with sodium borate electrolyte buffered at pH of 9 and a linear scan voltammetry was performed at a scan rate of 10 mV s^{-1} .

4.1.6. Conclusion

In summary we report a new experimental approach which, starting from the oxide material, enables the growth and the photo(electro)chemical characterization of oxynitride thin films with tunable crystallographic, morphological and optical (nitrogen content) properties, a goal that cannot be achieved with conventional powder samples. As a proof of concept we have demonstrated photocatalytic response of oxynitride thin films integrated into our model system. This work establishes the foundation of an effective experimental approach for future investigations into the oxynitride thin film class of photocatalyst. Gaining insight into the relationship between crystallographic properties and electrochemical response is expected to aid the development and design of better performing materials for solar-driven water splitting.

4.2. The role of the crystallographic surface orientation and chemical evolution of lanthanum titanium oxynitride in photoelectrochemistry

The results of this section are currently in preparation for submission. Authors are:

M. Pichler, D. Pergolesi, H. Téllez, J. Druce, E. Fabbri, M. El Kazzi, M. Döbeli, A. Wokaun, T. Lippert.

The samples were fabricated and characterized by Markus Pichler. Max Döbeli supervised RBS and ERDA measurements. LEIS and ToF-SIMS measurements were carried out by Hellena Téllez and John Druce. XPS data was collected by Emilliana Fabbri and Mario El Kazzi. The manuscript under preparation was written with contributions of all authors.

4.2.1. Thin film characterization

We investigate four representative LaTiO_xN_y thin films with different crystallographic properties to probe the influence of the crystallographic surface orientation and crystalline quality on the photoelectrochemical performance. Fig. 4.7 illustrates the X-Ray Diffraction (XRD) measurements of the four samples. Fig. 4.7a shows the $\theta/2\theta$ -scans and Fig. 4.7b the 2θ -scans in grazing incidence mode (GI-XRD). The samples include one polycrystalline (LTON-poly) and three oriented LaTiO_xN_y thin films grown on TiN-buffered substrates. The three oriented films are labeled LTON-hkl, where hkl indicates the preferential orientation.

LTON-poly and LTON-001 were grown on TiN-buffered (001)-oriented MgO and LTON-112 and LTON-011 were grown on TiN-buffered (0001)-oriented Al_2O_3 . The lattice parameters and crystal structures of MgO, Al_2O_3 , TiN and LaTiO_2N are reported in Table 4.1. The TiN buffer layer was grown epitaxially on both substrates and is used in this study as current collector for photoelectrochemical characterization of the oxynitride layers. Due to the relatively small

4.2. The role of the surface orientation and chemical evolution of LaTiO_xN_y in PEC

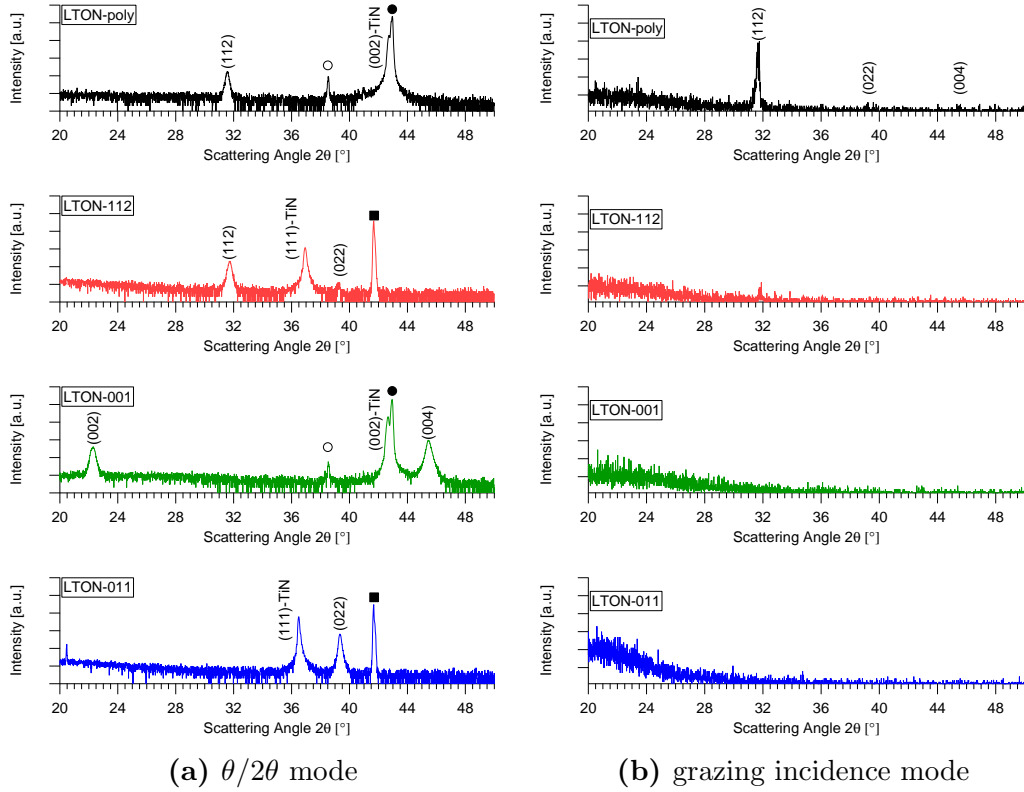


Figure 4.7.: X-Ray Diffraction pattern of LTON-poly, LTON-112, LTON-001 and LTON-011 shown by (a) the $\theta/2\theta$ -scan and (b) in the grazing incidence mode. The Al_2O_3 substrate is marked with a ■, the MgO substrate is marked with a ● and the $\text{K}\beta$ diffraction reflex from the MgO substrate is marked with a ○.

lattice mismatch of about 0.56 %, TiN grows cube-on-cube epitaxially-oriented on MgO ^[233,239–241], while the epitaxial relation between the (111)-oriented TiN surface and (0001)-oriented Al_2O_3 surface is discussed in detail in Ref.^[242].

LTON-poly has a polycrystalline structure. The $\theta/2\theta$ -scan mainly shows the (112) reflex (Fig. 4.7a), the crystallographic orientation with the largest relative intensity for this material. The GI-XRD measurements reveals a strong peak of the same reflex, but also the presence of the (022) and (004) reflexes confirming the polycrystalline nature of this sample (Fig. 4.7b).

LTON-112 shows a strong (112) reflection peak and traces of a minor (022) orientation. However, the GI-XRD measurement only shows one and very weak reflex at the (112) position (Fig. 4.7b). This suggests a highly textured microstructure of this film, characterized by adjacent grains (112)-oriented parallel to the substrate surface normal.

compound	crystal structure	lattice parameters Å		
		a	b	c
MgO	fcc	4.21130		
Al ₂ O ₃	hexagonal	4.76170		12.99900
TiN	fcc	4.23500		
LaTiO ₂ N	orthorhombic perovskite	5.60279	5.57137	7.87900

Table 4.1.: Lattice parameters of the two substrates MgO (ICSD Coll.Code: 158103) and Al₂O₃ (ICSD Coll.Code: 160604), the TiN buffer layer (ICSD Coll.Code: 152807) and the oxynitride photocatalyst LaTiO₂N (ICSD Coll.Code: 168551).

LTON-011 and LTON-001 grew epitaxially on (111)-oriented TiN-buffered Al₂O₃ and (001)-oriented MgO substrate, respectively. Neither sample shows any reflexes in the GI-XRD measurements (Fig. 4.7b) confirming their epitaxial relation.

Our previous study reports that the crystallographic properties and nitrogen content of LaTiO_xN_y grown on (001)-oriented TiN-buffered MgO substrate depend on the laser fluence^[165]. High laser fluence ensures a high nitrogen content, but also leads to a polycrystalline LaTiO_xN_y thin film. Lowering the laser fluence allows the epitaxial growth of LaTiO_xN_y, but at the same time decreases the nitrogen content. The same effect of an improved crystalline quality with decreasing the nitrogen content has been reported also for LaTiO_xN_y films grown by sputtering^[156]. For this work, TiN-coated MgO and Al₂O₃ substrates were used to grow LaTiO_xN_y films at high laser fluence (above 3 J cm⁻²) and at lower laser fluence (about 2 J cm⁻²) keeping all other deposition parameters constant.

The result obtained on (001)-oriented TiN-coated MgO confirms our previous finding concerning the crystallographic properties of the oxynitride films.

Concerning the films grown on TiN-coated sapphire substrates, the epitaxial growth of (011)-oriented LaTiO_xN_y films on (111)-oriented TiN surfaces can be explained assuming a domain matching epitaxy where 2 unit cells of LaTiO_xN_y match with 1 unit cell of TiN with a lattice misfit of about 6.5%. On the contrary, no lattice matching between the (112)-oriented LaTiO_xN_y surface and the (111)-oriented TiN could be identified. We assume that the driving force for the (112)-oriented growth of a textured film is in this case a combination between the selected deposition parameters and the low Gibbs' free energy of this surface.

4.2. The role of the surface orientation and chemical evolution of LaTiO_xN_y in PEC

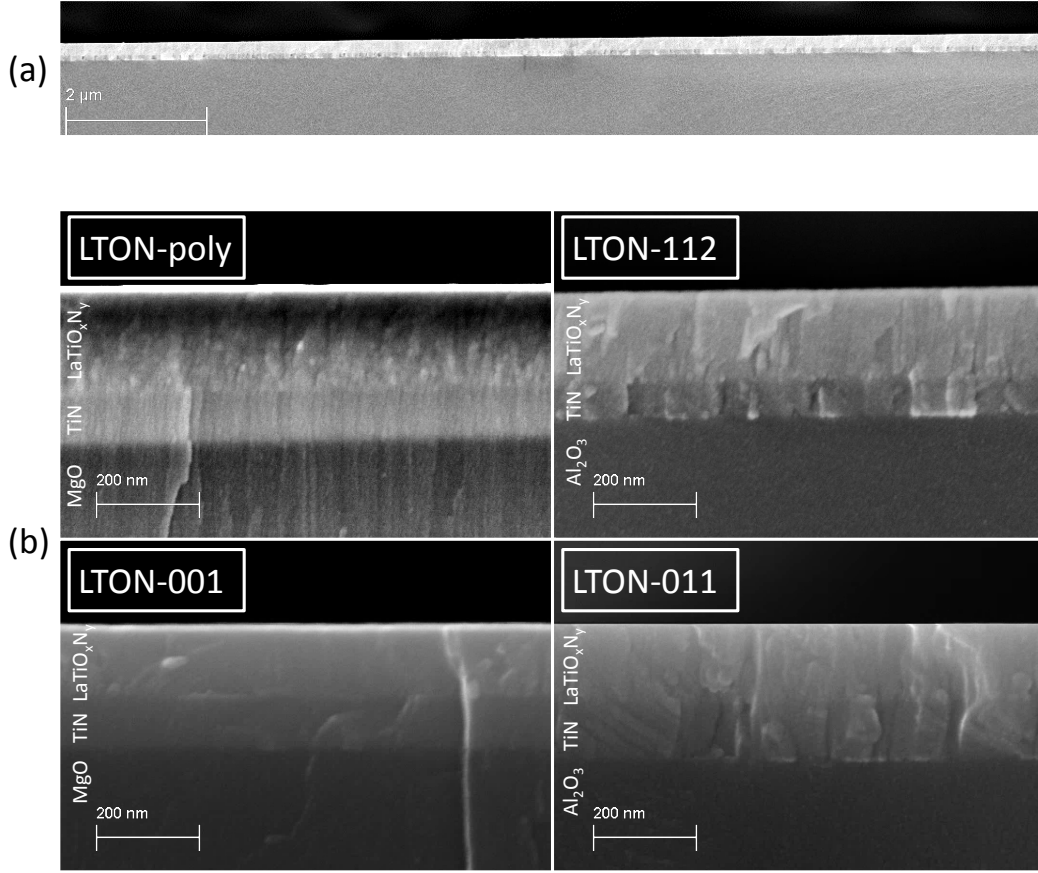


Figure 4.8.: SEM cross sections (fractured surface) of LTON-poly, LTON-112, LTON-001 and LTON-011.

As previously mentioned, the (112) XRD reflex shows in fact the highest relative intensity for this material.

Scanning Electron Microscopy (SEM) was used for morphological characterization. Fig. 4.8a shows a representative example of cross section SEM micrograph of one of the samples fabricated for this work. All films show good thickness uniformity of the specific morphological features. No significant evidence of microscopic defects, such as isolated micro particles, was observed.

Fig. 4.8b shows the acquired micrographs at higher magnification of the fractured cross sections of the four samples. The SEM cross section of LTON-poly shows a granular morphology without clear evidence of definite crystallographic structural planes. Such morphological features can be ascribed to a polycrystalline film, as revealed by XRD analysis. Moreover, no clear cleavage fractures that

sample	substrate	composition	N/O- ratio	thickness		laser
		by RBS	by ERDA	RBS	SEM	fluence
LTON-poly	TiN/MgO	$\text{La}_{1.03}\text{Ti}_{0.97}\text{O}_{2.20}\text{N}_{0.87}$	0.40	175 nm	175 nm	3.8 J cm^{-2}
LTON-112	TiN/ Al_2O_3	$\text{La}_{1.03}\text{Ti}_{0.97}\text{O}_{2.20}\text{N}_{0.90}$	0.41	155 nm	170 nm	3.1 J cm^{-2}
LTON-001	TiN/MgO	$\text{La}_{1.01}\text{Ti}_{0.99}\text{O}_{2.85}\text{N}_{0.38}$	0.13	140 nm	140 nm	2.2 J cm^{-2}
LTON-011	TiN/ Al_2O_3	$\text{La}_{1.04}\text{Ti}_{0.96}\text{O}_{2.75}\text{N}_{0.53}$	0.19	140 nm	140 nm	2.2 J cm^{-2}

Table 4.2.: Composition, nitrogen-to-oxygen ratio, thickness and used laser fluence of the described samples.

range through the whole sample are observed suggesting a film growth crystallographically decoupled from the TiN-coated MgO substrate.

The SEM micrograph of the other three samples show the typical features of a textured or highly ordered crystalline structure. In particular, in the epitaxial films continuous cleavage fractures are visible extending from the substrate through the TiN/ LaTiO_xN_y bi-layer. The films grown on sapphire show features that can be ascribed to grain boundaries. Grain boundaries and cleavage planes extend over the complete bi-layer in the LTON-011 film, while they look discontinuous at the TiN/ LaTiO_xN_y interface of the LTON-112 film. This observation agrees with the previous discussion of the XRD results suggesting an epitaxial growth of LTON-011 and a highly textured but not epitaxial growth of LTON-112. LTON-001 shows a very homogeneous cross section, almost featureless with the exception of continuous cleavage fractures. It is worth mentioning here that due to the different crystalline structures of the two substrates the fractured cross section of the samples grown on MgO look in general much more regular and smooth.

Atomic-Force Microscopy (AFM) was performed to further investigate the surface topography. For the oriented samples, AFM analysis shows a very smooth surface with an RMS value of the height distribution of less than 1 nm. The polycrystalline sample has a slightly rougher surface with an RMS value of 1.5 nm.

The chemical composition of the four samples described above was investig-

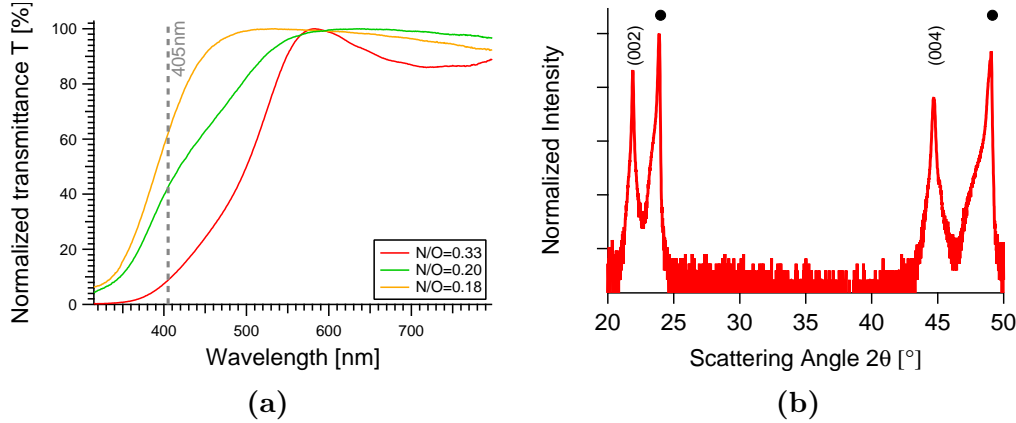


Figure 4.9.: (a) Normalized UV-Vis spectra of three LaTiO_xN_y samples grown on double-side polished YAlO_3 substrates with different nitrogen content to visualize the shift of the band gap to higher energies with decreasing of the nitrogen content. (b) X-ray diffraction pattern of one representative LaTiO_xN_y sample grown epitaxially and (001)-oriented on (110)-oriented YAlO_3 substrate. The YAlO_3 substrate is marked with a ●.

ated by Rutherford Backscattering (RBS) complemented by Elastic Recoil Detection Analysis (ERDA) used to determine the nitrogen-to-oxygen ratio (Table 4.2). We have evidence of a lanthanum content that is slightly larger than the stoichiometric composition at the expense of the titanium content. This over-stoichiometric composition of lanthanum, the heaviest element in the compound, can be explained as a result of the PLD process, where the chemical content of the film of lighter elements are prone to get reduced during deposition^[209,210]. The thickness of the oxynitride thin films were estimated by SEM and RBS. The two measurements are in quite good agreement (Table 4.2).

To investigate the optical properties of our films, UV-Vis measurements were performed. Fig. 4.9a shows the UV-Vis spectra acquired for three different LaTiO_xN_y epitaxial films, about 150 nm-thick, grown on double-side polished (110)-oriented YAlO_3 substrates with a nitrogen content comparable to that of the samples grown on TiN-coated substrates from table 4.2. The LaTiO_xN_y samples grown on the transparent YAlO_3 substrates were prepared using different laser fluences following the same procedure used for the LaTiO_xN_y samples described above. Fig. 4.9b shows the XRD analysis of one of these samples. As shown in previous studies^[157,165], the reduction in laser fluence leads to a reduction of the nitrogen content and therefore also an increase in the band gap, as

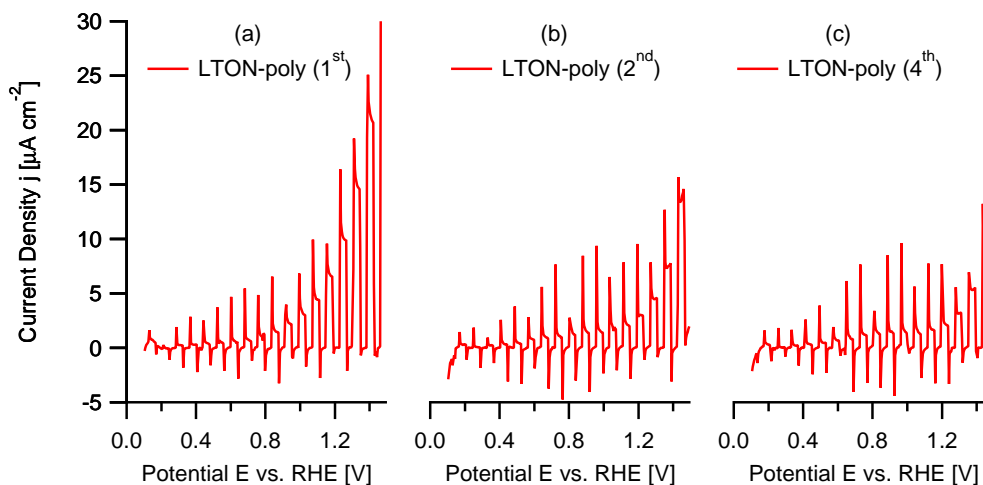


Figure 4.10.: Evolution of the photocurrent: (a) 1st, (b) 2nd and (c) 4th chopped potentiodynamic measurements with 10 mV s^{-1} of sample LTON-poly (4 s light on and 4 s light off). All measurements were performed in an electrolyte of 0.5 M NaOH (pH=13) using a 405 nm laser diode with a light intensity of 130 mW cm^{-2} . For the ease of comparison, the dark current is subtracted from the data.

revealed by the shift of the absorption edge towards smaller wavelengths.

Nitrogen-to-oxygen ratios of 0.33, 0.20 and 0.18 were measured by ERDA for the three films. The dashed line in Fig. 4.9a indicates the wavelength (405 nm) of the monochromatic light source used in this study for photoelectrochemical characterization. At this wavelength, a light absorption of 91 %, 57 % and 38 % can be estimated (neglecting reflectance) for the three samples from higher to lower nitrogen-to-oxygen ratios.

4.2.2. Photoelectrochemical characterization

The four described samples were used for photoelectrochemical (PEC) characterization to investigate the effect of the different crystallographic surface orientations on the visible light induced photocurrent using TiN-buffered substrates as current collector. The commonly used method to report PEC activity are potentiodynamic (PD) linear voltage scans using chopped illumination. In a PD scan the current is measured while sweeping the applied potential and turning on/off the light source.

Fig. 4.10a-c show the 1st, 2nd and 4th PD voltage scans of a LTON-poly

sample. A current density of more than $30 \mu\text{A cm}^{-2}$ at 1.5 V vs. RHE was measured during the first measurement (Fig. 4.10a). For this study the light source is a 405 nm laser diode with 5 mW power output focused on a spot area of about 0.03 cm^2 at the film surface. The current density is calculated considering the area of the laser spot. The surface area exposed to the electrolyte equals the area of the laser spot due to the very smooth surfaces of the samples, as observed by AFM, while for powder samples the exposed area can be about 50 times larger than the illuminated area. The typical loading density for powder samples ranges from 0.40 mg cm^{-2} to 0.45 mg cm^{-2} [130,132,243]. Assuming a typically surface area measured with the BET method of about $8.5 \text{ m}^2 \text{ g}^{-1}$ and $15 \text{ m}^2 \text{ g}^{-1}$ [90,121,217,244] for LaTiO_2N , it can be estimated that for powder samples the area exposed to the electrolyte is about 35 to 60 times larger than the illuminated area. Considering this, the measured photocurrent density in the range of few tens of $\mu\text{A cm}^{-2}$ are in line with those reported in literature for LaTiO_2N powder samples [115] as well as for thin films [156], where no co-catalysts or redox couples acting as sacrificial reagents were used.

The measured current density decreases, especially at higher applied potentials, with increasing number of voltage scans (Fig. 4.10c) before stabilizing. A current density of about $10 \mu\text{A cm}^{-2}$ was measured at 1.5 V vs. RHE after stabilization.

This reduction of the measured photocurrent within the first photoelectrochemical tests (about 4 – 6 voltage scans) is the symptom of an initial physico-chemical modification of the oxynitride semiconductor, and stability issues are well known for this class of materials [39,90,93,109,129,130]. In previous studies, nitrogen loss was observed for LaTiO_xN_y powder samples during O_2 evolution over a wide range of experimental conditions [39,90,109,116,129,130]. This finding suggests that nitrogen loss at the semiconductor/electrolyte interface is the primary degradation mechanism of oxynitride materials during PEC measurement.

For this work, to further investigate the reason of the initial degradation of the PEC performance XRD, ERDA, Low-Energy Ion Scattering spectroscopy (LEIS), and Time-of-Flight Secondary Ion Mass Spectrometry (ToF-SIMS) were applied.

For these investigations, two LaTiO_xN_y samples grown on TiN-buffered MgO

substrates were prepared simultaneously (during the same deposition process). One of these samples was used for PEC characterization. Hereinafter, we refer to this sample as “after PEC”, while the other non-tested sample (the LaTiO_xN_y thin film as grown) is called “before PEC”.

The samples denominated “after PEC” underwent several voltage scans up to at least 1.5 V vs. RHE and showed stable (fully stabilized) photocurrents. In our experimental setup, the area of the substrate into the electrolyte is about $5 \times 5 \text{ mm}^2$. At the center of this area the light source used for PEC measurements was focused on a circular spot of about 2 mm in diameter. All the above listed analyzes were performed in the central area of the part of the substrate immersed into the electrolyte, i.e. within the area of the laser spot, where oxygen evolution occurred under illumination.

XRD analysis yielded no significant differences (formation of secondary phases, changes of lattice parameter) before and after PEC.

ERDA yielded no changes of the nitrogen and oxygen contents in the bulk of the films, when comparing the samples before and after PEC. Only the surface, within the limits of surface sensitivity of ERDA, for both samples (before and after PEC) could a slight increased oxygen content and decreased nitrogen content be observed.

The LEIS surface analyzes performed on the LTON-poly sample showed the presence of several impurities after the PEC measurements, which were not present on the thin films as deposited. From the He spectra (Fig. 4.11a), a peak with an energy onset at 1580 eV was assigned to a Na impurity originating from the used electrolyte (NaOH). An additional peak from a heavier impurity could be also observed at $\sim 2450 \text{ eV}$ although, due to the lower mass resolution of the He beam for heavier species, could not be assigned to a specific element. The surface of the LTON-poly films was predominantly LaO-terminated, as indicated by the large surface peak at $\sim 2700 \text{ eV}$ (La) and at $\sim 1180 \text{ eV}$ (^{16}O). The presence of Ti at the outer layer was difficult to observe in the He spectra (theoretical peak position 2212 eV). Nevertheless, in the LaTiO_xN_y film after the deposition (black solid line), there is a distinct step in the spectral background with a small peak at the theoretical position for Ti species, indicating the presence of Ti atoms at the surface. After the PEC measurements (blue dashed line), the step in

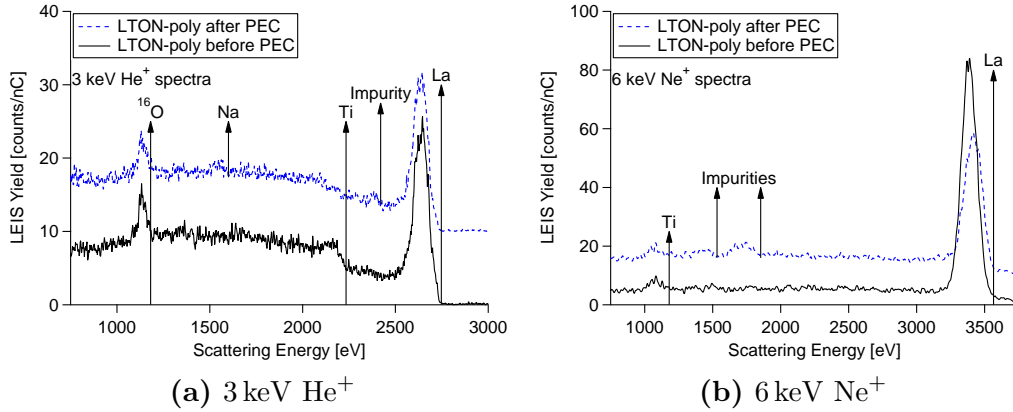


Figure 4.11.: LEIS surface spectra of the LTON-poly samples before and after PEC characterization obtained by probing with (a) 3 keV He⁺ and (b) 6 keV Ne⁺ beams. High energy offset of the species at the surface are indicated by arrows. Spectra have been offset for clarity.

the background signal at ~ 2210 eV is smoother and no surface peak could be detected. This suggests that Ti atoms are not exposed to the outer surface, at least to the limit of detection for the He primary species, but underneath the first atomic layer. This can be an effect of the presence of the impurities after the PEC measurements. The Ne analyzes (Fig. 4.11b) provided better limit of detection and resolution for the detection of heavier species and showed that the Ti atoms are present at the outer surface before and after the PEC measurements, although the Ti surface coverage is slightly decreased after the PEC characterization. Two different impurity peaks were observed at scattering energies at ~ 1530 eV and ~ 1840 eV, that could be attributed to Mn/Fe and Cu/Zn, respectively. The unequivocal identification of the species is not possible with the Ne primary species (the proper assignment of the impurities is later attempted by ToF-SIMS analysis).

LEIS depth profiling was performed to investigate the distribution of cations at the near-surface (Fig. 4.12). The cation peak areas, proportional to the surface coverage, showed that the outer surface is La-rich compared to the bulk composition for both LaTiO_xN_y films. As observed in the depth profile after PEC measurement (Fig. 4.12b), the surface impurity at ~ 1840 eV is very quickly sputtered by the Ar⁺ sputter beam, reaching the spectrum background level at an estimated depth of 0.25 nm (approximately a single atomic layer). From these depth profiles, a comparison of the Ti/La cation ratios could be obtained

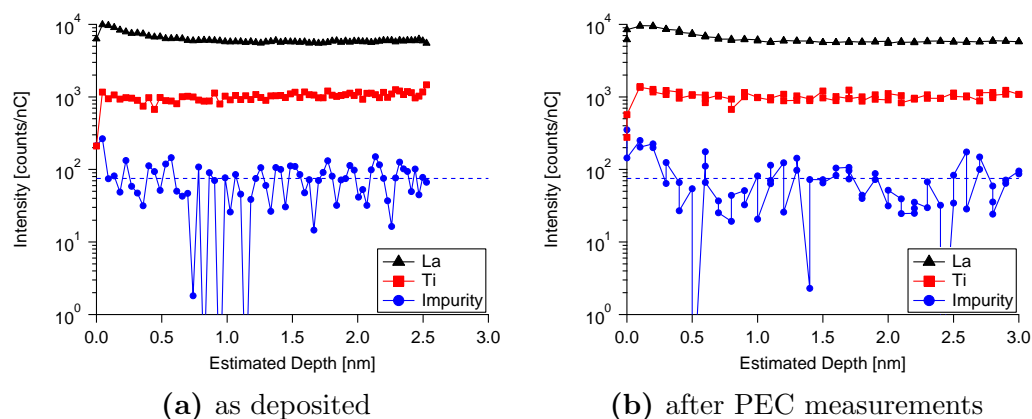


Figure 4.12.: LEIS depth profiles obtained for 6 keV Ne^+ scattering by the LTON-poly film (a) as deposited and (b) after PEC measurements. The background signal for the impurity peak is indicated as a dotted line.

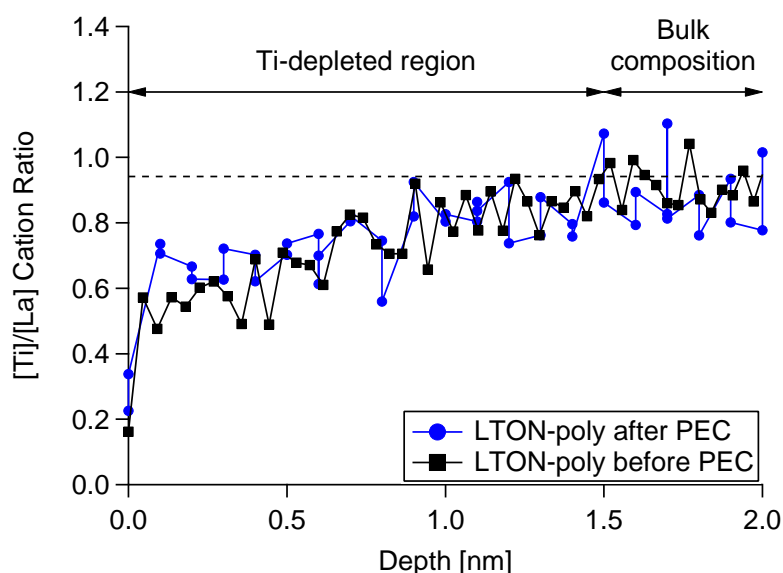


Figure 4.13.: Ti/La cation ratio normalized to the bulk stoichiometry as obtained from the LEIS depth profiles.

(Fig. 4.13). Please note that the ratios were normalized to the bulk cation stoichiometry. Both films showed a similar Ti-depleted region at the near-surface that is extended to the first 1.5 nm. It should be mentioned that the extend of the Ti-depleted region might be limited to the first or second atomic layers, even though the depth profile reveals a deeper length. This is explained with the ionic mixing produced by the 500 eV Ar^+ sputtering (the projected range of the sputter ions is around 1 nm as estimated for other perovskite materials). Such

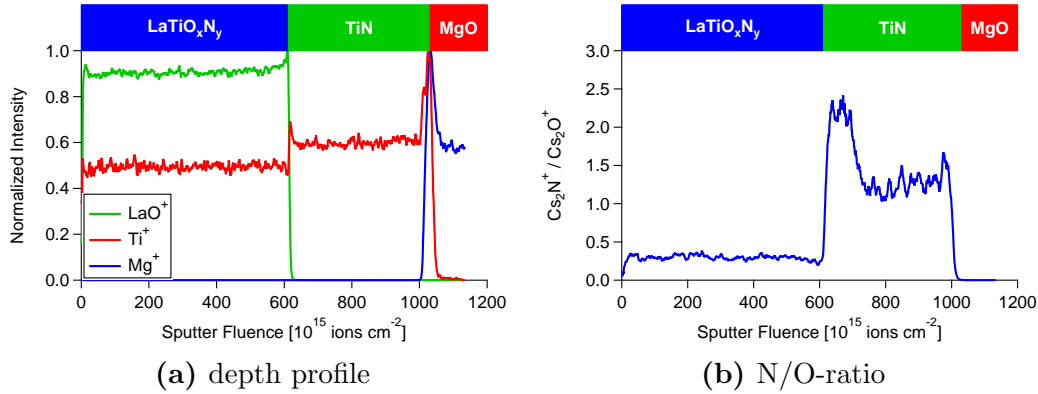


Figure 4.14.: (a) depth profile and (b) N/O-ratio of LTON-poly before PEC using ToF-SIMS.

an increased lanthanum content (titanium depletion) on the surface of our films is in agreement with Ref. [90], where a reduction of the Ti/La surface atomic ratio for LaTiO_2N nanoparticles was observed after nitridation ($\text{Ti/La} = 0.7$), while the bulk remained unaffected ($\text{Ti/La} = 1$). However, literature also reports Ti-enriched amorphous surface for LaTiO_2N powder samples after nitridation [245]. After annealing this Ti-rich amorphous layer was removed by exhibiting a La-rich layer. Further chemical etching in aqua regia removed the La-rich layer and the nanoparticles showed a reconstructed surface.

ToF-SIMS chemical depth profiles shows remarkably well-defined interfaces between the different layers (TiN/MgO and $\text{LaTiO}_x\text{N}_y/\text{TiN}$) and a uniform chemical composition of each layer throughout the films in very good agreement with RBS and ERDA measurements (see Fig 4.14a).

Incidentally, ToF-SIMS also indicates that the TiN buffer layer is not oxygen-free (see Fig 4.14b), as observed in previous studies [165] where it has been proven that this does not affect the PEC measurements. Interestingly, ToF-SIMS reveals that the nitrogen-to-oxygen ratio of the TiN layer is smaller at the MgO side suggesting diffusion of oxygen from the substrate into the TiN layer during deposition. This effect of oxygen diffusion into the deposited thin film is well known in literature for substrates like SrTiO_3 and LaAlO_3 [227].

ToF-SIMS also detected traces of surface contamination in the sample after PEC characterization not present in the bulk or at the surface of the sample before PEC. These contaminants could be assigned to chromium, manganese and iron.

Also hydrocarbon-derived contaminants were found on the PEC tested samples. We assume that these contaminants originate from the electrolyte.

In summary, the structural and chemical composition of the samples did not show any significant difference as a consequence of the PEC measurements highlighting the good physicochemical stability of the LaTiO_xN_y thin films. These findings also suggest that the reason for the initial reduction of the measured photocurrent has to be ascribed to changes of the local surface chemical environment of the constituent elements, rather than to changes in the bulk chemical content or chemical profile (i.e. loss of nitrogen).

X-ray Photoelectron Spectroscopy (XPS) was applied to gain further insights on this matter. The XPS results for Ti 2p and N 1s core levels are shown in Fig. 4.15, while the results for La 3d and O 1s are shown in Fig. 4.16-4.17. The LaTiO_xN_y sample before and after PEC were measured at normal incidence angle (90°), while the sample before PEC was also measured at 45° incidence angle to discriminate the components located at the surface. As a first observation, comparing the XPS measurements before and after PEC (at normal incidence angle), no significant changes of the Ti/La, N/La and N/Ti atomic ratios could be detected, suggesting that the surface composition and therefore also the nitrogen content remains unaffected by the PEC measurements (no nitrogen loss).

Concerning the nitrogen content comparing the samples before PEC at 90° and 45° incidence angle, a smaller nitrogen content can be observed for the latter. This is in agreement with the increased oxygen content due to the LaO-terminated surface observed by LEIS (see Fig. 4.11a).

An increased lanthanum surface content can be observed for both samples before and after PEC compared to bulk. This also confirms the preferential LaO surface termination (and Ti depletion) observed by LEIS (see Fig. 4.13). It is worth mentioning here that the XPS analyzes provide quantitative values mediated over a surface layer of about 5 nm thick. LEIS can assign this La-rich layer to the first nm, thus this LaO-termination is limited to the first or second atomic layer as mentioned above.

The analyzes of the shifts in the Ti binding energies finally shows remarkable difference between the two samples before and after PEC.

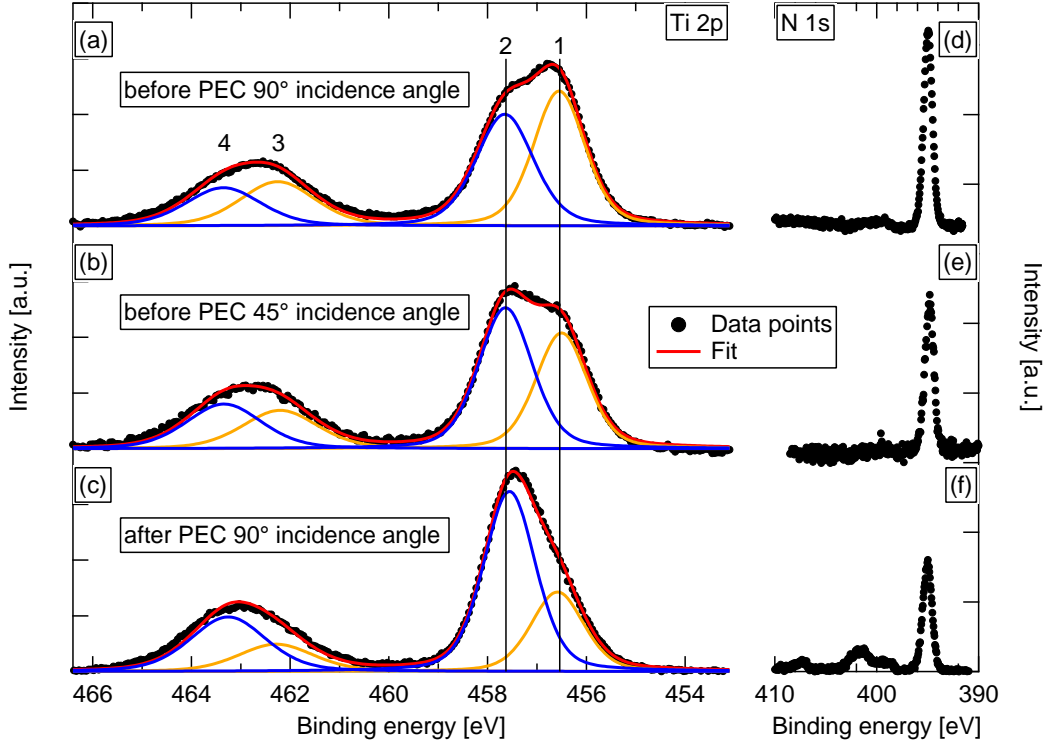


Figure 4.15.: XPS spectra of (a)-(c) Ti 2p, and (d)-(f) N 1s from LTON-poly before PEC (incidence angle of 90° and 45°) and after PEC.

Fig. 4.15a-c shows the Ti 2p XPS spectra of the LaTiO_xN_y films before PEC at 90° (Fig. 4.15a) and 45° incidence angle (Fig. 4.15b) as well as after PEC (Fig. 4.15c). Two main peaks can be identified at a binding energy of about 457 eV and 463 eV and they can be assigned to Ti $2p_{3/2}$ and Ti $2p_{1/2}$ spin orbit, respectively. Each main peak can be fitted with two Gaussians, component 1 (orange) and 2 (blue) in Fig. 4.15a-c. The peak positions of the two components are roughly the same for the three different measurements and are marked with two vertical lines in Fig. 4.15a-c.

The main peak located at 457 eV suggests that titanium is present in both, the Ti^{4+} oxidation state (Ti 2p peak for TiO_2 is ≈ 458 eV^[246–249]) and in the Ti^{3+} oxidation state (Ti 2p peak for TiN is ≈ 455 eV^[247–250]). This was expected due to the under-stoichiometric nitrogen content of our LaTiO_xN_y samples compared to LaTiO_2N , which requires a mixture of Ti^{4+} and Ti^{3+} oxidation states. Also for TiO_xN_y the Ti $2p_{3/2}$ peak was found between the Ti 2p peak positions of TiO_2 and TiN^[247–249,251]. On the basis of these considerations, we ascribe the binding

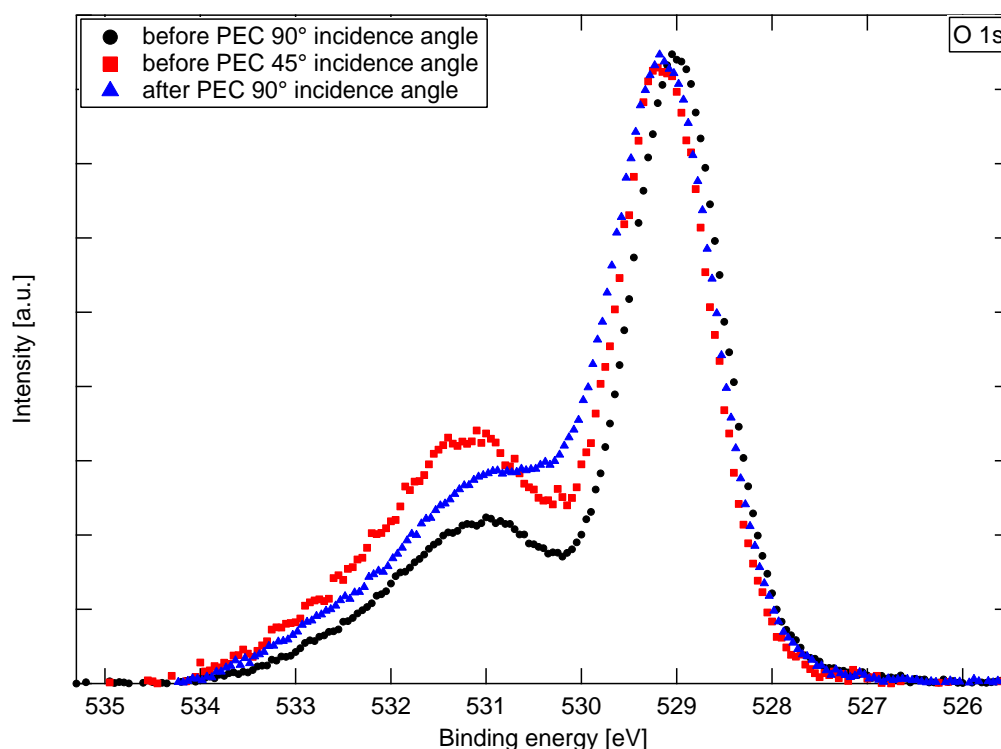


Figure 4.16.: XPS spectra of O 1s before PEC (incidence angle of 90° and 45°) and after PEC from LTON-poly.

energy of the component 1 in Fig. 4.15a-c to a less oxidized chemical environment (higher nitrogen content). Accordingly, the component 2 is assigned to a titanium chemical environment containing more oxygen (lower nitrogen content).

By comparing the Ti 2p XPS measurement at 90° and 45° incidence angle before PEC characterization in Fig. 4.15a and Fig. 4.15b, the binding energy of component 2 (more oxidized chemical environment) at 457.6 eV can be assigned to the titanium located closer to the LaO-terminated surface, since the peak intensity increases at 45° incidence angle compared to the measurement at normal incidence. Accordingly the binding energy of component 1 (less oxidized chemical environment) at about 456.6 eV can be assigned to the titanium mostly in the bulk. Comparing now Fig. 4.15a-b with Fig. 4.15c, we can see that the intensity of component 2 further increases after PEC characterization even though the XPS measurement was performed at normal incidence. This suggests that after PEC measurements titanium is more oxidized at the surface compared to the bulk.

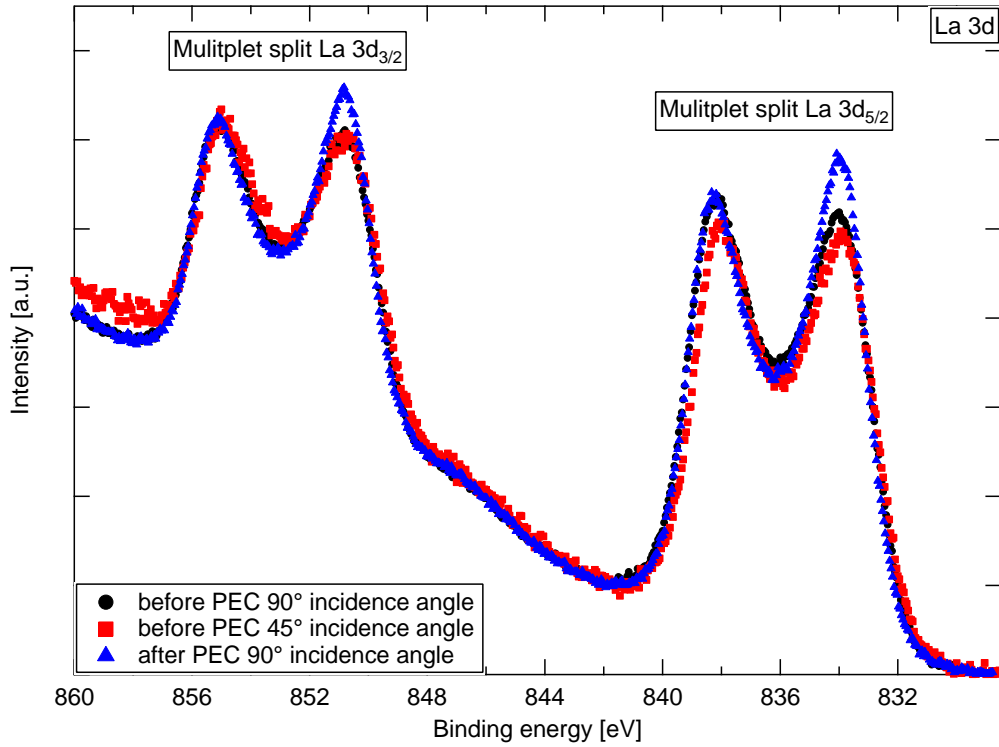


Figure 4.17.: XPS spectra of La 3d before PEC (incidence angle of 90° and 45°) and after PEC from LTON-poly.

Concerning the N 1s XPS spectra (Fig. 4.15d-f), no significant changes could be observed at 90° (Fig. 4.15d) and 45° (Fig. 4.15e) incidence angle before PEC. The peak at binding energy of about 395 eV is thus assigned to nitrogen in the chemical environment of LaTiO_xN_y . On the contrary, the comparison of the N 1s XPS spectra before PEC (Fig. 4.15d) and after PEC (Fig. 4.15f) exhibits changes, which are manifested in additional peaks at higher binding energies. The additional peaks are difficult to assign. In Ref.^[251] an additional peak of the N 1s XPS spectra at very similar binding energy was found after thermal annealing in air of TiN_xO_y . This peak was assigned to N-C bonds, which were formed with carbon surface contamination. A very similar evolution of the N 1s spectrum was observed in a study of the titanium nitride oxidation chemistry^[238]. In this work the additional N 1s spectra features appearing after oxidation were assigned to different types of bonding configuration for chemisorbed nitrogen.

Since the XPS results shown here indicate that the overall nitrogen content of our films remains almost unchanged after PEC measurements, we speculate

that in analogy to Ref. [238,251] the change of the N 1s XPS spectrum is due to nitrogen atoms that leave the LaTiO_xN_y structure replaced by oxygen and migrate to the surface to bond with hydrocarbon-derived contaminants as observed by ToF-SIMS. According to the NIST X-ray Photoelectron Spectroscopy Database [252] for N 1s, the peaks that appear at higher binding energies in the N 1s spectrum (Fig. 4.15f) can be assigned to nitrogen bonded with hydrogen, carbon and oxygen.

Literature reports that the nitrogen loss depends on the pH of the electrolyte with the effect becoming more important reducing the pH from 9 down to 4 [90]. To our best knowledge, no nitrogen loss was observed with a high pH (≥ 13) [116]. For this work an electrolyte with pH 13 was used thus making the nitrogen loss negligible.

The observed oxidation of titanium and the suggested replacement of nitrogen with oxygen at the surface does not necessarily lead to changes in the O 1s XPS spectra. However, the observed changes in the O 1s XPS spectra at higher binding energies (Fig. 4.16) are related to the adsorbed species at the surface of the measured samples as determined with ToF-SIMS. Whether or not the oxygen content is increased within the 5 nm of the XPS penetration depth cannot be identified and further investigation is required.

Further, the discussed changes in Ti 2p and N 1s XPS spectra also lead to changes in the chemical environment of lanthanum. Fig. 4.17 displays the La 3d multiplet, where the peaks at smaller binding energies of both doublets shows increased intensities after PEC.

To summarize, the reported characterizations suggest that the observed initial degradation of the PEC performance of our LaTiO_xN_y films may be due to the presence of a La-rich LaTiO_xN_y surface layer, where titanium undergoes further oxidation and nitrogen is partially depleted during operation.

4.2.3. Effect of the different crystallographic surface orientations on the visible light induced photocurrent

As shown above, PEC measurements performed using LTON-poly showed that the measured photocurrent gradually approaches a constant and reproducible

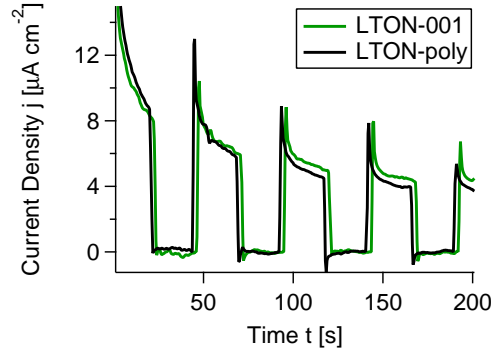


Figure 4.18.: Potentiostatic measurements at 1.5 V vs. RHE of sample LTON-001 and LTON-poly (24s light on and 24s light off). All measurements were performed in an electrolyte of 0.5 M NaOH (pH= 13) using a 405 nm laser diode with a light intensity of 130 mW cm^{-2} . For the ease of comparison, the dark current is subtracted from the data.

value after few voltage scans probably as a result of the initial surface characteristics and its evolution during operation. Moreover, PEC characterizations performed after sample stabilization by holding the potential stable (potentiostatic or chronoamperometric measurements) show that the photocurrent further decreases within the first few minutes before stabilizing. As an example, Fig. 4.18 shows the potentiostatic measurements of LTON-poly and LTON-001 performed by holding the applied voltage at 1.5 V vs. RHE for 200 s. Besides the initial spikes due to a charging and discharging of surface states or oxidation and reduction of surface species^[253], the photocurrents decrease from their initial values of more than 10 μA cm^{-2} , similar to those measured by potentiodynamic measurements at the same voltage after sample stabilization, down to about 6 μA cm^{-2} and 4 μA cm^{-2} for LTON-001 and LTON-poly, respectively. The extent of such a decrease of photocurrent and the time required for stabilization depends on the applied voltage and sample history (previously applied voltage, holding time, positive or negative voltage variation between two consecutive measurements). This effect may depend on adsorbed oxygen blocking the active sites, which hinder the electrochemical reaction. Of course, the use of appropriate co-catalysts may further improve the performance but it would drive the present investigation toward the study of the properties of different electrochemical systems.

The purpose of this investigation is the comparison of the electrochemical properties of photo-anode surfaces with different crystallographic orientations and

the establishment of an experimental approach that will enable the extension of such a comparison to different materials. Previous considerations suggest that the typical anodic (from low to high voltage scan) potentiodynamic characterization widely used in the literature may be not the most reliable approach. Following such an approach in fact, for different surface orientations or using different materials the questions would be: How many potentiodynamic scans are required to achieve full surface stabilization? How a potentiodynamic measurement is influenced by the voltage history of the sample under investigation? How much these effects of surface evolution differ for different crystallographic orientations? In addition, since the measured photo-current is intrinsically small (in the range of few $\mu\text{A cm}^{-2}$ due the much smaller electrochemically active area for thin films compared to powder samples), how much does the capacitive current, which is proportional to the voltage scan rate in a potentiodynamic measurement, affect the measured photo-current?

These uncertainties have led us to select a different investigation approach, that is the comparison between potentiostatic photocurrent measurements performed during cathodic voltage scans (from high to low applied potential).

Fig. 4.19a shows the results of these measurements. For each sample 1.5 V vs. RHE was first applied for 200 s, which reveals that the photocurrent decays, as shown in Fig. 4.18. The voltage was then reduced in steps of 25 mV holding the potential constant for 200 s and the steady state photocurrent values at the different potentials are summarized in Fig. 4.19a. After the first 200 s at the highest voltage, at all lower voltages the photocurrent stabilizes in much shorter times. Below 1.4 V vs. RHE only few seconds are needed to achieve a steady photocurrent density. The photocurrent measured at the highest voltage of 1.5 V vs. RHE was used as sample pre-conditioning but not taken into account in Fig. 4.19a since, as shown in Fig. 4.18, the photocurrent seems to be not yet fully stabilized after 200 s. The difference between the anodic potentiodynamic measurement and the cathodic potentiostatic measurement of LTON-001 is shown in Fig. 4.19b as a representative example. The cathodic potentiostatic photocurrent is significantly smaller (a factor of 5 at 1.4 V vs. RHE, as an example) but we do believe that this measurement is much less sensitive to spurious effects and/or sample history.

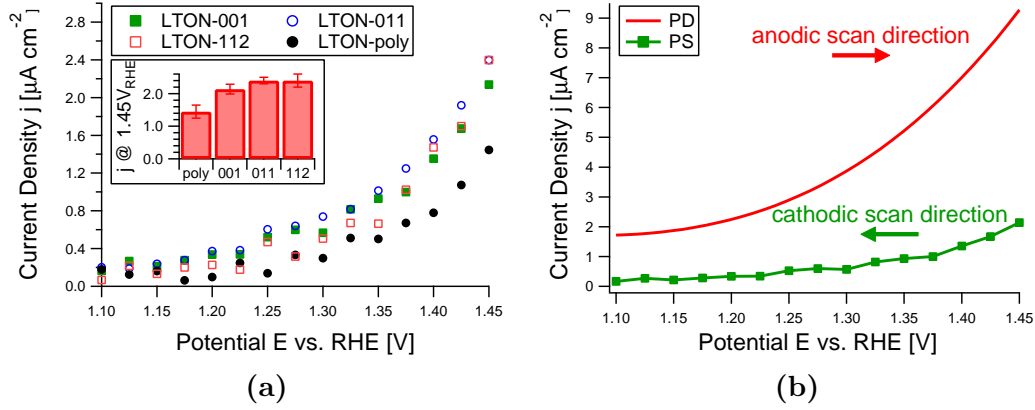


Figure 4.19.: (a) PEC characterization of the (001)-oriented sample LTON-001 (open green squares), the (011)-oriented sample LTON-011 (open blue circles), the (112)-oriented sample LTON-112 (full red squares), the polycrystalline sample LTON-poly (full black circles). Every experimental value in this j - E curve was obtained from a single potentiostatic measurement using the value of the stabilized and dark current subtracted photocurrent. (b) 4th potentiodynamic measurement in comparison with potentiostatic measurement using sample LTON-001. The scan direction for the potentiodynamic measurement is from low to high voltage (anodic scan) and the scan direction for the potentiodynamic measurement is from high to low voltage (cathodic scan).

Fig. 4.19a clearly shows that, in agreement with previous studies^[156], crystalline quality matters. As an example, at 1.45 V vs. RHE about 60 % larger photocurrents were measured with the textured and epitaxial samples.

Fig. 4.19a also shows that similar photocurrent densities were measured for the three different orientations. However, the different nitrogen content and, as a consequence, the different light absorption properties must be taken into account.

As previously pointed out, the nitrogen content of the LaTiO_xN_y films increases with increasing the laser fluence at the expense of the crystalline quality of the films, as shown in Table 4.2. Epitaxial films have in fact lower nitrogen-to-oxygen ratios (in the range of 0.13 to 0.20) than polycrystalline or textured films (about 0.4). By comparison with the UV-vis measurements in Fig. 4.9a, in our experimental condition we can estimate (neglecting reflectance) a light absorption of about 95 % for LTON-poly and LTON-112, 50 % for LTON-011 and 30 % for LTON-001. The light absorbed in the underlying TiN layer does not affect the photocurrent as confirmed in Ref.^[165].

Sample	Absorption	Photocurrent density [$\mu\text{A cm}^{-2}$] at 1.45 V vs. RHE	APCE [10^{-5}] at 1.45 V vs. RHE
LTON-poly	95 %	1.455	3.6
LTON-112	95 %	2.399	5.9
LTON-011	50 %	2.398	11.3
LTON-001	30 %	2.138	16.8

Table 4.3.: Absorbed-photons-to-current efficiency values of the four described samples using formula 4.1 with $P_{in} = 130 \text{ mW cm}^{-2}$, $\lambda = 405 \text{ nm}$ and the obtained photocurrent densities ($J_{ph}(\lambda)$) from Fig. 4.19a at an applied potential of 1.45 V vs. RHE.

Considering the absorbed-photons-to-current efficiency (APCE) defined as

$$APCE(\lambda) = \frac{hc}{e} \frac{J_{ph}(\lambda)}{\lambda AP_{in}(\lambda)} \quad (4.1)$$

where $J_{ph}(\lambda)$ is the measured current density at a specific applied potential, $P_{in}(\lambda)$ is the power density of the monochromatic light source at the semiconductor surface, A is the light absorption (in percent), h the Planck constant, c the speed of light and e the elementary charge ($\frac{hc}{e} = 1240 \text{ V nm}$), we conclude that while the measured photocurrent densities of the three crystallographically ordered samples were similar, the respective APCE is indeed significantly different. As an example, Table 4.3 shows the APCE values of the four samples evaluated at an applied potential of 1.45 V vs. RHE.

It is interesting to note that the polycrystalline (LTON-poly) and the textured (LTON-112) samples are both mainly (112)-oriented and have very similar nitrogen content and optical properties. By comparing the PEC measurements of these two samples we most likely observe the effect of the different crystalline quality. Instead, for the two epitaxial films (LTON-011 and LTON-001) the effect of high crystalline quality is combined with the influence of the different surface orientation.

We conclude that the crystalline quality of the semiconductor certainly affects the PEC performance by increasing the mobility of the photo-generated charge carriers. But also the crystallographic surface orientation plays an im-

portant role, most probably by influencing the charge transfer at the semiconductor/electrolyte interface.

The availability of different crystallographic surface orientations will allow investigating the role of suitable co-catalysts with different interfaces with the semiconducting photo-anode. This is of course essential to effectively make the photo-generated charge carriers available for the electrochemical reaction.

4.2.4. Conclusion

We investigated the effect of the crystalline quality and crystallographic surface orientation of LaTiO_xN_y thin films on the visible light induced photocurrent using TiN-buffered substrates as current collectors.

The analysis of the chemical composition of the as prepared sample surfaces revealed the presence of a La-terminated surface layer, where during the first electrochemical tests titanium undergoes further oxidation and nitrogen is partially depleted. No significant nitrogen loss was observed in the applied experimental conditions.

We showed that such chemical evolution of the surface reduces the measured current. A large part of the current measured during the first potentiodynamic tests can possibly be ascribed to this electrochemical surface oxidation and is not (or at least not only) the result of the water splitting process. After few potentiodynamic scans the current reaches a stable and reproducible value which we assign to the real photocurrent associated to visible light induced water splitting.

In order to characterize thin film photoanodes with different crystallographic properties after chemical stabilization and minimizing the influence of spurious effects and/or voltage history we propose the use of potentiostatic cathodic voltage scans, as alternative to the potentiodynamic anodic measurements typically applied in literature.

These measurements confirm that the crystalline quality of the sample has an important influence on the PEC performance; better crystalline quality increases the attainable photocurrent for semiconducting photoanode with comparable optical properties. But we also show that the absorbed-photon-to-current efficiency

can be tuned by selecting different crystallographic surface orientations. In particular, the (001)-oriented surface shows an APCE value almost five times higher than the (112)-oriented surface. This is the XRD reflex with the largest relative intensity for this material, and possible the energetically favored surface orientation for LaTiO_xN_y nanoparticles.

The results of this investigation point at new goals to achieve next: optimize the chemical composition of LaTiO_xN_y films (bulk and surface), increase the nitrogen content of highly ordered films, and a coupling of selected surface orientations with suitable co-catalysts.

5

Final remarks

5.1. Conclusion

This thesis was dedicated towards gaining fundamental knowledge on oxynitride photoelectrode materials particularly in the context of solar water splitting. This includes open questions of how the nitrogen incorporation affects the electronic and optical properties, how the crystalline quality and crystallographic surface orientation affects the photoelectrochemical (PEC) activity.

To answer these research questions the sample needs to fulfill certain requirements, such as tunable nitrogen content, controllable crystalline quality and surface orientation. These requirements cannot be addressed with conventional powder samples and therefore the goal was to find a suitable platform to investigate certain properties of oxynitride materials.

The strategy used for this work was the deposition of oxynitride thin films by a modified Pulsed Laser Deposition (PLD), namely Pulsed Reactive Crossed-beam Laser Ablation (PRCLA). Using this sample preparation method the sample requirements are fulfilled. As representative oxynitride compound lanthanum titanium oxynitride (LaTiO_2N) was chosen.

To investigate the influence of the nitrogen incorporation on the electronic and optical properties, oxide and oxynitride samples (LaTiO_{3+z} and LaTiO_xN_y thin films) with the same crystalline structure were fabricated as confirmed with X-Ray Diffraction (XRD). The optical properties were investigated with UV-Vis spectroscopy, where a shift to larger wavelengths of the absorption edge was observed for the oxynitride compared to the oxide. The oxynitride revealed a band gap of about 2.30 eV, which is about 0.96 eV smaller compared to the oxide films.

This reduction of the band gap of the oxynitride compared to the oxide could be confirmed with X-ray Absorption Spectroscopy (XAS) and non-resonant X-ray Emission Spectroscopy (XES) performed using the Swiss Light Source (SLS) at PSI. However, not only a shift of the valence band edge of the oxynitride to higher energies as predicted in the literature, but also an additional shift of the conduction band edge to lower energies was observed. The shift at the valence band of 0.66 eV was assigned to additional states formed due to a hybridization of the O 2p and the energetically higher lying N 2p orbitals, as indicated by theoretical calculations. The additional shift at the conduction band of 0.28 eV (total shift of 0.94 eV) was observed for the first time. Unfortunately, a clear assignment of the origin of this shift cannot be found with the presented data and for this set of samples having the same crystalline structure and cationic composition.

As mentioned previously, using PRCLA the nitrogen content and the crystalline properties of oxynitride thin films can be controlled. This enables the possibility to investigate the effect of crystallographic, morphological and optical (nitrogen content) properties on the PEC activity of oxynitride thin films. The introduced new model system using TiN-buffered substrates as current collector was specially designed for such investigations. It was shown that TiN is stable in the reducing environment and at high temperatures ($> 800^{\circ}\text{C}$) needed for the LaTiO_xN_y film growth. Further, TiN allows the growth of highly ordered thin films needed for further investigations of how the crystalline quality and crystallographic surface orientation affects the PEC activity. It was also observed that TiN enables better control of the nitrogen content in the LaTiO_xN_y thin film where only the applied laser fluence needs to be changed. As a proof of concept we have demonstrated the photocatalytic response of LaTiO_xN_y thin films integrated into our model system.

Further PEC investigations using this model system revealed a reduction of the photocurrent of the LaTiO_xN_y thin films caused by changes at the surface during operation. This surface evolution can be assigned to a stronger oxidation of the titanium at the LaO-terminated surface compared to the bulk after PEC characterization, as observed with X-ray Photoelectron Spectroscopy (XPS), which mainly accounts for the initial measured photocurrent. Even though this could indicate a loss of nitrogen, the nitrogen-to-titanium ratio determined from XPS

data remained constant before and after the PEC measurements. Since the nitrogen is not leaving the sample it may migrate from the crystal to the surface and segregates thereby also forming compounds with the adsorbed hydrocarbon-derived contaminants as observed by Time-of-Flight Secondary Ion Mass Spectrometry (ToF-SIMS). Additionally, ToF-SIMS measurements, together with XRD and heavy-ion Elastic Recoil Detection Analysis (ERDA), observed that the bulk remains unchanged by performing PEC measurements indicating that only the surface becomes modified.

For a subsequent investigation of the influence of the crystalline quality and crystallographic surface orientation on the PEC activity, the samples were characterized by potentiostatic measurements to ensure fully stabilized and from the surface evolution uninfluenced samples. These investigations revealed a strong dependence of the crystalline quality and crystallographic surface orientation on the PEC activity. A 60 % gain was observed for highly ordered thin films by comparing with polycrystalline samples. The calculation of the absorbed-photons-to-current efficiency gives additional information on the influence of the crystallographic surface orientation on the photoelectrochemical activity, showing the highest efficiency for the sample with a (001) out-of-plane orientation.

This work establishes the foundation of an effective experimental approach for investigations of LaTiO_xN_y thin films as photocatalysts. The reported results and investigations suggest that this experimental approach can be extended to other oxynitride compounds.

5.2. Outlook

It could be shown that the nitrogen incorporation affects not only the valence band, but also the conduction band. A further systematic investigation of how both shifts are correlated with the nitrogen content is of interest. For this a set of LaTiO_xN_y samples with different nitrogen contents needs to be prepared and measured at the SLS by XAS and XES.

Another use of X-ray spectroscopy could be the investigation whether LaTiO_xN_y thin film samples have a direct or indirect band gap. In literature LaTiO_2N is known as a direct band gap semiconductor^[156,157], but measurements using spectroscopic ellipsometry and UV-Vis spectroscopy indicate that LaTiO_xN_y thin film samples fabricated for this work by PRCLA have an indirect band gap. Certainty of the true nature of the band gap can be ensured by performing Resonant Inelastic X-ray Scattering (RIXS) as shown for BiVO_4 in Fig. 5.1. Also BiVO_4 was known in the literature as a direct band gap semiconductor. However, in Ref. [254] RIXS is used to investigate the real nature of the band gap of BiVO_4 . In the case of a direct band gap, the emission energy has to decrease with increasing excitation energy as shown in Fig. 5.1a (assuming momentum conservation, thus e.g. no photon-phonon interaction). Accordingly, in the case of an indirect band gap, the emission energy has to increase with increasing excitation energy. Fig. 5.1c shows an increase of the emission energy with increasing excitation energy of the O K-edge, thus revealing an indirect band gap for BiVO_4 .

RIXS was also applied to measure LaTiO_xN_y thin film samples. An analysis of the RIXS plot according to Ref. [254] was performed and the result is shown in Fig. 5.2. Also here an increase of the emission energy with increasing excitation energy can be observed between 4975 eV and 4995 eV indicating that LaTiO_xN_y thin film samples have an indirect band gap. However, the measurements were influenced by an overlapping of the XES data with the corresponding elastic scattering peak of the emitted X-rays (see Fig. 3.1), which leads to a difficult analysis of the data and to data points not matching the trend (two points marked with a blue circle in Fig. 5.2). It needs to be clarified whether measurements with higher resolution are needed or required to better process the data for a reliable investigation of the nature of the LaTiO_xN_y band gap. Further, a systematic

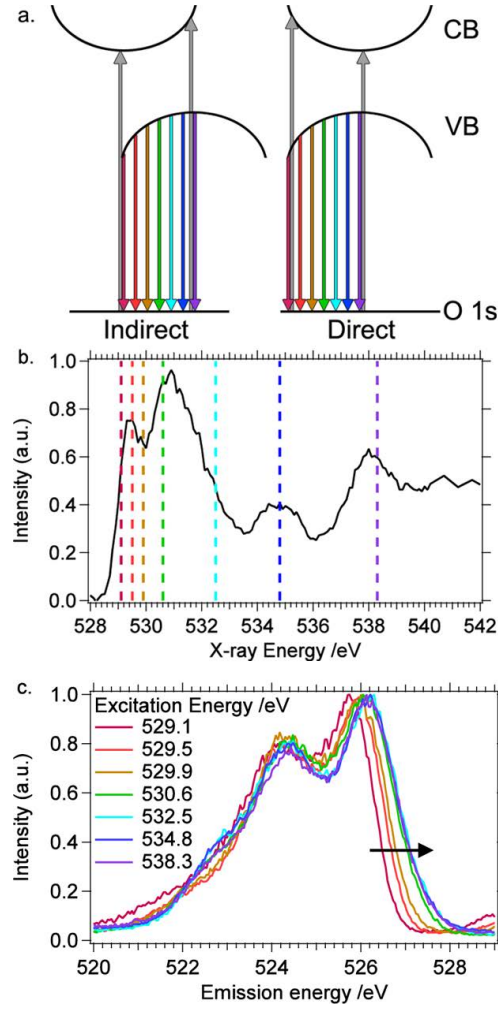


Figure 5.1.: (a) Scheme of how the emission energy depends on the excitation energy using Resonant Inelastic X-ray Scattering (assuming momentum conservation). Indirect band gap (left): with increasing excitation energy (gray arrow) the emission energy (colored arrows) increases as well indicating a blue-shift. Direct band gap (right): with increasing excitation energy the emission energy decreases (red-shift). (b) XAS of the O K-edge as an example for BiVO₄. The vertical lines indicates the used excitation energies used in (c) to demonstrate with the XES data the blue-shift observed for BiVO₄. (Figure modified from ^[254]).

investigation using LaTiO_xN_y thin film samples with different nitrogen content would help to better understand how the indirect band gap is formed.

X-ray spectroscopy can be further used to determine the electronic structure of LaTiO_xN_y thin films in operating conditions by measuring XAS and XES during PEC characterization. This could give further details of how the oxyini-

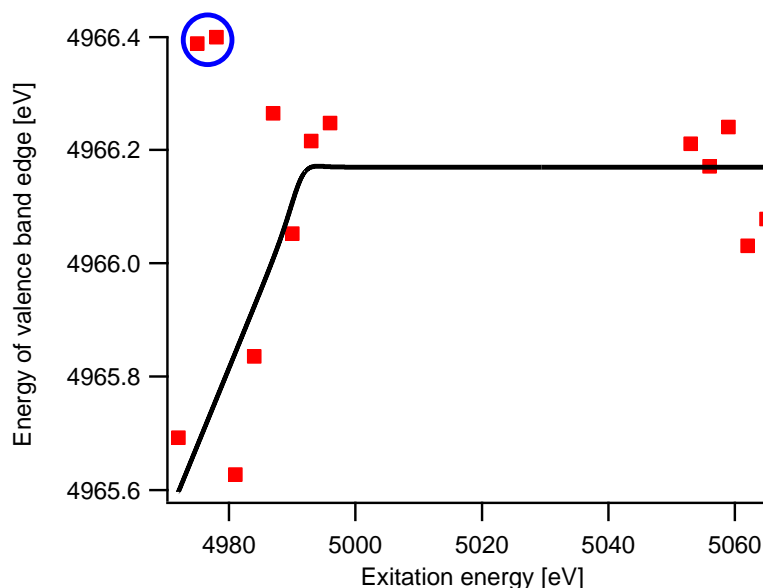


Figure 5.2.: The determined energy of the valence band edge in dependence on the excitation energy for a LaTiO_xN_y thin film sample using the X-ray Emission Spectroscopy data extracted from the Resonant Inelastic X-ray Scattering measurements performed according to Ref. [254] to investigate the nature of the band gap. The positive slope in the range between 4975 eV and 4995 eV indicates a blue-shift, thus an indirect band gap.

tride photoelectrode is behaving in operating conditions and how the electronic structure is modified by the illumination of light.

The reported PEC results show a strong dependence of the crystalline quality and crystallographic surface orientation on the PEC activity. However, XPS and Low-Energy Ion Scattering (LEIS) spectroscopy further observed a lanthanum-rich surface, which extends until about 1 nm from the surface into the sample. Thus, a closer investigation regarding the role of the lanthanum-rich surface on the observed photocurrents needs to be targeted. This can be addressed by a surface etching procedure specifically developed for our thin films to remove the top layer and to expose the buried LaTiO_xN_y surface with the bulk composition and crystallographic orientation. The thermal treatment and chemical etching as suggested in Ref. [245] can be used as a starting point.

Apart from these topics, the investigation of how the crystallographic surface orientation influences the charge transfer from the oxynitride photocatalyst to a co-catalyst is an important topic. According to the literature, and also confirmed

in this work, the use of a co-catalyst is essential for an efficient future application. Therefore, it makes sense to extend future research on oxynitride materials with the investigation on how the use of a co-catalyst improves the photocatalytic output.

Further, an investigation of the spatially resolved transport of charge carriers in the oxynitride is of great interest. A possibility of such an investigation can be found in the use of Near-field Scanning Optical Microscopy (NSOM). Using a Scanning Electron Microscope (SEM) the non-equilibrium charge carrier recombination can be imaged and allows the spatially resolved observation of the charge carrier motion^[255]. This investigation would give further details about how the charge carriers are moving in the oxynitride, i.e. whether an anisotropic charge transport in the holes or electrons is observed.

Finally, the competencies and investigatory frameworks developed and proposed in this thesis can be used to further examine other photocatalytic active oxynitride compounds beyond the representative oxynitride, LaTiO_2N , such as BaTaO_2N and TaON .

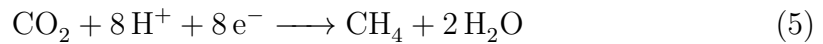
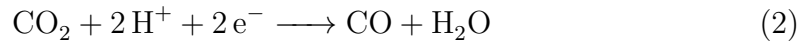
Appendix

A. Photocatalytic Characterization

This section summarizes the work done on the setup of a photocatalytic reactor cell. This reactor cell was made to investigate the photocatalytic (PC) activity of thin inorganic films in converting CO_2 and H_2O to CH_4 , H_2 and other carbon containing products by mass spectrometry analysis. This idea was initially intended to be independent of the electrically conductive buffer layer, but was then abandoned because of the too low sensitivity for the oxynitride thin film samples acting as photocatalysts. Due to the very smooth surfaces of thin film samples made by PLD, the active surface area is much smaller compared to powder samples, which are mainly used for PEC and PC.

A.1. Introduction

To evaluate the photocatalytic activity of inorganic thin films, an experimental setup was assembled to detect and analyze gas phase photochemical products. The considered reactions were the catalyzed reaction of water, CO_2 and light (of certain wavelengths) at a photocatalyst surface to the products CH_4 , O_2 and other possible species with C, O and H that could be used as “solar” fuels. Example reactions follow below^[256]:



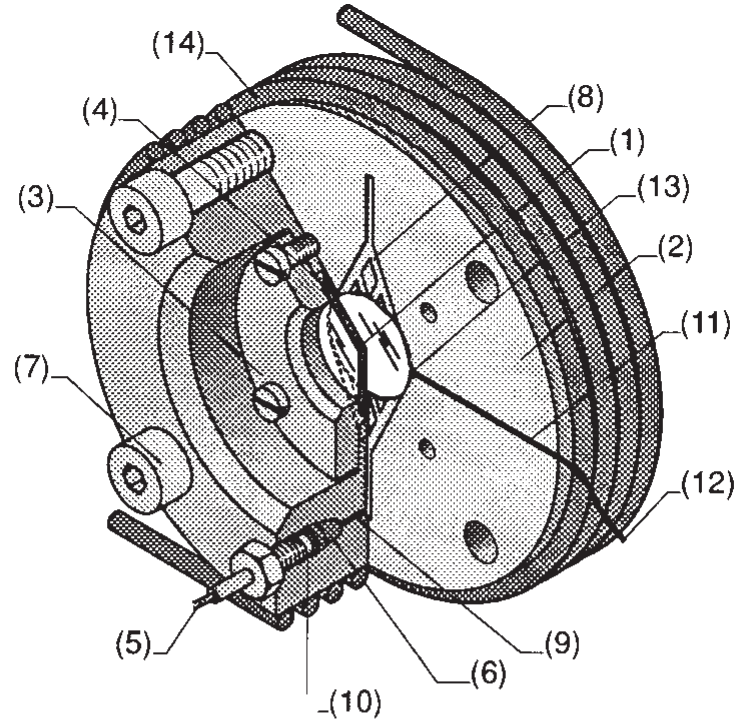
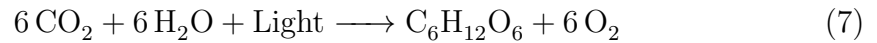


Figure 1.: Overview of reactor (from Saladin et al.^[257]).

(1) windows, (2) main body, (3) flanges, (4) Viton seals, (5) passivated fused silica capillaries, (6) polyimide fittings, (7) screws, (8) arc eroded channels, (9) gas inlet and outlet, (10) female connections for polyimide fittings, (11) arc eroded grooves, (12) thermocouple, (13) tip of the thermocouple to measure the gas temperature, (14) heating wire.

This is similar to the overall reaction of the photosynthesis that occurs in plants:



To do this in the gas-phase with samples of about 0.5 cm^2 to 1.0 cm^2 size it is important to have a reactor cell with a small volume to maximize sensitivity. A reactor cell for this purpose was obtained from Ivo Alkneit of the Solar Technology group of PSI where similar experiments were performed between 1995 and 1999 and a custom-made cell reactor was designed and constructed at PSI. A depiction of the reactor cell and a cross section is shown in Figure 1^[257–260].

The reactor cell is connected to a mass spectrometer (MS) with capillary

tubing so that the atmosphere inside the cell can be analyzed. The inlet of the cell reactor is connected to a gas source by capillary tubing. The reactant gas (CO_2) that is led into the reactor cell is saturated with water vapor by passing it through a bubbler filled with water. The important conditions for this measurement to work are listed below:

- (i) A small volume where the reaction takes place as compared to the volume of the photo-catalyst to increase sensitivity \rightarrow Reactor cell with a small volume.
- (ii) A suitable mixture of reactant gas (CO_2 , 99.998 % purity) saturated with water vapor (H_2O) by passing through a bubbler filled with water.
- (iii) Small volume of the tubing to minimize dilution of products to be analyzed.
- (iv) Heating of the tubing to avoid condensation of water in the narrow tubing.

In general a measurement consists of flushing the line with an inert carrier gas (e.g. N_2) that will not interfere too much with the analysis, then filling the cell with the $\text{CO}_2/\text{H}_2\text{O}$ mixture and followed by closing the cell and illuminating it through the window. After a certain time the light is removed and the cell is flushed with the gas from the cell being pushed through and analyzed for photocatalytic products.

A.2. Experimental

The full photocatalytic setup is schematically shown in Figure 2 where the second gas supply next to CO_2 is an inert carrier gas such as N_2 . Photographs of the instrumentation are shown in Figure 3

The instruments and materials used in the final configuration of the setup are shown in the list below:

- Reaction gas: CO_2 (4.5), purity 99.998 %, Messer (overpressure 0.2 bar to 0.5 bar)
- Carrier gas: N_2 (overpressure \sim 0.2 bar to 1.0 bar)

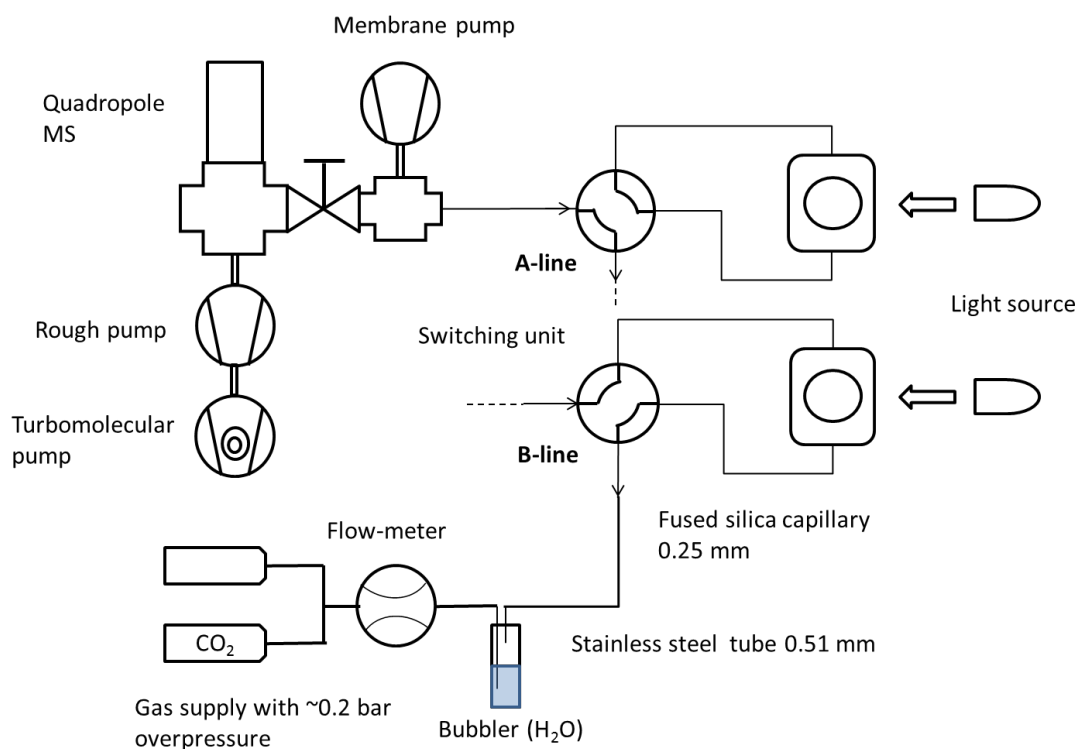


Figure 2.: Schematic view of photocatalytic setup with both pathways for the gas line shown as A- and B-line.

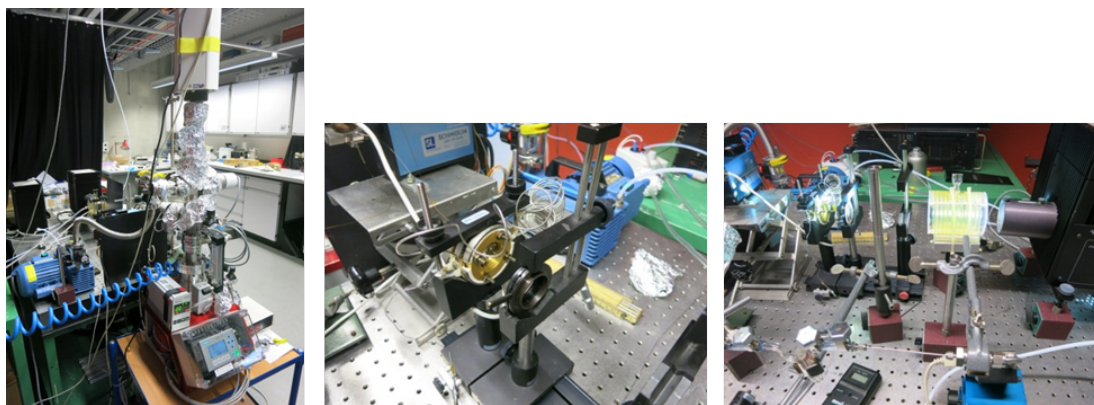


Figure 3.: Photographs of the photocatalytic reactor cell and the rest of the experimental setup.

- Flowmeter: Pneucleus Technologies MicroFlo Mass Flow Controller (1-1000 SCCM, ml min^{-1}). It is calibrated for Ar so it needs to be calibrated for CO_2 or N_2 .
- Sigma-Aldrich micro bubbler with deionized water at $\sim 18^\circ\text{C}$ (291 K) \rightarrow

Partial pressure ~ 2058 Pa ($\sim 2\%$ water at 1 bar) connected to Swagelok tubing by 6 mm PVC.

- Swagelok connectors for stainless steel tubing ($1.59\text{ mm} \times 0.51\text{ mm}$) connecting gas line supply with capillary.
- Fused silica capillary (ID: $250\text{ }\mu\text{m}$).
- Switch unit VICI AG.
- Hg(Xe) lamp (Müller SVX-LAX 1530).
- Membrane pump.
- Pfeiffer needle valve UDV 046.
- Balzers mass spectrometer (Balzers QME200 / Analysator QMA200 quadrupole mass spectrometer) with a turbo molecular pump (Pfeiffer HiCube 80 Eco pumping station).

A.3. Short history of the preparation

The needle valve was purchased to fit with the vacuum/MS system from the vacuum group at PSI and was attached to a capillary tube directly. Measurements with this new inlet showed that the “dead” volume in the inlet dilutes the gas to be analyzed and also yielded very long residence times in the sampling line. To improve the situation an inlet was especially designed and constructed in the workshop of PSI to get the capillary tubing closer to the needle valve hole, where the gas species can be gathered if close enough. This was partially successful but still gave long response times. The second modification was to add a t-shaped chamber at the inlet and connect it to a membrane pump (capacity of ~ 1 mbar) so that the inlet is always evacuated. Combining the vacuum pumped inlet with a capillary tube that gets as close as possible to the needle valve “hole” gives a much improved sensitivity and response time. The following measurements were done with this configuration.

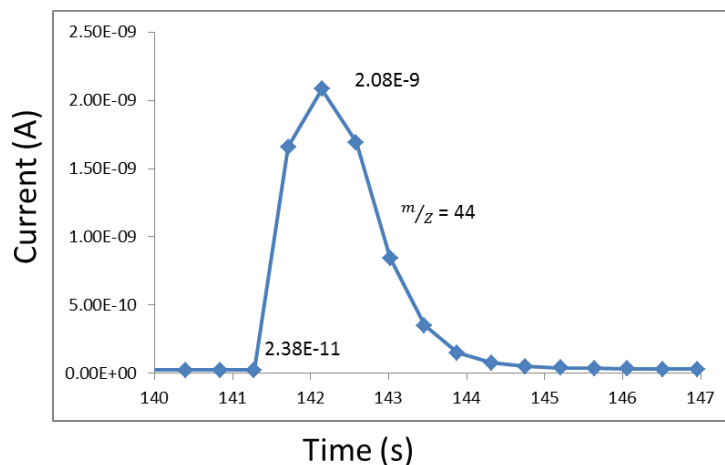


Figure 4.: Ion current from m/Z ratio 44 when line B is opened after the cell was filled with CO_2 .

A.4. Test measurements

To evaluate the system and determine the purging behavior of the system, the reactor was filled with CO_2 and then closed off. Nitrogen was used as purging gas to carry the gas from the reactor to the MS. In Figure 4 such a response curve can be seen. This is done at a fixed pressure at the inlet valve ($\sim 1 \times 10^{-6}$ mbar) and a controlled flow of the purging/carrier gas ($\sim 1 \text{ ml min}^{-1}$ to 5 ml min^{-1}). The integration time of the CO_2 signal is about 4 s to 5 s but ideally for a higher sensitivity it should be longer or the sampling rate has to be higher. The optimum sampling rate for a channel was found to be about once every 200 ms to 250 ms (see Figure 5).

The gas mixture that was used for calibrating the current response was: CO_2 : 1 %, CO : 1 %, H_2 : 1 %, CH_4 : 1 %, O_2 : 1 %, N_2 : 1 % and Ar is the rest. In Figure 6 the reactor cell is filled with a gas mixture for calibration and purged to be measured in the MS. The m/Z ratios can be compared to the relative ion-currents in Table 1 for clarification.

The plot in Figure 7 shows the tendency for leakage in the cell reactor visible in the signal increase of $m/Z = 32$ (O_2). A leak detection was performed to find the source of the leakage by blowing helium gas at different parts of the whole instrument. As it is seen in Figure 8 the leak detection with Helium gas shows the only leak coming from the cell reactor windows.

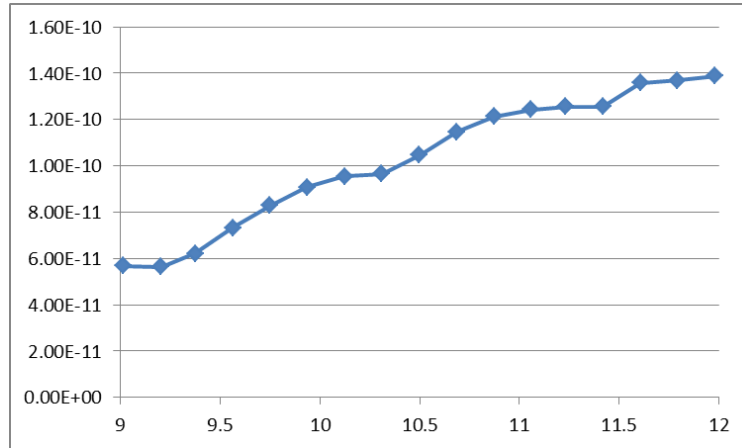


Figure 5.: The graph shows the maximum time resolution of the ion current with the X-axis showing the time in seconds.

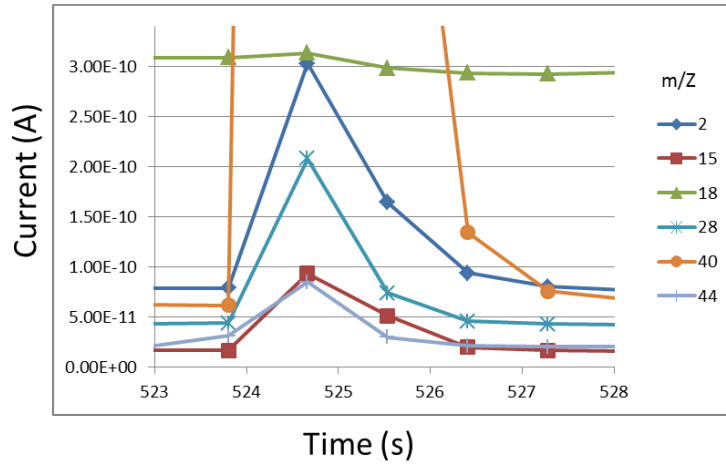


Figure 6.: Ion currents for a defined gas mixture with line B opened at 523.8s.

Preparation of TiO_2 solution and preparation of powder samples on cell window:

- Weigh 20 mg TiO_2 (P25, average particle size: 20 nm, 2:1 anatase to rutile) per 50 ml solvent (deionized water). An alternative solid to TiO_2 can also be used in a similar fashion.
- Add deionized water and stir solution.
- Sonicate solution for better dispersion.
- Clean sapphire windows mechanically with water and tissue.

Appendix

Table 1.: Relative ion-currents from fragments of ionized molecules are tabulated. Taken from Balzers.

Mass number	H ₂	He	CH ₄	H ₂ O	Ne	N ₂	CO	C ₂ H ₆	O ₂	Ar	CO ₂	C ₃ H ₈
1	3		13.5	2.4				9.6				5
2	100											
4		100										
12			3				6.3	0.7			9.7	0.6
13			7.8					1.2				0.9
14			16			14	0.8	303				2.3
15			85					4.7				7.2
16			100	1.8			2.8		18		16	
17			1.2	23								
18				100								
20					100					22.6		
22					10.2						2.1	
25								3.8				0.8
26								22.2				9.8
27								33.4				43.5
28						100	100	100			13	61
29						0.7	1.2	20				100
30								22.2				21.7
31												
32									100			
34									0.4			
36										0.34		
37												4.6
38										0.06		6.7
39												20.2
40										100		2.6
41												15
42												4.8
43												22.8
44											100	24
45											1.2	0.8

- Put window in Ultrasonic bath: 5 minutes in water, 10 minutes in acetone and 10 minutes in isopropanol.
- Blow dry with compressed N₂.
- Insert window into sample holder and screw tight.
- Take a freshly sonicated TiO₂ solution (200 μ l) and add into the sample

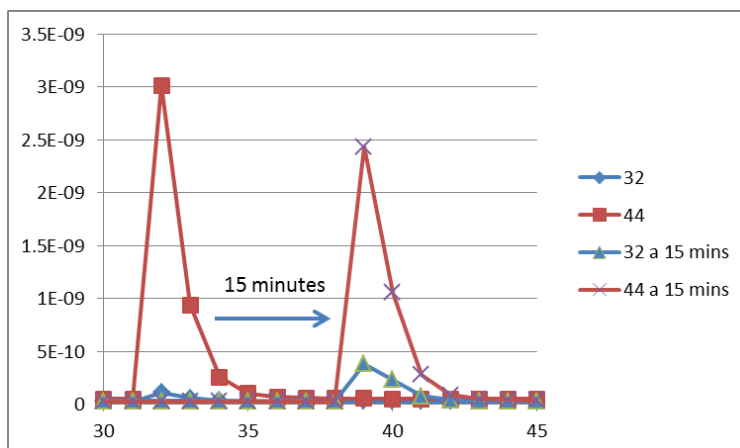


Figure 7.: Gas detection from cell reactor after 0 minutes and 15 minutes time with the signals of O_2 and CO_2 .

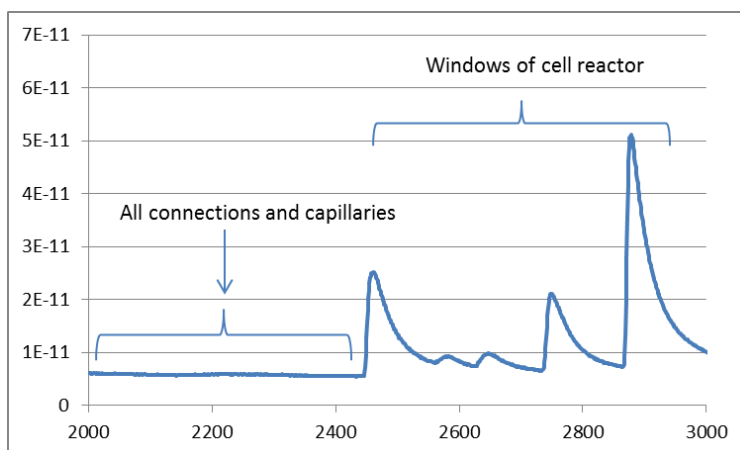


Figure 8.: Leak detection with He.

holder (Fig. 9).

- Let solution settle overnight.
- To remove water increase evaporation by heating sample holder to $\sim 50^\circ C$ to $60^\circ C$.
- Replace window in reactor cell with the newly prepared ones.

Measurement of photocatalytic reactions:

- Switch on rough pump at inlet and open valve.

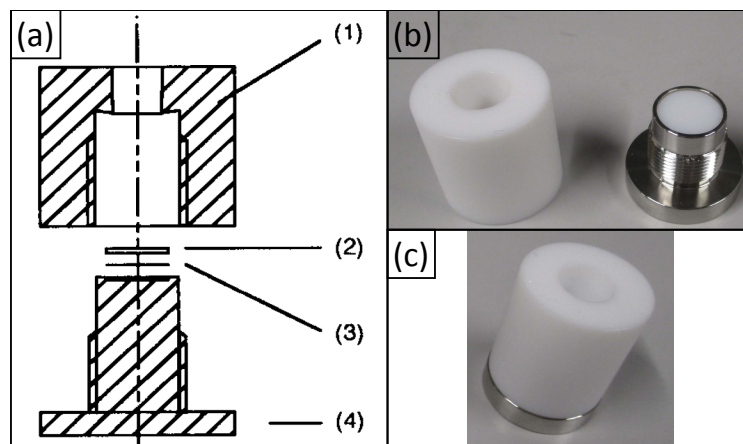


Figure 9.: (a) technical drawing of the sample holder (from Saladin et al. ^[257]). (1) nut made of Teflon with a 10 mm central hole, (2) window with 12.7 mm diameter and 1 mm thickness, (3) Teflon sheet to protect the window and (4) stainless steel holder. (b) separated and (c) assembled part (1) and (2) (recreated at the PSI workshop according to (a))

- Switch on water flow for water filter placed in between lamp and reactor cell. The water filter is needed to block IR radiation that should prevent unintended heating of the sample.
- If needed a filter to remove UV light can be added in the beam path.
- Switch on Hg(Xe) lamp. It usually needs about 15 min to warm up. Measure the intensity of the radiation if possible.
- Mass spectrometer pump should already be on.
- Close needle valve to a pressure between 1×10^{-7} mbar and 3×10^{-6} mbar. The lower pressure may reduce the pressure change when switching between line A and B (Figure 2). This may be crucial detecting a weak ion current.
- Switch on flow-meter and set it (5 ml min^{-1} to 100 ml min^{-1}).
- Switch on laptop, and then plug MS power.
- Open software and switch on MS and measurement.
- Flush line with N_2 with open needle valve (do not allow pressure to go above 5×10^{-6} mbar unless MS is off!).
- Set the needle valve again to a pressure between 1×10^{-7} mbar to 3×10^{-6} mbar.

- Fill cell with water saturated CO₂ gas.
- Illuminate sample with lamp for certain time. A certain time is needed to produce enough gaseous products to measure but at same time a longer time will lead to more leakage. Testing with times between 1 min and 15 min is a good rule.
- Toggle from line B (reactor cell) to line A.
- Switch off/block light.
- Let carrier gas on until steady signal. The carrier gas could also be the CO₂ if the other carrier gas, e.g. N₂ gas feed, is suspected to have contamination.

A.5. Measurement

Several attempts at photocatalysis reactions were made with P25 Titania films on the cell windows. By tuning the reaction time for an optimum combination of reducing leakage and maximizing product yield, a weak signal at $m/Z = 15$ could be identified. The peak that is visible in Figure 10 is just about strong enough to be distinguished from the noise. An estimate of the signal strength that is needed is about 5×10^{-13} A. If we compare this number with the current magnitude for a 1 % gas content (10 000 ppm) in Figure 6, $\sim 1 \times 10^{-10}$ A, we can see that the detection limit can be estimated very roughly to at least 50 ppm. This detection sensitivity may not be enough.

The molar content of gas in the cell can be estimated to 2.5 μmol from the cell volume 60 μl and the molar volume of gases in ambient conditions ($\sim 24 \text{ l mol}^{-1}$ at room temperature). In Ref. [257] the production rate of CH₄ over TiO₂ is about 4 $\mu\text{mol g}^{-1}$ TiO₂ / 10 min illumination. The cell has about 160 μg TiO₂ on the windows and this equates to about 0.64 nmol per 10 min illumination in the reactor cell. This would be equal about 250 ppm of CH₄ after 10 min illumination, which should allow for a signal to be detected. Although with a detection limit of > 50 ppm it will be a very weak signal as is indeed shown in Figure 10. The illumination time in Figure 10 is 5 min and longer times did not improve upon signal strength. Unfortunately it was the leakage in the reactor cell that seemed to make the measurements very inconsistent. An improvement of the detection

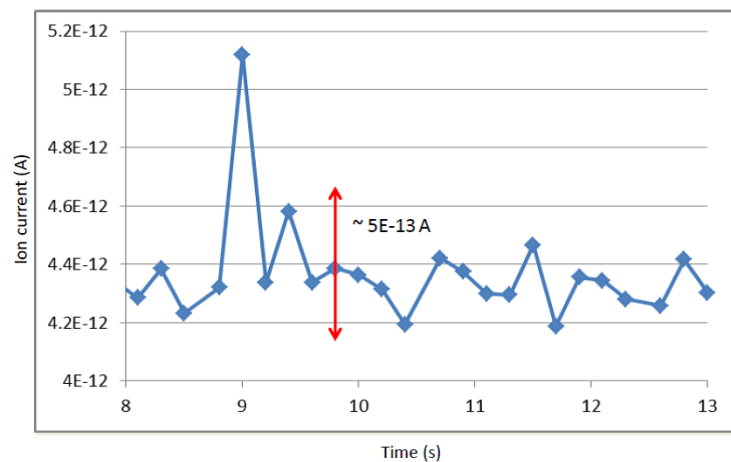


Figure 10.: Plot of ion current of $m/Z = 15$ channel when cell reactor is opened and the gas contents flushed into the MS.

limit to below 10 ppm would probably allow for a better and more reproducible detection. Unfortunately the slight signal at $m/Z = 15$ was also observed in dark reactions. The dark reaction signal is not yet explained.

In summary, independent on the shown results, thin films would always yield a low amount of products. Therefore, the idea of using this photocatalytic reactor cell was abandoned and we switched to photoelectrochemical investigations.

List of Figures

1.1.	Estimated world population (left axis): historical estimation until 1950 (dark blue) ^[3] , actual recorded population from 1950 to 2015 (blue), global primary energy consumption (right axis): estimation from 1965 to 2014 (green) ^[4] , estimation from 1800 to 1995 (dark green) ^[5] , CO ₂ concentration (second right axis): CO ₂ concentration from West Antarctic Ice Sheet Divide ice cores (dark gray) ^[6] CO ₂ annual mean data from Mauna Loa (gray) ^[7]	2
1.2.	Two ways of hydrogen production by using solar energy: Combination of photovoltaic and electrolysis or directly with photocatalytic water splitting	3
1.3.	(a) Schematic of the principle of electrolysis. A minimum applied voltage of 1.23 V (usually > 1.6 V due to overpotentials ^[25]) between the two electrodes is needed to split H ₂ O into its constituents, thus H ₂ and O ₂ . (b) In PEC water splitting, at least one of the electrode is replaced by a semiconducting material, which is illuminated to generate electron-hole pairs. (c) Adsorption of ions (here anions) from the solution on the photoelectrode forms a space-charge layer at the surface of the semiconductor needed for charge separation. For a proper transfer of the the charge carriers (here electrons) to the counter electrode, a current collector is needed. (d) Oxidation of H ₂ O to O ₂ with the holes at the photoanode and reduction of H ₂ O to H ₂ with the electrons at the cathode.	6
1.4.	Valence and conduction band position for straddling the reduction and oxidation potentials of water.	8
1.5.	To summarize alternative water splitting systems. (a) photoelectrochemical water splitting system using a photoanode (b) photoelectrochemical water splitting system using a photocathode (c) photoelectrochemical water splitting system using a photoanode and photocathode in tandem configuration. (d) photocatalytic water splitting system based on one-step excitation (e) photocatalytic water splitting system based on two-step excitation (Z-scheme). The tandem cell configuration (c) and the Z-scheme (e) allow the usage of semiconductors with smaller band gaps. (Figure modified from ^[28]).	10
1.6.	Reference Solar Spectral Irradiance: Air Mass 1.5 from Ref. ^[44] showing the direct and circumsolar radiation.	12
1.7.	Measurements used for efficiency calculations (Figure modified from Ref. ^[27]).	15
1.8.	Valence and conduction band positions (including uncertainties) of some semiconductors used in photoelectrochemistry. Figure also shows some important redox potentials at pH 14. (Figure modified from Ref. ^[8]).	18
1.9.	Valence and conduction band positions of Ta ₂ O ₅ , TaON and Ta ₃ N ₅ to visualize the effect of the nitrogen incorporation. (Figure modified from Ref. ^[93]).	21
1.10.	Schematically shown particle transfer method. (Figure modified from Ref. ^[116]).	23
1.11.	Different powder synthesis routes for LaTiO ₂ N: the soft-chemistry (SC) route and the solid-state (SS) route with and without NaCl/KCl flux (Fx). Typical characteristics (shape, particle size, band gap, BET surface area) are reported in the figure. (Figure modified from Ref. ^[121]).	24
1.12.	Photocurrents LaTiO ₂ N photoanodes with CoO _x loading: soft-chemistry synthesis without flux (black), soft-chemistry synthesis with flux (red), solid-state synthesis without flux (blue), solid-state synthesis with flux (magenta). The measurements are performed in 0.1 mol dm ⁻³ aqueous solution of Na ₂ SO ₄ (NaOH adjusted pH to 13.40), with a scan rate of 10 mV s ⁻¹ and with chopped illumination (100 mW cm ⁻² , cut-off filter at $\lambda = 420$ nm). (Figure modified from Ref. ^[121]).	25
1.13.	O ₂ gas evolution measured over time for (a) untreated LaTiO ₂ N, (b) LaTiO ₂ N with 5 % Ca ²⁺ -backfilled, (c) LaTiO ₂ N with 5 % Ca ²⁺ -substituted, (d) LaTiO ₂ N with 5 % Ca ²⁺ -excess as reference sample prepared using stoichiometric La ₂ Ti ₂ O ₇ (backfilling synthesis method) and (e) TiO ₂ reference (Degussa P25). N ₂ evolution was approximately the same for all samples (including TiO ₂). (Figure modified from Ref. ^[127]).	27

1.14. Cations used for solar water splitting: in red materials of the d^0 -group and in green the materials of the d^{10} -group. (Figure modified from Ref. [93]).	29
1.15. Optical and photocatalytical investigation of $(1-x)\text{GaN}:x\text{ZnO}$: (a) Quantum efficiency and absorbance vs. wavelength, and (b) 35 h time course of the H_2 and O_2 gas evolution with evacuation of the system every 5 h showing a ratio of almost 2:1, respectively, indicating overall water splitting. (Figure modified from Ref. [92]).	30
2.1. Schematically shown working principle of a pulsed laser deposition (PLD) setup.	40
2.2. Schematically shown working principle of a PRCLA setup.	43
2.3. Example of an RBS spectrum of a LaTiO_xN_y sample grown on TiN-coated MgO substrate.	46
2.4. Example of an UV-Vis spectrum of a LaTiO_xN_y sample grown on a double-side polished Al_2O_3 substrate.	49
2.5. Example of a profilometry measurement of a LaTiO_xN_y sample grown on a Al_2O_3 substrate. The data (red) was fitted with the function $f(x) = y_0 + \frac{A}{\exp \frac{x_0 - x}{c} + 1}$ (black) to better estimate the thickness of the measured sample. A corresponds to the thickness, x_0 is the x-value of the inflection point, c defines the slope of the function and y_0 is the offset.	51
2.6. Schematically shown working principle of the X-ray spectroscopy measurements performed at the SuperXAS beamline of the Swiss Light Source at PSI [201]: (a) Resonant Inelastic X-ray Scattering (RIXS) and (b) X-ray Absorption Spectroscopy (XAS) and non-resonant X-ray Emission Spectroscopy (XES).	53
2.7. Photoelectrochemical test setup at EMPA using the so-called “cappuccino cell” [208]. The light intensity is adjusted to 100 mW cm^{-2} with a reference Si photodiode.	55
2.8. The new photoelectrochemical test setup established for this project. The light intensity is about 130 mW cm^{-2} (reflection losses corrected).	56
3.1. RIXS map of $\text{La}_2\text{Ti}_2\text{O}_7$.	59
3.2. (a) extracted spectra of HR-XAS (red) and valence-to-core XES (blue); (b) FEFF calculated orbital contribution.	60
3.3. X-Ray Diffraction pattern of (a) polycrystalline LaTiO_xN_y and (b) polycrystalline LaTiO_{3+z} thin film samples performed in grazing incidence mode.	64
3.4. Normalized UV-Vis transmittance spectra of LaTiO_{3+z} and LaTiO_xN_y thin film samples grown on double-side polished Al_2O_3 substrates. Due to the thicknesses of the samples, interference fringes are observed during the UV-Vis measurement [196]. The dashed lines mark approximately the band gap values of the samples. For the ease of comparison, the transmittance data is normalized to 100 %.	66
3.5. (a) Conduction and valence band electronic structure determined from X-ray emission and absorption spectroscopy measurements of LaTiO_{3+z} and LaTiO_xN_y thin films. (b) Calculated orbital contributions. (The markers in (a) correspond to the measured data and the lines act as a guide.)	68
3.6. Representation of the crystal structures of (a) $\text{LaTiO}_{2.25}\text{N}_{0.75}$ and (b) $\text{La}_5\text{Ti}_5\text{O}_{17}$ (i.e., $\text{LaTiO}_{3.4}$).	71
4.1. XRD patterns of two representative LaTiO_xN_y samples grown on SrTiO_3 substrates by PRCLA with different laser fluences.	76
4.2. a) XRD pattern of a polycrystalline $\text{La}_{1.01}\text{Ti}_{0.99}\text{O}_{2.2}\text{N}_{0.8}$ thin film deposited on TiN-buffered MgO substrate using PRCLA with a laser fluence of 3.7 J cm^{-2} . The peak marked with an X is the K_β diffraction reflex from the MgO substrate. b) Cross section micrograph (fractured surface). c) The corresponding RBS spectrum (black points) analyzed with the RUMP program (red line) and using the N/O ratio determined by ERDA.	79
4.3. N/O ratio of LaTiO_xN_y thin films grown on different substrates as a function of laser fluence. Used substrates are SrTiO_3 (blue ◀), YAlO_3 (black ▼), LaAlO_3 (light green ▲), TiN-coated MgO (red ■). All thin films are grown at 870°C and are $\sim 200 \text{ nm}$ thick.	82

4.4. UV-Vis spectra of three LaTiO_xN_y samples grown on LaAlO_3 substrates with different nitrogen content showing the effect on the optical properties of nitrogen substitution into the native oxide. All samples are about 200 nm thick and therefore interference fringes are observed during the UV-Vis measurement ^[196] . For comparison, the transmittance spectrum of the $\text{La}_2\text{Ti}_2\text{O}_7$ thin film of the same thickness is also shown.	83
4.5. XRD pattern of the epitaxial (001)-oriented $\text{La}_{1.04}\text{Ti}_{0.96}\text{O}_{2.26}\text{N}_{0.67}$ thin film grown by PRCLA with a laser fluence of 3.0 J cm^{-2} . The peak marked with an X is the K_β diffraction reflex from the MgO substrate.	85
4.6. PEC measurement of the polycrystalline $\text{La}_{1.01}\text{Ti}_{0.99}\text{O}_{2.2}\text{N}_{0.8}$ sample prepared on a TiN-buffered MgO substrate. The measurement was performed under chopped illumination (100 mW cm^{-2} with UV cutoff filter at $\lambda = 420 \text{ nm}$) to simultaneously measure the dark current and the photocurrent. The cell was filled with sodium borate electrolyte buffered at pH of 9 and a linear scan voltammetry was performed at a scan rate of 10 mV s^{-1}	87
4.7. X-Ray Diffraction pattern of LTON-poly, LTON-112, LTON-001 and LTON-011 shown by (a) the $\theta/2\theta$ -scan and (b) in the grazing incidence mode. The Al_2O_3 substrate is marked with a ■, the MgO substrate is marked with a ● and the K_β diffraction reflex from the MgO substrate is marked with a ○.	89
4.8. SEM cross sections (fractured surface) of LTON-poly, LTON-112, LTON-001 and LTON-011.	91
4.9. (a) Normalized UV-Vis spectra of three LaTiO_xN_y samples grown on double-side polished YAlO_3 substrates with different nitrogen content to visualize the shift of the band gap to higher energies with decreasing of the nitrogen content. (b) X-ray diffraction pattern of one representative LaTiO_xN_y sample grown epitaxially and (001)-oriented on (110)-oriented YAlO_3 substrate. The YAlO_3 substrate is marked with a ●.	93
4.10. Evolution of the photocurrent: (a) 1 st , (b) 2 nd and (c) 4 th chopped potentiodynamic measurements with 10 mV s^{-1} of sample LTON-poly (4 s light on and 4 s light off). All measurements were performed in an electrolyte of 0.5 M NaOH (pH= 13) using a 405 nm laser diode with a light intensity of 130 mW cm^{-2} . For the ease of comparison, the dark current is subtracted from the data.	94
4.11. LEIS surface spectra of the LTON-poly samples before and after PEC characterization obtained by probing with (a) 3 keV He^+ and (b) 6 keV Ne^+ beams. High energy offset of the species at the surface are indicated by arrows. Spectra have been offset for clarity.	97
4.12. LEIS depth profiles obtained for 6 keV Ne^+ scattering by the LTON-poly film (a) as deposited and (b) after PEC measurements. The background signal for the impurity peak in indicated as a dotted line.	98
4.13. Ti/La cation ratio normalized to the bulk stoichiometry as obtained from the LEIS depth profiles.	98
4.14. (a) depth profile and (b) N/O-ratio of LTON-poly before PEC using ToF-SIMS.	99
4.15. XPS spectra of (a)-(c) Ti 2p, and (d)-(f) N 1s from LTON-poly before PEC (incidence angle of 90° and 45°) and after PEC.	101
4.16. XPS spectra of O 1s before PEC (incidence angle of 90° and 45°) and after PEC from LTON-poly.	102
4.17. XPS spectra of La 3d before PEC (incidence angle of 90° and 45°) and after PEC from LTON-poly.	103
4.18. Potentiostatic measurements at 1.5 V vs. RHE of sample LTON-001 and LTON-poly (24 s light on and 24 s light off). All measurements were performed in an electrolyte of 0.5 M NaOH (pH= 13) using a 405 nm laser diode with a light intensity of 130 mW cm^{-2} . For the ease of comparison, the dark current is subtracted from the data.	105
4.19. (a) PEC characterization of the (001)-oriented sample LTON-001 (open green squares), the (011)-oriented sample LTON-011 (open blue circles), the (112)-oriented sample LTON-112 (full red squares), the polycrystalline sample LTON-poly (full black circles). Every experimental value in this j-E curve was obtained from a single potentiostatic measurement using the value of the stabilized and dark current subtracted photocurrent. (b) 4 th potentiodynamic measurement in comparison with potentiostatic measurement using sample LTON-001. The scan direction for the potentiodynamic measurement is from low to high voltage (anodic scan) and the scan direction for the potentiodynamic measurement is from high to low voltage (cathodic scan).	107

List of Figures

5.1.	(a) Scheme of how the emission energy depends on the excitation energy using Resonant Inelastic X-ray Scattering (assuming momentum conservation). Indirect band gap (left): with increasing excitation energy (gray arrow) the emission energy (colored arrows) increases as well indicating a blue-shift. Direct band gap (right): with increasing excitation energy the emission energy decreases (red-shift). (b) XAS of the O K-edge as an example for BiVO_4 . The vertical lines indicates the used excitation energies used in (c) to demonstrate with the XES data the blue-shift observed for BiVO_4 . (Figure modified from ^[254]).	115
5.2.	The determined energy of the valence band edge in dependence on the excitation energy for a LaTiO_xN_y thin film sample using the X-ray Emission Spectroscopy data extracted from the Resonant Inelastic X-ray Scattering measurements performed according to Ref. ^[254] to investigate the nature of the band gap. The positive slope in the range between 4975 eV and 4995 eV indicates a blue-shift, thus an indirect band gap.	116
1.	Overview of reactor (from Saladin et al. ^[257]). (1) windows, (2) main body, (3) flanges, (4) Viton seals, (5) passivated fused silica capillaries, (6) polyimide fittings, (7) screws, (8) arc eroded channels, (9) gas inlet and outlet, (10) female connections for polyimide fittings, (11) arc eroded grooves, (12) thermocouple, (13) tip of the thermocouple to measure the gas temperature, (14) heating wire.	II
2.	Schematic view of photocatalytic setup with both pathways for the gas line shown as A- and B-line.	IV
3.	Photographs of the photocatalytic reactor cell and the rest of the experimental setup.	IV
4.	Ion current from m/Z ratio 44 when line B is opened after the cell was filled with CO_2 .	VI
5.	The graph shows the maximum time resolution of the ion current with the X-axis showing the time in seconds.	VII
6.	Ion currents for a defined gas mixture with line B opened at 523.8 s.	VII
7.	Gas detection from cell reactor after 0 minutes and 15 minutes time with the signals of O_2 and CO_2 .	IX
8.	Leak detection with He.	IX
9.	(a) technical drawing of the sample holder (from Saladin et al. ^[257]). (1) nut made of Teflon with a 10 mm central hole, (2) window with 12.7 mm diameter and 1 mm thickness, (3) Teflon sheet to protect the window and (4) stainless steel holder. (b) separated and (c) assembled part (1) and (2) (recreated at the PSI workshop according to (a)).	X
10.	Plot of ion current of m/Z = 15 channel when cell reactor is opened and the gas contents flushed into the MS.	XII

List of Tables

4.1. Lattice parameters of the two substrates MgO (ICSD Coll.Code: 158103) and Al_2O_3 (ICSD Coll.Code: 160604), the TiN buffer layer (ICSD Coll.Code: 152807) and the oxynitride photocatalyst LaTiO_2N (ICSD Coll.Code: 168551).	90
4.2. Composition, nitrogen-to-oxygen ratio, thickness and used laser fluence of the described samples.	92
4.3. Absorbed-photons-to-current efficiency values of the four described samples using formula 4.1 with $P_{in} = 130 \text{ mW cm}^{-2}$, $\lambda = 405 \text{ nm}$ and the obtained photocurrent densities ($J_{ph}(\lambda)$) from Fig. 4.19a at an applied potential of 1.45 V vs. RHE.	108
1. Relative ion-currents from fragments of ionized molecules are tabulated. Taken from Balzers.	VIII

References

- [1] The International Energy Agency. 2015 Key World Energy STATISTICS, 2015.
- [2] T. F. Stocker and Others. *IPCC, 2013: climate change 2013: the physical science basis. Contribution of working group I to the fifth assessment report of the intergovernmental panel on climate change*. Cambridge University Press, 2013. URL http://www.climatechange2013.org/images/report/WG1AR5_SummaryVolume_FINAL.pdf.
- [3] U.S. Census Bureau (USCB). Historical Estimates of World Population, 2013. URL https://www.census.gov/population/international/data/worldpop/table_history.php.
- [4] B. plc. BP Statistical Review of World Energy June 2015, 2015. URL <http://www.bp.com/en/global/corporate/energy-economics/statistical-review-of-world-energy/downloads.html>.
- [5] PBL Netherlands Environmental Assessment Agency. Total final energy consumption, 2010. URL <http://themasites.pbl.nl/tridion/en/themasites/hyde/consumptiondata/totalenergy/index-2.html>.
- [6] N. C. D. C. (NCDC). National Climatic Data Center, oct 2012. URL <https://www.ncdc.noaa.gov/cdo/f?p=517:1:0::APP:PROXYDATASETLIST:7>.
- [7] E. S. R. L. US Department of Commerce, NOAA. ESRL Global Monitoring Division - Global Greenhouse Gas Reference Network, 2014. URL http://www.esrl.noaa.gov/gmd/ccgg/trends/#mlo_data.
- [8] R. van de Krol and M. Grätzel. *Photoelectrochemical Hydrogen Production*. Springer Science+Business Media, LLC, 233 Spring Street, New York, NY 10013, USA, 2012. URL <http://dx.doi.org/10.1007/978-1-4614-1380-6>.
- [9] G. Zini and P. Tartarini. *Solar Hydrogen Energy Systems*. Springer Milan, Milano, 2012. ISBN 978-88-470-1997-3. URL <http://dx.doi.org/10.1007/978-88-470-1998-0>.
- [10] A. Fujishima and K. Honda. Electrochemical Photolysis of Water at a Semiconductor Electrode. *Nature*, 238(5358):37–38, jul 1972. ISSN 0028-0836. URL <http://dx.doi.org/10.1038/238037a0>.
- [11] A. J. Bard. Photoelectrochemistry and heterogeneous photo-catalysis at semiconductors. *Journal of Photochemistry*, 10(1):59–75, jan 1979. ISSN 00472670. URL [http://dx.doi.org/10.1016/0047-2670\(79\)80037-4](http://dx.doi.org/10.1016/0047-2670(79)80037-4).
- [12] K. Domen, S. Naito, M. Soma, T. Onishi, and K. Tamaru. Photocatalytic decomposition of water vapour on an NiO-SrTiO₃ catalyst. *J. Chem. Soc., Chem. Commun.*, 0(12):543–544, jan 1980. ISSN 0022-4936. URL <http://dx.doi.org/10.1039/C39800000543>.
- [13] S. Sato and J. White. Photodecomposition of water over Pt/TiO₂ catalysts. *Chemical Physics Letters*, 72(1):83–86, may 1980. ISSN 00092614. URL [http://dx.doi.org/10.1016/0009-2614\(80\)80246-6](http://dx.doi.org/10.1016/0009-2614(80)80246-6).
- [14] O. Khaselev. A Monolithic Photovoltaic-Photoelectrochemical Device for Hydrogen Production via Water Splitting. *Science*, 280(5362):425–427, apr 1998. ISSN 00368075. URL <http://dx.doi.org/10.1126/science.280.5362.425>.
- [15] D. Yokoyama, T. Minegishi, K. Jimbo, T. Hisatomi, G. Ma, M. Katayama, J. Kubota, H. Katagiri, and K. Domen. H₂ Evolution from Water on Modified Cu₂ ZnSnS₄ Photoelectrode under Solar Light. *Applied Physics Express*, 3(10):101202, oct 2010. ISSN 1882-0778. URL <http://dx.doi.org/10.1143/APEX.3.101202>.

References

- [16] L. Rovelli, S. D. Tilley, and K. Sivula. Optimization and stabilization of electrodeposited $\text{Cu}_2\text{ZnSnS}_4$ photocathodes for solar water reduction. *ACS applied materials & interfaces*, 5(16):8018–24, aug 2013. ISSN 1944-8252. URL <http://dx.doi.org/10.1021/am402096r>.
- [17] W. Septina, S. Ikeda, T. Harada, M. Higashi, R. Abe, and M. Matsumura. Photosplitting of Water from Wide-Gap $\text{Cu}(\text{In,Ga})\text{S}_2$ Thin Films Modified with a CdS Layer and Pt Nanoparticles for a High-Onset-Potential Photocathode. *The Journal of Physical Chemistry C*, 119(16):8576–8583, apr 2015. ISSN 1932-7447. URL <http://dx.doi.org/10.1021/acs.jpcc.5b02068>.
- [18] A. Fujishima, T. N. Rao, and D. A. Tryk. Titanium dioxide photocatalysis. *Journal of Photochemistry and Photobiology C: Photochemistry Reviews*, 1(1):1–21, jun 2000. ISSN 13895567. URL [http://dx.doi.org/10.1016/S1389-5567\(00\)00002-2](http://dx.doi.org/10.1016/S1389-5567(00)00002-2).
- [19] M. Jansen and H. Letschert. Inorganic yellow-red pigments without toxic metals. *Nature*, 404(6781):980–2, apr 2000. ISSN 1476-4687. URL <http://dx.doi.org/10.1038/35010082>.
- [20] S. G. Ebbinghaus, H.-P. Abicht, R. Dronskowski, T. Müller, A. Reller, and A. Weidenkaff. Perovskite-related oxynitrides Recent developments in synthesis, characterisation and investigations of physical properties. *Progress in Solid State Chemistry*, 37(2):173–205, 2009. URL <http://dx.doi.org/10.1016/j.progsolidstchem.2009.11.003>.
- [21] A. Kasahara, K. Nukumizu, G. Hitoki, T. Takata, J. N. Kondo, M. Hara, H. Kobayashi, and K. Domen. Photoreactions on LaTiO_2N under Visible Light Irradiation. *The Journal of Physical Chemistry A*, 106(29):6750–6753, jul 2002. ISSN 1089-5639. URL <http://dx.doi.org/10.1021/jp025961+>.
- [22] G. Hitoki, T. Takata, J. N. Kondo, M. Hara, H. Kobayashi, and K. Domen. An oxynitride, TaON, as an efficient water oxidation photocatalyst under visible light irradiation ($\lambda < 500$ nm). *Chemical Communications*, 0(16):1698–1699, jul 2002. ISSN 13597345. URL <http://dx.doi.org/10.1039/b202393h>.
- [23] Z. Chen, H. N. Dinh, and E. Miller. *Photoelectrochemical Water Splitting*. SpringerBriefs in Energy. Springer New York, New York, NY, 2013. ISBN 978-1-4614-8297-0. URL <http://dx.doi.org/10.1007/978-1-4614-8298-7>.
- [24] F. E. Osterloh. Inorganic Materials as Catalysts for Photochemical Splitting of Water. *Chemistry of Materials*, 20(1):35–54, jan 2008. ISSN 0897-4756. URL <http://dx.doi.org/10.1021/cm7024203>.
- [25] M. Carmo, D. L. Fritz, J. Mergel, and D. Stolten. A comprehensive review on PEM water electrolysis. *International Journal of Hydrogen Energy*, 38(12):4901–4934, apr 2013. ISSN 03603199. URL <http://dx.doi.org/10.1016/j.ijhydene.2013.01.151>.
- [26] T. Takata, C. Pan, and K. Domen. Recent progress in oxynitride photocatalysts for visible-light-driven water splitting. *Science and Technology of Advanced Materials*, 16(3):033506, jun 2015. ISSN 1468-6996. URL <http://dx.doi.org/10.1088/1468-6996/16/3/033506>.
- [27] K. Sivula and R. van de Krol. Semiconducting materials for photoelectrochemical energy conversion. *Nature Reviews Materials*, 1:15010, jan 2016. ISSN 2058-8437. URL <http://dx.doi.org/10.1038/natrevmats.2015.10>.
- [28] T. Hisatomi, J. Kubota, and K. Domen. Recent advances in semiconductors for photocatalytic and photoelectrochemical water splitting. *Chemical Society reviews*, 43(22):7520–7535, jan 2014. ISSN 1460-4744. URL <http://dx.doi.org/10.1039/c3cs60378d>.
- [29] K. Maeda. Z-Scheme Water Splitting Using Two Different Semiconductor Photocatalysts. *ACS Catalysis*, 3(7):1486–1503, jul 2013. ISSN 2155-5435. URL <http://dx.doi.org/10.1021/cs4002089>.

-
- [30] J. Ran, J. Zhang, J. Yu, M. Jaroniec, and S. Z. Qiao. Earth-abundant cocatalysts for semiconductor-based photocatalytic water splitting. *Chemical Society reviews*, 43(22):7787–812, nov 2014. ISSN 1460-4744. URL <http://dx.doi.org/10.1039/c3cs60425j>.
- [31] M. Tabata, K. Maeda, M. Higashi, D. Lu, T. Takata, R. Abe, and K. Domen. Modified Ta₃N₅ powder as a photocatalyst for O₂ evolution in a two-step water splitting system with an iodate/iodide shuttle redox mediator under visible light. *Langmuir : the ACS journal of surfaces and colloids*, 26(12):9161–5, jun 2010. ISSN 1520-5827. URL <http://dx.doi.org/10.1021/la100722w>.
- [32] M. Hara, J. Nunoshige, T. Takata, J. N. Kondo, and K. Domen. Unusual enhancement of H₂ evolution by Ru on TaON photocatalyst under visible light irradiation. *Chemical Communications*, 0(24):3000, dec 2003. ISSN 1359-7345. URL <http://dx.doi.org/10.1039/b309935k>.
- [33] Y. Sasaki, A. Iwase, H. Kato, and A. Kudo. The effect of co-catalyst for Z-scheme photocatalysis systems with an Fe³⁺/Fe²⁺ electron mediator on overall water splitting under visible light irradiation. *Journal of Catalysis*, 259(1):133–137, oct 2008. ISSN 00219517. URL <http://dx.doi.org/10.1016/j.jcat.2008.07.017>.
- [34] A. V. Korzhak, N. I. Ermokhina, A. L. Stroyuk, V. K. Bukhtiyarov, A. E. Raevskaya, V. I. Litvin, S. Y. Kuchmiy, V. G. Ilyin, and P. A. Manorik. Photocatalytic hydrogen evolution over mesoporous TiO₂/metal nanocomposites. *Journal of Photochemistry and Photobiology A: Chemistry*, 198(2-3):126–134, aug 2008. ISSN 10106030. URL <http://dx.doi.org/10.1016/j.jphotochem.2008.02.026>.
- [35] H. Yan, J. Yang, G. Ma, G. Wu, X. Zong, Z. Lei, J. Shi, and C. Li. Visible-light-driven hydrogen production with extremely high quantum efficiency on PtPdS/CdS photocatalyst. *Journal of Catalysis*, 266(2):165–168, sep 2009. ISSN 00219517. URL <http://dx.doi.org/10.1016/j.jcat.2009.06.024>.
- [36] K. Maeda, M. Higashi, D. Lu, R. Abe, and K. Domen. Efficient nonsacrificial water splitting through two-step photoexcitation by visible light using a modified oxynitride as a hydrogen evolution photocatalyst. *Journal of the American Chemical Society*, 132(16):5858–68, apr 2010. ISSN 1520-5126. URL <http://dx.doi.org/10.1021/ja1009025>.
- [37] K. Maeda, N. Sakamoto, T. Ikeda, H. Ohtsuka, A. Xiong, D. Lu, M. Kanehara, T. Teranishi, and K. Domen. Preparation of core-shell-structured nanoparticles (with a noble-metal or metal oxide core and a chromia shell) and their application in water splitting by means of visible light. *Chemistry (Weinheim an der Bergstrasse, Germany)*, 16(26):7750–9, jul 2010. ISSN 1521-3765. URL <http://dx.doi.org/10.1002/chem.201000616>.
- [38] J. Zhang, M. Grzelczak, Y. Hou, K. Maeda, K. Domen, X. Fu, M. Antonietti, and X. Wang. Photocatalytic oxidation of water by polymeric carbon nitride nanohybrids made of sustainable elements. *Chem. Sci.*, 3(2):443–446, jan 2012. ISSN 2041-6520. URL <http://dx.doi.org/10.1039/C1SC00644D>.
- [39] F. Zhang, A. Yamakata, K. Maeda, Y. Moriya, T. Takata, J. Kubota, K. Teshima, S. Oishi, and K. Domen. Cobalt-modified porous single-crystalline LaTiO₂N for highly efficient water oxidation under visible light. *Journal of the American Chemical Society*, 134(20):8348–51, may 2012. ISSN 1520-5126. URL <http://dx.doi.org/10.1021/ja301726c>.
- [40] D. K. Zhong, J. Sun, H. Inumaru, and D. R. Gamelin. Solar water oxidation by composite catalyst/ α -Fe₂O₃ photoanodes. *Journal of the American Chemical Society*, 131(17):6086–7, may 2009. ISSN 1520-5126. URL <http://dx.doi.org/10.1021/ja9016478>.
- [41] L. Liu, Z. Ji, W. Zou, X. Gu, Y. Deng, F. Gao, C. Tang, and L. Dong. In Situ Loading Transition Metal Oxide Clusters on TiO₂ Nanosheets As Co-catalysts for Exceptional High Photoactivity. *ACS Catalysis*, 3(9):2052–2061, sep 2013. ISSN 2155-5435. URL <http://dx.doi.org/10.1021/cs4002755>.

References

- [42] S. Onsuratoom, T. Puangpetch, and S. Chavadej. Comparative investigation of hydrogen production over Ag-, Ni²⁺, and Cu-loaded mesoporous-assembled TiO₂-ZrO₂ mixed oxide nanocrystal photocatalysts. *Chemical Engineering Journal*, 173(2):667–675, sep 2011. ISSN 13858947. URL <http://dx.doi.org/10.1016/j.cej.2011.08.016>.
- [43] R.-J. Xie and H. T. Bert Hintzen. Optical Properties of (Oxy)Nitride Materials: A Review. *Journal of the American Ceramic Society*, 96(3):665–687, mar 2013. ISSN 00027820. URL <http://dx.doi.org/10.1111/jace.12197>.
- [44] National Renewable Energy Laboratory. Reference Solar Spectral Irradiance: Air Mass 1.5, 2012.
- [45] Z. Li, W. Luo, M. Zhang, J. Feng, and Z. Zou. Photoelectrochemical cells for solar hydrogen production: current state of promising photoelectrodes, methods to improve their properties, and outlook. *Energy Environ. Sci.*, 6(2):347–370, jul 2013. ISSN 1754-5692. URL <http://dx.doi.org/10.1039/C2EE22618A>.
- [46] S. M. Sze and K. N. Kwok. Physics of Semiconductor Devices, 3rd Edition, 2006.
- [47] D. Ostermann, H. Jacobs, and B. Harbrecht. Natriumoxonitridometallate(VI) von Molybdän und Wolfram, Na₄ MO₂ N₂ (M = Mo, W). *Zeitschrift für anorganische und allgemeine Chemie*, 619(7): 1277–1282, jul 1993. ISSN 0044-2313. URL <http://dx.doi.org/10.1002/zaac.19936190721>.
- [48] M. G. Walter, E. L. Warren, J. R. McKone, S. W. Boettcher, Q. Mi, E. A. Santori, and N. S. Lewis. Solar water splitting cells. *Chemical reviews*, 110(11):6446–73, nov 2010. ISSN 1520-6890. URL <http://dx.doi.org/10.1021/cr1002326>.
- [49] A. J. Nozik. Photoelectrochemistry: Applications to Solar Energy Conversion. *Annual Review of Physical Chemistry*, 29(1):189–222, oct 1978. ISSN 0066-426X. URL <http://dx.doi.org/10.1146/annurev.pc.29.100178.001201>.
- [50] M. Grätzel. Photoelectrochemical cells. *Nature*, 414(6861):338–344, 2001. URL <http://dx.doi.org/10.1038/35104607>.
- [51] K. Hanjalic, R. Van de Krol, and A. Lekić, editors. *Sustainable Energy Technologies*. Springer Netherlands, Dordrecht, 2008. ISBN 978-1-4020-6723-5. URL <http://dx.doi.org/10.1007/978-1-4020-6724-2>.
- [52] S.-M. Park and M. E. Barber. Thermodynamic stabilities of semiconductor electrodes. *Journal of Electroanalytical Chemistry and Interfacial Electrochemistry*, 99(1):67–75, may 1979. ISSN 00220728. URL [http://dx.doi.org/10.1016/S0022-0728\(79\)80411-8](http://dx.doi.org/10.1016/S0022-0728(79)80411-8).
- [53] M. Liao, J. Feng, W. Luo, Z. Wang, J. Zhang, Z. Li, T. Yu, and Z. Zou. Co₃ O₄ Nanoparticles as Robust Water Oxidation Catalysts Towards Remarkably Enhanced Photostability of a Ta₃ N₅ Photoanode. *Advanced Functional Materials*, 22(14):3066–3074, jul 2012. ISSN 1616301X. URL <http://dx.doi.org/10.1002/adfm.201102966>.
- [54] A. Paracchino, V. Laporte, K. Sivula, M. Grätzel, and E. Thimsen. Highly active oxide photocathode for photoelectrochemical water reduction. *Nature materials*, 10(6):456–61, jun 2011. ISSN 1476-1122. URL <http://dx.doi.org/10.1038/nmat3017>.
- [55] J. R. Bolton, S. J. Strickler, and J. S. Connolly. Limiting and realizable efficiencies of solar photolysis of water. *Nature*, 316(6028):495–500, aug 1985. ISSN 0028-0836. URL <http://dx.doi.org/10.1038/316495a0>.
- [56] A. Murphy, P. Barnes, L. Randeniya, I. Plumb, I. Grey, M. Horne, and J. Glasscock. Efficiency of solar water splitting using semiconductor electrodes. *International Journal of Hydrogen Energy*, 31(14): 1999–2017, nov 2006. ISSN 03603199. URL <http://dx.doi.org/10.1016/j.ijhydene.2006.01.014>.

-
- [57] R. Abe, T. Takata, H. Sugihara, and K. Domen. Photocatalytic overall water splitting under visible light by TaON and WO₃ with an IO₃[−]/I[−] shuttle redox mediator. *Chemical communications (Cambridge, England)*, 0(30):3829–31, aug 2005. ISSN 1359-7345. URL <http://dx.doi.org/10.1039/b505646b>.
- [58] P. J. Boddy. Oxygen Evolution on Semiconducting TiO₂. *Journal of The Electrochemical Society*, 115(2):199, feb 1968. ISSN 00134651. URL <http://dx.doi.org/10.1149/1.2411080>.
- [59] A. Kay, I. Cesar, and M. Grätzel. New benchmark for water photooxidation by nanostructured α-Fe₂ O₃ films. *Journal of the American Chemical Society*, 128(49):15714–21, dec 2006. ISSN 0002-7863. URL <http://dx.doi.org/10.1021/ja0643801>.
- [60] K. J. McDonald and K.-S. Choi. Synthesis and Photoelectrochemical Properties of Fe₂ O₃/ZnFe₂ O₄ Composite Photoanodes for Use in Solar Water Oxidation. *Chemistry of Materials*, 23(21):4863–4869, nov 2011. ISSN 0897-4756. URL <http://dx.doi.org/10.1021/cm202399g>.
- [61] K. Sivula, F. Le Formal, and M. Grätzel. Solar water splitting: progress using hematite (α-Fe₂ O₃) photoelectrodes. *ChemSusChem*, 4(4):432–49, apr 2011. ISSN 1864-564X. URL <http://dx.doi.org/10.1002/cssc.201000416>.
- [62] M. Li, L. Zhao, and L. Guo. Preparation and photoelectrochemical study of BiVO₄ thin films deposited by ultrasonic spray pyrolysis. *International Journal of Hydrogen Energy*, 35(13):7127–7133, jul 2010. ISSN 03603199. URL <http://dx.doi.org/10.1016/j.ijhydene.2010.02.026>.
- [63] Y. Liang, T. Tsubota, L. P. A. Mooij, and R. van de Krol. Highly Improved Quantum Efficiencies for Thin Film BiVO₄ Photoanodes. *The Journal of Physical Chemistry C*, 115(35):17594–17598, sep 2011. ISSN 1932-7447. URL <http://dx.doi.org/10.1021/jp203004v>.
- [64] X. Liu, F. Wang, and Q. Wang. Nanostructure-based WO₃ photoanodes for photoelectrochemical water splitting. *Physical chemistry chemical physics : PCCP*, 14(22):7894–911, jun 2012. ISSN 1463-9084. URL <http://dx.doi.org/10.1039/c2cp40976c>.
- [65] A. Kudo and Y. Miseki. Heterogeneous photocatalyst materials for water splitting. *Chemical Society reviews*, 38(1):253–78, jan 2009. ISSN 0306-0012. URL <http://dx.doi.org/10.1039/b800489g>.
- [66] K. Maeda. Photocatalytic water splitting using semiconductor particles: History and recent developments. *Journal of Photochemistry and Photobiology C: Photochemistry Reviews*, 12(4):237–268, dec 2011. ISSN 13895567. URL <http://dx.doi.org/10.1016/j.jphotochemrev.2011.07.001>.
- [67] S. Cho, J. -W. Jang, K.-H. Lee, and J. S. Lee. Research Update: Strategies for efficient photoelectrochemical water splitting using metal oxide photoanodes. *APL Materials*, 2(1):010703, jan 2014. ISSN 2166-532X. URL <http://dx.doi.org/10.1063/1.4861798>.
- [68] I. E. Castelli, T. Olsen, S. Datta, D. D. Landis, S. Dahl, K. S. Thygesen, and K. W. Jacobsen. Computational screening of perovskite metal oxides for optimal solar light capture. *Energy & Environmental Science*, 5(2):5814, jan 2012. ISSN 1754-5692. URL <http://dx.doi.org/10.1039/c1ee02717d>.
- [69] I. E. Castelli, D. D. Landis, K. S. Thygesen, S. Dahl, I. Chorkendorff, T. F. Jaramillo, and K. W. Jacobsen. New cubic perovskites for one- and two-photon water splitting using the computational materials repository. *Energy & Environmental Science*, 5(10):9034, sep 2012. ISSN 1754-5692. URL <http://dx.doi.org/10.1039/c2ee22341d>.
- [70] F. Wang, C. DiValentin, and G. Pacchioni. Rational Band Gap Engineering of WO₃ Photocatalyst for Visible light Water Splitting. *ChemCatChem*, 4(4):476–478, apr 2012. ISSN 18673880. URL <http://dx.doi.org/10.1002/cctc.201100446>.

References

- [71] W. Li, E. Ionescu, R. Riedel, and A. Gurlo. Can we predict the formability of perovskite oxynitrides from tolerance and octahedral factors? *Journal of Materials Chemistry A*, 1(39):12239, sep 2013. ISSN 2050-7488. URL <http://dx.doi.org/10.1039/c3ta10216e>.
- [72] J. Yao, X. Li, Y. Li, and S. Le. Density Functional Theory Investigations on the Structure and Electronic Properties of Normal Spinel ZnFe_2O_4 . *Integrated Ferroelectrics*, 145(1):17–23, jan 2013. ISSN 1058-4587. URL <http://dx.doi.org/10.1080/10584587.2013.788310>.
- [73] A. K. Singh, K. Mathew, H. L. Zhuang, and R. G. Hennig. Computational Screening of 2D Materials for Photocatalysis. *The Journal of Physical Chemistry Letters*, 6(6):1087–1098, mar 2015. ISSN 1948-7185. URL <http://dx.doi.org/10.1021/jz502646d>.
- [74] I. E. Castelli, F. Hüser, M. Pandey, H. Li, K. S. Thygesen, B. Seger, A. Jain, K. A. Persson, G. Ceder, and K. W. Jacobsen. New Light-Harvesting Materials Using Accurate and Efficient Bandgap Calculations. *Advanced Energy Materials*, 5(2):14009151–14009157, jan 2015. ISSN 16146832. URL <http://dx.doi.org/10.1002/aenm.201400915>.
- [75] Y. Sakata, Y. Matsuda, T. Nakagawa, R. Yasunaga, H. Imamura, and K. Teramura. Remarkable improvement of the photocatalytic activity of Ga_2O_3 towards the overall splitting of H_2O . *ChemSusChem*, 4(2):181–4, feb 2011. ISSN 1864-564X. URL <http://dx.doi.org/10.1002/cssc.201000258>.
- [76] J. G. Mavroides, J. A. Kafalas, and D. F. Kolesar. Photoelectrolysis of water in cells with SrTiO_3 anodes. *Applied Physics Letters*, 28(5):241, aug 1976. ISSN 00036951. URL <http://dx.doi.org/10.1063/1.88723>.
- [77] A. B. Ellis, S. W. Kaiser, and M. S. Wrighton. Semiconducting potassium tantalate electrodes. Photoassistance agents for the efficient electrolysis of water. *The Journal of Physical Chemistry*, 80(12):1325–1328, jun 1976. ISSN 0022-3654. URL <http://dx.doi.org/10.1021/j100553a014>.
- [78] H. Kato, K. Asakura, and A. Kudo. Highly efficient water splitting into H_2 and O_2 over lanthanum-doped NaTaO_3 photocatalysts with high crystallinity and surface nanostructure. *Journal of the American Chemical Society*, 125(10):3082–9, mar 2003. ISSN 0002-7863. URL <http://dx.doi.org/10.1021/ja027751g>.
- [79] M. Higashi, R. Abe, A. Ishikawa, T. Takata, B. Ohtani, and K. Domen. Z-scheme Overall Water Splitting on Modified-TaON Photocatalysts under Visible Light ($\lambda < 500\text{ nm}$). *Chemistry Letters*, 37(2):138–139, dec 2008. ISSN 1348-0715. URL <http://dx.doi.org/10.1246/cl.2008.138>.
- [80] P. S. Bassi, Gurudayal, L. H. Wong, and J. Barber. Iron based photoanodes for solar fuel production. *Physical chemistry chemical physics : PCCP*, 16(24):11834–42, jun 2014. ISSN 1463-9084. URL <http://dx.doi.org/10.1039/c3cp55174a>.
- [81] Y. Guo, Y. Fu, Y. Liu, and S. Shen. Photoelectrochemical activity of ZnFe_2O_4 modified $\alpha\text{-Fe}_2\text{O}_3$ nanorod array films. *RSC Advances*, 4(70):36967, aug 2014. ISSN 2046-2069. URL <http://dx.doi.org/10.1039/C4RA05289G>.
- [82] A. Walsh, Y. Yan, M. N. Huda, M. M. Al-Jassim, and S.-H. Wei. Band Edge Electronic Structure of BiVO_4 : Elucidating the Role of the Bi s and V d Orbitals. *Chemistry of Materials*, 21(3):547–551, feb 2009. ISSN 0897-4756. URL <http://dx.doi.org/10.1021/cm802894z>.
- [83] A. Kudo, K. Ueda, H. Kato, and I. Mikami. Photocatalytic O_2 evolution under visible light irradiation on BiVO_4 in aqueous AgNO_3 solution. *Catalysis Letters*, 53(3-4):229–230, 1998. ISSN 1572-879X. URL <http://dx.doi.org/10.1023/A:1019034728816>.
- [84] K. Sayama, A. Nomura, T. Arai, T. Sugita, R. Abe, M. Yanagida, T. Oi, Y. Iwasaki, Y. Abe, and H. Sugihara. Photoelectrochemical decomposition of water into H_2 and O_2 on porous BiVO_4 thin-film electrodes under visible light and significant effect of Ag ion treatment. *The journal of physical chemistry. B*, 110(23):11352–60, jun 2006. ISSN 1520-6106. URL <http://dx.doi.org/10.1021/jp057539+>.

-
- [85] Y. Pihosh, I. Turkevych, K. Mawatari, J. Uemura, Y. Kazoe, S. Kosar, K. Makita, T. Sugaya, T. Matsui, D. Fujita, M. Tosa, M. Kondo, and T. Kitamori. Photocatalytic generation of hydrogen by core-shell $\text{WO}_3/\text{BiVO}_4$ nanorods with ultimate water splitting efficiency. *Scientific reports*, 5:11141, jan 2015. ISSN 2045-2322. URL <http://dx.doi.org/10.1038/srep11141>.
- [86] D. Scaife. Oxide semiconductors in photoelectrochemical conversion of solar energy. *Solar Energy*, 25(1): 41–54, jan 1980. ISSN 0038092X. URL [http://dx.doi.org/10.1016/0038-092X\(80\)90405-3](http://dx.doi.org/10.1016/0038-092X(80)90405-3).
- [87] X. Fan, J. Fan, X. Hu, E. Liu, L. Kang, C. Tang, Y. Ma, H. Wu, and Y. Li. Preparation and characterization of Ag deposited and Fe doped TiO_2 nanotube arrays for photocatalytic hydrogen production by water splitting. *Ceramics International*, 40(10):15907–15917, dec 2014. ISSN 02728842. URL <http://dx.doi.org/10.1016/j.ceramint.2014.07.119>.
- [88] K. Maeda and K. Domen. Oxynitride materials for solar water splitting. *MRS Bulletin*, 36(01):25–31, 2011. ISSN 08837694. URL <http://dx.doi.org/10.1557/mrs.2010.4>.
- [89] K. Maeda and K. Domen. Solid Solution of GaN and ZnO as a Stable Photocatalyst for Overall Water Splitting under Visible Light. *Chemistry of Materials*, 22(3):612–623, feb 2010. ISSN 0897-4756. URL <http://dx.doi.org/10.1021/cm901917a>.
- [90] A. Kasahara, K. Nukumizu, T. Takata, J. N. Kondo, M. Hara, H. Kobayashi, and K. Domen. LaTiO_2N as a Visible-Light (600 nm)-Driven Photocatalyst (2). *The Journal of Physical Chemistry B*, 107(3): 791–797, jan 2003. ISSN 1520-6106. URL <http://dx.doi.org/10.1021/jp026767q>.
- [91] K. Maeda, D. Lu, and K. Domen. Direct water splitting into hydrogen and oxygen under visible light by using modified TaON photocatalysts with d(0) electronic configuration. *Chemistry (Weinheim an der Bergstrasse, Germany)*, 19(16):4986–91, apr 2013. ISSN 1521-3765. URL <http://dx.doi.org/10.1002/chem.201300158>.
- [92] K. Maeda, K. Teramura, D. Lu, T. Takata, N. Saito, Y. Inoue, and K. Domen. Photocatalyst releasing hydrogen from water. *Nature*, 440(7082):295, mar 2006. ISSN 1476-4687. URL <http://dx.doi.org/10.1038/440295a>.
- [93] K. Maeda and K. Domen. New Non-Oxide Photocatalysts Designed for Overall Water Splitting under Visible Light. *Journal of Physical Chemistry C*, 111(22):7851–7861, jun 2007. ISSN 1932-7447. URL <http://dx.doi.org/10.1021/jp070911w>.
- [94] O. Diwald, T. L. Thompson, T. Zubkov, S. D. Walck, and J. T. Yates. Photochemical Activity of Nitrogen-Doped Rutile TiO_2 (110) in Visible Light. *The Journal of Physical Chemistry B*, 108(19):6004–6008, may 2004. ISSN 1520-6106. URL <http://dx.doi.org/10.1021/jp031267y>.
- [95] R. Nakamura, T. Tanaka, and Y. Nakato. Mechanism for Visible Light Responses in Anodic Photocurrents at N-Doped TiO_2 Film Electrodes. *The Journal of Physical Chemistry B*, 108(30):10617–10620, jul 2004. ISSN 1520-6106. URL <http://dx.doi.org/10.1021/jp048112q>.
- [96] R. Asahi, T. Morikawa, T. Ohwaki, K. Aoki, and Y. Taga. Visible-light photocatalysis in nitrogen-doped titanium oxides. *Science (New York, N.Y.)*, 293(5528):269–71, jul 2001. ISSN 0036-8075. URL <http://dx.doi.org/10.1126/science.1061051>.
- [97] G. R. Torres, T. Lindgren, J. Lu, C.-G. Granqvist, and S.-E. Lindquist. Photoelectrochemical Study of Nitrogen-Doped Titanium Dioxide for Water Oxidation. *The Journal of Physical Chemistry B*, 108(19): 5995–6003, may 2004. ISSN 1520-6106. URL <http://dx.doi.org/10.1021/jp037477s>.

References

- [98] X. Chen and S. S. Mao. Titanium dioxide nanomaterials: synthesis, properties, modifications, and applications. *Chemical reviews*, 107(7):2891–959, jul 2007. ISSN 0009-2665. URL <http://dx.doi.org/10.1021/cr0500535>.
- [99] J. Cao, Y. Zhang, H. Tong, P. Li, T. Kako, and J. Ye. Selective local nitrogen doping in a TiO₂ electrode for enhancing photoelectrochemical water splitting. *Chemical communications (Cambridge, England)*, 48(69):8649–51, sep 2012. ISSN 1364-548X. URL <http://dx.doi.org/10.1039/c2cc33662f>.
- [100] E. Nurlaela, S. Ould-Chikh, I. Llorens, J.-L. Hazemann, and K. Takanabe. Establishing Efficient Cobalt-Based Catalytic Sites for Oxygen Evolution on a Ta₃ N₅ Photocatalyst. *Chemistry of Materials*, 27(16):5685–5694, aug 2015. ISSN 0897-4756. URL <http://dx.doi.org/10.1021/acs.chemmater.5b02139>.
- [101] A. Dabirian and R. van de Krol. High-Temperature Ammonolysis of Thin Film Ta₂ O₅ Photoanodes: Evolution of Structural, Optical, and Photoelectrochemical Properties. *Chemistry of Materials*, 27(3):708–715, feb 2015. ISSN 0897-4756. URL <http://dx.doi.org/10.1021/cm503215p>.
- [102] P. Zhang, J. Zhang, and J. Gong. Tantalum-based semiconductors for solar water splitting. *Chemical Society reviews*, 43(13):4395–422, jul 2014. ISSN 1460-4744. URL <http://dx.doi.org/10.1039/c3cs60438a>.
- [103] A. Suzuki, Y. Hirose, D. Oka, S. Nakao, T. Fukumura, S. Ishii, K. Sasa, H. Matsuzaki, and T. Hasegawa. High-Mobility Electron Conduction in Oxynitride: Anatase TaON. *Chemistry of Materials*, 26(2):976–981, jan 2014. ISSN 0897-4756. URL <http://dx.doi.org/10.1021/cm402720d>.
- [104] M. Higashi, K. Domen, and R. Abe. Highly stable water splitting on oxynitride TaON photoanode system under visible light irradiation. *Journal of the American Chemical Society*, 134(16):6968–71, apr 2012. ISSN 1520-5126. URL <http://dx.doi.org/10.1021/ja302059g>.
- [105] G. Hitoki, A. Ishikawa, T. Takata, J. N. Kondo, M. Hara, and K. Domen. Ta₃ N₅ as a Novel Visible Light-Driven Photocatalyst ($\lambda < 600$ nm). *Chemistry Letters*, 0(7):736–736, jul 2002. ISSN 03667022. URL <http://dx.doi.org/10.1246/cl.2002.736>.
- [106] M. Li, W. Luo, D. Cao, X. Zhao, Z. Li, T. Yu, and Z. Zou. A co-catalyst-loaded Ta₃ N₅ photoanode with a high solar photocurrent for water splitting upon facile removal of the surface layer. *Angewandte Chemie (International ed. in English)*, 52(42):11016–20, oct 2013. ISSN 1521-3773. URL <http://dx.doi.org/10.1002/anie.201305350>.
- [107] Y. Li, L. Zhang, A. Torres-Pardo, J. M. González-Calbet, Y. Ma, P. Oleynikov, O. Terasaki, S. Asahina, M. Shima, D. Cha, L. Zhao, K. Takanabe, J. Kubota, and K. Domen. Cobalt phosphate-modified barium-doped tantalum nitride nanorod photoanode with 1.5% solar energy conversion efficiency. *Nature communications*, 4:2566, jan 2013. ISSN 2041-1723. URL <http://dx.doi.org/10.1038/ncomms3566>.
- [108] B. Siritanaratkul, K. Maeda, T. Hisatomi, and K. Domen. Synthesis and photocatalytic activity of perovskite niobium oxynitrides with wide visible-light absorption bands. *ChemSusChem*, 4(1):74–8, jan 2011. ISSN 1864-564X. URL <http://dx.doi.org/10.1002/cssc.201000207>.
- [109] K. Maeda, M. Higashi, B. Siritanaratkul, R. Abe, and K. Domen. SrNbO₂ N as a water-splitting photoanode with a wide visible-light absorption band. *Journal of the American Chemical Society*, 133(32):12334–7, aug 2011. ISSN 1520-5126. URL <http://dx.doi.org/10.1021/ja203391w>.
- [110] M. Higashi, R. Abe, K. Teramura, T. Takata, B. Ohtani, and K. Domen. Two step water splitting into H₂ and O₂ under visible light by ATaO₂ N (A=Ca, Sr, Ba) and WO₃ with IO³⁻/I⁻ shuttle redox mediator. *Chemical Physics Letters*, 452(1-3):120–123, 2008. ISSN 00092614. URL <http://dx.doi.org/10.1016/j.cplett.2007.12.021>.

-
- [111] J. Xu, C. Pan, T. Takata, and K. Domen. Photocatalytic overall water splitting on the perovskite-type transition metal oxynitride CaTaO_2N under visible light irradiation. *Chemical communications (Cambridge, England)*, 51(33):7191–4, apr 2015. ISSN 1364-548X. URL <http://dx.doi.org/10.1039/c5cc01728a>.
- [112] C. Zhen, R. Chen, L. Wang, G. Liu, and H. -M. Cheng. Tantalum (oxy)nitride based photoanodes for solar-driven water oxidation. *J. Mater. Chem. A*, 4(8):2783–2800, feb 2016. ISSN 2050-7488. URL <http://dx.doi.org/10.1039/C5TA07057K>.
- [113] M. Higashi, Y. Yamanaka, O. Tomita, and R. Abe. Fabrication of cation-doped BaTaO_2N photoanodes for efficient photoelectrochemical water splitting under visible light irradiation. *APL Materials*, 3(10):104418, oct 2015. ISSN 2166-532X. URL <http://dx.doi.org/10.1063/1.4931487>.
- [114] K. Ueda, T. Minegishi, J. Clune, M. Nakabayashi, T. Hisatomi, H. Nishiyama, M. Katayama, N. Shibata, J. Kubota, T. Yamada, and K. Domen. Photoelectrochemical oxidation of water using BaTaO_2N photoanodes prepared by particle transfer method. *Journal of the American Chemical Society*, 137(6):2227–30, feb 2015. ISSN 1520-5126. URL <http://dx.doi.org/10.1021/ja5131879>.
- [115] N. Nishimura, B. Raphael, K. Maeda, L. Le Gendre, R. Abe, J. Kubota, and K. Domen. Effect of TiCl_4 treatment on the photoelectrochemical properties of LaTiO_2N electrodes for water splitting under visible light. *Thin Solid Films*, 518(20):5855–5859, aug 2010. ISSN 00406090. URL <http://dx.doi.org/10.1016/j.tsf.2010.05.094>.
- [116] T. Minegishi, N. Nishimura, J. Kubota, and K. Domen. Photoelectrochemical properties of LaTiO_2N electrodes prepared by particle transfer for sunlight-driven water splitting. *Chemical Science*, 4(3):1120, feb 2013. ISSN 2041-6520. URL <http://dx.doi.org/10.1039/c2sc21845c>.
- [117] J. Feng, W. Luo, T. Fang, H. Lv, Z. Wang, J. Gao, W. Liu, T. Yu, Z. Li, and Z. Zou. Highly Photo-Responsive LaTiO_2N Photoanodes by Improvement of Charge Carrier Transport among Film Particles. *Advanced Functional Materials*, 24(23):3535–3542, jun 2014. ISSN 1616301X. URL <http://dx.doi.org/10.1002/adfm.201304046>.
- [118] M. Liu, W. You, Z. Lei, T. Takata, K. Domen, and C. Li. Photocatalytic Water Splitting to Hydrogen over a Visible Light-Driven LaTaON_2 Catalyst. *Chinese Journal of Catalysis*, 27(7):556–558, jul 2006. ISSN 18722067. URL [http://dx.doi.org/10.1016/S1872-2067\(06\)60032-6](http://dx.doi.org/10.1016/S1872-2067(06)60032-6).
- [119] L. Zhang, Y. Song, J. Feng, T. Fang, Y. Zhong, Z. Li, and Z. Zou. Photoelectrochemical water oxidation of LaTaON_2 under visible-light irradiation. *International Journal of Hydrogen Energy*, 39(15):7697–7704, may 2014. ISSN 03603199. URL <http://dx.doi.org/10.1016/j.ijhydene.2014.02.177>.
- [120] C. Izawa, T. Kobayashi, K. Kishida, and T. Watanabe. Ammonothermal Synthesis and Photocatalytic Activity of Lower Valence Cation-Doped LaNbON_2 . *Advances in Materials Science and Engineering*, 2014:5, 2014. URL <http://dx.doi.org/10.1155/2014/465720>.
- [121] S. Landsmann, A. E. Maegli, M. Trottmann, C. Battaglia, A. Weidenkaff, and S. Pokrant. Design Guidelines for High-Performance Particle-Based Photoanodes for Water Splitting: Lanthanum Titanium Oxynitride as a Model. *ChemSusChem*, sep 2015. ISSN 1864-564X. URL <http://dx.doi.org/10.1002/cssc.201500830>.
- [122] A. E. Maegli, S. Pokrant, T. Hisatomi, M. Trottmann, K. Domen, and A. Weidenkaff. Enhancement of Photocatalytic Water Oxidation by the Morphological Control of LaTiO_2N and Cobalt Oxide Catalysts. *The Journal of Physical Chemistry C*, 118(30):16344–16351, jul 2014. ISSN 1932-7447. URL <http://dx.doi.org/10.1021/jp4084162>.
- [123] Quandl. Quandl: Iridium, 2016.

References

- [124] InvestmentMine. Iridium Prices and Iridium Price Charts, 2016.
- [125] The London Metal Exchange. London Metal Exchange: Cobalt, 2016.
- [126] InvestmentMine. Cobalt Prices and Cobalt Price Charts, 2016.
- [127] A. E. Maegli, T. Hisatomi, E. H. Otal, S. Yoon, S. Pokrant, M. Grätzel, and A. Weidenkaff. Structural and photocatalytic properties of perovskite-type $(\text{La,Ca})\text{Ti}(\text{O,N})_3$ prepared from A-site deficient precursors. *Journal of Materials Chemistry*, 22(34):17906–17913, aug 2012. ISSN 0959-9428. URL <http://dx.doi.org/10.1039/c2jm32718j>.
- [128] Y. Masuda, R. Mashima, M. Yamada, K. Ikeuchi, K. -i. Murai, G. I. N. Waterhouse, J. B. Metson, and T. Moriga. Relationship between anion and cation nonstoichiometries and valence state of titanium in perovskite-type oxynitrides LaTiO_2N . *Journal of the Ceramic Society of Japan*, 117(1361):76–81, jan 2009. ISSN 1882-0743. URL <http://dx.doi.org/10.2109/jcersj2.117.76>.
- [129] R. Abe, M. Higashi, and K. Domen. Facile fabrication of an efficient oxynitride TaON photoanode for overall water splitting into H_2 and O_2 under visible light irradiation. *Journal of the American Chemical Society*, 132(34):11828–9, sep 2010. ISSN 1520-5126. URL <http://dx.doi.org/10.1021/ja1016552>.
- [130] M. Higashi, K. Domen, and R. Abe. Fabrication of efficient TaON and Ta_3N_5 photoanodes for water splitting under visible light irradiation. *Energy & Environmental Science*, 4(10):4138, sep 2011. ISSN 1754-5692. URL <http://dx.doi.org/10.1039/c1ee01878g>.
- [131] C. Pan, T. Takata, M. Nakabayashi, T. Matsumoto, N. Shibata, Y. Ikuhara, and K. Domen. A complex perovskite-type oxynitride: the first photocatalyst for water splitting operable at up to 600nm. *Angewandte Chemie (International ed. in English)*, 54(10):2955–9, mar 2015. ISSN 1521-3773. URL <http://dx.doi.org/10.1002/anie.201410961>.
- [132] M. Higashi, K. Domen, and R. Abe. Fabrication of an efficient BaTaO_2N photoanode harvesting a wide range of visible light for water splitting. *Journal of the American Chemical Society*, 135(28):10238–41, jul 2013. ISSN 1520-5126. URL <http://dx.doi.org/10.1021/ja404030x>.
- [133] K. Maeda, D. Lu, and K. Domen. Solar-Driven Z-scheme Water Splitting Using Modified BaZrO_3 - BaTaO_2N Solid Solutions as Photocatalysts. *ACS Catalysis*, 3(5):1026–1033, may 2013. ISSN 2155-5435. URL <http://dx.doi.org/10.1021/cs400156m>.
- [134] Y. Moriya, T. Takata, and K. Domen. Recent progress in the development of (oxy)nitride photocatalysts for water splitting under visible-light irradiation. *Coordination Chemistry Reviews*, null(null), feb 2013. ISSN 00108545. URL <http://dx.doi.org/10.1016/j.ccr.2013.01.021>.
- [135] K. Maeda, K. Teramura, T. Takata, M. Hara, N. Saito, K. Toda, Y. Inoue, H. Kobayashi, and K. Domen. Overall water splitting on $(\text{Ga}_{1-x}\text{Zn}_x)(\text{N}_{1-x}\text{O}_x)$ solid solution photocatalyst: relationship between physical properties and photocatalytic activity. *The journal of physical chemistry. B*, 109(43):20504–10, nov 2005. ISSN 1520-6106. URL <http://dx.doi.org/10.1021/jp053499y>.
- [136] T. Hirai, K. Maeda, M. Yoshida, J. Kubota, S. Ikeda, M. Matsumura, and K. Domen. Origin of Visible Light Absorption in GaN-Rich $(\text{Ga}_{1-x}\text{Zn}_x)(\text{N}_{1-x}\text{O}_x)$ Photocatalysts. *Journal of Physical Chemistry C*, 111(51):18853–18855, dec 2007. ISSN 1932-7447. URL <http://dx.doi.org/10.1021/jp709811k>.
- [137] L. Jensen, J. Muckerman, and M. Newton. First-Principles Studies of the Structural and Electronic Properties of the $(\text{Ga}_{1-x}\text{Zn}_x)(\text{N}_{1-x}\text{O}_x)$ Solid Solution Photocatalyst. *Journal of Physical Chemistry C*, 112(9):3439–3446, mar 2008. ISSN 1932-7447. URL <http://dx.doi.org/10.1021/jp073554y>.

-
- [138] E. J. McDermott, E. Z. Kurmaev, T. D. Boyko, L. D. Finkelstein, R. J. Green, K. Maeda, K. Domen, and A. Moewes. Structural and Band Gap Investigation of GaN:ZnO Heterojunction Solid Solution Photocatalyst Probed by Soft X-ray Spectroscopy. *The Journal of Physical Chemistry C*, 116(14):7694–7700, apr 2012. ISSN 1932-7447. URL <http://dx.doi.org/10.1021/jp301231p>.
- [139] W. -Q. Han, Z. Liu, and H.-G. Yu. Synthesis and optical properties of GaN/ZnO solid solution nanocrystals. *Applied Physics Letters*, 96(18):183112, may 2010. ISSN 00036951. URL <http://dx.doi.org/10.1063/1.3428393>.
- [140] K. Lee, B. M. Tienes, M. B. Wilker, K. J. Schnitzenbaumer, and G. Dukovic. $(\text{Ga}_{1-x}\text{Zn}_x)(\text{N}_{1-x}\text{O}_x)$ nanocrystals: visible absorbers with tunable composition and absorption spectra. *Nano letters*, 12(6):3268–72, jun 2012. ISSN 1530-6992. URL <http://dx.doi.org/10.1021/nl301338z>.
- [141] R. B. Singh, H. Matsuzaki, Y. Suzuki, K. Seki, T. Minegishi, T. Hisatomi, K. Domen, and A. Furube. Trapped state sensitive kinetics in LaTiO₂ N solid photocatalyst with and without cocatalyst loading. *Journal of the American Chemical Society*, 136(49):17324–31, dec 2014. ISSN 1520-5126. URL <http://dx.doi.org/10.1021/ja5102823>.
- [142] D. Yamasita. Recent progress of visible-light-driven heterogeneous photocatalysts for overall water splitting. *Solid State Ionics*, 172(1-4):591–595, aug 2004. ISSN 01672738. URL <http://dx.doi.org/10.1016/j.ssi.2004.04.033>.
- [143] I. K. Konstantinou and T. A. Albanis. TiO₂-assisted photocatalytic degradation of azo dyes in aqueous solution: kinetic and mechanistic investigations. *Applied Catalysis B: Environmental*, 49(1):1–14, apr 2004. ISSN 09263373. URL <http://dx.doi.org/10.1016/j.apcatb.2003.11.010>.
- [144] B. Barrocas, O. Monteiro, M. M. Jorge, and S. Sérgio. Photocatalytic activity and reusability study of nanocrystalline TiO₂ films prepared by sputtering technique. *Applied Surface Science*, 264:111–116, jan 2013. ISSN 01694332. URL <http://dx.doi.org/10.1016/j.apsusc.2012.09.136>.
- [145] F. Oehler and S. G. Ebbinghaus. Photocatalytic properties of CoO_x-loaded nano-crystalline perovskite oxynitrides ABO₂N (A=Ca, Sr, Ba, La; B=Nb, Ta). *Solid State Sciences*, sep 2015. ISSN 12932558. URL <http://dx.doi.org/10.1016/j.solidstatesciences.2015.09.003>.
- [146] S. Li, B. Alotaibi, W. Huang, Z. Mi, N. Serpone, R. Nechache, and F. Rosei. Epitaxial Bi₂FeCrO₆ Multiferroic Thin Film as a New Visible Light Absorbing Photocathode Material. *Small*, 11(32):4018–4026, aug 2015. ISSN 16136810. URL <http://dx.doi.org/10.1002/sml.201403206>.
- [147] W. Ji, K. Yao, Y.-F. Lim, Y. C. Liang, and A. Suwardi. Epitaxial ferroelectric BiFeO₃ thin films for unassisted photocatalytic water splitting. *Applied Physics Letters*, 103(6):062901, aug 2013. ISSN 00036951. URL <http://dx.doi.org/10.1063/1.4817907>.
- [148] P. A. Morris Hotsenpiller, J. D. Bolt, W. E. Farneth, J. B. Lowekamp, and G. S. Rohrer. Orientation Dependence of Photochemical Reactions on TiO₂ Surfaces. *The Journal of Physical Chemistry B*, 102(17):3216–3226, apr 1998. ISSN 1520-6106. URL <http://dx.doi.org/10.1021/jp980104k>.
- [149] J. B. Lowekamp, G. S. Rohrer, P. A. Morris Hotsenpiller, J. D. Bolt, and W. E. Farneth. Anisotropic Photochemical Reactivity of Bulk TiO₂ Crystals. *The Journal of Physical Chemistry B*, 102(38):7323–7327, sep 1998. ISSN 1520-6106. URL <http://dx.doi.org/10.1021/jp982721e>.
- [150] W. E. Farneth, R. S. McLean, J. D. Bolt, E. Dokou, and M. A. Barteau. Tapping Mode Atomic Force Microscopy Studies of the Photoreduction of Ag⁺ on Individual Submicrometer TiO₂ Particles. *Langmuir*, 15(25):8569–8573, dec 1999. ISSN 0743-7463. URL <http://dx.doi.org/10.1021/la9908844>.

References

- [151] T. Ohno, K. Sarukawa, and M. Matsumura. Crystal faces of rutile and anatase TiO_2 particles and their roles in photocatalytic reactions. *New Journal of Chemistry*, 26(9):1167–1170, aug 2002. ISSN 11440546. URL <http://dx.doi.org/10.1039/b202140d>.
- [152] A. Tsujiko, T. Kisumi, Y. Magari, K. Murakoshi, and Y. Nakato. Selective Formation of Nanoholes with (100)-Face Walls by Photoetching of n - TiO_2 (Rutile) Electrodes, Accompanied by Increases in Water-Oxidation Photocurrent. *The Journal of Physical Chemistry B*, 104(20):4873–4879, may 2000. ISSN 1520-6106. URL <http://dx.doi.org/10.1021/jp993285e>.
- [153] C. Leroy, R. Sanjines, K. Sivula, M. Cornuz, N. Xanthopoulos, V. Laporte, and M. Gratzel. $\text{TaO}_x \text{N}_y$ Sputtered Photoanodes For Solar Water Splitting. *Energy Procedia*, 22:119–126, 2012. ISSN 18766102. URL <http://dx.doi.org/10.1016/j.egypro.2012.05.223>.
- [154] H. Fakhouri, J. Pulpytel, W. Smith, A. Zolfaghari, H. R. Mortaheb, F. Meshkini, R. Jafari, E. Sutter, and F. Arefi-Khonsari. Control of the visible and UV light water splitting and photocatalysis of nitrogen doped TiO_2 thin films deposited by reactive magnetron sputtering. *Applied Catalysis B: Environmental*, 144:12–21, jan 2014. ISSN 09263373. URL <http://dx.doi.org/10.1016/j.apcatb.2013.06.028>.
- [155] J. M. Mwabora, T. Lindgren, E. Avendaño, T. F. Jaramillo, J. Lu, S.-E. Lindquist, and C.-G. Granqvist. Structure, Composition, and Morphology of Photoelectrochemically Active $\text{TiO}_{2-x} \text{N}_x$ Thin Films Deposited by Reactive DC Magnetron Sputtering. *The Journal of Physical Chemistry B*, 108(52):20193–20198, dec 2004. ISSN 1520-6106. URL <http://dx.doi.org/10.1021/jp0368987>.
- [156] C. Le Paven-Thivet, A. Ishikawa, A. Ziani, L. Le Gendre, M. Yoshida, J. Kubota, F. Tessier, and K. Domen. Photoelectrochemical Properties of Crystalline Perovskite Lanthanum Titanium Oxynitride Films under Visible Light. *The Journal of Physical Chemistry C*, 113(15):6156–6162, apr 2009. ISSN 1932-7447. URL <http://dx.doi.org/10.1021/jp811100r>.
- [157] I. Marozau, A. Shkabko, M. Döbeli, T. Lippert, M. Mallepell, C. Schneider, A. Weidenkaff, and A. Wokaun. Pulsed laser deposition and characterisation of perovskite-type $\text{LaTiO}_{3-x} \text{N}_x$ thin films. *Acta Materialia*, 59(19):7145–7154, nov 2011. ISSN 13596454. URL <http://dx.doi.org/10.1016/j.actamat.2011.08.019>.
- [158] Y.-I. Kim, W. Si, P. M. Woodward, E. Sutter, S. Park, and T. Vogt. Epitaxial Thin-Film Deposition and Dielectric Properties of the Perovskite Oxynitride $\text{BaTaO}_2 \text{N}$. *Chemistry of Materials*, 19(3):618–623, feb 2007. ISSN 0897-4756. URL <http://dx.doi.org/10.1021/cm062480k>.
- [159] F. Fabreguette, L. Imhoff, J. Guillot, B. Domenichini, M. Marco de Lucas, P. Sibillot, S. Bourgeois, and M. Sacilotti. Temperature and substrate influence on the structure of $\text{TiN}_x \text{O}_y$ thin films grown by low pressure metal organic chemical vapour deposition. *Surface and Coatings Technology*, 125(1-3):396–399, mar 2000. ISSN 02578972. URL [http://dx.doi.org/10.1016/S0257-8972\(99\)00588-5](http://dx.doi.org/10.1016/S0257-8972(99)00588-5).
- [160] G. Hyett, M. A. Green, and I. P. Parkin. The Use of Combinatorial Chemical Vapor Deposition in the Synthesis of $\text{Ti}_{3-\delta} \text{O}_4 \text{N}$ with $0.06 < \delta < 0.25$: A Titanium Oxynitride Phase Isostructural to Anosovite. *Journal of the American Chemical Society*, 129(50):15541–15548, dec 2007. ISSN 0002-7863. URL <http://dx.doi.org/10.1021/ja073355s>.
- [161] I. Marozau, A. Shkabko, G. Dinescu, M. Döbeli, T. Lippert, D. Logvinovich, M. Mallepell, C. Schneider, A. Weidenkaff, and A. Wokaun. Pulsed laser deposition and characterization of nitrogen-substituted SrTiO_3 thin films. *Applied Surface Science*, 255(10):5252–5255, mar 2009. ISSN 01694332. URL <http://dx.doi.org/10.1016/j.apsusc.2008.07.159>.
- [162] W.-J. Chun, A. Ishikawa, H. Fujisawa, T. Takata, J. N. Kondo, M. Hara, M. Kawai, Y. Matsumoto, and K. Domen. Conduction and Valence Band Positions of $\text{Ta}_2 \text{O}_5$, TaON , and $\text{Ta}_3 \text{N}_5$ by UPS and Electrochemical Methods. *The Journal of Physical Chemistry B*, 107(8):1798–1803, feb 2003. ISSN 1520-6106. URL <http://dx.doi.org/10.1021/jp027593f>.

-
- [163] R. Aguiar, D. Logvinovich, A. Weidenkaff, A. Rachel, A. Reller, and S. G. Ebbinghaus. The vast colour spectrum of ternary metal oxynitride pigments. *Dyes and Pigments*, 76(1):70–75, jan 2008. ISSN 01437208. URL <http://dx.doi.org/10.1016/j.dyepig.2006.08.029>.
- [164] S. Balaz, S. H. Porter, P. M. Woodward, and L. J. Brillson. Electronic Structure of Tantalum Oxynitride Perovskite Photocatalysts. *Chemistry of Materials*, 25(16):3337–3343, aug 2013. ISSN 0897-4756. URL <http://dx.doi.org/10.1021/cm401815w>.
- [165] M. Pichler, D. Pergolesi, S. Landsmann, V. Chawla, J. Michler, M. Döbeli, A. Wokaun, and T. Lippert. TiN-buffered substrates for photoelectrochemical measurements of oxynitride thin films. *Applied Surface Science*, 369:67–75, apr 2016. ISSN 01694332. URL <http://dx.doi.org/10.1016/j.apsusc.2016.01.197>.
- [166] G. Vankó, F. Renz, G. Molnár, T. Neisius, and S. Kárpáti. Hard-X-ray-induced excited-spin-state trapping. *Angewandte Chemie (International ed. in English)*, 46(28):5306–9, jan 2007. ISSN 1433-7851. URL <http://dx.doi.org/10.1002/anie.200604432>.
- [167] U. Bergmann and P. Glatzel. X-ray emission spectroscopy. *Photosynthesis research*, 102(2-3):255–66, jan 2009. ISSN 1573-5079. URL <http://dx.doi.org/10.1007/s11120-009-9483-6>.
- [168] P. Glatzel, U. Bergmann, F. M. F. de Groot, B. M. Weckhuysen, and S. P. Cramer. A Study of Transition Metal K Absorption Pre-Edges by Resonant Inelastic X-Ray Scattering RIXS. *Physica Scripta*, 2005 (T115):1032, 2005. ISSN 0031-8949. URL <http://dx.doi.org/10.1238/Physica.Topical.115a01032>.
- [169] J. Czapla, W. M. Kwiatek, J. Lekki, J. Dulińska-Litewka, R. Steininger, and J. Göttlicher. Chemical species of sulfur in prostate cancer cells studied by XANES spectroscopy. *Radiation Physics and Chemistry*, 93:154–159, dec 2013. ISSN 0969806X. URL <http://dx.doi.org/10.1016/j.radphyschem.2013.05.021>.
- [170] J. Szlachetko, D. Ferri, V. Marchionni, A. Kambolis, O. V. Safonova, C. J. Milne, O. Kröcher, M. Nachtegaal, and J. Sá. Subsecond and in situ chemical speciation of Pt/Al₂O₃ during oxidation-reduction cycles monitored by high-energy resolution off-resonant X-ray spectroscopy. *Journal of the American Chemical Society*, 135(51):19071–4, dec 2013. ISSN 1520-5126. URL <http://dx.doi.org/10.1021/ja410146c>.
- [171] M. Sikora, A. Juhin, T.-C. Weng, P. Sainctavit, C. Detlefs, F. de Groot, and P. Glatzel. Strong K-edge magnetic circular dichroism observed in photon-in-photon-out spectroscopy. *Physical review letters*, 105 (3):037202, jul 2010. ISSN 1079-7114. URL <http://dx.doi.org/10.1103/PhysRevLett.105.037202>.
- [172] J. Singh, C. Lamberti, and J. A. van Bokhoven. Advanced X-ray absorption and emission spectroscopy: in situ catalytic studies. *Chemical Society reviews*, 39(12):4754–66, dec 2010. ISSN 1460-4744. URL <http://dx.doi.org/10.1039/c0cs00054j>.
- [173] K. M. Lancaster, M. Roemelt, P. Ettenhuber, Y. Hu, M. W. Ribbe, F. Neese, U. Bergmann, and S. DeBeer. X-ray emission spectroscopy evidences a central carbon in the nitrogenase iron-molybdenum cofactor. *Science (New York, N.Y.)*, 334(6058):974–7, nov 2011. ISSN 1095-9203. URL <http://dx.doi.org/10.1126/science.1206445>.
- [174] W. M. Kwiatek, J. Czapla, M. Podgórczyk, A. Kisiel, J. Konior, and A. Balerna. First approach to studies of sulphur electron DOS in prostate cancer cell lines and tissues studied by XANES. *Radiation Physics and Chemistry*, 80(10):1104–1108, oct 2011. ISSN 0969806X. URL <http://dx.doi.org/10.1016/j.radphyschem.2011.05.005>.
- [175] J. Szlachetko, J. Sá, M. Nachtegaal, U. Hartfelder, J.-C. Dousse, J. Hozzowska, D. L. Abreu Fernandes, H. Shi, and C. Stampfl. Real Time Determination of the Electronic Structure of Unstable Reaction Intermediates during Au₂O₃ Reduction. *The journal of physical chemistry letters*, 5(1):80–4, jan 2014. ISSN 1948-7185. URL <http://dx.doi.org/10.1021/jz402309s>.

References

- [176] J. Szlachetko and J. Sá. Rational design of oxynitride materials: From theory to experiment. *CrystEngComm*, 15(14):2583, 2013. ISSN 1466-8033. URL <http://dx.doi.org/10.1039/c3ce26909d>.
- [177] J. Szlachetko, M. Pichler, D. Pergolesi, J. Sá, and T. Lippert. Determination of conduction and valence band electronic structure of $\text{La}_2\text{Ti}_2\text{O}_7$ thin film. *RSC Advances*, 4(22):11420, feb 2014. ISSN 2046-2069. URL <http://dx.doi.org/10.1039/c3ra47357k>.
- [178] K. Kollbek, M. Sikora, C. Kapusta, J. Szlachetko, K. Zakrzewska, K. Kowalski, and M. Radecka. X-ray spectroscopic methods in the studies of nonstoichiometric TiO_{2-x} thin films. *Applied Surface Science*, 281:100–104, sep 2013. ISSN 01694332. URL <http://dx.doi.org/10.1016/j.apsusc.2013.02.119>.
- [179] J. Sá, Y. Kayser, C. J. Milne, D. L. Abreu Fernandes, and J. Szlachetko. Temperature-programmed reduction of NiO nanoparticles followed by time-resolved RIXS. *Physical chemistry chemical physics : PCCP*, 16(17):7692–6, may 2014. ISSN 1463-9084. URL <http://dx.doi.org/10.1039/c3cp54622e>.
- [180] J. J. Rehr, J. J. Kas, F. D. Vila, M. P. Prange, and K. Jorissen. Parameter-free calculations of X-ray spectra with FEFF9. *Physical chemistry chemical physics : PCCP*, 12(21):5503–13, jun 2010. ISSN 1463-9084. URL <http://dx.doi.org/10.1039/b926434e>.
- [181] J. J. Rehr, J. J. Kas, M. P. Prange, A. P. Sorini, Y. Takimoto, and F. Vila. Ab initio theory and calculations of X-ray spectra. *Comptes Rendus Physique*, 10(6):548–559, jul 2009. ISSN 16310705. URL <http://dx.doi.org/10.1016/j.crhy.2008.08.004>.
- [182] M. Lorenz and M. S. Ramachandra Rao. 25 years of pulsed laser deposition. *Journal of Physics D: Applied Physics*, 47(3):030301, jan 2014. ISSN 0022-3727. URL <http://dx.doi.org/10.1088/0022-3727/47/3/030301>.
- [183] P. Willmott. Pulsed reactive crossed-beam laser ablation. *Applied Physics A: Materials Science & Processing*, 69(7):S437–S440, dec 1999. ISSN 0947-8396. URL <http://dx.doi.org/10.1007/s003399900354>.
- [184] J. Chen, D. Stender, M. Pichler, M. Döbeli, D. Pergolesi, C. W. Schneider, A. Wokaun, and T. Lippert. Tracing the plasma interactions for pulsed reactive crossed-beam laser ablation. *Journal of Applied Physics*, 118(16):165306, oct 2015. ISSN 0021-8979. URL <http://dx.doi.org/10.1063/1.4934553>.
- [185] L. R. Doolittle. A semiautomatic algorithm for rutherford backscattering analysis. *Nuclear Instruments and Methods in Physics Research Section B: Beam Interactions with Materials and Atoms*, 15(1-6):227–231, apr 1986. ISSN 0168583X. URL [http://dx.doi.org/10.1016/0168-583X\(86\)90291-0](http://dx.doi.org/10.1016/0168-583X(86)90291-0).
- [186] C. Kottler, M. Döbeli, F. Glaus, and M. Suter. A spectrometer for low-energy heavy ion ERDA. *Nuclear instruments & methods in physics research. Section B, Beam interactions with materials and atoms*, 248(1):155–162, 2006. URL <http://dx.doi.org/10.1016/j.nimb.2006.02.013>.
- [187] D. A. Shirley. High-Resolution X-Ray Photoemission Spectrum of the Valence Bands of Gold. *Physical Review B*, 5(12):4709–4714, jun 1972. ISSN 0556-2805. URL <http://dx.doi.org/10.1103/PhysRevB.5.4709>.
- [188] J. Scofield. Hartree-Slater subshell photoionization cross-sections at 1254 and 1487 eV. *Journal of Electron Spectroscopy and Related Phenomena*, 8(2):129–137, jan 1976. ISSN 03682048. URL [http://dx.doi.org/10.1016/0368-2048\(76\)80015-1](http://dx.doi.org/10.1016/0368-2048(76)80015-1).
- [189] H. H. Brongersma. Low-Energy Ion Scattering. In *E.N. Kaufmann (Ed.) Characterization of Materials*, pages 2024–2044. John Wiley & Sons Inc., New York, second edition, 2012. URL <http://dx.doi.org/10.1002/0471266965>.

-
- [190] H. Brongersma, M. Draxler, M. Deridder, and P. Bauer. Surface composition analysis by low-energy ion scattering. *Surface Science Reports*, 62(3):63–109, mar 2007. ISSN 01675729. URL <http://dx.doi.org/10.1016/j.surfrep.2006.12.002>.
- [191] M. de Ridder, R. G. van Welzenis, and H. H. Brongersma. Surface cleaning and characterization of yttria-stabilized zirconia. *Surface and Interface Analysis*, 33(4):309–317, apr 2002. ISSN 0142-2421. URL <http://dx.doi.org/10.1002/sia.1196>.
- [192] H. Téllez, A. Aguadero, J. Druce, M. Burriel, S. Fearn, T. Ishihara, D. S. McPhail, and J. A. Kilner. New perspectives in the surface analysis of energy materials by combined time-of-flight secondary ion mass spectrometry (ToF-SIMS) and high sensitivity low-energy ion scattering (HS-LEIS). *Journal of Analytical Atomic Spectrometry*, 29(8):1361, may 2014. ISSN 0267-9477. URL <http://dx.doi.org/10.1039/C3JA50292A>.
- [193] M. Kiuchi and A. Chayahara. Titanium nitride for transparent conductors. *Applied Physics Letters*, 64(8):1048, feb 1994. ISSN 00036951. URL <http://dx.doi.org/10.1063/1.110966>.
- [194] M. Kiuchi, A. Chayahara, M. Tarutani, Y. Takai, and R. Shimizu. The microstructure of transparent and electrically conducting titanium nitride films. *Materials Chemistry and Physics*, 54(1):330–333, 1998.
- [195] V. Craciun, D. Craciun, C. Ghica, L. Trupina, C. Flueraru, and N. Nastase. Growth of thin transparent titanium nitride layers by reactive laser ablation. *Applied Surface Science*, 138:593–598, 1999.
- [196] R. Swanepoel. Determination of the thickness and optical constants of amorphous silicon. *Journal of Physics E: Scientific Instruments*, 16(12):1214–1222, dec 1983. ISSN 0022-3735. URL <http://dx.doi.org/10.1088/0022-3735/16/12/023>.
- [197] H. W. Eng, P. W. Barnes, B. M. Auer, and P. M. Woodward. Investigations of the electronic structure of d0 transition metal oxides belonging to the perovskite family. *Journal of Solid State Chemistry*, 175(1):94–109, oct 2003. ISSN 00224596. URL [http://dx.doi.org/10.1016/S0022-4596\(03\)00289-5](http://dx.doi.org/10.1016/S0022-4596(03)00289-5).
- [198] M. Birkholz. *Thin Film Analysis by X-Ray Scattering*. WILEY-VCH Verlag GmbH & Co. KG, 2005.
- [199] A. Murphy. Band-gap determination from diffuse reflectance measurements of semiconductor films, and application to photoelectrochemical water-splitting. *Solar Energy Materials and Solar Cells*, 91(14):1326–1337, sep 2007. ISSN 09270248. URL <http://dx.doi.org/10.1016/j.solmat.2007.05.005>.
- [200] K. A. Michalow, D. Logvinovich, A. Weidenkaff, M. Amberg, G. Fortunato, A. Heel, T. Graule, and M. Rekas. Synthesis, characterization and electronic structure of nitrogen-doped TiO₂ nanopowder. *Catalysis Today*, 144(1-2):7–12, jun 2009. ISSN 09205861. URL <http://dx.doi.org/10.1016/j.cattod.2008.12.015>.
- [201] F. de Groot and A. Kotani. *Core Level Spectroscopy of Solids*. CRC Press, 2008. ISBN 1420008420.
- [202] J. Szlachetko, M. Nachtegaal, E. de Boni, M. Willmann, O. Safonova, J. Sa, G. Smolentsev, M. Szlachetko, J. A. van Bokhoven, J.-C. Dousse, J. Hoszowska, Y. Kayser, P. Jagodzinski, A. Bergamaschi, B. Schmitt, C. David, and A. Lücke. A von Hamos x-ray spectrometer based on a segmented-type diffraction crystal for single-shot x-ray emission spectroscopy and time-resolved resonant inelastic x-ray scattering studies. *The Review of scientific instruments*, 83(10):103105, oct 2012. ISSN 1089-7623. URL <http://dx.doi.org/10.1063/1.4756691>.
- [203] S. Univ. of Washington. DOS calculations with the FEFF9.0 code, 1990.

References

- [204] A. L. Ankudinov, B. Ravel, J. J. Rehr, and S. D. Conradson. Real-space multiple-scattering calculation and interpretation of x-ray-absorption near-edge structure. *Physical Review B*, 58(12):7565–7576, sep 1998. ISSN 0163-1829. URL <http://dx.doi.org/10.1103/PhysRevB.58.7565>.
- [205] J. J. Rehr and R. C. Albers. Theoretical approaches to x-ray absorption fine structure. *Reviews of Modern Physics*, 72(3):621–654, jul 2000. ISSN 0034-6861. URL <http://dx.doi.org/10.1103/RevModPhys.72.621>.
- [206] A. L. Ankudinov, J. J. Rehr, J. Low, and S. R. Bare. Effect of Hydrogen Adsorption on the X-Ray Absorption Spectra of Small Pt Clusters. *Physical Review Letters*, 86(8):1642–1645, feb 2001. ISSN 0031-9007. URL <http://dx.doi.org/10.1103/PhysRevLett.86.1642>.
- [207] J. Sá, G. Tagliabue, P. Friedli, J. Szlachetko, M. H. Rittmann-Frank, F. G. Santomauro, C. J. Milne, and H. Sigg. Direct observation of charge separation on Au localized surface plasmons. *Energy & Environmental Science*, 6(12):3584, nov 2013. ISSN 1754-5692. URL <http://dx.doi.org/10.1039/c3ee42731e>.
- [208] T. Lopes, L. Andrade, H. A. Ribeiro, and A. Mendes. Characterization of photoelectrochemical cells for water splitting by electrochemical impedance spectroscopy. *International Journal of Hydrogen Energy*, 35(20):11601–11608, oct 2010. ISSN 0360-3199. URL <http://dx.doi.org/10.1016/j.ijhydene.2010.04.001>.
- [209] J. Schou. Physical aspects of the pulsed laser deposition technique: The stoichiometric transfer of material from target to film. *Applied Surface Science*, 255(10):5191–5198, mar 2009. ISSN 0169-4332. URL <http://dx.doi.org/10.1016/j.apsusc.2008.10.101>.
- [210] A. Ojeda-G-P, C. W. Schneider, M. Döbeli, T. Lippert, and A. Wokaun. Angular distribution of species in pulsed laser deposition of $\text{La}_x\text{Ca}_{1-x}\text{MnO}_3$. *Applied Surface Science*, 336:150–156, may 2015. ISSN 0169-4332. URL <http://dx.doi.org/10.1016/j.apsusc.2014.10.089>.
- [211] L. K. Joseph, K. R. Dayas, S. Damodar, B. Krishnan, K. Krishnankutty, V. P. N. Nampoory, and P. Radhakrishnan. Photoluminescence studies on rare earth titanates prepared by self-propagating high temperature synthesis method. *Spectrochimica acta. Part A, Molecular and biomolecular spectroscopy*, 71(4):1281–5, dec 2008. ISSN 1386-1425. URL <http://dx.doi.org/10.1016/j.saa.2008.03.030>.
- [212] L. Fleming, C. C. Fulton, G. Lucovsky, J. E. Rowe, M. D. Ulrich, and J. Luning. Local bonding analysis of the valence and conduction band features of TiO_2 . *Journal of Applied Physics*, 102(3):033707, aug 2007. ISSN 0021-8979. URL <http://dx.doi.org/10.1063/1.2764004>.
- [213] H. G. Kim, D. W. Hwang, S. W. Bae, J. H. Jung, and J. S. Lee. Photocatalytic Water Splitting over $\text{La}_2\text{Ti}_2\text{O}_7$ Synthesized by the Polymerizable Complex Method. *Catalysis Letters*, 91(3/4):193–198, dec 2003. ISSN 1011-372X. URL <http://dx.doi.org/10.1023/B:CATL.0000007154.30343.23>.
- [214] F. Lichtenberg, D. Widmer, J. G. Bednorz, T. Williams, and A. Reller. Phase diagram of LaTiO_x : from 2D layered ferroelectric insulator to 3D weak ferromagnetic semiconductor. *Zeitschrift für Physik B Condensed Matter*, 82(2):211–216, jun 1991. ISSN 0722-3277. URL <http://dx.doi.org/10.1007/BF01324328>.
- [215] S. Havelia, K. Balasubramaniam, S. Spurgeon, F. Cormack, and P. Salvador. Growth of $\text{La}_2\text{Ti}_2\text{O}_7$ and LaTiO_3 thin films using pulsed laser deposition. *Journal of Crystal Growth*, 310(7-9):1985–1990, apr 2008. ISSN 0022-0248. URL <http://dx.doi.org/10.1016/j.jcrysgro.2007.12.006>.
- [216] F. Lichtenberg. Synthesis of perovskite-related layered $\text{A}_n\text{B}_n\text{O}_{3n+2} = \text{ABOX}$ type niobates and titanates and study of their structural, electric and magnetic properties. *Progress in Solid State Chemistry*, 29(1-2):1–70, jan 2001. ISSN 0079-6786. URL [http://dx.doi.org/10.1016/S0079-6786\(01\)00002-4](http://dx.doi.org/10.1016/S0079-6786(01)00002-4).

-
- [217] A. E. Maegli, E. H. Otal, T. Hisatomi, S. Yoon, C. M. Leroy, N. Schäuble, Y. Lu, M. Grätzel, and A. Weidenkaff. Perovskite-Type LaTiO_2 N Oxynitrides for Solar Water Splitting: Influence of the Synthesis Conditions. *Energy Procedia*, 22(null):61–66, jan 2012. ISSN 18766102. URL <http://dx.doi.org/10.1016/j.egypro.2012.05.218>.
- [218] K. Domen, M. Hara, J. N. Kondo, T. Takata, A. Kudo, H. Kobayashi, and Y. Inoue. New aspects of heterogeneous photocatalysts for water decomposition. *Korean Journal of Chemical Engineering*, 18(6): 862–866, nov 2001. ISSN 0256-1115. URL <http://dx.doi.org/10.1007/BF02705609>.
- [219] C. Di Valentin, G. Pacchioni, and A. Selloni. Origin of the different photoactivity of N -doped anatase and rutile TiO_2 . *Physical Review B*, 70(8):085116, aug 2004. ISSN 1098-0121. URL <http://dx.doi.org/10.1103/PhysRevB.70.085116>.
- [220] P. Glatzel, M. Sikora, and M. Fernández-García. Resonant X-ray spectroscopy to study K absorption pre-edges in 3d transition metal compounds. *The European Physical Journal Special Topics*, 169(1): 207–214, may 2009. ISSN 1951-6355. URL <http://dx.doi.org/10.1140/epjst/e2009-00994-7>.
- [221] J. J. Mortensen, L. B. Hansen, and K. W. Jacobsen. Real-space grid implementation of the projector augmented wave method. *Physical Review B*, 71(3):035109, jan 2005. ISSN 1098-0121. URL <http://dx.doi.org/10.1103/PhysRevB.71.035109>.
- [222] J. Enkovaara, C. Rostgaard, J. J. Mortensen, J. Chen, M. Dulak, L. Ferrighi, J. Gavnholt, C. Glinsvad, V. Haikola, H. A. Hansen, H. H. Kristoffersen, M. Kuisma, A. H. Larsen, L. Lehtovaara, M. Ljungberg, O. Lopez-Acevedo, P. G. Moses, J. Ojanen, T. Olsen, V. Petzold, N. A. Romero, J. Stausholm-Møller, M. Strange, G. A. Tritsarlis, M. Vanin, M. Walter, B. Hammer, H. Häkkinen, G. K. H. Madsen, R. M. Nieminen, J. K. Nørskov, M. Puska, T. T. Rantala, J. Schiøtz, K. S. Thygesen, and K. W. Jacobsen. Electronic structure calculations with GPAW: a real-space implementation of the projector augmented-wave method. *Journal of physics. Condensed matter : an Institute of Physics journal*, 22(25):253202, jun 2010. ISSN 1361-648X. URL <http://dx.doi.org/10.1088/0953-8984/22/25/253202>.
- [223] J. P. Perdew, A. Ruzsinszky, G. I. Csonka, O. A. Vydrov, G. E. Scuseria, L. A. Constantin, X. Zhou, and K. Burke. Restoring the density-gradient expansion for exchange in solids and surfaces. *Physical review letters*, 100(13):136406, apr 2008. ISSN 0031-9007. URL <http://dx.doi.org/10.1103/PhysRevLett.100.136406>.
- [224] I. E. Castelli, K. S. Thygesen, and K. W. Jacobsen. Calculated optical absorption of different perovskite phases. *J. Mater. Chem. A*, 3(23):12343–12349, jun 2015. ISSN 2050-7488. URL <http://dx.doi.org/10.1039/C5TA01586C>.
- [225] R. F. W. Bader. *Atoms in Molecules: A Quantum Theory*. Oxford University Press, New York, 1990. ISBN 9780198558651. URL <http://dx.doi.org/10.1002/0470845015>.
- [226] W. Tang, E. Sanville, and G. Henkelman. A grid-based Bader analysis algorithm without lattice bias. *Journal of physics. Condensed matter : an Institute of Physics journal*, 21(8):084204, feb 2009. ISSN 0953-8984. URL <http://dx.doi.org/10.1088/0953-8984/21/8/084204>.
- [227] C. W. Schneider, M. Esposito, I. Marozau, K. Conder, M. Doebeli, Y. Hu, M. Mallepell, A. Wokaun, and T. Lippert. The origin of oxygen in oxide thin films: Role of the substrate. *Applied Physics Letters*, 97(19):192107, nov 2010. ISSN 00036951. URL <http://dx.doi.org/10.1063/1.3515849>.
- [228] H. N. Lee, H. M. Christen, M. F. Chisholm, C. M. Rouleau, and D. H. Lowndes. Thermal stability of epitaxial SrRuO_3 films as a function of oxygen pressure. *Applied Physics Letters*, 84(20):4107, may 2004. ISSN 00036951. URL <http://dx.doi.org/10.1063/1.1753650>.

References

- [229] J. Shin, S. Kalinin, H. Lee, H. Christen, R. Moore, E. Plummer, and A. Baddorf. Surface stability of epitaxial SrRuO₃ films. *Surface Science*, 581(2-3):118–132, may 2005. ISSN 00396028. URL <http://dx.doi.org/10.1016/j.susc.2005.02.038>.
- [230] K. Mougín, Z. Zheng, N. Piazzon, E. Gnecco, and H. Haidara. Thermal stability and reconstruction of nanoparticulate Au film on model molecular surfaces. *Journal of colloid and interface science*, 333(2): 719–24, may 2009. ISSN 1095-7103. URL <http://dx.doi.org/10.1016/j.jcis.2009.01.044>.
- [231] D. Pergolesi, E. Fabbri, S. N. Cook, V. Roddatis, E. Traversa, and J. A. Kilner. Tensile lattice distortion does not affect oxygen transport in yttria-stabilized zirconia-CeO₂ heterointerfaces. *ACS nano*, 6(12): 10524–34, dec 2012. ISSN 1936-086X. URL <http://dx.doi.org/10.1021/nn302812m>.
- [232] S. Sanna, V. Esposito, D. Pergolesi, A. Orsini, A. Tebano, S. Licoccia, G. Balestrino, and E. Traversa. Fabrication and Electrochemical Properties of Epitaxial Samarium-Doped Ceria Films on SrTiO₃-Buffered MgO Substrates. *Advanced Functional Materials*, 19(11):1713–1719, jun 2009. ISSN 1616301X. URL <http://dx.doi.org/10.1002/adfm.200801768>.
- [233] A. Tiwari, J. Narayan, C. Jin, and A. Kvit. Growth of epitaxial NdNiO₃ and integration with Si(100). *Applied Physics Letters*, 80(8):1337, feb 2002. ISSN 00036951. URL <http://dx.doi.org/10.1063/1.1451984>.
- [234] K. Wong and Y. Leung. Heteroepitaxial growth of La_{0.7}Ca_{0.3}MnO₃/SrTiO₃/TiN/Si by pulsed laser deposition. *Thin Solid Films*, 354(1-2):55–58, oct 1999. ISSN 00406090. URL [http://dx.doi.org/10.1016/S0040-6090\(99\)00529-5](http://dx.doi.org/10.1016/S0040-6090(99)00529-5).
- [235] W. Wu, K. Wong, and C. Choy. Epitaxial growth of SrTiO₃ films with different orientations on TiN buffered Si(001) by pulsed laser deposition. *Thin Solid Films*, 360(1-2):103–106, feb 2000. ISSN 00406090. URL [http://dx.doi.org/10.1016/S0040-6090\(99\)01091-3](http://dx.doi.org/10.1016/S0040-6090(99)01091-3).
- [236] R. Pérez Casero, R. Gómez San Román, J. Perrière, A. Laurent, W. Seiler, P. Gergaud, and D. Keller. Epitaxial growth of CeO₂ on MgO by pulsed laser deposition. *Applied Surface Science*, 109-110:341–344, feb 1997. ISSN 01694332. URL [http://dx.doi.org/10.1016/S0169-4332\(96\)00671-X](http://dx.doi.org/10.1016/S0169-4332(96)00671-X).
- [237] L. Chen, C. L. Chen, X. Chen, W. Donner, S. W. Liu, Y. Lin, D. X. Huang, and A. J. Jacobson. Electrical properties of a highly oriented, textured thin film of the ionic conductor Gd:CeO_{2-δ} on (001) MgO. *Applied Physics Letters*, 83(23):4737, dec 2003. ISSN 00036951. URL <http://dx.doi.org/10.1063/1.1629378>.
- [238] N. C. Saha and H. G. Tompkins. Titanium nitride oxidation chemistry: An x-ray photoelectron spectroscopy study. *Journal of Applied Physics*, 72(7):3072, oct 1992. ISSN 00218979. URL <http://dx.doi.org/10.1063/1.351465>.
- [239] L. Hultman, S. Barnett, J.-E. Sundgren, and J. Greene. Growth of epitaxial TiN films deposited on MgO(100) by reactive magnetron sputtering: The role of low-energy ion irradiation during deposition. *Journal of Crystal Growth*, 92(3-4):639–656, oct 1988. ISSN 00220248. URL [http://dx.doi.org/10.1016/0022-0248\(88\)90048-6](http://dx.doi.org/10.1016/0022-0248(88)90048-6).
- [240] A. K. Sharma, A. Kvit, and J. Narayan. Growth of single crystal MgO on TiN/Si heterostructure by pulsed laser deposition. *Journal of Vacuum Science & Technology A: Vacuum, Surfaces, and Films*, 17(6):3393, nov 1999. ISSN 07342101. URL <http://dx.doi.org/10.1116/1.582071>.
- [241] R. M. Costescu, M. A. Wall, and D. G. Cahill. Thermal conductance of epitaxial interfaces. *Physical Review B*, 67(5):054302, feb 2003. ISSN 0163-1829. URL <http://dx.doi.org/10.1103/PhysRevB.67.054302>.

-
- [242] W. -C. Chen, Y.-R. Lin, X.-J. Guo, and S.-T. Wu. Heteroepitaxial TiN of Very Low Mosaic Spread on Al₂O₃. *Japanese Journal of Applied Physics*, 42(Part 1, No. 1):208–212, jan 2003. ISSN 0021-4922. URL <http://dx.doi.org/10.1143/JJAP.42.208>.
- [243] X. Lu, A. Bandara, M. Katayama, A. Yamakata, J. Kubota, and K. Domen. Infrared Spectroscopic Study of the Potential Change at Cocatalyst Particles on Oxynitride Photocatalysts for Water Splitting by Visible Light Irradiation. *The Journal of Physical Chemistry C*, 115(48):23902–23907, dec 2011. ISSN 1932-7447. URL <http://dx.doi.org/10.1021/jp207484q>.
- [244] N. G. Sarda, M. Omune, T. Hayashi, A. Chan, S. Kataoka, K. -I. Murai, G. I. Waterhouse, and T. Moriga. Structural and optical properties of perovskite-type LaTiO₂N synthesized using urea or thiourea as co-nitriding agents. *Journal of the European Ceramic Society*, 35(12):3311–3317, oct 2015. ISSN 09552219. URL <http://dx.doi.org/10.1016/j.jeurceramsoc.2015.02.019>.
- [245] M. Matsukawa, R. Ishikawa, T. Hisatomi, Y. Moriya, N. Shibata, J. Kubota, Y. Ikuhara, and K. Domen. Enhancing Photocatalytic Activity of LaTiO₂N by Removal of Surface Reconstruction Layer. *Nano letters*, jan 2014. ISSN 1530-6992. URL <http://dx.doi.org/10.1021/nl404688h>.
- [246] H. Bender, W. Chen, J. Portillo, L. Van den Hove, and W. Vandervorst. AES and XPS analysis of the interaction of Ti with Si and SiO₂ during RTA. *Applied Surface Science*, 38(1-4):37–47, sep 1989. ISSN 01694332. URL [http://dx.doi.org/10.1016/0169-4332\(89\)90516-3](http://dx.doi.org/10.1016/0169-4332(89)90516-3).
- [247] H. Man, Z. Cui, and X. Yang. Analysis of laser gas nitrided titanium by X-ray photoelectron spectroscopy. *Applied Surface Science*, 199(1-4):293–302, oct 2002. ISSN 01694332. URL [http://dx.doi.org/10.1016/S0169-4332\(02\)00866-8](http://dx.doi.org/10.1016/S0169-4332(02)00866-8).
- [248] J. F. Marco, A. C. Agudelo, J. R. Gancedo, and D. Hanžel. Corrosion resistance of single TiN layers, Ti/TiN bilayers and Ti/TiN/Ti/TiN multilayers on iron under a salt fog spray (phohesion) test: an evaluation by XPS. *Surface and Interface Analysis*, 27(2):71–75, feb 1999. ISSN 0142-2421. URL [http://dx.doi.org/10.1002/\(SICI\)1096-9918\(199902\)27:2<71::AID-SIA469>3.0.CO;2-G](http://dx.doi.org/10.1002/(SICI)1096-9918(199902)27:2<71::AID-SIA469>3.0.CO;2-G).
- [249] M. Matsuoka, S. Isotani, J. C. R. Mittani, J. F. D. Chubaci, K. Ogata, and N. Kuratani. Effects of arrival rate and gas pressure on the chemical bonding and composition in titanium nitride films prepared on Si(100) substrates by ion beam and vapor deposition. *Journal of Vacuum Science & Technology A: Vacuum, Surfaces, and Films*, 23(1):137, dec 2005. ISSN 07342101. URL <http://dx.doi.org/10.1116/1.1839895>.
- [250] S. Badrinarayanan, S. Sinha, and A. Mandale. XPS studies of nitrogen ion implanted zirconium and titanium. *Journal of Electron Spectroscopy and Related Phenomena*, 49(3):303–309, jan 1989. ISSN 03682048. URL [http://dx.doi.org/10.1016/0368-2048\(89\)85018-2](http://dx.doi.org/10.1016/0368-2048(89)85018-2).
- [251] X. Song, D. Gopireddy, and C. G. Takoudis. Characterization of titanium oxynitride films deposited by low pressure chemical vapor deposition using amide Ti precursor. *Thin Solid Films*, 516(18):6330–6335, jul 2008. ISSN 00406090. URL <http://dx.doi.org/10.1016/j.tsf.2007.12.148>.
- [252] U.S. Secretary of Commerce on behalf of the United States of America. NIST XPS Database, 2012.
- [253] B. Klahr, S. Gimenez, F. Fabregat-Santiago, J. Bisquert, and T. W. Hamann. Photoelectrochemical and impedance spectroscopic investigation of water oxidation with "Co-Pi"-coated hematite electrodes. *Journal of the American Chemical Society*, 134(40):16693–700, oct 2012. ISSN 1520-5126. URL <http://dx.doi.org/10.1021/ja306427f>.
- [254] J. K. Cooper, S. Gul, F. M. Toma, L. Chen, Y. -S. Liu, J. Guo, J. W. Ager, J. Yano, and I. D. Sharp. Indirect Bandgap and Optical Properties of Monoclinic Bismuth Vanadate. *The Journal of Physical Chemistry C*, 119(6):2969–2974, feb 2015. ISSN 1932-7447. URL <http://dx.doi.org/10.1021/jp512169w>.

References

- [255] N. M. Haegel. Integrating electron and near-field optics: dual vision for the nanoworld. *Nanophotonics*, 3(1-2):75–89, jan 2014. ISSN 2192-8614. URL <http://dx.doi.org/10.1515/nanoph-2013-0048>.
- [256] S. N. Habisreutinger, L. Schmidt-Mende, and J. K. Stolarczyk. Photocatalytic reduction of CO₂ on TiO₂ and other semiconductors. *Angewandte Chemie (International ed. in English)*, 52(29):7372–408, jul 2013. ISSN 1521-3773. URL <http://dx.doi.org/10.1002/anie.201207199>.
- [257] F. Saladin, A. Meier, and I. Kamber. A miniaturized reactor for photocatalysis and for simultaneous in situ spectroscopy. *Review of Scientific Instruments*, 67(6):2406, jun 1996. ISSN 00346748. URL <http://dx.doi.org/10.1063/1.1147008>.
- [258] F. Saladin and I. Alxneit. Temperature dependence of the photochemical reduction of CO₂ in the presence of H₂ O at the solid/gas interface of TiO₂. *Journal of the Chemical Society, Faraday Transactions*, 93(23):4159–4163, jan 1997. ISSN 09565000. URL <http://dx.doi.org/10.1039/a704801g>.
- [259] I. Alxneit and M. Corboz. Influence of photoadsorbed O₂ on the photoreduction of CO₂ with H₂ O at the surface of TiO₂. *Le Journal de Physique IV*, 09(PR3):Pr3–295–Pr3–299, mar 1999. ISSN 1155-4339. URL <http://dx.doi.org/10.1051/jp4:1999345>.
- [260] M. Corboz, I. Alxneit, G. Stoll, and H. R. Tschudi. On the Determination of Quantum Efficiencies in Heterogeneous Photocatalysis. *The Journal of Physical Chemistry B*, 104(45):10569–10577, nov 2000. ISSN 1520-6106. URL <http://dx.doi.org/10.1021/jp000253e>.

Acknowledgment

During the last three and a half years, I had the great opportunity to conduct my PhD in the Materials Group of Thomas Lippert at the Paul Scherrer Institute (PSI). In this time I had the change to meet a lot of excellent people, who helped and supported me a lot, which also made this thesis possible. Therefore my special thanks go to:

First I want to thank Prof. Dr. Alexander Wokaun and Prof. Dr. Dr. *h.c.* Thomas Lippert for their supervision of my PhD. Further, my thanks go to Prof. Dr. Christophe Copéret and Prof. Dr. Maria Dinescu, for taking the time to be my co-examiner and to review my thesis.

My thanks also go to Romania, to the Photonic Processing of Advanced Materials Group at the National Institute for Laser, Plasma and Radiation Physics. My special thanks go to Prof. Dr. Maria Dinescu, Dr. Nicu Scarisoreanu, Dr. Valentin Ion, Dr. Mihaela Filipescu and Antoniu Moldovan for the good collaboration in the joined project (SNF funding No IZERZ0_142176 from the Romanian-Swiss Research Program).

It was a big advantage having the Electrochemistry Laboratory (LEC) around the corner at PSI. Special thanks to Dr. Emiliana Fabbri, Dr. Anastasia Aleksandrovna Permyakova and Sandra Temmel for their help with the start-up of our new photoelectrochemical test setup and for fruitful discussion of the obtained results. Thanks also to Dr. Mario El Kazzi and Dr. Emiliana Fabbri for their scientific support regarding the performed X-ray Photoelectron Spectroscopy measurements and analysis.

It was a pleasure having Dr. Jakub Szlachetko in the team for the X-ray spectroscopy measurements at the Swiss Light Source at PSI. He was a great help for performing the measurement and for analyzing the data.

Dr. Max Döbeli from ETH Zurich (Laboratory of Ion Beam Physics, Institute for Particle Physics, Department of Physics) was for this work indispensable. PhD life would have been much more difficult (and sometimes easier) without the Rutherford Backscattering and Heavy-Ion Elastic Recoil Detection Analysis

measurements. Thank you for all the discussions during the many visits at Hönggerberg and for introducing me into the world of material analysis by nuclear techniques.

Thanks to Dr. Helena Téllez and Dr. John Druce from the Kyushu University (International Institute for Carbon-Neutral Energy Research (I2CNER), Electrochemical Energy Conversion Division, Japan) for the very helpful Low-energy ion scattering spectroscopy and Time-of-Flight Secondary Ion Mass Spectrometry measurements, that lead to a deeper understanding of my oxynitride thin film samples.

For the initial photoelectrochemical measurements I had the opportunity to go to the Swiss Federal Laboratories for Materials Science and Technology (EMPA) in Dübendorf (Laboratory Materials for Energy Conversion). Thanks to Dr. Steve Landsmann, Dr. Alexandra Mägli and Matthias Trottmann for induct me to the field of photoelectrochemistry during the many visits in your group and for the pleasant company.

I appreciate the help of Dr. Vipin Chawla and Dr. Johann Michler from EMPA in Thun (Laboratory for Mechanics of Materials and Nanostructures). The provision of many TiN-coated substrates facilitated the foundation of the described model system, which is the basis of the photoelectrochemistry part of my thesis.

I really cherished the teamwork in the Materials Group. Thanks to all the former and current group members for their continuous support, be it for the highly appreciated input on my papers (in alphabetic order, Daniele, Mike, Wen-ping) or the helping hand in the lab (in alphabetic order, Alejandro, Alexandra, Aline, Christof, Daniele, Dieter, Fatima, Kenta, Mike, Sandra, Thomas, Wen-ping, Xiang) or for the free time spent together.

My deepest gratitude belongs also to my family with their love and support on my way through life. Thanks to Jasmin for being the sunshine in my life and for your support during the time of my PhD.



Eidgenössische Technische Hochschule Zürich
Swiss Federal Institute of Technology Zurich

PAUL SCHERRER INSTITUT

